UNIVERSITY OF CALIFORNIA,
IRVINE

Integration of Solid Oxide Fuel Cell with Liquid Desiccant Cooling for Generation of Combined Cooling and Power for Data Center Application

DISSERTATION

submitted in partial satisfaction of the requirements
for the degree of

DOCTOR OF PHILOSOPHY

in Mechanical & Aerospace Engineering

by

Maryam Asghari

Dissertation Committee:
Professor Jack Brouwer, Chair
Professor Yun Wang
Professor Michael Green

2022

DEDICATION

To

Ghazal
&
Beautiful souls we lost in flight PS752

that didn't get the chance to finish their journey

TABLE OF CONTENTS

Page

LIST OF FIGURES ix

LIST OF TABLES xvii

ACRONYMS xix

ACKNOWLEDGEMENTS xxiii

VITA xxv

ABSTRACT OF THE DISSERTATION xxx

1 Introduction 1

1.1 Motivation 1

1.2 Overview 4

1.3 Goal & objectives 6

1.4 Approach 8

2 Background & Literature Review 10

2.1 Data center 10

2.1.1 Data center power infrastructure 10

2.1.2 Data center cooling 12

2.2 Solid Oxide Fuel Cell technology and system 17

2.2.1 Fuel cell 17

2.2.2 Integrated SOFC system 22

2.2.3 SOFC driven data center 26

2.2.4 Ammonia for SOFC 27

2.3 Liquid desiccant technology and system 29

2.3.1 Liquid desiccant solution 32

2.3.2 Liquid desiccant system classification and design 35

2.3.3 Integrated liquid desiccant air conditioning 38

2.3.3.1 Liquid desiccant integrated with SOFC system 49

3 SOFC System Modeling 53

3.1 SOFC stack model 53

3.1.1 Governing Equations 57

3.1.1.1 Energy balance 57

3.1.1.2 Mass balance 60

3.1.1.3 Polarization model 62

3.2 SOFC stack results 66

3.3 SOFC system design & control 69

3.3.1 Balance of plant model 70

3.3.1.1 Blower 70

3.3.1.2 Heat exchanger 71

3.3.1.3 Mixer 71

3.3.1.4 Reformer 72

3.3.1.5 Oxidizer 72
3.3.2 Control strategy 73
3.3.2.1 Temperature control 73
3.3.2.2 Stack power management 73
3.3.2.3 Fuel utilization 73
3.3.2.4 Steam-to-carbon ratio 74
3.4 Steady state results 74
3.5 SOFC dynamic result 76
3.6 Summary 81
4 Liquid Desiccant Dehumidifier Modeling 82
4.1 Liquid desiccant component modeling 82
4.1.1 Dehumidifier modeling 82
4.1.2 Indirect evaporative cooling modeling 86
4.1.3 Regenerator modeling 88
4.2 Control strategy for the liquid desiccant system 90
4.3 Liquid desiccant system model verification 90
4.3.1 Dehumidifier verification 91
4.3.2 Indirect evaporative cooler verification 93
4.4 Summary 95
5 Data Center Cooling Demand Model 96

5.1 Data Center modeling 97

5.2 Data Center cooling demand results 99

5.3 Summary 106

6 Integrated System Analysis 108

6.1 Integrated system design 108

6.2 Spontaneous integrated system performance 109

6.3 LiCl daily storage 113

6.4 LiCl yearly storage 117

6.4.1 First scenario: Rack level regenerator and dehumidifier results 119

6.4.2 First scenario: Rack level storage 125

6.4.3 Second scenario: Row level regenerator and dehumidifier results 128

6.4.4 Second scenario: Row level storage 134

6.4.5 Rack and Row level Comparison: 136

6.5 Summary 137

7 SOFC experimental and degradation analysis 139

7.1 Integrated system experimental setup 139

7.1.1 SOFC system 140

7.1.2 Server rack 144

7.2 SOFC system experimental analysis 145

7.2.1 SOFC system dynamic results 145

7.3 SOFC Degradation Results 153

7.4 SOFC cell experimental analysis 155

7.4.1 SOFC Cell experimental setup 156

7.4.2 Test conditions 158

7.5 SOFC cell experimental results 159

7.5.1 Voltage degradation 159

7.5.2 Fuel Composition effect 161

7.5.3 Effect of time on different fuel for SOFC 163

7.5.4 Microstructural analysis 164

7.6 Summary 167

8 Summary and Conclusions 168

8.1 Summary 168

8.2 Conclusions 168

8.2.1 Integrated SOFC-AC for data center 168

8.2.2 SOFC experimental and degradation analysis 169

8.3 Future Work 170

8.3.1 Integrated SOFC-AC for data center 170

8.3.2 SOFC experimental and degradation analysis 170

REFERENCES 171

APPENDIX A 181

APPENDIX B 187

B.1. Rack level results 187

B.2. Row level results 199

LIST OF FIGURES

Page

Figure 1. Global electricity demand of data centers 2010-2030 [2]. 2

Figure 2: Traditional data center system losses [7]. 3

Figure 3: Electricity consumption for data centers [8]. 3

Figure 4. integrated SOFC- LDAC concept for server. 7

Figure 5. Simplified heat removal methods in data centers [18]. 13

Figure 6. Indirect adiabatic cooler [21]. 15

Figure 7. Ideal and Actual Voltage Current Density Curve of Fuel Cell [18]. 20

Figure 8. Schematic configuration of the SOFC-ORC-AC system [47]. 25

Figure 9. Proposed SOFC trigeneration system, consisting of three subsystems: SOFC-CHP system, adsorption refrigeration system, and water tank equipped with a temperature controller[54]. 26

Figure 10. Liquid desiccant comparison to conventional air conditioning system. 30

Figure 11. Conceptual layout of industrial liquid-desiccant system [75]. 32

Figure 12. Equilibrium relative humidity for lithium chloride. 34

Figure 13. Major components and packaging of the AILR LDAC [83]. 38

Figure 14. Physical DEVap Concept description[83]. 39

Figure 15. DEVap air conditioner schematic. (a) four stack channel pairs (b) top view, one channel pair[83]. 42

Figure 16. DEVap airstreams on a psychrometric chart [97]. 43

Figure 17. Heat pump driven liquid desiccant air handling devices [75]. 45

Figure 18. Planar fuel cell model. 53

Figure 19. Geometric parameters of a fuel cell. 56

Figure 20. State spatial distribution of temperature. 66

Figure 21. Steady-state spatial distribution of Nernst voltage. 67

Figure 22. Steady-state spatial distribution of losses. 68

Figure 23. Steady-state spatial distribution of voltage. 68

Figure 24. Steady-state spatial distribution of current density. 69

Figure 25. SOFC system configuration. 70

Figure 26. SOFC polarization curve for the BlueGEN data compared to the current physical SOFC system model. 75

Figure 27. SOFC model power output following the residential electricity demand 77

Figure 28. Variation of electrical efficiency versus time. 78

Figure 29. Exhaust gas temperature of the SOFC system. 79

Figure 30. Exhaust gas mass flow rate of the SOFC system. 79

Figure 31. PEN average temperature. 80

Figure 32. Stack temperature difference. 81

Figure 33. Configuration of the LLD system. 82

Figure 34. Dehumidifier unit schematic. 83

Figure 35. Indirect evaporative cooler schematic. 86

Figure 36. Regenerator unit schematic. 88

Figure 37. Model-experiment comparison of dehumidifier. (top) Change in supply-side air, temperature (bottom) change in relative humidity. 92

Figure 38. Model-experiment comparison of indirect evaporative cooler. (top) Change in supply-side air, temperature (bottom) change in relative humidity. 94

Figure 39. Cooling system type for 7 locations based on ASHRAE recommended (left bar) & allowable (right bar) range. 100

Figure 40. Load profile for the RSF data center over the first 11 months of operations Illustration by Chad Lobato, NREL[141]. 101

Figure 41. TMY data for California and Texas throughout the year. 102

Figure 42. Data Center power demand breakdown throughout a year for California and Texas. 103

Figure 43. Data Center power demand percentage for California and Texas. 103

Figure 44. PUE for California and Texas for the entire year. 104

Figure 45. Data center energy usage for a 50MW data center. 105

Figure 46. Energy consumed by different part of data center for various combinations. 106

Figure 47. System configuration for server rack level power and cooling. 108

Figure 48. Integrated SOFC-LDD system model schematic. 109

Figure 49. Airstream at 25˚C and 70% RH with simulated LDD processes on a psychrometric chart at 100kPa. 111

Figure 50. Airstream at 35˚C and 45%RH with simulated LDD processes on a psychrometric chart at 100kPa. 112

Figure 51. Airstream at 40˚C and 20% RH process on a psychrometric chart at 100kPa. 113

Figure 52. Microsoft data center location in the US. 114

Figure 53. Temperature of 7 different location for 24 hours on July 20, 2018. 114

Figure 54. Dew point temperature of 7 different locations for 24 hours on July 20, 2018. 115

Figure 55. SOFC-LDD schematic for considering storage capacity. 116

Figure 56. Dew point for the seven locations of the study for the entire year. 118

Figure 57. Schematic of row level server cooling. 119

Figure 58. Mixture air temperature before and after regeneration process for the entire year at Illinois location. 120

Figure 59. Mixture air humidity ratio before and after regeneration process for the entire year at Illinois location. 120

Figure 60. Return air percentages for regeneration process at Illinois location. 121

Figure 61. Rate of regenerated desiccant flow for the entire year at Illinois location. 121

Figure 62. Desiccant inlet and outlet concentration in regenerator at Illinois location. 122

Figure 63. Hot water inlet and outlet from regenerator at Illinois location. 122

Figure 64. Supply air inlet and outlet temperature in dehumidifier for the entire year at Illinois location. 123

Figure 65. Cooling air inlet and outlet temperature in dehumidifier for the entire year at Illinois location. 123

Figure 66. Return air percentages for dehumidifier process for the entire year at Illinois location. 124

Figure 67. Humidity ratio of inlet and outlet supply air for the entire year at Illinois location. 124

Figure 68. Desiccant flow that is needed for the entire year to dehumidify the air for the servers at Illinois location. 125

Figure 69. Desiccant inlet and outlet concentration in dehumidifier at Illinois location. 125

Figure 70. Net desiccant consumption and production for the entire year for Virginia, Texas, Iowa, and Illinois. 126

Figure 71. State of storage (charge) of strong desiccant for all four locations. 127

Figure 72. Mixture air temperature before and after the regeneration process at Illinois location. 129

Figure 73. Mixture air humidity before and after the regeneration process at Illinois location. 129

Figure 74. Return air percentage for regenerator at Illinois location. 129

Figure 75. Regenerated desiccant flow rate throughout the year at Illinois location. 130

Figure 76. Desiccant concentration inlet and outlet in regenerator at Illinois location. 130

Figure 77. Hot water inlet and outlet temperature before and after regenerator at Illinois location. 131

Figure 78. Supply air inlet and outlet temperature in dehumidifier at Illinois location. 131

Figure 79. Cooling air inlet and outlet temperature in dehumidifier at Illinois location. 132

Figure 80. Return air percentage in dehumidifier at Illinois location. 132

Figure 81. Cooling air inlet and outlet humidity ratio in dehumidifier at Illinois location. 133
Figure 82. Desiccant flow rate in dehumidifier for the entire rate at Illinois location. 133
Figure 83. Desiccant inlet and outlet desiccant concentration at Illinois location. 133
Figure 84. Net desiccant consumption and production for Virginia, Texas, Iowa, and Illinois in row level storage. 135
Figure 85. the state of storage of strong desiccant for Virginia, Texas, Iowa, and Illinois in row level storage. 136
Figure 86. Experiment set-up concept schematic. 139
Figure 87. BlueGEN systems in the NFCRC laboratory. 140
Figure 88. Water connections schematic. 142
Figure 89. Pump used for fuel cell water rejection connection. 142
Figure 90. Manifold and valves for fuel cell supply water. 143
Figure 91. BlueGEN exhaust manifold. 144
Figure 92. Server rack at NFCRC laboratory 145
Figure 93. BlueGEN dynamic operation data. 146
Figure 94. BlueGEN dynamic operation data. 147
Figure 95. BlueGEN stack power cycle- 24h. 148
Figure 96. BlueGEN current density and voltage on a 24h cycle. 149
Figure 97. BlueGEN stack temperature on a 24h cycle. 149
Figure 98. BlueGEN performance under ramp test. 150
Figure 99. BlueGEN performance under ramp test. 151

Figure 100. BlueGEN stack power cycle- one week. 152

Figure 101. BlueGEN voltage on a one-week cycle. 153

Figure 102. BlueGEN stack temperature on a one-week cycle. 153

Figure 103. BlueGEN V-J characteristics curve for a 24h power cycle for 42 days 154

Figure 104. BlueGEN power profile over 6000h operation. 155

Figure 105. BlueGEN stack voltage (V) during 6000h operation. 155

Figure 106. a) 1st layer of mica on the setup b) Nickel mesh along with mica and glass seals (c) Anode supported SOFC placed on the nickel mesh and the glass seal, (d) first layer of alumina felt and gold mesh (e) Alumina felt layer on top of the gold mesh and current collector lead (f) The single cell SOFC subsystem upon closing the top plate. 157

Figure 107. Experimental setup of single cell SOFC system. 158

Figure 108. Voltage versus time characteristics of the 3 SOFC cells for the duration of 1000h. 160

Figure 109. Temperature versus time of the three SOFC cells for the duration of 1000h. 160

Figure 110. J-V characteristic curve for N_2-H_2, H_2 and NH_3 fuel composition at 750C. 161

Figure 111. Effect of changing different fuel composition (N_2-H_2, NH_3, H_2) at t=0 and t=800hr. (a) Inductance and capacitance corrected EIS spectra at t=0hr, (b) Inductance and capacitance corrected EIS spectra at =800, (c) Inductance corrected Bode plot at t=0, (d) Inductance corrected Bode plot at t=800. 163

Figure 112. Effect of time on inductance and capacitance corrected EIS on left side and Bode plot on right side for H_2, N_2-H_2, and NH_3. 164

Figure 113. SEM-images taken of the anode surface at fuel inlet (left) and fuel outlet (right) region for (a) reference cell, (b, c) after operation with H_2-N_2 (d, e) after operation with H_2 (f, g) after operation with NH_3. 166

Figure 114. ZrO_2 agglomeration on the surface of anode at N_2-H_2 cell. 167

LIST OF TABLES

Page

Table 1. Comparison between liquid desiccant and vapor compression cooling [81]. 31

Table 2. Fuel cell material properties. 55

Table 3. Fuel cell geometrical parameters. 57

Table 4. SOFC Parameters and Design Operating Conditions. 76

Table 5. SOFC steady state performance parameters. 76

Table 6. Dehumidifier unit verification input and output parameter. 91

Table 7. Indirect evaporative cooler verification input and output parameter. 93

Table 8. ASHRAE 2016 Thermal Guidelines [17]. 96

Table 9. Zone Boundaries for Recommended Environmental Envelope for IT Equipment. 97

Table 10. effect of dry bulb temperature on air cooled chillers efficiency. 99

Table 11. effect of dry bulb temperature on water cooled chillers efficiency. 99

Table 12. Average PUE for 7 data center target location. 105

Table 13. percentage of energy consumed by different part of data center for various combinations. 106

Table 14. Inlet and outlet conditions of the regenerator stage. 110

Table 15. Inlet and outlet conditions of the dehumidifier stage. 110

Table 16. Inlet and outlet conditions of the IEC stage. 110

Table 17. 24-hour average weather data on July 20, 2018. 116

Table 18. Daily storage capacity for 7 data center locations during July 20th. 117

Table 19. Rack level storage results for Virginia, Texas, Iowa, and Illinois. 128

Table 20. Rack level storage results for the four locations. 136

Table 21. Rack and Row level storage comparison. 137

Table 22. BlueGEN degradation analysis. 155

Table 23. Fuel conditions related to each cell. 159

Table 24. Effect of changing different fuel composition (N_2-H_2, NH_3, H_2) on resistance. 162

Table 25. EDX quantification analysis for reference cell and after operating on H_2, NH_3, N_2-H_2. 166

ACRONYMS

AC	Alternative Current
A/C	Air Conditioning
ADR	Ammonia Decomposition Reaction
APEP	Advanced Power and Energy Program
ASHRAE	American Society of Heating, Refrigerating and Air-conditioning Engineers
$CaCl_2$	Calcium Chloride
CCHP	Combined Cooling, Heating, and Power
CFCL	Ceramic Fuel Cells Ltd
CFM	Cubic Feet per Minute
CHP	Combined Heat and Power
CRAC	Computer Room Air Conditioners
CPU	Central Processing Unit
CRAH	Computer Room Air Handling
COP	Coefficient of Performance
DC	Direct Current
DEVap	Desiccant enhanced EVaporative air-conditioning
DOE	Department of Energy
DRT	Distribution of Relaxation Times

DX	Direct eXpansion cooling
EAGERS	Efficient Allocation of Grid Energy Resources including Storage
EDX	Energy Dispersive X-Ray
EES	Engineering Equation Solver
EIS	Electrochemical Impedance Spectroscopy
EPFL	École Polytechnique Fédérale de Lausanne
GDC	Gadolinium Doped Ceria oxide
GEM	Group of Energy Material
GHG	Green House Gas
GT	Gas Turbine
HMX	Heat and Mass eXchanger
HP	Heat Pump
HVAC	Heating, Ventilation, and Air Conditioning
IDCS	Integrated Desiccant air Conditioning System
IEC	Indirect Evaporative Cooler
IHX	interchange Heat eXchanger
IT	Information Technology
KCOOH	Potassium Formate
KK	Kramer Kronig
LD	Liquid Desiccant
LDAC	Liquid Desiccant Air Conditioning

LDD	Liquid Desiccant Dehumidifier
LHV	Lower Heating Value
LiBr	Lithium Bromide
LiCl	Lithium Chloride
NFCRC	National Fuel Cell Research Center
NREL	National Renewable Energy Laboratory
OCV	Open Circuit Voltage
ODE	Ordinary Differential Equation
ORC	Organic Rankine Cycle
PEN	Positive electrode, Electrolyte, Negative electrode
PUE	Power Usage Efficiency
PVC	PolyVinyl Chloride
R&D	Research & Development
RH	Relative Humidity
RIEC	Regenerative Indirect Evaporative Cooling
SEM	Scan Electron Microscopy
S2C	Steam to (2) Carbon
SDCS	Separated Liquid Desiccant air Conditioning System
SHR	Sensible Heat Ratio
SMR	Steam Methane Reforming

SOFC	Solid Oxide Fuel Cell
TMY	Typical Meteorological Year
TPB	Triple-Phase Boundary
UPS	Uninterruptible Power Sources
VC	Vapor Compression
VCS	Vapor Compression Systems
VFD	Variable Frequency Drive
WGS	Water Gas Shift
YSZ	Yttria-Stabalised Zirconia

ACKNOWLEDGEMENTS

My PhD journey has been touched and shaped by many beautiful souls within and outside UCI. I truly believe I won't be where I am today without the love and support that I received from loved ones, family, friends, and mentors.

First, I would like to start with my amazing advisor, Professor Jack Brouwer. I cannot thank you enough for the impact you have in my life. You gave me the opportunity to explore my passion, you taught me persistence, you supported me all along, you trusted me with my ideas, and you allowed me to explore within and beyond research. You have been a great advisor, an extra ordinary mentor, a true supporter, and an amazing friend. I admire your enthusiasm, tirelessness and leadership that continues to inspire me and guide me along the way. I also want to thank you for being like a father, caring about wellbeing of your students specially at the beginning of my journey, you made me feel home at UCI while thousands of miles away from home. Thank you for all your supports. Words cannot express my gratitude and appreciation for having you in my life. THANK YOU

My gratitude goes to Professor Scott Samuelsen who has been an inspiration to me through his example as a leader in alternative energy and his dedication to the field. Through his leadership, a unique lab culture has cultivated at the Advanced Power and Energy Program.

I thank my committee members, Professor Yun Wang, and Professor Michael Green, for serving on my dissertation committee. Also, I would like to thank you for your helpful advice on this work.

I would like to acknowledge and thank my colleagues and friends at the APEP not only for collaboration in research but mostly for the friendship and positive experiences that I have had over the past seven year. APEP was truly a family. Max Venaas, Luca Mastropasqua, Philipp Ahrend, Daniel James, Alejandra Hormoza, Alejandro Lavernia, and Melina Arrizon Melchor thanks for your support and friendship.

I would also like to thank my host advisor, at EPFL, Prof. Jan Van Herle, while I was a visiting Fulbright research scholar in Switzerland. Thank you for giving me the opportunity to experiment and research under your supervision at GEM. I want to also thank my colleagues and friends at GEM for their support and friendship. I want to specially thank Suhas and Samaneh for their help and support during my time at GEM. During my visit at EPFL, I made new friends, Samaneh, Souror, Zohreh, Fatemeh, and Bardiya, who welcomed me in Sion and made my stay enjoyable. Thank you!

Negin and Mina, you two proved me that our friendship is immune by distance. I never felt how far we are because you were there whenever I needed you. Thank you.

Yasaman, Navid, Elmira, Siavash, Kimia, Erfan, Negar, and Arian you are truly the friends that helped me go through this journey's ups and downs day to day. Thanks for listening to my complains and being my family in Irvine. I cannot count the number of days and weeks that I went through with the motivation of our time together at the end of the day and week. I love you and I am grateful for your friendship. Yasaman, you stayed by my side through my hardest days during this journey. Thanks for always being there for me and helping me making the hard decisions of my life. Your home became my happy place quickly. I truly cannot go through life without having you by my side. I believe all I need for finding solutions to my problems is a chat with you.

Masoumeh and Jafar, my amazing Mom and Dad, I truly believe I am who I am today because of you two. It's been a privilege to be your daughter. Thanks for believing in me and being my biggest fan. It doesn't matter how far we are; I feel your presence in my life every day. Dad, I learned to be ambitious and never settle for anything in life from you, because of you I know nothing is impossible in life. Mom, I learned who I want to be in life as a human being from you; you have been my go-to person when I need the extra ordinary power in life to calm me from the storm of life. I love you two so much and I am so grateful to have you in my life. My amazing sisters, Elahe and Azadeh, I am so grateful to have you two in my life. Azadeh, you are the symbol of kindness and persistence for me. Elahe thanks for always reminding me that there is more to life than what I see, for pushing me to be alive and live the life that makes me happy. I love you so much.

My dearest, Alireza, my amazing husband, I don't know where to begin. I cannot find proper words to describe my appreciation for having you in my life. I simply cannot imagine what my life would have looked like without you. I am a better person because of you. You picked me up every single time I fell. When I am down, you cheer me up. When I see darkness, you become my light. You supported me all along in every aspect of life. For the last 10 years of my life, since the day that I know you, you have been my first person to go for every research question and the last as well, because there is no problem that you don't have the answer to. You are the smartest person I know, and you amaze me every single day. You taught me persistence, hard work, and dedication. Thank you for staying by my side, listening to my never ending complains, and helping me through my journey, no matter how hard it got. I love you so much and thank you for being my safest place in the world. Thanks for being my light in the darkest day. I could not imagine going through this journey without you, you are the best partner I could have asked for. I am grateful to have you in my life. I love you forever.

VITA

Maryam Asghari

EDUCATION

Ph.D., University of California, Irvine, (June. 2022)
Department of Mechanical & Aerospace Engineering, GPA: 4 out of 4
Dissertation: Integration of Solid Oxide Fuel Cell with Liquid Desiccant Cooling for Generation of Combined Cooling and Power for Data Center Application. Chair: Jack Brouwer, Ph.D.

M.Sc., University of California, Irvine, (Dec. 2017)
Department of Mechanical & Aerospace Engineering, GPA: 4 out of 4
Dissertation: Integration of a Solid Oxide Fuel Cell with an Organic Rankine Cycle and Absorption Chiller for Dynamic Generation of Power and Cooling for a Residential Application. Advisor: Jack Brouwer, Ph.D.

B.Sc., University of Tehran, (Jul. 2015)
Department of Mechanical Engineering, GPA: 3.74 out of 4
Dissertation: Determination of Gas Power Plant Chimney's Standards According to Power Plant Standards and Determination of Optimal Diameter and Height with These Standards. Advisor: Mehdi Ashjaee, Ph.D.

PROFESSIONAL EXPERIENCES

Graduate Researcher, Advanced Power and Energy Program, UC Irvine (Jan. 2016 – Jun. 2022)

- Developed and validated dynamic physical models for the Solid Oxide Fuel Cell (SOFC), Organic Rankine Cycle and Desiccant Cooling system in MATLAB/Simulink
- Assessed and Created model for an integrated SOFC with an Organic Rankine Cycle and Absorption Chiller for dynamic generation of power and cooling in residential complex
- Evaluated and developed an integrated model for SOFC with Desiccant Cooling System for dynamic generation of power and cooling for data center applications
- Built and demonstrated combined SOFC, Dehumidification and server rack in laboratory scale
- Developed a model for designing a 100% renewable data center
- Assessed techno-economic pathways to zero carbon mining industry

Fulbright Visiting Researcher, Group of Energy Materials, EPFL (Sep. 2021 – Apr. 2022)

- Building a SOFC single cell setup, and performing long term tests on SOFC with NH_3, H_2N_2, and H_2 fuel
- Performing EIS and IV measurement on SOFC single cell over 1000hr lifetime
- Analysis of effects of NH_3 on degradation of SOFC under 1000hr operation

ESG Consultant Intern, DataBank, Ltd. (Jun. 2021 – Sep. 2021)

- Research corporate sustainability best practices particularly within data center sector.
- Gather quantitative data on various DataBank data centers (i.e. energy, water, etc.) to compile a qualitative review of the company's current sustainability landscape.

- Research on incentive programs and government supportive policies for decarbonizing data centers
- Pinpoint strategies and Priority rank proposed strategies by weighing factors like projected financial returns, reduction of environmental impacts based on DataBank's sustainability goals.
- **Energy Engineer Intern, California Energy Commission** (Jun. 2019 - Sept. 2019)
- Evaluated Electric Program Investment Charge (EPIC) funding benefits
- Conducted study on low income family barriers for clean energy
- Organized a workshop on advancing energy equity

Thermal Engineer Intern, Altura Associates, Inc (Jun. 2018 - Sept. 2018)

- Reviewed data analysis of city center power plant in Las Vegas
- Developed energy model and optimized chilled water plant systems
- Established energy optimization model in Skyspark Axon Language

Undergraduate Researcher, University of Tehran (Sept. 2013 - Jun. 2015)

- Formed an engineering software to optimize diameter and height of gas turbine power plant chimney based upon construction and environmental standards in design process
- Assessed technical, economic, and environmental aspects of using Combined Cooling, Heating, and Power (CCHP) in Buildings. Designed a ventilation system for university of Tehran new building by implementing CCHP
- Designed a 50-ton industrial refrigeration system for meat storage

HONORS, AWARDS, & FELLOWSHIP

- US Fulbright Scholarship/ Swiss Government Excellence Scholarship (2021-2022)
- UCI Public Impact Fellowship (2020)
- UCI Chancellor's Club Fellowship (2020)
- National Science Foundation Graduate Research Program Fellowship (NSF-GRFP) (2017-2020)
- Association of Energy Engineers (AEE) Foundation Scholarship Recipient (2020)
- Carbon Neutrality Initiative (CNI) Fellowship (2019-2020)
- Achievement Rewards for College Scientists (ARCS) Scholar Award (2018-2020)
- Society of Women Engineers- Orange County (SWE-OC) graduate student scholarship (2019)
- Fanni Reunion Foundation (FRF) award of excellence in engineering education (2017)
- Received Graduate Assistance in Areas of National Need (GAANN) fellowship (2016-2017)
- Awarded for full scholarship from university of Tehran for mechanical engineering M.Sc. program, exemption from university entrance exam (2015)
- Winner of *Harekat* festival prize as a member of best innovative scientific association in Iran (2012)
- Received full scholarship to attend university of Tehran for undergraduate studies (2011)
- Ranked 697 among more than 400,000 participants in nation-wide exam of Iranian universities (2011)

PUBLICATIONS

- **Asghari, M**., Sampathkumar, S.N., Frntz, C., Brouwer, J., Van Herle J., Effect of ammonia fuel on single cell performance and degradation (under preparation)
- **Asghari, M**., Lavernia, A., Mastropasqua, L. Brouwer, J., LiCl Storage for cooling of SOFC Powered data center (under preparation)
- **Asghari, M**., Sampathkumar, Daviran, S.N., Frntz, C., Brouwer, J., Van Herle J., Effect of ammonia fuel on single cell degradation. Proceeding of 15th European SOFC & SOE Forum. 2022
- Lavernia, A. C., **Asghari, M.**, Mastropasqua, L., & Brouwer, J. Design Optimization of a Thermally Integrated Solid Oxide Fuel Cell with Triple Effect Absorption Chiller. ECS Transactions, 2021, 103(1), 807.
- Lavernia, A., **Asghari, M**., Luca, M., & Brower, J. Absorption Cooling for Data Centers powered by Solid Oxide Fuel Cell Waste Heat. (2021). International Refrigeration and Air Conditioning Conference. Paper 2220.
- Lavernia, A., **Asghari, M**, Brouwer J. Absorption cooling for data centers powered by solid oxide fuel cell waste heat. ASHRAE Transactions, 2020, 126, 204-211.
- **Asghari M**, Lavernia A, Saeedmanesh A, James S, Brouwer J. Integration of solid oxide fuel cell with liquid desiccant cooling for generation of combined cooling and power for a server. ECS Transactions. 2019 Jul 10;91(1):167-77
- **Asghari M**, Brouwer J. Integration of a solid oxide fuel cell with an organic rankine cycle and absorption chiller for dynamic generation of power and cooling for a residential application. Fuel Cells. 2019 Aug;19(4):361-73
- **Asghari, M**., Brouwer, J. "Integration of a solid oxide fuel cell with an organic rankine cycle and absorption chiller for dynamic generation of power and cooling for a residential application." Proceeding of 13th European SOFC & SOE Forum. 2018
- **Asghari M**, McVay D, Brouwer J. Integration of a solid oxide fuel cell with an absorption chiller for dynamic generation of combined cooling and power for a residential application. ECS Transactions. 2017 May 30;78(1):243-55

CONFERENCE PRESENTATIONS

PAPER PRESENTATIONS

- **Asghari, M**., Sampathkumar, S.N., Frntz, C., Brouwer, J., Van Herle J., Effect of ammonia fuel on single cell degradation. Proceeding of 15th European SOFC & SOE Forum. (Jul. 2022)
- **Asghari, M.**, & Brouwer, J. "Rack Level Server Power and Cooling by Solid Oxide Fuel Cell and Liquid Desiccant System in Humid Climate." Presented at the International Mechanical Engineering Congress and Exposition, Virtual. (Nov. 2020)
- **Asghari, M.**, Lavernia, C. A., Saeedmanesh, A., James, S., & Brouwer, J. "Integration of Solid Oxide Fuel Cell with Liquid Desiccant Cooling for Generation of Combined Cooling and Power for a Server." Paper presented at 16th International Symposium on Solid Oxide Fuel Cells (SOFC-XVI) in Kyoto, Japan. (Sept. 2019)
- **Asghari, M.**, McVay, D., & Brouwer, J. "Integration of a Solid Oxide Fuel Cell with an Absorption Chiller for Dynamic Generation of Combined Cooling and Power for a Residential Application." Paper presented at 15th International Symposium on Solid Oxide Fuel Cells (SOFC-XV) Florida, USA. (Jul. 2017)

POSTER PRESENTATIONS

- **Asghari, M**., Brouwer, J. "Integration of a Solid Oxide Fuel Cell with an Organic Rankine Cycle and Absorption Chiller for Dynamic Generation of Power and Cooling for a Residential Application". 13th European SOFC & SOE Forum. Lucerne, Switzerland. (Jun. 2018)
- **Asghari, M**., & Brouwer, J. "Integration of an SOFC with organic Rankine cycle and absorption chiller for dynamic tri-generation of power, hydrogen and cooling." Poster session presented at the 14th International Symposium on Solid Oxide Fuel Cells: Materials, Science and Technology. Florida, USA. (Jan. 2017)

SYNERGISTIC & SERVICE ACTIVITIES

- **Consultant & Project Manager,** Seed Consulting Group (2021)
- **External Vice President,** Society of Women Engineering, Orange County (2020-2021)
- **President,** Mechanical & Aerospace Engineering Graduate Student Association, UCI (2020-2021)
- **Mentor,** Society of Women Engineering (2020-2021)
- **Council Member,** University of California Global Climate Leadership Council (2019-2021)
- **Committee Member,** University of California UC Sustainability Steering Committee (2019-2021)
- **MAE Representative,** Diverse Educational Community and Doctoral Experience (DECADE) Council, UCI (2019-2021)
- **Campaign Manager,** University of California Graduate and Professional council (UCGPC) (2019-2020)
- **UCGPC Liaison,** Association of Graduate Student, UCI (2019-2020)
- **Diversity/External Organizations Chair,** Society of Women Engineering, Orange County (2019-2020)
- **Diversity Ambassador,** Mechanical & Aerospace Engineering Department, UCI (2018-2020)
- **External Vice President,** MAE Graduate Student Association, UCI (2017-2020)
- **Council Member,** Association of Energy Engineering, UCI chapter (2017-2020)
- **President,** Association of Energy Engineering, UCI chapter (2018-2019)
- **STEM Co-Chair,** Diverse Educational Community and Doctoral Experience Council, UCI (2018-2019)
- **Legislative Director,** Association of Graduate Student, UCI (2018-2019)
- **Mentor**, International graduate students peer mentor (2017-2019)
- **Council Member,** Association of Graduate Student, UCI (2017-2019)
- **Professional Development Co-Chair,** Association of Graduate Student, UCI (2017-2018)
- **Symposium Co-chair,** Association of Graduate Student, UCI (2017-2018)
- **Co-Chair,** ICS & engineering DECADE Council, UCI (2017-2018)
- **Council Member,** ICS & engineering DECADE, UCI (2016-2021)
- **Council Member,** of Verano Place Resident council (2016-2021)
- **Council Member**, Scientific Association of Mechanical Engineering, university of Tehran (2011-2014)

PATENTS

- **Maryam Asghari,** Mina Vaez, Nasim Madani, "**Generating Electricity by Foot Pressure throughout Walking**", February 2010, Department of Companies Registration & Industrial Property. (2010)

ABSTRACT OF THE DISSERTATION

Integration of Solid Oxide Fuel Cell with Liquid Desiccant Cooling for Generation of Combined Cooling and Power for Data Center Application

by

Maryam Asghari

Doctor of Philosophy in Mechanical & Aerospace Engineering

University of California, Irvine, 2022

Professor Jack Brouwer, Chair

Electricity consumption projections place data centers at up to 13% of global electricity demand in 2030 due to the expected growth in the production and use of electronic devices, cloud services, and computer networks. Cooling infrastructure accounts for up to 40% of the total energy delivered to a data center. With business and society relying so much on data centers, there is a greater need for reliable and clean electric power for data centers. Solid Oxide Fuel Cell (SOFC) systems have the potential to provide more reliable and cleaner electrical load-following characteristics compared to other technologies while enabling dynamic operation and control. High temperature exhaust of SOFC can be used to run a bottoming cycle such as cooling system which makes it an attractive integrated system for data center applications. However, cost and durability are major challenges associated with SOFC technology. On the other hand, the biggest challenge for using hydrogen as an

energy carrier for SOFC is the very high pressure or very low temperature required for its storage, transmission, and distribution, which makes the need for a more dense liquid energy carrier like ammonia inevitable.

This dissertation, first, focuses on evaluating the integrated system concept and assesses the achievable air conditioning from SOFC waste heat. To explore the feasibility of thermally integrating SOFC with liquid desiccant dehumidification (LDD), a spatially resolved physical model developed in MATLAB is used to simulate the operating characteristics of this SOFC system. A corresponding physical model is developed to simulate the liquid desiccant air conditioner for dehumidification. This research evaluated SOFC systems for powering demand of a single server rack (~12kW) to powering a row of servers (~240kW). The LDD operation is based on distributed waste heat from SOFC that powers the servers. This research indicates whether waste-heat based cooling and dehumidification could power the servers and maintain server operating temperatures and humidity in the safe range for different weather conditions. It calculated the yearly storage capacity required for each location to meet the demand of the data center for the entire year.

Next, the performance and degradation of a 1.5kW (AC) commercial system, that is proposed for source of power and cooling of servers, is evaluated under steady state and dynamic load cycling conditions for over 6000 hours. The degradation rate and performance characteristics of the SOFC system is analyzed to determine the long-term performance and durability of SOFC system under dynamic condition. Finally, to analyze and compare the degradation of single cell SOFC directly fed with ammonia (NH_3), externally reformed ammonia (N_2-H_2) and pure hydrogen (H_2), three durability tests are conducted on anode

supported SOFC. Electrochemical impedance spectroscopy (EIS) and scanning electron microscopy (SEM) are conducted to study the performance losses during operation and to observe the microstructure changes of the cell after testing.

1 Introduction

1.1 Motivation

The rapid growth of internet use, cloud computing and data-driven machines and services is increasing the electric power consumption and carbon footprint of data centers. Data center electricity demand was around 200TWh (1% of global electricity consumption) in 2018 [1] However, due to the expected growth in the production and use of electronic devices, cloud services, and computer networks, electricity consumption projections place data centers at up to 13% of global electricity demand in 2030 [2]. As shown in Figure 1 in the best-case scenario data center electricity consumption doubles in the next 10 years. Associated with this massive electricity consumption are greenhouse gas (GHG) and criteria pollutant emissions due to the use of conventional fossil energy resources to power data center electric loads. In 2020, the information and communications technology sector represented 2.3% of global GHG emissions, 28.8% of which were associated with data centers [3]. In addition, as a result of the COVID-19 pandemic, dependency upon internet technology, and cloud services, data center demands are only increased further. Data centers will use around 3–13% of global electricity in 2030 compared to 1% in 2010 [2]. In order to meet the emissions reduction targets imposed by many IT companies like Microsoft, the power supply for data centers must come from renewable energy sources. The trend of using renewable power (primarily via market mechanisms) is being used widely [4,5] and likely many data centers can be run with low GHG and pollutant emissions, even if they do not find ways to reduce their absolute electricity usage [2].

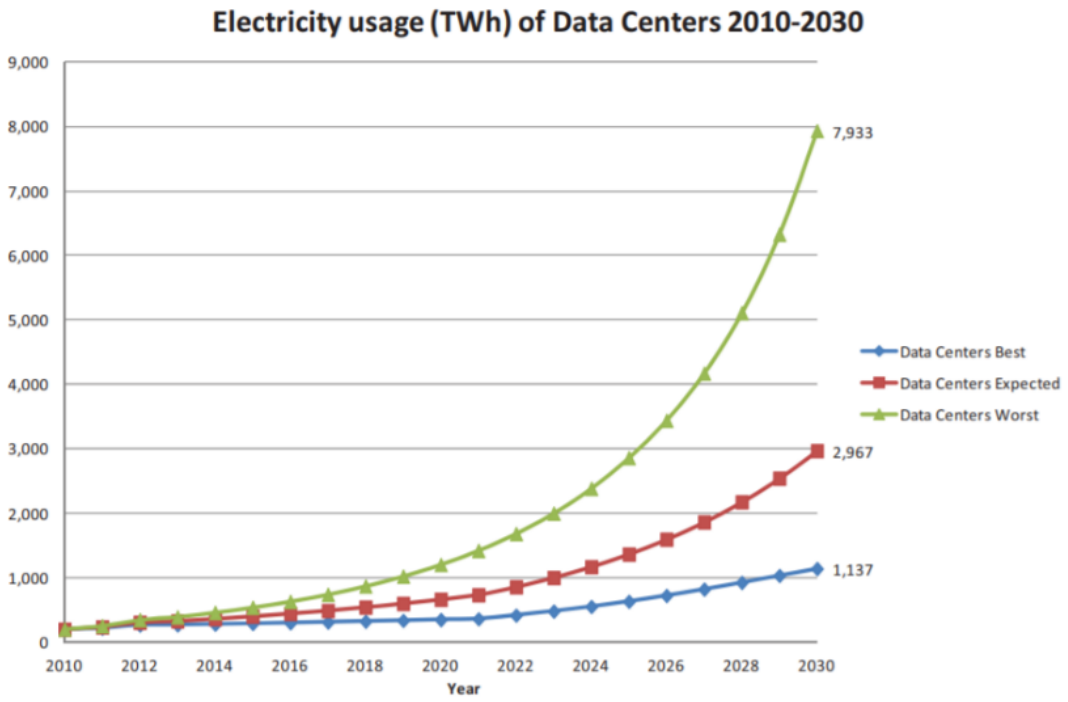

Figure 1. Global electricity demand of data centers 2010-2030 [2].

In a traditional data center connected to the electric grid, less than 35% of the energy from the fuel source that is supplied to the power plant is delivered to the data center. Power plant generation losses and transmission and distribution losses are the most significant inefficiencies in data center [6]. Figure 2 shows the process of power loss through the transportation and distribution network of the electric grid starting from the fuel source up to the power supplied to the consumer. It is evident that the largest inefficiency is from the power generated at the power plant level with additional losses associated with the transmission and distribution to the data center, where the data center receives roughly 30% of the total energy that could have been supplied ideally from the fuel source. There are further losses associated with the infrastructure required for daily reliable operation (i.e., cooling, lighting, and Uninterruptible Power Supply (UPS) systems). The additional power consumed by the cooling, lighting, and energy storage, means approximately less than 17.5% of the energy supplied to the power plant is ultimately delivered to the servers [7].

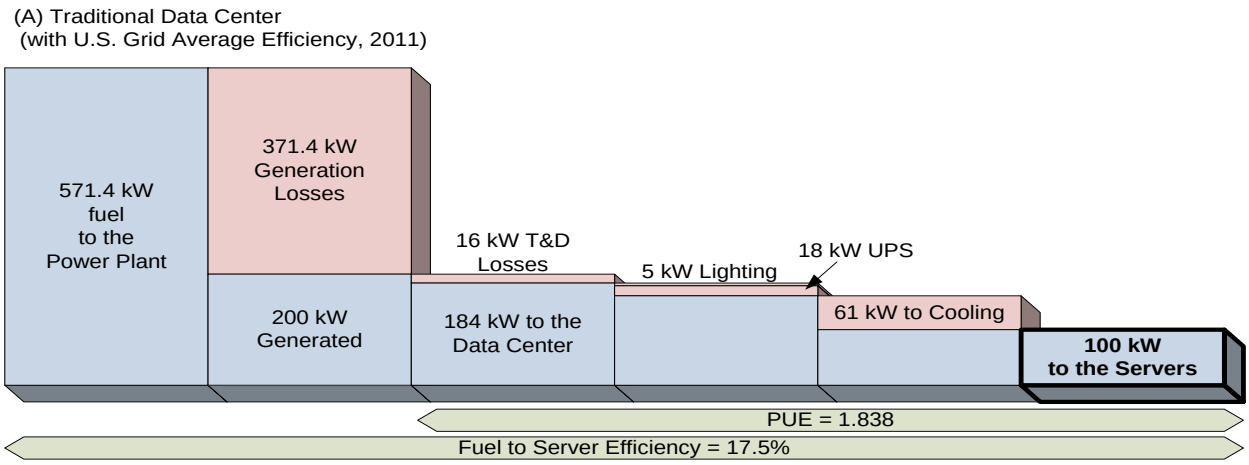

Figure 2: Traditional data center system losses [7].

Information Technology (IT) equipment (e.g., servers, networks, storage, etc.) and cooling infrastructure are the two major power consumers. As shown in Figure 3 cooling infrastructure is a large electricity consumer in the data center and can account for up to 40% of the total energy delivered to the data center [8]. Cooling also represents the biggest slice of the total cost in a data center. With more capacity and higher density there is an increased need for energy-efficient cooling of the IT equipment. While data centers need cooling to protect servers and other equipment, an additional challenge is humidity control. Too much humidity can cause corrosion of metal parts of the servers leading to short circuiting of electronics. On the other hand, low humidity allows the servers to develop electrostatic charges that can cause damage to sensitive equipment.

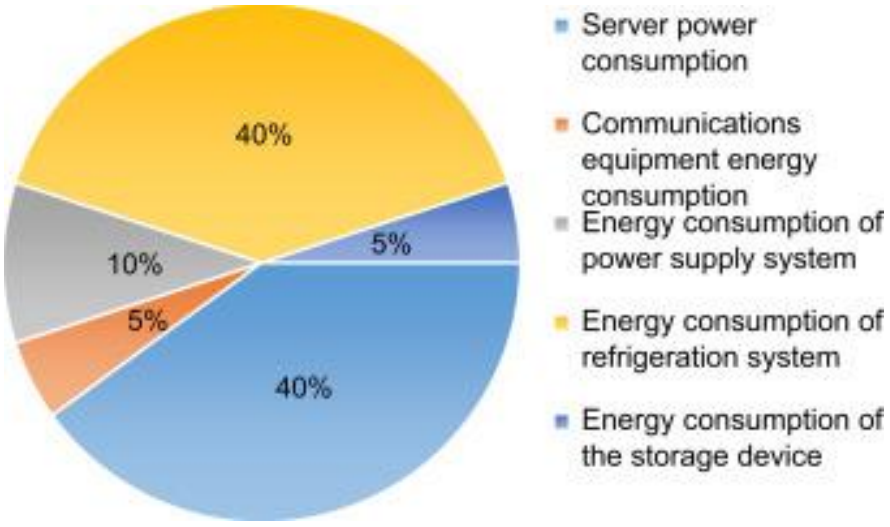

Figure 3: Electricity consumption for data centers [8].

According to Uptime Institute [9], electric power outages are the main causes of the increasing outage trend in data centers. According to the Eaton Blackout Tracker [10], the US experienced more than 3,500 utility power outages in 2017, the vast majority of which were attributed to faults in the transmission and distribution system. This number represents a 62% increase in outages from a decade ago. In 2018, a storm interrupted grid power to Microsoft's San Antonio Azure data center, knocking cooling systems offline, damaging a significant amount of equipment, and bringing down Active Directory and Visual Studio Team Services for almost 24 hours [11]. In some areas, rising temperatures are driving up the cost of data centers. In other areas, extreme rainfall and flooding have damaged equipment, and prevented the fuel deliveries which are so critical to the traditional back-up power solutions. And power costs continuously increase. The global cost of power for data centers is expected to increase 80% in the next five years. At 35% of total costs, electric power continues to represent the largest portion of data center operating costs [12]. Every power generation system that supplies a data center must comply with stringent reliability and availability constraints to ensure 99.9999% server uptime. With business and society relying so much on data centers, and data centers growing more and more, there is a greater need for reliable and clean electric power for data centers.

1.2 Overview

Our solution is using small scale Solid Oxide Fuel Cell (SOFC) for rack level power generation, which is capable of delivering uninterrupted, 24×7 power that is resilient and clean and eliminates the need for back up generation (due to the limited failure domain associated with a single rack) and is also able to provide high quality heat to run a liquid desiccant dehumidification system to provide cooled and dehumidified air for servers. Generating power on-site, at the point of consumption, rather than centrally, eliminate the cost, complexity, interdependencies, and inefficiencies associated with electrical transmission and distribution. Providing the required cooling for servers through liquid desiccant dehumidification run by high quality exhaust of SOFC has the potential to decrease the power consumption of data centers by up to 40%.

In this research, first, I investigate the integration of rack level fuel cell powered servers with Liquid Desiccant Dehumidifier technology that can be dynamically dispatched to produce electricity and cooling in various amounts to meet power and air conditioning demands of data centers. This thesis focusses first on evaluating the integrated system concept and to assess the achievable air conditioning from SOFC waste heat. To explore the feasibility of thermally integrating SOFC with LDD, a spatially resolved physical model developed in Matlab is used to simulate the operating characteristics of this SOFC system. A corresponding physical model is developed to simulate the liquid desiccant air conditioner for dehumidification. This study considers SOFC systems capable of powering a 1. single server rack (~12kW) and the operation of an LDD for cooling and dehumidification of that same rack, and 2. SOFC and LDD systems designed for a row of 20 servers. The LDD operation is based on distributed waste heat from SOFC that powers the servers. The analysis will indicate whether waste-heat based cooling and dehumidification is capable of powering the servers and maintaining server operating temperatures and humidity in the safe range for different weather conditions.

Even though SOFC technology offers several advantages such as fuel flexibility, high efficiency, and zero criteria pollutant emissions, cost and durability are major challenges associated with current SOFC technology. Durability of SOFC technology is a key aspect for its commercialization and long-lasting deployment in different applications. Dynamic operating conditions have considerable effects on the long-term performance and durability of SOFC systems. On the other hand, while many studies have focused on green hydrogen produced through electrolysis from sun and wind, as a clean fuel for fuel cells, the biggest challenge for using hydrogen as an energy carrier is the very high pressure or very low temperature required for its storage, transmission and distribution, which makes the need for a more dense liquid energy carrier like ammonia inevitable. I propose that ammonia made in a sustainable way (e.g., from renewable electricity that powers electrolyzers to produce hydrogen that is reacted with nitrogen to produce ammonia) can serve as a sustainable, low-cost, and high-density energy carrier and the fuel for SOFC systems in the future.

In the second part of this research, I first evaluate the performance and degradation of a 1.5kW Alternating Current (AC) commercial SOFC system that is proposed for source of power and cooling of servers under steady state and dynamic load cycling conditions for over 6000 hours. I monitored and analyzed the degradation rate and performance characteristics of the SOFC system to determine the long-term performance and durability of SOFC system under dynamic operating conditions. Second, I evaluate the effect of ammonia as fuel on SOFC performance. I study and compare the degradation of an SOFC single cell fed with fed with ammonia (NH_3), externally reformed ammonia (N_2-H_2 mixture) and pure hydrogen (H_2).

1.3 Goal & objectives

The goal of this thesis in to evaluate the integration of SOFC with Liquid Desiccant Air Conditioning (LDAC) for efficient, reliable, and grid-independent data center power and cooling. The integrated system will supply electricity and cooling to data center applications. This configuration offers the potential for high energy efficiency, environmental and economic benefits. The integrated concept is shown in Figure 4. The SOFC generates electricity from natural gas which is used directly for powering a rack of servers. The SOFC thermal exhaust will be used to produce hot water which is used for regenerating the liquid desiccant. Concentrated liquid desiccant will be stored and is used for dehumidifying the air when there is a cooling demand. The integrated system is expected to have high efficiency, low emission and provide reliable power and cooling for data center applications. This integrated configuration eliminates grid connection and any transmission line for powering servers as well as significantly decreasing the electric power used for providing cooling to servers.

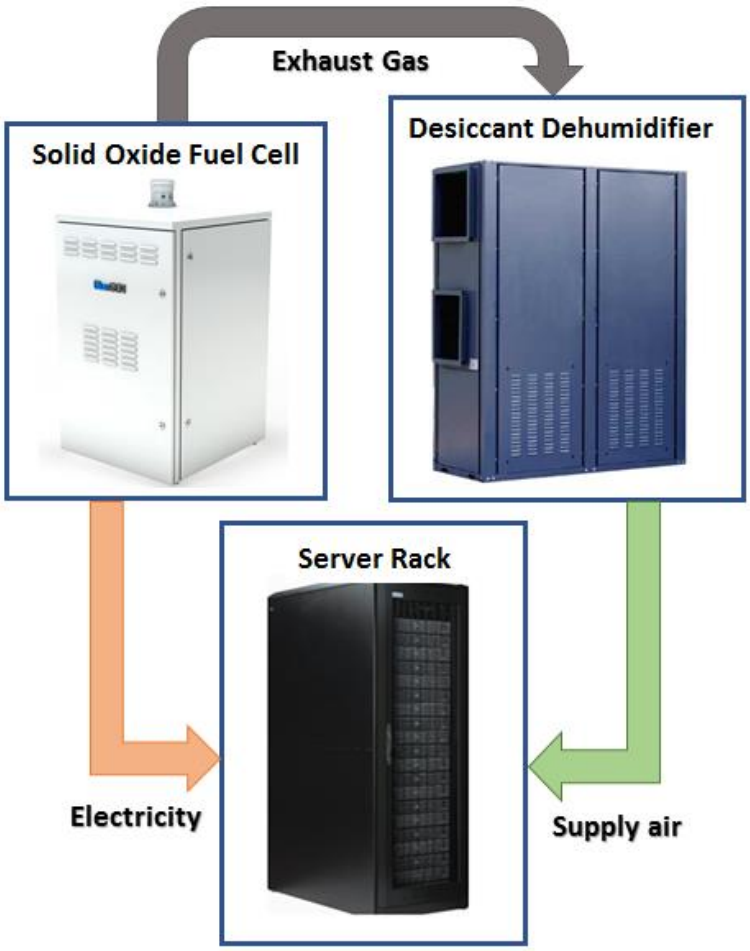

Figure 4. integrated SOFC- LDAC concept for server.

To achieve the research goal, the following objectives are prescribed:

1. Continue literature review on SOFC Technology, liquid desiccant dehumidification technology, and data center power and cooling.
2. Develop and verify a dynamic SOFC system model that simulates the physical operation of the SOFC system (BlueGEN) based upon Efficient Allocation of Grid Energy Resources including Storage (EAGERS).
3. Develop and verify a physical model for liquid desiccant air conditioning system including dehumidifier, regeneration, and evaporative cooler.
4. Develop a model to calculate data center demand based on cooling type and weather conditions.

5. Theoretical analysis for integrated system in different weather condition and determining the storage capacity for yearly demand.
6. Experimental set-up and long-term test and evaluation of SOFC system degradation under steady-state and dynamic operation.
7. Experimental set-up and long-term test and evaluation of SOFC degradation fed by alternative fuels.

1.4 Approach

This dissertation includes six key tasks, with one task established for each of the objectives described previously to meet the goal.

Task 1: Background & literature review (Chapter 2)

A comprehensive literature review was conducted throughout this research on the following topics: SOFC systems and modeling, data center power and cooling systems, liquid desiccant cooling technology and modeling, data center load demands, SOFC degradation test and modeling, alternative fuels for SOFC, Electrochemical Impedance Spectroscopy (EIS) and characterization methods.

Task 2: Develop a physical dynamic model and control strategies for an SOFC system that simulates the operation of the SOFC system (Chapter 3)

A quasi-3D dynamic model was developed and modified for solid oxide fuel cell as well as an appropriate balance of plant that matches the performance of the commercialized SOFC system of this research. A control strategy was developed for dynamic operation of the system. In this task, dynamic behavior of SOFC system was evaluated.

Task 3: Develop a physical model for liquid desiccant dehumidifier simulation (Chapter 4)

A physical model was developed for dehumidifier, regenerator and indirect evaporative cooler to simulate the process of producing strong desiccant from exhaust of SOFC and cooled and dehumidified air for servers cooling. A control strategy has been developed for the LDAC system. The developed model has been verified with literature in this task.

Task 4: Develop a data center cooling demand model (Chapter 5)

A data center cooling demand prediction model is developed. The model calculates the cooling demand required of data center for the entire year based on the weather condition. Cooling demand of seven different locations that is home to data center is calculated and analyzed in this task.

Task 5: Investigate SOFC integrated system with LDAC and the storage capacity required for providing cooling and power for the entire year (Chapter 6)

The dehumidification capability in typical data center locations is analyzed based on SOFC exhaust effect. different configuration for integrated system is evaluated. Also, a SOFC-LDAC system is designed based on the storage size and demand of data center in various locations. Finally, yearly storage capacity for different weather conditions and different configuration is evaluated.

Task 6: Develop and operate an experimental setup to evaluate SOFC degradation (Chapter 7)

In this task, I Installed the components and connections of eight BlueGEN system. Long term steady state and dynamic test on SOFC system is developed. The effect of dynamic operation on SOFC degradation is investigated. In the second part of this task, SOFC single cell setup was developed, and four cells was mounted. Three separate 100 hour is performed on NH_3, N_2-H_2, and H_2. EIS and polarization curve (IV) measurements were performed every hundred hours. Effect of different fuels on SOFC degradation is investigated. Also, Scanning Electron Microscopy (SEM) was performed to observe the microstructure changes of the cell after testing

2 Background & Literature Review

2.1 Data center

Data centers are centralized locations with computing and networking equipment for collecting, storing, processing, distributing or allowing access to large amounts of data. Because of their high concentrations of computer servers, often stacked in racks that are placed in rows, data centers are sometimes called server farms. Data centers provide services such as data storage, backup and recovery, data management and networking. These centers can run e-mail and instant messaging services, store and serve up web sites, provide cloud storage and applications, enable e-commerce transactions, power online gaming communities, etc.

Some components for supporting data center infrastructure include:

- Uninterruptible power supplies (UPS) – battery banks, fueled generators, and redundant power sources.
- Environmental Control – Computer Room Air Conditioners (CRAC), Heating, Ventilation, and Air Conditioning (HVAC) systems, and exhaust systems.
- Security Systems – biometrics and video surveillance systems.
- IT equipment – actual equipment for IT operations and storage of the organization's data. This includes servers, storage hardware, cables, and racks [13].
- Backup Power – a set of fueled combustion-based power generators usually powered by natural gas or diesel.

2.1.1 Data center power infrastructure

Most traditional data centers get their primary electricity from utility electric grid. The facility will then either have one or several transformers in place to take in the energy, while also ensuring the power coming in is of the right voltage and the right type of current (converted from AC to Direct Current (DC) typically). Some data centers supplement their energy from the grid or completely remove it by on-site electrical generation equipment -

either in the form of combustion-based generators or with alternative energy sources such as solar photovoltaic panels and wind-powered turbines. The power then gets transferred to the main distribution boards which house fuses, circuit breakers, and ground leakage protection units, take the low-voltage electricity and distribute it to a number of UPS systems. UPS are responsible for supplying power to a number of racks while helping clean up the electricity pulsing through by ensuring that issues like surges don't impact equipment. UPS systems also serve as an initial backup, in case of a power outage or similar issue. In a nutshell, a UPS battery turns on after the system senses a loss of power. Their purpose is to maintain the infrastructure until consistent power returns, or if needed, until longer-term emergency power backup systems kick in. A typical UPS can provide power to servers and breakers for up to five minutes; that way, there's enough time to get a backup generator going immediately following an outage or similar issue with the wider electric grid. In order to ensure continuous uptime and minimize outages as much as possible, most data centers have a backup power source on site or nearby. Often backup power supply comes from a fuel generator powered by gasoline or diesel [14].

In a data center, not only servers and other critical pieces of IT equipment require a lot of electricity to operate, but also all of the ancillary equipment. Lights, cooling systems, monitors, humidifiers, etc. also need electricity. The amount of electricity that goes towards servers versus non-IT equipment is called Power Usage Efficiency (PUE) score which measures usage effectiveness. A score of 1 means that all the energy in a data center goes towards servers, while a score of 2 means that ancillary equipment uses just as much electricity as servers and other IT components [14]. The Uptime Institute survey shows that the average PUE of a data center stands at 1.58. The average PUE for a Google data center is 1.12, but its facility in Oklahoma had a score of just 1.08 during the last three months of 2018 [15].

Today, the average power consumption for a rack is around 7kW depending upon the data center. However, almost two-thirds of data centers in the US experience higher peak demands, with a power density of around 15kW to 16kW per rack. Some data centers may hit 20kW or more per rack at times [16]. The Uptime Institute's latest survey found that around one in five have a density of 30kWor higher, indicating the growing presence of high-

density computing. Half said their current rack density was between 10kW and 29kW [15]. One of the most critical challenges associated with increasing power density within data centers is cooling. Alternative cooling technologies and methodologies such as liquid cooling, use of solar and wind for power cooling systems are being developed against that need.

2.1.2 Data center cooling

One of the largest operational expenses of data centers is the cost of energy. Cooling power consumption accounts for up to 40% of data center energy use [10]. The original American Society of Heating, Refrigerating and Air-Conditioning Engineers (ASHRAE) air temperature envelope was 20-25℃ in 2004 based on reliability and uptime as the primary concern. Nowadays, changes to data center environmental conditions are being driven by the need to save energy and reduce operational expenses. From 2016, ASHRAE recommended range of temperature and humidity is 18˚C to 28˚C dry bulb temperature, 9˚C to 15˚C dew point and 60% relative humidity [17]. The Uptime Institute, however, recommends an upper limit of 25˚C [15].

There are different common ways of to remove excess heat in data centers as shown in Figure 5.

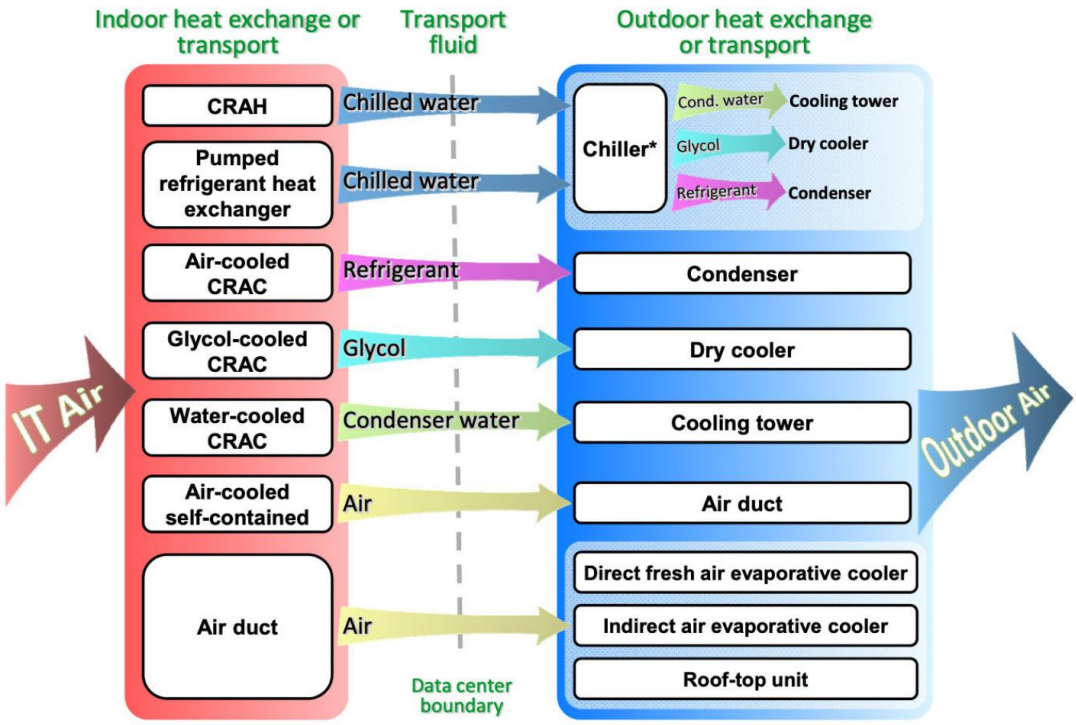

Figure 5. Simplified heat removal methods in data centers [18].

A Computer Room Air Handling (CRAH) is similar to a chilled water air handling system. In this system, the cooling is accomplished by blowing air over the cooling coil filled with the chilled water. The chilled water is typically supplied to the CRAHs by an electric powered chiller. The chiller then removes the heat from the warmer chilled water and transfers it to another stream of circulating water called condenser water which flows through a cooling tower. These CRAHs can have Variable Frequency Drives (VFD) that modulate fan speed to maintain a set static pressure either under floor or in the overhead ducts. Heat removed from the returning chilled water can be rejected to a condenser water loop for transport to the outside atmosphere or to an air-cooled condenser, or to a glycol cooled chiller.

A CRAC unit works like an air conditioner which has an in-built direct expansion refrigeration cycle. The compressors which are required to power the refrigeration cycle is also located within the CRAC unit. Thus, the cooling is accomplished by blowing the air over the cooling coil filled with refrigerant. Heat from the IT environment is pumped to the outdoor environment using this circulating flow of refrigerant. New CRAC units are

developed that can vary the airflow with the help of multistage compressors. However, most of the existing ones have on/off control only.

Modern data centers try to use adiabatic direct air cooling whenever the weather conditions allow. The common types of cooling are as follows:

Free Cooling: Free cooling is an approach for cooling the air temperature in the target environment by using ambient cool air or water from the local environment instead of mechanical refrigeration. In this method, pumps, fans, and other air/water-handling equipment are needed. Cooling systems that use this approach are also called air-side economizers. The primary method is evaporative cooling, where ambient air is passed through a wet filter that cools it. The air then enters the cooling system at a lower temperature, which allows for more efficient operation. Evaporative assist is most beneficial in dry climates. Alternatively, in water side economizer a source of cold water from local rivers, lakes or oceans is circulated into a data center and used instead of refrigerating a closed water loop with a chiller [19]. Evaporative assist is an adiabatic cooling system which does not have heat exchange to the environment. Adiabatic cooling incorporates both evaporative and air cooling into a single system [20].

An indirect ambient air cooling system uses outdoor air to indirectly cool data center air when the temperature outside is lower than the temperature set point of the IT inlet air, resulting in significant energy savings. Fans blow cold outside air through an air-to-air heat exchanger which in turn cools the hot data center air on the other side of the heat exchanger, thereby completely isolating the data center air from the outside air. Heat exchangers can be of the plate or rotating type. Heat removal method normally uses evaporative assist whereby the outside of the air-to-air heat exchanger is sprayed with water which further lowers the temperature of the outside air and thus the hot data center air [18].

Indirect adiabatic data center cooling: The indirect adiabatic cooling consists of two different airflows named primary and secondary airflow as shown Figure 6.

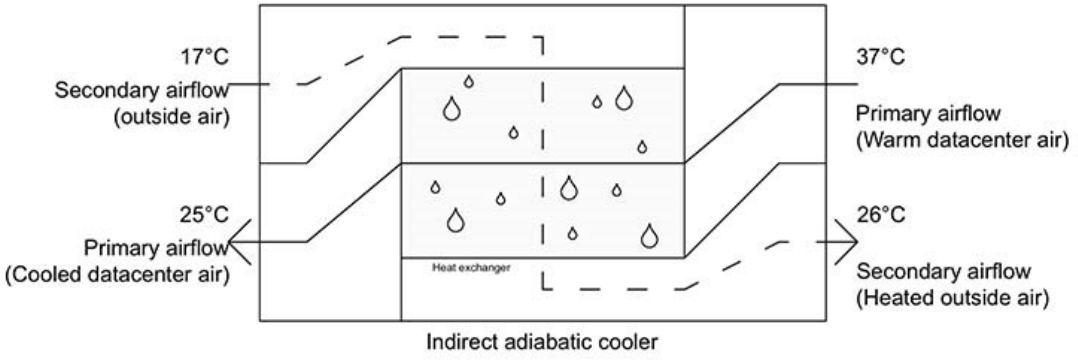

Figure 6. Indirect adiabatic cooler [21].

Primary airflow is the airflow that is used to cool the IT load. The secondary airflow is the outside or the ambient air which is used to discharge the IT load of the primary airflow. The primary airflow and secondary airflow are completely separated from each other because mixing them will create pollution and inconsistencies. During warm days water is sprayed on the heat exchanger to increase the cooling capacity of the secondary airflow according to the physical laws of psychrometrics. The water also provides a better conductivity between the two airflows by optimizing the energy transfer. Most units require a basic water softening system to produce the required water. A water storage tank is required to store a certain amount of water in case of water outage from the main water connection. There are basically two operating modes, Summer/wet: If conditions are not met for the secondary airflow, the air is humidified by adding a specific amount of water to the secondary air flow to increase its cooling capacity.

In addition to these adiabatic cooling systems, direct expansion (DX) cooling systems (i.e., those that use the vapor compression thermodynamic cycle), powered by electricity, may be required in specific locations to reach the cooling demand of the data center. Winter/dry: Primary airflow transfers its heat towards the cooler secondary airflow without the requirement of water. The indirect adiabatic cooler is known for its high energy efficiency reaching a cooling PUE of 1.05 at a single moment [21].

There are three basic approaches for distributing air in a data center: flooded, targeted, and contained. In a flooded supply and return air distribution system, the only constraints to the

supply and return air flow are the walls, ceiling, and floor of the room. This leads to heavy mixing of the hot and cold air flows. In a targeted supply and return air distribution system, a mechanism (e.g., duct, perforated tile, cooling unit placed within IT rows) directs the supply and return airflow within 3m (10ft) of the IT equipment intake and exhaust. In a contained supply and return air distribution system, the IT equipment supply and return air flow is completely enclosed to eliminate air mixing between the supply and the return air streams [22]. Hot aisle/cold aisle arrangements lower cooling costs by better managing airflow, thereby accommodating lower fan speeds and increasing the use of air-side or water-side economizers. When used in combination with containment, Department of Energy (DOE) estimates reduction in fan energy use of 20% to 25% [23].

Another data center cooling technique is open bath immersion cooling which implies fully submerging IT equipment in a dielectric liquid. These baths allow the coolant fluid to be moved through the hardware components or servers submerged in it. Single phase immersion requires circulation of the dielectric liquids by pumps or by natural convection flow. These liquids always remain in the liquid state while operating. The dielectric coolant is either pumped through an external heat exchanger where it is cooled with any facility coolant, or the facility coolant is pumped through an immersed heat exchanger, which facilitates heat transfer within the dielectric liquid. In two-phase immersion systems, heat is removed through the phase change that the coolant undergoes at its operating temperature. The server heat literally boils the dielectric fluid that has an appropriate boiling point temperature. This two-phase immersion system takes advantage of the dielectric fluid latent heat of vaporization. This occurs when the two-phase coolant comes in contact with the heated electronics in the bath that are above the coolants boiling point. Once the two-phase coolant enters its gas phase it must be cooled or condensed, typically through the use of water-cooled coils placed in the top of the tank. Once condensed the two-phase coolant drips back into the primary cooling tank. The two-phase coolant in the tank generally remains at its “saturation temperature”. Energy transferred from the servers into the two-phase coolant will cause a portion of it to boil off into a gas. The gas rises above the liquid level where it contacts a condenser which is cooler than the saturation temperature. This causes the gaseous state coolant to condense back into a liquid form and fall back into the bath [24]. In

order to safely submerge an electronic device in a liquid, the liquid must be nonconductive to avoid short-circuit electronic signals or change in the signal characteristics of sensitive, high-speed electronic devices, such as Central Processing Unit (CPU)s and memory modules. The liquid must also be completely noncorrosive and avoid any sort of damage to electronic packaging, contacts, or printed wet or dry circuit layouts. The liquid must be nonflammable, nontoxic, and easy to clean up if there is a spill. Immersion cooling mainly work in baths of mineral oil, and companies that have developed liquids such as Novec, which meet the criteria for electronic immersion cooling [25].

2.2 Solid Oxide Fuel Cell technology and system

2.2.1 Fuel cell

Fuel cell devices are capable of converting fuel directly into electricity without the need of turbines or any major moving parts. The following section discusses how fuel cells work and some of the motivating principles behind their operation. Hydrogen is the most basic fuel used in the fuel cell electrochemical reactions, but fuel cell systems can operate on a wide variety of fuels. All fuel cells also require an oxidant, which is usually oxygen taken from air. The fuel and oxidant are separated by the membrane-electrode assembly. The membrane-electrode assembly is made up of anode and cathode electrodes and an electrolyte which is sandwiched between the two electrodes. The electrodes are permeable to gas so that the gases can make contact with the electrolyte. Points at which the gas, electrode, and electrolyte meet are points where an electrochemical reaction can occur which liberates an electron into or out of the electrode as an ion is transferred through the electrolyte. These points are called triple-phase boundaries (TPB). For example, with hydrogen electrochemistry and with proton-conducting electrolytes, the hydrogen splits, releasing two electrons into the anode while the hydrogen ions (protons) travel through the electrolyte. The ions then react with oxygen atoms and electrons at TPB locations in the cathode compartment to form water. A voltage (potential) difference between the anode and cathode is produced by the electrochemical reactions, which drives an electric current

through the external circuit. The overall reaction of fuel and oxidant to form products in a hydrogen fuel cell is as follows:

$$H_2 + \frac{1}{2}O_2 \rightarrow H_2O$$ Equation 1

Equation 1 shows the overall reaction of the fuel cell while two electrochemical half-reactions are accomplished at the anode and cathode TPBs as follows:

$$H_2 \rightarrow 2H^+ + 2e^-$$ Equation 2

$$\frac{1}{2}O_2 + 2H^+ + 2e^- \rightarrow H_2O$$ Equation 3

Equation 2 and Equation 3 are the two half reactions which occur at the anode and cathode, respectively. Fuel cells are often categorized by the type of electrolyte they have and their operating temperature. The various materials that are used to make up different electrolytes often require different electrochemical reactions to take place. However, the characteristics of these different fuel cells are governed by the same fundamental principles. Analyzing from a thermodynamic point of view, the maximum work output obtained from the above reaction is related to the free-energy change of the reaction. The above reaction is spontaneous and thermodynamically favored because the free energy of the products is less than that of the reactants. The standard free energy change of the fuel cell reaction is indicated by the equation:

$$\Delta G = -nFE$$ Equation 4

Where ΔG is the Gibbs free energy change, n is the number of moles of electrons involved, E is the reversible potential, and F is Faraday's constant. If the reactants and the products are in their standard states, the equation can be represented as:

$$\Delta G_0 = -nFE_0$$ Equation 5

The ideal performance of a fuel cell can be represented in different ways. The most commonly used practice is to define it by the Nernst potential which defines the maximum

realizable voltage accounting for non-standard conditions of temperature and pressure and the extent of reaction. The Nernst equation is a representation of the relationship between the ideal standard potential "E_0" for the fuel cell reaction and the reversible potential "E" at other temperatures and pressures of reactants and products. Once the ideal potential at standard conditions is known, the maximum realizable voltage can be determined at other temperatures, pressures, and extents of reaction through the use of these equations. According to the Nernst equation for hydrogen oxidation, the maximum cell potential at a given temperature can be increased by operating the cell at higher reactant activities, a. Improvements in fuel cell performance have been observed at higher pressures and temperatures. The symbol E represents the reversible potential, E_0 the standard potential, P the gas pressure, R the universal gas constant, F Faraday's constant and T the absolute temperature. Nernst voltage V_{Nernst} is defined:

$$V_{Nernst} = E_0 - \frac{RT}{zF} ln\left(\frac{\prod(a_{products})}{\prod(a_{reactants})}\right) \qquad \text{Equation 6}$$

The minus sign is turned positive if the activity of the reactants and products are flipped in accordance with properties of logarithms. If water is assumed to be in the form of steam (vapor), and partial pressures are substituted into the expression for gas-phase activities, then the Nernst voltage for the Equation 6 becomes:

$$V_{Nernst} = E_0 - \frac{RT}{2F} ln\left(\frac{P_{H_2O}}{P_{H_2} P_{O_2}^{\frac{1}{2}}}\right) \qquad \text{Equation 7}$$

While the Nernst voltage can be realized when a fuel cell does no net work (thermodynamic equilibrium conditions are established with no flow of current flows leading to a measured open circuit voltage that is close to the Nernst potential), once electric current flows, additional voltage losses are realized. Figure 7 displays the ideal and actual responses of a fuel cell to increasing current demands. Electrical energy is obtained from a fuel cell when a current is drawn, but the actual cell potential is lowered from its equilibrium potential because of irreversible losses due to various reasons. Several factors contribute to the irreversible losses in a practical fuel cell. The losses, which are generally called polarization or over potential, originate primarily from activation polarization, ohmic polarization, and

gas concentration polarization. These losses result in a cell potential for a fuel cell that is less than its ideal potential.

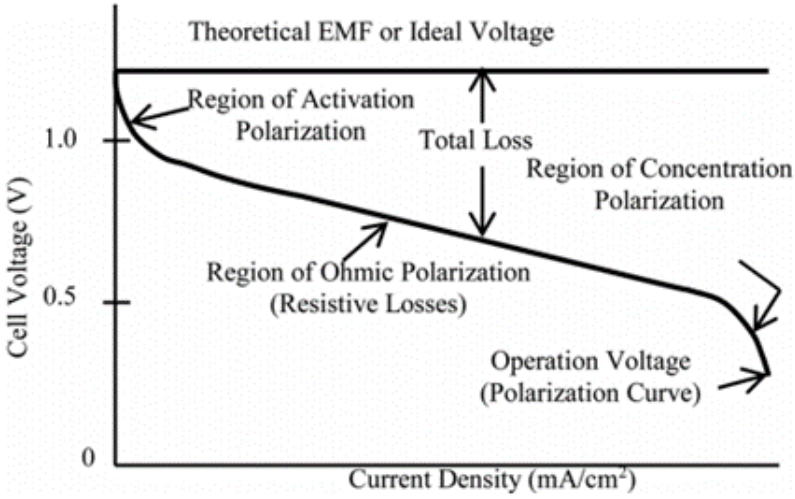

Figure 7. Ideal and Actual Voltage Current Density Curve of Fuel Cell [18].

The first of these three major polarizations is the activation loss, which is pronounced in the low current region. In this region electrochemical reaction kinetics barriers must be overcome before the advent of current and ionic flow. The activation loss is directly proportional to the increase in current flow. The activation polarization can be represented as:

$$\eta_{act} = \frac{RT}{\alpha nF} \ln\left(\frac{i}{i_0}\right) \qquad \text{Equation 8}$$

Where η_{act} is the activation polarization, R the universal gas constant, T the temperature, α the charge transfer coefficient, n the number of electrons involved, F the Faraday constant, i the current density, and i_0 the exchange current density. Activation polarization is due to the slow electrochemical reactions at the electrode surface, where the species are oxidized or reduced in a fuel cell reaction. Activation polarization is directly related to the rate at which the fuel or the oxidant is oxidized or reduced. In the case of fuel cell reactions, the activation barrier must be overcome by the reacting species.

The ohmic polarization varies proportionally to the increase in current and increases over the entire range of currents due to the constant nature of the overall fuel cell resistance. The ohmic polarization can be represented as:

$$\eta_{ohm} = iR_c \qquad \text{Equation 9}$$

Where η_{ohm} is the ohmic polarization and R_c is the overall cell resistance. The origin of ohmic polarization comes from the resistance to the flow of ions in the electrolyte (primarily) and from the flow of electrons through the electrodes, current collectors, bipolar plates, etc. Ohmic polarization can be decreased by increasing ionic conductivity of the electrolyte or shortening the ion conduction length (i.e., using a thinner electrolyte or modifying of the electrolyte properties).

The concentration losses occur over the entire range of current density, but these losses become prominent at high limiting currents where it becomes difficult for gas reactants to diffuse through the porous gas electrodes to the fuel cell reaction sites (TPB) and products to diffuse from these same sites fast enough to keep up with the rate required to maintain the electric current flow. The concentration polarization can be represented as:

$$\eta_{con} = \left(\frac{RT}{nF}\right)\ln\left(1 - \frac{i}{i_L}\right) \qquad \text{Equation 10}$$

Where η_{con} is the concentration polarization, which is the limiting current density. As the reactant gas is consumed at the TPBs through the electrochemical reactions, there will be a potential drop due to the drop in the TPB concentration compared to that in the bulk of the fluid. This leads to the formation of a concentration gradient across both of the electrode thicknesses. Several processes are responsible for the formation of the concentration polarization. These are (1) solution of reactants into the electrolyte, (2) dissolution of products out of the electrolyte, and (3) diffusion of reactants to and products from the reaction sites, through the electrode. At practical current densities reactant and product diffusion rates are sufficient to avoid significant concentration polarization, but, at high current densities these rates of diffusion can become comparable to reaction rates leading to concentration polarization.

2.2.2 Integrated SOFC system

SOFC usually operate at high temperatures in the range of about 600-1000°C, which temperature range is well-suited to integrating bottoming cycles for additional power, heating or cooling production, which results in improved overall system efficiency when compared to an individual stand-alone system. An analysis of a hybrid system of micro-turbine and fuel cell as a prime mover of Combined Cooling, Heating, and Power (CCHP) plants was carried out by Saito et al. [22]. They carried out electricity demand and consumption analyses of apartments, offices and hotels in Japan with the use of the hybrid system. They found that the annual fuel consumption dropped by 32%, 36% and 42% for the apartments, offices and hotels, respectively. One general method to recover the waste heat from the SOFC is the SOFC-GT system, in which SOFC is coupled with a Gas Turbine (GT) as the bottom cycle to increase the overall efficiency by recovering waste heat from SOFC exhaust. The concept of SOFC-GT hybrid system was proposed for decades, and many researchers have studied the theoretical analysis of this hybrid system [23–29]. Siemens-Westinghouse Power Corporation developed the first hybrid power system, which integrated an SOFC stack with a gas turbine engine. The pressurized (3atm) system generated 220kW of electrical power at a net electrical efficiency of 53.5% [30]. Mueller et al. [31] designed a theoretical solid oxide fuel cell-gas turbine hybrid system using a 60kW micro-gas turbine. Although using a gas turbine can recover waste heat from an SOFC, the exhaust gas from the gas turbine still has relatively high temperature that could be used in other bottoming cycles. If the waste heat from gas turbine can also be recovered by some method, then the energy conversion efficiency can increase further.

Another method to recover the waste heat from the SOFC is the SOFC- Organic Rankine Cycle (ORC) combined system. Using ORC as a bottoming cycle of the SOFC, the system can fully recover the waste heat from the SOFC. Some research has been conducted on the waste heat recovery of the exhaust from the SOFC by ORC. Akkaya and Sahin [32] presented an energetic analysis for a combined power generation system consisting of an SOFC and an ORC. The results showed that the efficiency was increased by about 14-25% by recovering SOFC waste heat through ORC based on investigated design parameter conditions. And there existed an

optimum value of fuel utilization factor maximizing the efficiency. Al-Sulaiman et al. [33] proposed a cooling, heating and power production system based on the SOFC and ORC. The energy analysis showed that at least a 22% gain in efficiency was achieved compared with the stand-alone SOFC system. Ghirardo et al. [34] conducted a study on heat recovery for a 250kW SOFC onboard a ship. Using ORC could produce 35kW of electricity from the waste heat of 181 kW. The overall efficiency increased from 44% to 49% and the cost of energy dropped from 0.25$/kWh to 0.22$/kWh. In another study, Al-Sulaiman et al. [35] analyzed CO_2 emissions from the CCHP system. The study showed that the CO_2 emissions per MWh are significantly less than that of the CO_2 emissions per MWh of the electricity produced by the SOFC alone or the net electrical power of the system. In another study, Al-Sulaiman et al. [36] studied the feasibility of using a CCHP plant based on ORC and solid oxide fuel cells. In their study, it was shown that there is 3–25% gain on exergy efficiency when compared with the power cycle only. In a different study, Al-Sulaiman et al. [37] examined a CCHP system using a biomass combustor and an ORC. In their study, it was shown that the exergy efficiency of the CCHP system increases significantly to 27% as compared with the exergy efficiency of the electrical power case, which is around 11%. In [38], the performances of a 100kW SOFC-ORC system coupled with a gasification facility was carried out by means of a multi-objective optimization. Their results show that efficiencies in the range of 54-56% can be achieved by wisely selecting the organic fluid properties. In [39], Al-Sulaiman et al. compared performance of three different CCHP systems based on SOFC, Biomass, and Solar using ORC. This study shows that the SOFC CCHP system has the highest electrical efficiency among the three systems.

In SOFC-ORC combined systems, it is a novel idea to use the ORC waste heat for cooling purposes. Several studies were conducted in using absorption chiller as a bottoming cycle of the SOFC for cooling. Margalef and Samuelsen [40] studied an integrated molten carbonate fuel cell and absorption chiller cogeneration system, showing that the overall electrical and cooling efficiency can achieve 71.7%. Furthermore, Silveira et al. [41,42] examined a molten carbonate fuel cell cogeneration system integrated with absorption refrigeration which was applied to a dairy for electricity and cold water production. The results showed that the electrical efficiency of the system and the second law efficiency of the fuel cell unit were 49%

and 46%, respectively. Leong [43] analyzed an integrated natural gas fed solid oxide fuel cell with a zeolite/water adsorption chiller. The results show that the proposed cogeneration system can achieve a total efficiency (combined electrical power and cooling power) of more than 77%. A steady state mathematical model was developed to simulate the effects of different SOFC operating conditions on an energy system incorporating SOFC and exhaust gas driven absorption chiller. The effect of fuel utilization factor on electrical, cooling, and total efficiency was investigated [44]. Zink et al. [45] studied an integrated solid oxide fuel cell absorption heating and cooling system for buildings, concluding that the combined system demonstrated great advantages in both technical and environmental aspects. An integrated SOFC and a double effect water/Lithium Bromide absorption chiller were presented by Yu et al. [46]. The system performance was analyzed under different fuel utilization ratio, fuel flow ratio, and air inlet temperature. Al-Sulaiman et al. studied the use of an SOFC integrated with both ORC and absorption chiller [33]. In this study, the waste heat from the ORC is used to produce cooling using a single-effect absorption chiller. The study shows that the maximum efficiency of the trigeneration plant is 74%, heating cogeneration is 71%, cooling cogeneration is 57% and net electricity is 46%. Asghari et al. [47] studied dynamic integration of SOFC with AC and ORC. Figure 8 shows the schematic of configuration of this study. Results showed that the SOFC was capable of following the highly dynamic load with an average electrical efficiency of 46%. An average of 7% more power was produced through the ORC cycle with an average efficiency of 10%. The AC generated an average 125kW of cooling with an average Coefficient of Performance (COP) of 1.08.

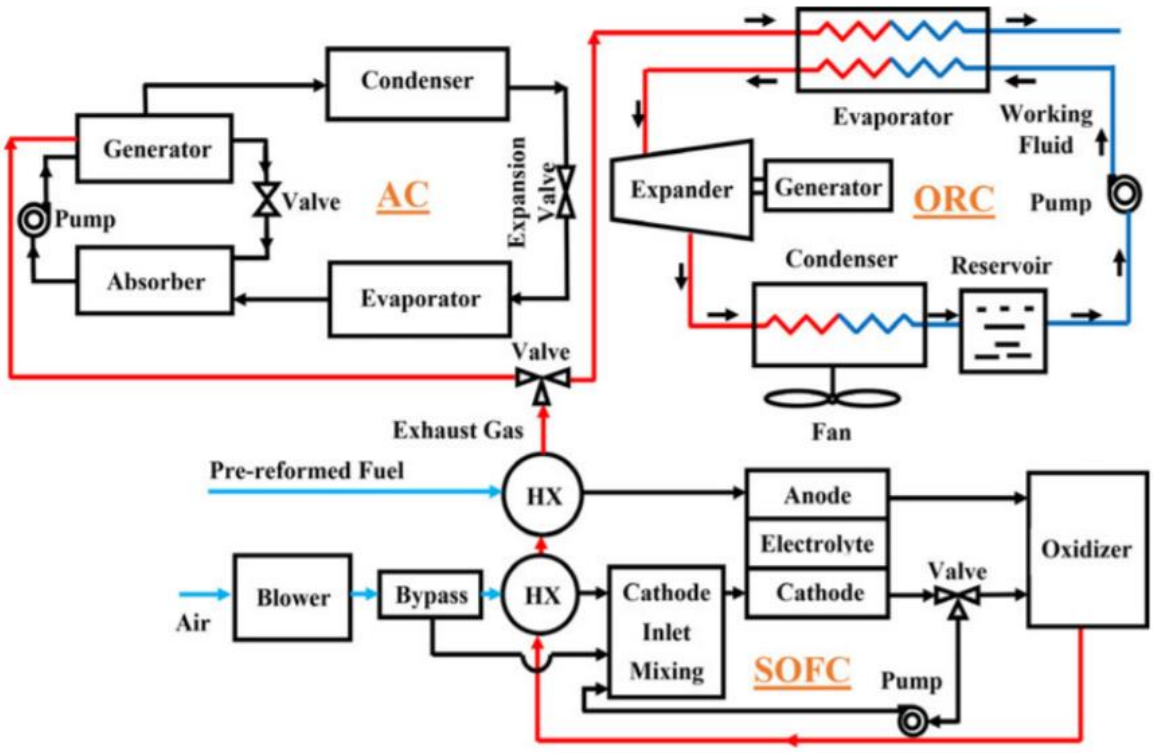

Figure 8. Schematic configuration of the SOFC-ORC-AC system [47].

Mehpoya et al. [48] investigated optimal design of solid oxide fuel cell-gas turbine power plant, Rankine steam cycle and ammonia-water absorption refrigeration. Results indicate that electrical efficiency of the combined system is 62.4% Lower Heating Value (LHV). Produced refrigeration (at 10^{o}C) and heat recovery are 101kW and 22.1kW respectively. In [49], Rokni studied SOFC system integrated with an absorption chiller for special applications such as hotels, resorts, hospitals, etc. with a focus on plant design and performance. The proposal system is based on the idea of gasifying the municipal waste, producing syngas serving as fuel for the trigeneration system. It is shown that the energy efficiency of such small tri-generation system is more than 83% with net power of 170kW and district energy of about 250W. Tian et al. [50] proposed and investigated an integrated SOFC system, an ORC, and an ammonia water absorption chiller with a CO_2 capture system is proposed and investigated. The results show that the net electrical efficiency and the exergy efficiency of the integrated system can reach 52.83% and 59.96%, respectively. The trigeneration efficiencies of the combined system without and with CO_2 capture are 74.28% and 72.23%, respectively.

During recent years there have been some research on integration of SOFC with adsorption technologies [51–54]. In [54] Wu et al. have studies SOFC combined heat and power system integrated with adsorption refrigeration subsystem. Figure 9 shows the proposed system schematic. The authors dynamically simulated the integrated system. Simulation results show the proposed system produces 4.35kW of electrical power, 2.448kW of exhaust heat power, and 1.348kW of cooling power. The energy efficiency of the system is 64.9% and the COP of the refrigeration system is 0.32.

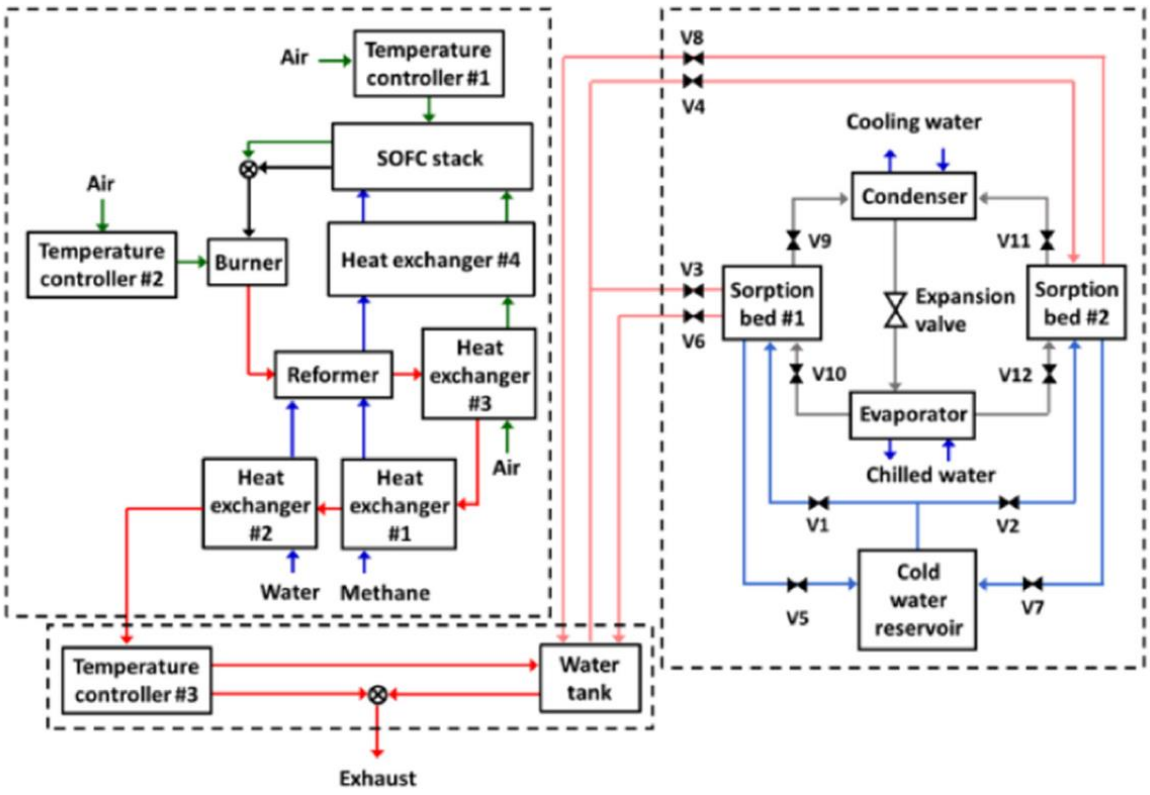

Figure 9. Proposed SOFC trigeneration system, consisting of three subsystems: SOFC-CHP system, adsorption refrigeration system, and water tank equipped with a temperature controller[54].

2.2.3 SOFC driven data center

The implementation of SOFC technology in data centers has many advantages including fuel flexibility, lower emissions, higher production efficiency, and the production of high-quality exhaust heat for co-generation applications. These advantages could reduce the data center's footprint through the synergistic integration of power and cooling to supply the data center.

eBay installed 6MW of fuel cell from Bloom Energy as the primary power source for their data center in Utah while using the local utility grid for backup [55]. In 2013, Apple installed 10MW capacity high temperature fuel cells to power their entire data center [56]. Equinix started a project in 2017 to power 12 data centers in US with a total capacity of more than 37MW of Bloom fuel cell [57]. Microsoft in collaboration with the National Fuel Cell Research Center (NFCRC) demonstrated the concept of a rack of data center servers powered directly by the DC output of a fuel cell stack for the first time at the NFCRC in University of California, Irvine [58]. Etemadieh [59] looked into using SOFC system for data center application. Later, Microsoft started a new Advanced Energy Lab in Seattle, Washington to power 20 data center racks directly from DC power of SOFC systems [60]. Direct highly efficient power generation at the rack level removes the need for complex power distribution systems, reduces costs significantly, and allows decentralized architecture. Having shown [61] that the desired reliability is achievable through well-designed distributed fuel cell power systems, backup power sources are no longer required. National Renewable Energy Laboratory (NREL) [62] recently have started looking at rack level powered data centers using PEM fuel cells while producing hydrogen fuel for fuel cells by on site electrolysis using renewable resources.

2.2.4 Ammonia for SOFC

SOFCs are promising technology that can directly operate on variety of fuels and the high temperature operation allows internal reforming of carbonated gas. As an alternate to carbonated fuel and due to high pressure required for storage of H_2, ammonia is getting more attention as a potential fuel for SOFC. Ammonia is carbon free, widely available, and has comparative price as hydrocarbons. Is it easily liquified and volumetric energy density of liquefied ammonia is higher than that of liquid hydrogen, which is useful in transport and storage. Anode and cathode half reactions of ammonia fed SOFC are presented by Equation 11to Equation 14 . The route of utilization of ammonia on SOFC is a two-step process [63–67]. The ammonia first decomposes to hydrogen on the anode side (Equation 11), followed by electrochemical oxidation of generated hydrogen to form water (Equation 14).

Anode side: $2NH_3 \rightarrow 3H_2 + N_2$ Equation 11

Anode side: $H_2 \rightarrow 2H^+ + 2e^-$ Equation 12

Cathode side: $O_2 + 2e \rightarrow 2O^{2-}$ Equation 13

Overall reaction: $2NH_3 + O_2 \rightarrow N_2 + 2H_2O$ Equation 14

A few groups have reported the promising performance of ammonia-fueled SOFCs [67–73], however, there are very few studies looking into long term degradation effect of SOFC fueled by ammonia [65]. Bernhard et al. [73] tested the performance of ammonia as fuel for SOFC, their results showed that ammonia exhibits excellent performance as fuel for SOFC however, in their EIS measurements they observed significant increase in ohmic resistance. They found that operating at counter flow is more favorable to co-flow as less ohmic and diffusion resistance was measured. Occurrence of nickel nitrite, microscopic pores and particle enlargement and agglomerations was observed in microstructure imaging. Hung et al. [74] studied the effect of pressurized ammonia fed on anode supported SOFC. Their finding showed that pressurizing and increasing temperature enhances the performance of ammonia fed SOFC. In addition, the SEM results of 10h stability test shows no microstructure change or degradation as well as the same element atomic percentage on Ni-YSZ on anode surface from Energy Dispersive X-Ray (EDX) spectra. Fuerte et al. [65] research showed similar behavior for ammonia fed SOFC compared to hydrogen fed SOFC at 700°C. However, Yang et al. [64] studied ammonia fed Ni/YSZ anode at 600°C and 700°C and their results demonstrated Ni was partially nitrated under the ammonia atmosphere. Literature findings on effect of ammonia on degradation of SOFC is inconsistent, as a result further investigation specially for long term degradation seems necessary. This work evaluates the long-term degradation effect of direct ammonia conversion on SOFC. EIS characterization, SEM Imaging and EDX quantifications are tools used in investigating the degradation of SOFC.

2.3 Liquid desiccant technology and system

Liquid desiccants have been used to produce dry air first in 1930s by Frigidaire Division of General Motors. The interest in liquid desiccants was increased after energy crisis and gas bubble in 1970s and 1980s. most on the interest was limited to Research & Development (R&D) activities until 1997, when Drykor started selling several thousands of LDAC until 2004 [75]. Interest in liquid desiccant dehumidification and cooling has increased due to liquid desiccant multiple benefits such as [76,77]:

- LDACs do not run based on climate polluting or toxic refrigerants.
- LDACs can be powered by low grade waste heat (45°C upwards).
- LDACs can dehumidify the air at a temperature above its dew point, therefore they do not need a reheat process such as that required by conventional AC technologies.
- LDACs run mostly on heat; their electric demand is typically one-fourth that of

a vapor-compression air conditioner.

- LDAC decouples latent and sensible heat removal.
- LDACs are exceptionally good at dehumidifying air; almost all the cooling they provide can be latent cooling.

These benefits allow LDACs to overcome problems with the conventional air conditioning. The most commonly used air conditioning is Vapor Compression Systems (VCS) due to stability in performance, lower cost, long life and resendable COP of between 2-4 [76]. However, VCS use harmful refrigerants such as R-22, R-41-A, and R- 134A which have high global warming potential and consume significant amount of electrical energy to drive the compressor [77]. Conventional cooling system such as chilled water or VCS cannot meet the latent cooling load on humid days. The other popular air conditioning systems are absorption chillers, which replace the electric driven compressor with a heat driven absorber and generator. The COP of these systems is in the range of 0.5 in single effect cycles and up to 1.2 in double effect cycles [78]. All conventional chillers and air conditioners cool the air sensibly and, dehumidify the air by lowering the air temperature below its dewpoint

so that moisture condenses and can be removed. The air that leaves this cooling coil in these traditional cooling systems is thus close to saturated conditions [79].

For supplying air at 18°C and 50% relative humidity, a conventional cooling system cools the air to 8°C as and then reheats the air to 18°C as it is shown with blue lines in Figure 10. In this case the air conditioner is overcoming roughly 30% more than is required to meet the load, and then also using even more power to reheat the air to desired supply temperature. A LDAC uses liquid desiccant to dehumidify the air the supply air to 25% relative humidity and a temperature that is 10C above the desired temperature. It performs almost 100% latent cooling (in case of internal cooling), then relies on a separate cooling for remaining sensible cooling and eliminate the overcooling/heating process [79,80]. Table 1 shows the comparison of liquid desiccant dehumidifier and VCS [81].

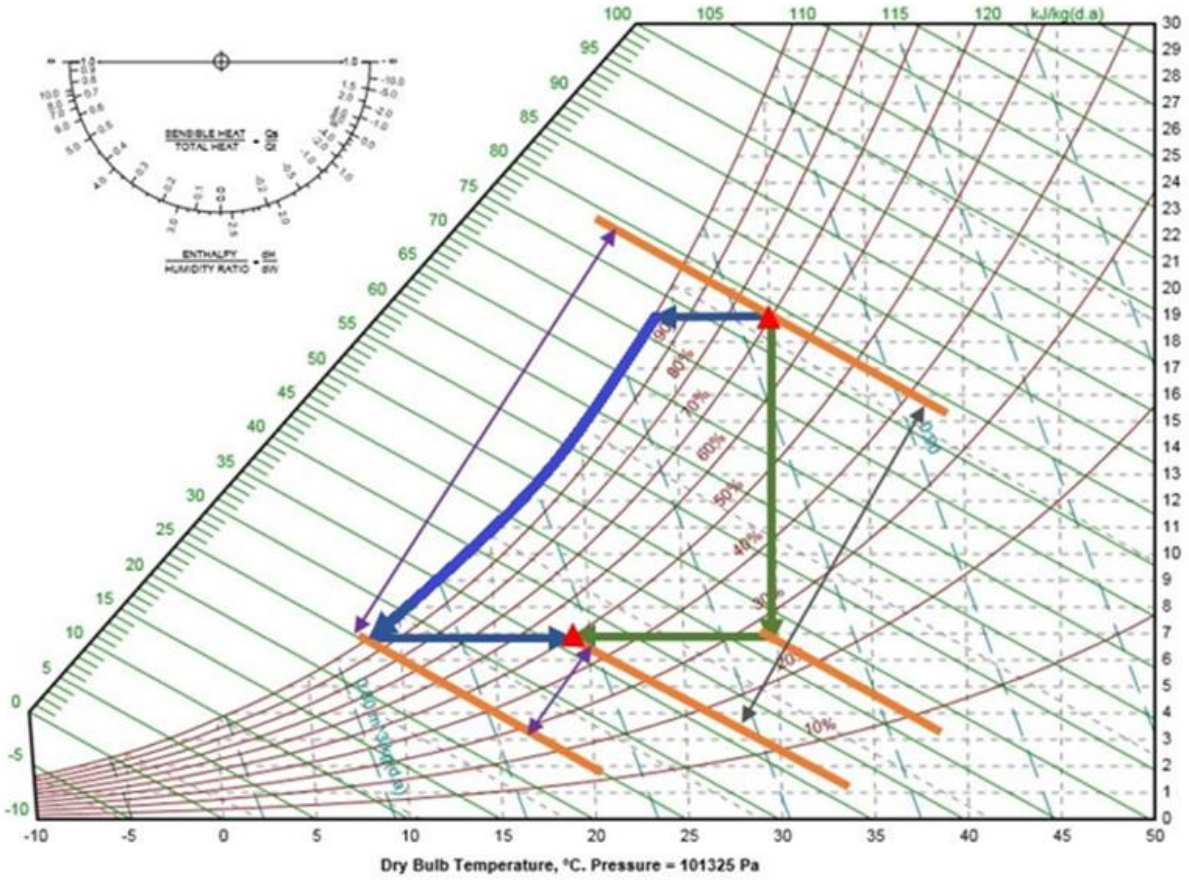

Figure 10. Liquid desiccant comparison to conventional air conditioning system.

Table 1. Comparison between liquid desiccant and vapor compression cooling [81].

Parameter	**Vapor Compression**	**Liquid Desiccant**
Initial Investment	Similar	Similar
Operation cost	High	Up to 40% saving
Driving Energy Source	Electricity, natural gas	Low-grade heat
Humidity Control	Average	Accurate
Temperature Control	Accurate	Average
Indoor Air Quality	Average	Good
Location Specific	Slightly	Yes
System Instalment	Average	Complicated
System Storage Capacity	Bad	Good

Figure 11 shows a typical industrial liquid desiccant system. In the absorber (also called conditioner) liquid desiccant absorbs the water from the air and dehumidifies the air. In this case, the regenerator is a bed of structured contact media similar to cooling tower. Liquid desiccant is first cooled to increase the ability of it to absorb water, and then sprayed onto the contact media. In this system, high flow rate of desiccant limits the desiccant temperature rises during absorption process. The air comes in direct contact with the liquid desiccant and gets dried and cooled. Typically, a ratio of the desiccant-to-air mass flow ratio that is on the order of one will limit the temperature rise of the desiccant. During the absorption process the liquid desiccant fluid becomes "weak," that is, the desiccant concentration in water is lowered. The desiccant fluid must then be regenerated (concentration of desiccant in water raised) to remove the water that was absorbed in the absorber. The regeneration process is the reverse of absorption. The desiccant is heated to a temperature at which the water equilibrium pressure is higher than the ambient air water vapor pressure. Hot desiccant, typically between 70℃ to 90℃, is sprayed over a bed of porous structure. The water is desorbed from the hot desiccant to flowing air through the bed. This air is typically exhausted to ambient. To reduce the energy use in the heater and cooler, usually an

interchange heat exchanger is used to preheat the weak desiccant and leaving the conditioner with hot strong desiccant leaving the regenerator [75,82]

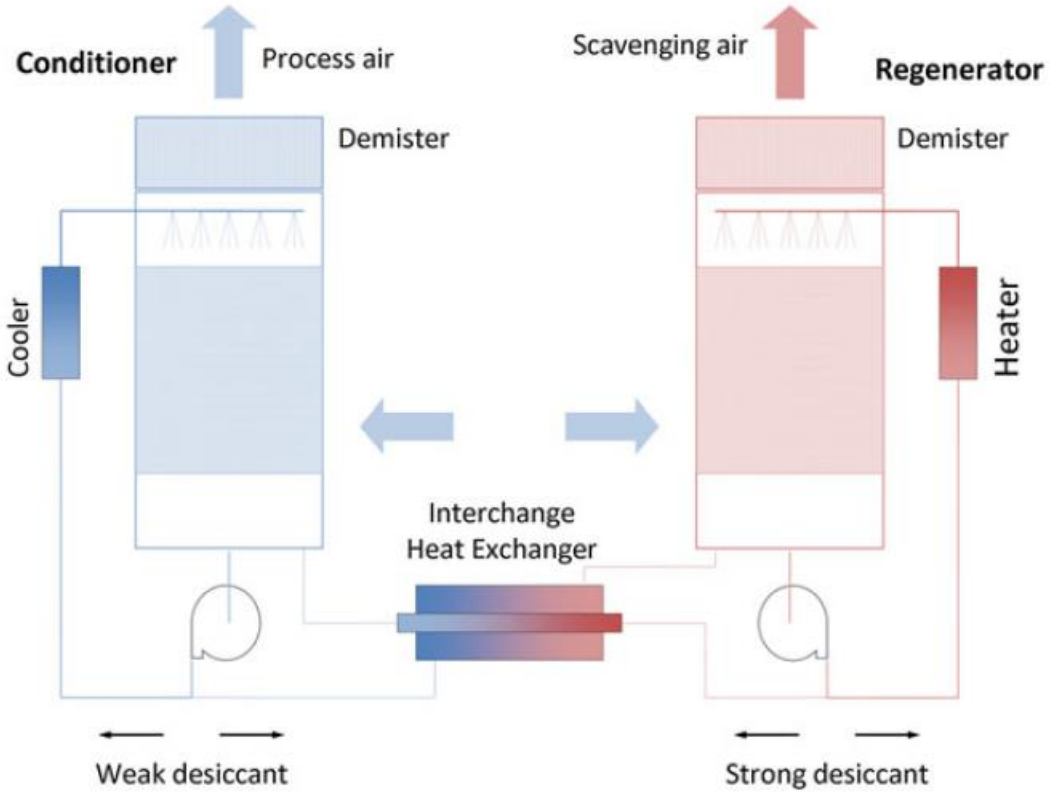

Figure 11. Conceptual layout of industrial liquid-desiccant system [75].

Liquid desiccants have lower regeneration temperatures, higher dehumidification capacity and lower air side pressure drop which reduces the fan power. Liquid desiccant makes energy storage possible and has higher capacities to hold moisture than solid desiccants. With liquid desiccant simultaneous cooling and dehumidification is achievable. Solid desiccants are compact, simple, less subject to carryover and corrosion which the carry over problem of LDAC has been solved with new generation of liquid desiccant. Also, the cost of manufacturing a liquid desiccant system is lower than that of a solid desiccant wheel [76,83].

2.3.1 Liquid desiccant solution

Liquid desiccants are material that have high attraction to water. Lithium chloride (LiCl), Calcium Chloride ($CaCl_2$) and Lithium Bromide (LiBr) are common types of liquid desiccants.

$CaCl_2$ is the cheapest solution [84] but has the poorest absorption ability. The strength of a desiccant is measured by its vapor pressure. When liquid desiccant is in equilibrium with the humid air, the temperature and vapor pressure of the humid air and the liquid desiccant should be the same. The equivalent humidity ratio of liquid desiccant (w_e can be found with the equilibrium state of the air as shown in Equation 15, where P is atmospheric pressure and p_s is the desiccant's vapor pressure).

$$w_e = 0.622 \frac{p_s}{P - p_s} \qquad \text{Equation 15}$$

At any given temperature, desiccant that has a water vapor pressure in equilibrium with the humidity ratio of the air (iso-concentration line), produces a line that is closely in line with a constant relative humidity line on psychometric chart. Lower concentrations of desiccant come into equilibrium at higher ambient air Relative Humidity (RH) levels. Liquid desiccant dehumidification is the inverse of evaporative cooling. Liquid desiccant can either absorb or desorb water from the air based on its relative humidity. If the equilibrium relative humidity of desiccant is below the relative humidity of the air, the desiccant absorbs water from the air and its temperature increases. The temperature that the air-desiccant interface approaches is called the brine-bulb temperature. This temperature is dependent upon air temperature and humidity, and liquid desiccant concentration in solution with water. The brine temperature is slightly higher than the temperature of intersection of constant enthalpy line from air state to equilibrium relative humidity of desiccant. This is due to the chemical heat of mixing between water and desiccant that is released in addition to latent heat of condensation.

During the dehumidification process, liquid desiccant absorbs the water from the air and releases heat, which decreases its water vapor pressure and ability to absorb water. Desiccant's ability to absorbs water also decreases by increasing its temperature. For example, if a 43% LiCl at 26.6°C can dry the air to 23.2 grains. But, absorbing the amount of water that dilutes it from 43% to 42% would increase the desiccant temperature to 50.5°C which decreases the ability of desiccant to dry the air to 107.6 grains, whereas if we keep the desiccant temperature at 26.6°C, the 42% solution can dry air to 25.7 grains. The red arrow in Figure 12 shows the ambient air driving to equilibrium with LiCl in case of keeping the

free surface of the desiccant at 26.6 C temperature. Increasing the temperature has the highest effects on desiccant losing its drying potential. Liu XH et al. [85], showed that in order to obtain better humidification performance, liquid desiccant should be heated rather than the air, and counter flow configuration is recommended.

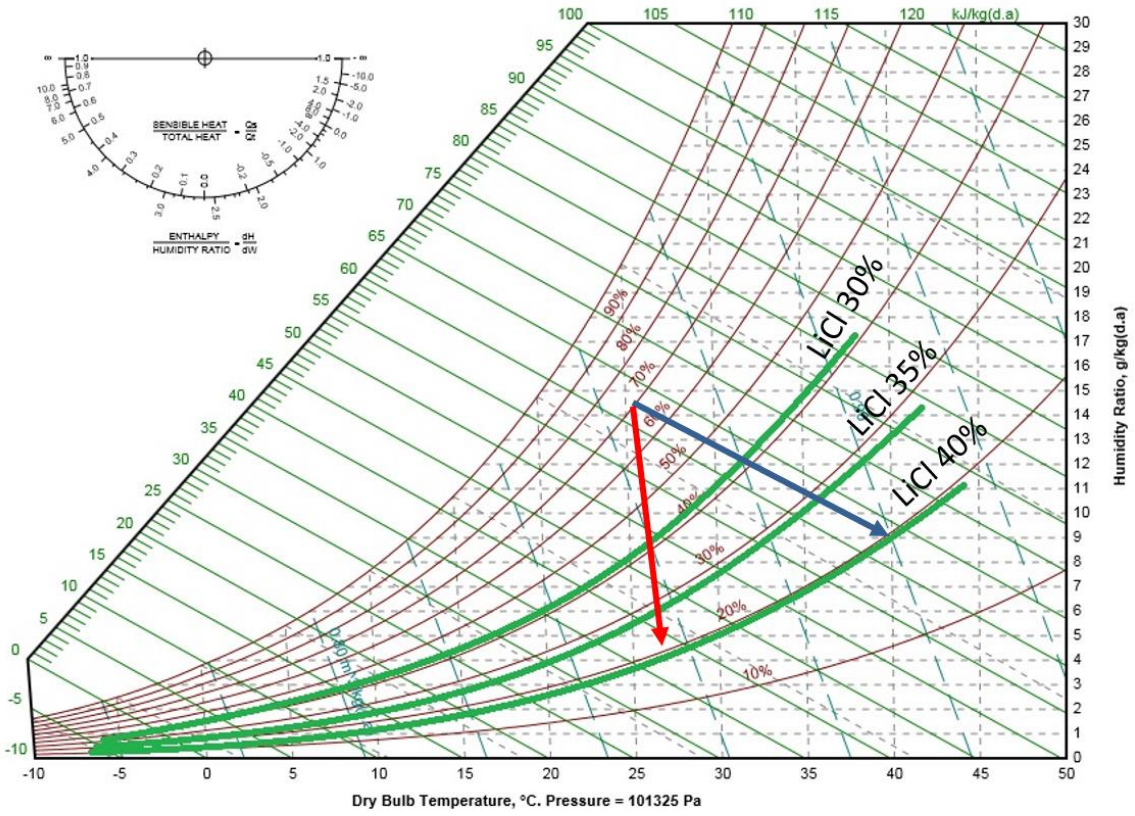

Figure 12. Equilibrium relative humidity for lithium chloride.

Design of a liquid desiccant system depends on the choice of desiccant. Both glycols and solutions halide salts are used in LDAC. LiCl, $CaCl_2$ and LiBr are three of the most widely used halide salt desiccant solutions. Different Studies [86–88] measured thermodynamic properties of these three desiccants, and they found that LiCl solution is the most stable liquid desiccant, which offers the lowest water vapor pressure and dehydration concentration 30-40%. However, the cost of LiCl is relatively high. LiBr solution offers similar characteristics during dehumidification and regeneration process, but the cost of LiBr is about 20% higher than LiCl. Lithium based desiccants can be expensive especially when the storage of concentrated desiccant is important [75]. LiBr and LiCl are strong desiccants that can respectively dry the air to 6% relative humidity and 11% if they are

saturates solution. LiBr is mainly used in closed system that doesn't have direct contact with air due to their higher oxidation potential and LiCl is mainly used in open systems. $CaCl_2$ solution is the cheapest and most widely available desiccant, but it can be unstable, depending on the air inlet conditions and the solution concentration rate. Halide salts are very corrosive to metals, so all the equipment is typically made of fiberglass, plastic, or other nonmetallic materials. For the cases that metal must be used, titanium is commonly specified [83]. As a less corrosive and more environmentally friendly solution, Potassium Formate (KCOOH) solution has recently been applied in desiccant cooling unit. KCOOH solution has low toxicity and viscosity, and they are neither corrosive nor volatile [89]. However, Longo and Gasperella [90] experimentally tested the performances of a liquid desiccant cooling system using LiBr, LiCl and KCOOH solutions. Results show that LiCl and LiBr solutions demonstrated better dehumidification performance compared with KCOOH solution, which performed better in regeneration process.

Glycols are mainly used in industrial equipment. Glycols such as triethylene and propylene have low toxicity and compatible with most metals, but they are volatile. A mixture of 96% triethylene glycol and 4% water the same effect as a 42% lithium chloride solution. However, at equilibrium, the molar concentration of the glycol in air will be in the order of 1% that of the water vapor. The environmental impact and economic penalty of the triethylene glycol volatility in unacceptable in LDACs [75,83].

2.3.2 Liquid desiccant system classification and design

Liquid desiccant systems can be classified as direct-contact or indirect contact, as adiabatic or intercooler, and by flow pattern: parallel flow, cross flow, counter flow and counter-cross flow. Contactors (porous beds of various designs) are typically used to bring the desiccant solution and air stream into contact for both the dehumidification and regeneration processes. In direct-contact dehumidifiers/regenerators, heat and water vapor transfer take place between air and desiccant solution streams through direct contact. Desiccant solution usually flows downward due to gravity. The processed air can either flow in a parallel, counter or a cross flow (the most commonly used) manner across the contactor surface. However, counter flow systems are generally showing better dehumidification ability

compared with other two flow patterns due to the fact that the outlet air stream is located at the entrance of the fresh desiccant solution's inlet [91] .This can be either in a direct or in direct manner. In an adiabatic dehumidifier, the solution temperature increases which gradually decreases the solution dehumidification capability [92]. By introducing internal cooling, the heat can be removed from liquid desiccant, which keeps the solution vapor pressure at lower level and improving the dehumidification process. Experimental and theoretical research [92,93] results indicate that internally cooled dehumidifier offers higher dehumidification effectiveness.

The most commonly used and studied liquid desiccant dehumidifier/regenerator systems amongst the various direct contact types incorporate packed beds [94]. In this design, solution is usually distributed from the top of the packed bed with the help of spray nozzles and flows over the packed bed where it comes in direct contact with the air stream. This design is inexpensive and widely used for commercial and residential because it allows large contacting area between air and desiccant with simple configuration. High heat and mass transfer efficiency but the air flowing through the highly flooded porous beds causes a large pressure drop on process air side and, thus, high parasitic power consumption while flowing through the packing material. It also requires a separate heat exchanger to cool the desiccant before it is delivered to the porous bed, and the air may entrain droplets of desiccant as it flows through the highly flooded porous bed. This last disadvantage is particularly important because of the corrosiveness of the desiccant. Carryover of desiccant droplets can be eliminated by droplet filters, but at the expense of additional pressure drop. In an internally cooled/heated (i.e. isothermal) packed bed, the solution is continuously cooled/heated by a third fluid (e.g. water) as it passes through the packed bed. As a result, the solution experiences no (or small) change in its temperature as it passes through the packed bed, and consequently the potential for mass transfer is improved compared to an adiabatic packed bed [94]. Bansal et al. [95] compared the experimental performances of adiabatic and internally-cooled packed-bed dehumidifiers. It was found that the effectiveness of the internally-cooled packed bed is 28–45% higher than the effectiveness of the adiabatic packed bed, depending on the operating conditions. It was found that the counter flow configuration has the highest effectiveness under air dehumidification and hot desiccant-

driven regeneration conditions, compared to parallel-flow and cross-flow configurations, while, the parallel-flow configuration resulted in the highest effectiveness under hot air-driven regeneration conditions [85,96]. Although the packed-bed design is characterized by several advantages, the transfer of liquid droplets to the air stream (called carryover) is a drawback of the packed-bed design especially when it is operated under high flow rates. Thus, a mist eliminator is usually installed at the air exit to capture any entrained desiccant droplets, which increases the air-side pressure drop, as well as the capital and operating costs of the packed bed LDAC system [75,79,94].

AIL Research patented a low flow LDAC with more than an order of magnitude less flow of desiccant compared to flooded-bed systems in 1994. This design replaces the bed of porous contact media with a plastic heat exchanger that has internal cooling/heating. In high flow LDAC, depending on the whether it's a conditioner or regenerator, the liquid desiccant is either cooled or heated before it is sprayed or dripped onto the packed bed. Low flow LDAC has internal cooling or heating in which heat transfer fluid flows within the plates of the heat exchanger, desiccant flows on the outer surface of the plates, and air flows between the plates which are spaced 0.25in. This system does not rely on thermal mass of liquid desiccant to control its temperature [83]. Figure 13 shows the main three components of internal cooling systems: the conditioner, the regenerator, and the Interchange Heat Exchanger (IHX). The conditioner and regenerator both are liquid to air heat exchanger. A very thin film of desiccant flow in wicks on the outer surfaces of the plates, and air flows in the gaps between the plates. For conditioner a coolant typically water from cooling tower (55°–85°F) flows within the plates, however, for regenerator, hot water (160°–212°F) which can be supplied by boiler or solar thermal collectors, recovered heat from an engine or fuel cell, or other energy source flows within the plates. An interchange heat exchanger is used to increases the efficiency of the regenerator and decreases the cooling load on the conditioner. The warm, humid air leaving the regenerator can also be used in an air to air heat exchanger to preheat the air that enters the regenerator.

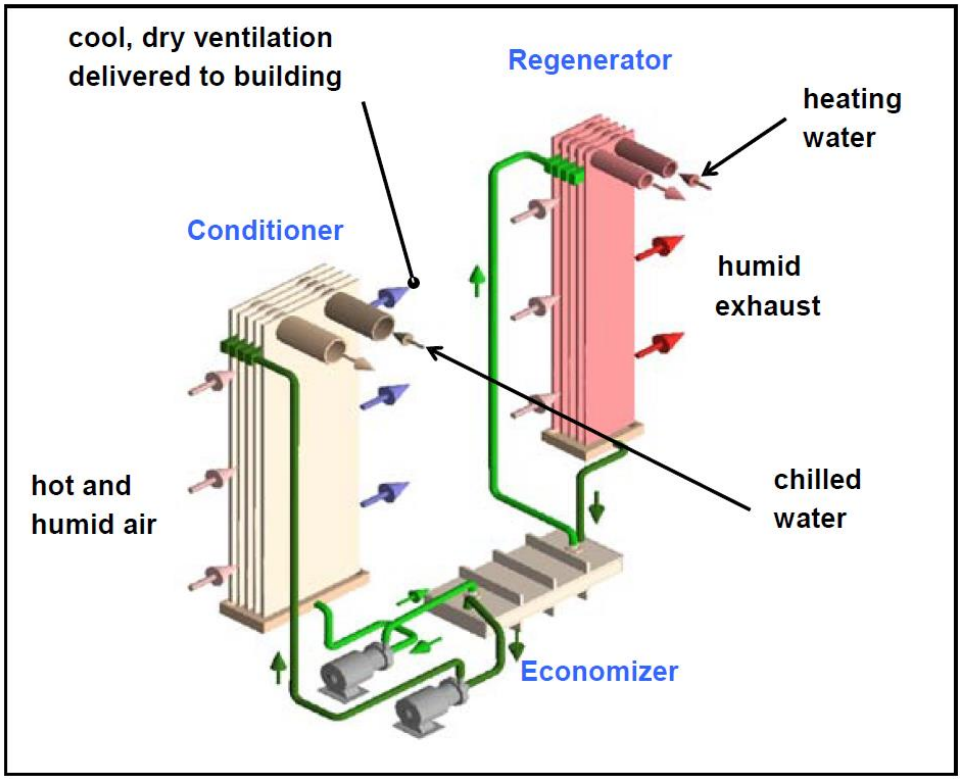

Figure 13. Major components and packaging of the AILR LDAC [83].

Three basic ways to regenerate the desiccant system is with a thermal source: solar, water heater, and a double effect. The water heater or boiler can be fueled by many sources, including natural gas, Combined Heat and Power (CHP), or even biofuels. Hot water can also be produced by recovered heat from an engine or fuel cell, or other energy source flows within the plates. Thermally driven single stage regenerators are typically supplied by hot water above 70°C, but preferably 82°C. The higher fluid temperatures increase the water removal capacity of regenerator significantly [75,83].

2.3.3 Integrated liquid desiccant air conditioning

Integration of LDAC with a dewpoint indirect evaporative cooler can efficiently deliver both latent and sensible cooling with minimal electric demands. This integration has been developed and patented by NREL (Alliance for Sustainable Energy LLC 2008) and been named Desiccant enhanced Evaporative air-conditioning (DEVap) [83]. As shown in Figure 14 in DEVap concept a portion of warm indoor air is mixed with ventilation air. This mixed

air goes through the heat exchanger and comes into contact with the liquid desiccant through a permeable channel. The desiccant absorbs the water vapor in the air. Then, air is cooled and supplied to the building space. A portion of supplied air which has its dew point reduced is recirculated as the secondary air stream. This secondary air comes into contact with the water layer through a permeable membrane. Water evaporates into the air through the membrane. The two air steams are separated through the plastic sheets thermal energy including the heat of absorption flows.

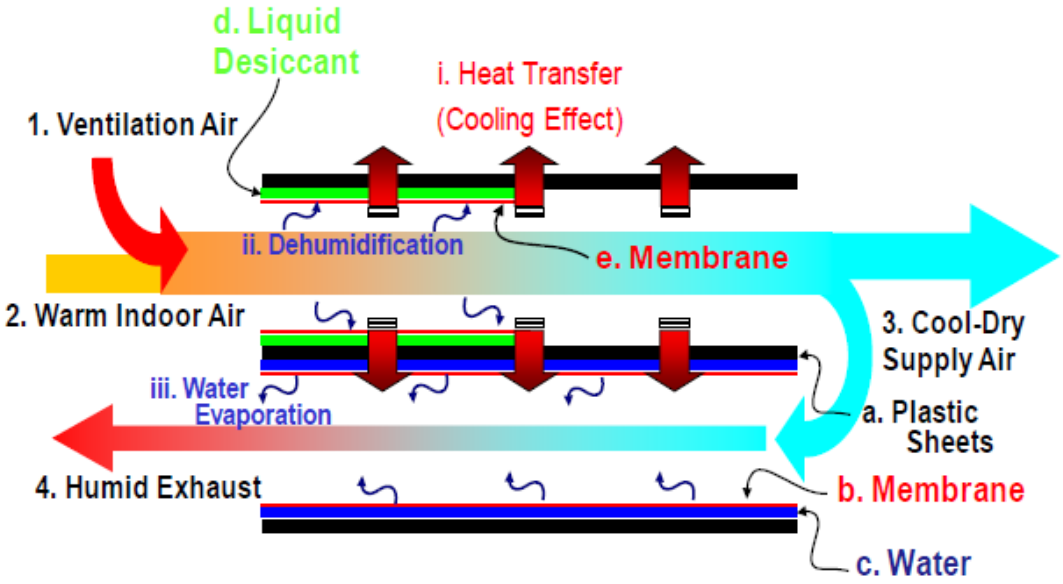

Figure 14. Physical DEVap Concept description[83].

The use of membrane technology prevents the desiccant carry over into the supply air stream and it provides a large contact surface area for the heat and mass transfer between the liquid and air. As a result, membrane-based contactors can effectively improve the performance of a liquid desiccant-based air conditioning processes. The introduction of a membrane provides additional resistance to heat and mass transfer, therefore much work is focused on improving this with novel supported liquid membranes [75]. The waterside membrane is not necessary and omitting it can reduce the cost. However, the semipermeable membrane is necessary for desiccant side to prevent desiccant leak to the air. The breakthrough pressure should be 20psi or lower to avoid desiccant leakage. The membrane

should be 25μm and have pore size of 0.1μm. Its open area should exceed 70% to promote vapor transport. Polypropylene membrane from Celgard is one possible candidate for DEVap application [83]. The deep cooling of the indirect evaporative cooler section requires a dry cooling sink; thus, some dry supply air is siphoned off (5%–30% under maximum cooling load) to provide this exhaust air stream. This section is placed in a counter flow arrangement to maximize the use of this air stream. This is essential because it has been dried with desiccant, and thus has a higher embodied energy than unconditioned air. The result is that the temperature of supply air is limited by its dew point and will come out between 55°–75°F depending on how much is siphoned off. Combined with the desiccant's variable drying ability, the DEVap Air Conditioning (A/C) system controls sensible and latent cooling independently. DEVap does not require a cooling tower, which reduces its maintenance requirements. Dehumidification can be controlled by the desiccant concentration that is supplied to the device. The outlet humidity level can be controlled by controlling the supplied desiccant concentration or decreasing the flow of highly concentrated desiccant. The latter allows the highly concentrated desiccant to quickly be diluted and thus act as a weaker desiccant solution in the device. From inspection, the peak electricity draw of the DEVap A/C is considerably less than the standard A/C. This is primarily because compressor power is eliminated and replaced with only fan power to push air through the DEVap cooling core [83].

NREL have designed a 1-ton DEVap system for a typical Gulf Coast condition with no water side membrane and LiCl as the desiccant as shown in Figure 15. Figure 16 shows the airstream process of DEVap on psychrometric chart. The design criteria were to supply cooling to the building at 7Btu/lb (380cfm/ton) and a Sensible Heat Ratio (SHR) of 0.6 while maintaining 55% indoor RH. NREL models shows that in all residential cases, the DEVap A/C provided more than necessary humidity control. Allowing indoor humidity to rise above 50% RH would have significant energy improvement. In the summertime, when sensible loads are high (high SHR), the DEVap A/C continuously maintained the space at less than 50% RH. This level of humidity control can be reduced to create higher energy savings. In general, DEVap perform better in new construction building with added ventilation and tighter envelope because sensible heat ratio decreases. Their analysis shows regional water

use (site + off-site) for the DEVap system is 2.0–3.0gal/ton.hr, is similar to the regional impact that DX A/C imposes (off-site only). The DEVap A/C does increase site water use, but in general, the regional impact is small. Implementation of the DEVap A/C in commercial cases shows a higher energy savings level than the residential cases, primarily because of the higher cooling loads of commercial buildings and their increased ventilation requirements. DEVap regional water use is expected to be 2.0–3.0gal/ton.hr for commercial buildings. Similar to the residential case, the DEVap A/C has minimal impact on regional water use compared to DX A/C [83,97].

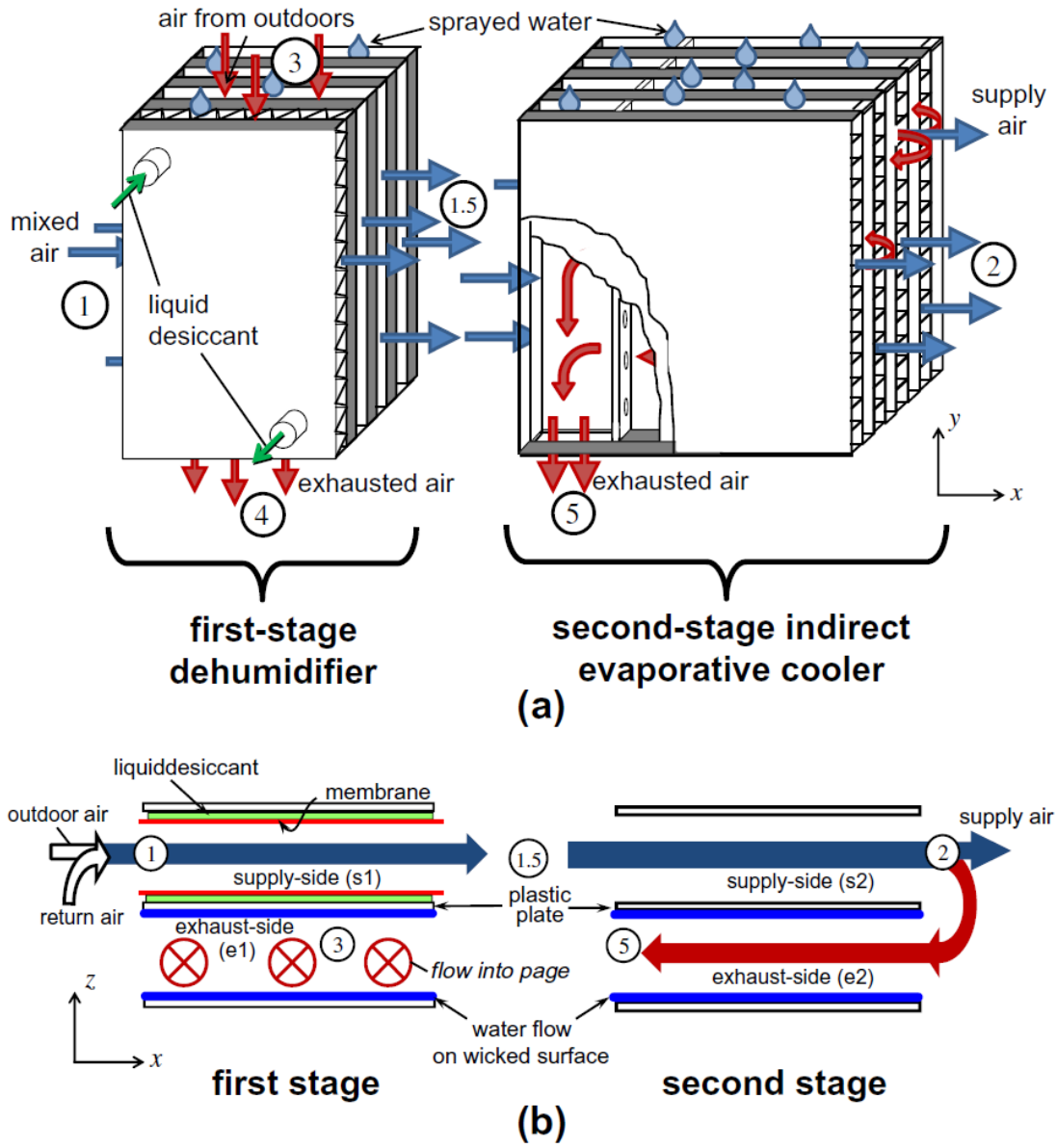

Figure 15. DEVap air conditioner schematic. (a) four stack channel pairs (b) top view, one channel pair[83].

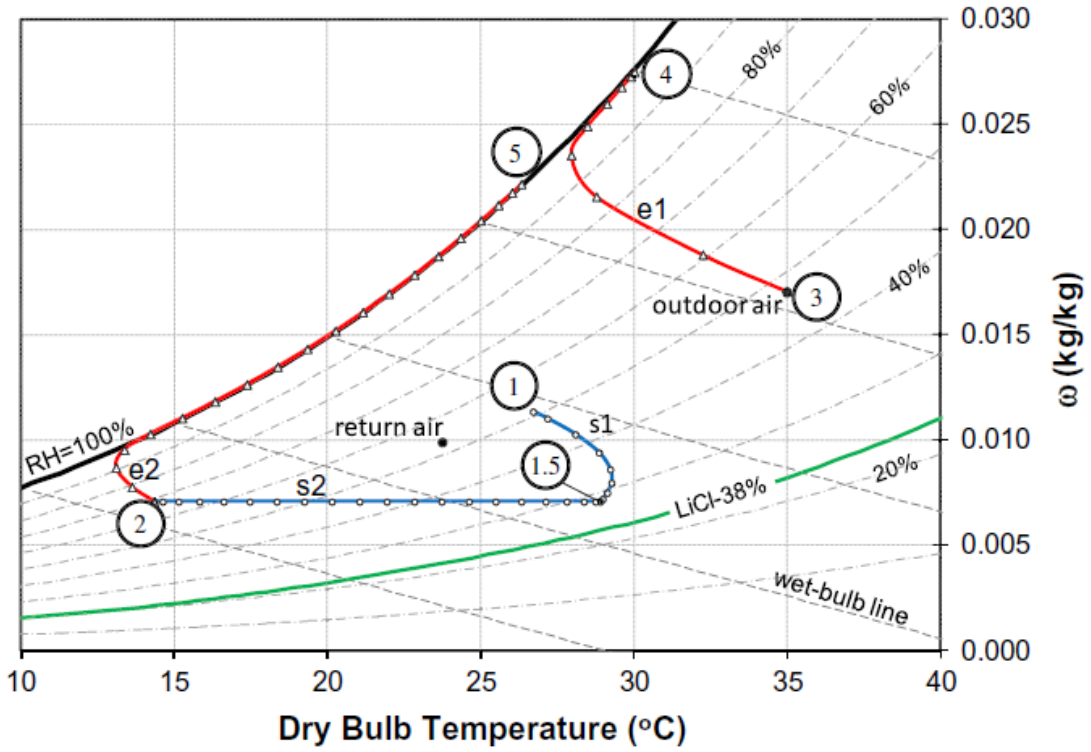

Figure 16. DEVap airstreams on a psychrometric chart [97].

The integration of LDCS with VCS can provide subcooling effect from the condenser outlet to the compressor inlet which leads to improved system performance. She et al. [98] proposed a new energy-efficient refrigeration system subcooled by liquid desiccant dehumidification and evaporation. In the proposed system, liquid desiccant system produces very dry air for an indirect evaporative cooler, which sub-cools the vapor compression refrigeration system to get higher COP than conventional refrigeration system. The desiccant cooling system uses the condensation heat for the desiccant regeneration. The results show great improvement of COP for the proposed system, with maximum COPs about 18.8% higher than that of conventional VCS. Khalil [99] experimentally investigate a multipurpose desiccant integrated with vapor-compression air conditioning. The system is designed to meet the cooling load of spaces with large latent heat and at the same time to extract water from atmospheric air. Te integrated system total cooling capacity is up to 6.2kW. The effect of regeneration temperature, condenser and evaporator temperature on the system COP and specific moisture recovery were analyzed under different liquid desiccant flow rates. The authors concluded that the COP of the proposed system was as high as 3.8 (68% higher than

that of conventional VCS), with further 53% more annual energy saving. Based on the similar testing, Bassuoni [100] has applied $CaCl_2$ as the desiccant for the experimental testing. The results showed that about 54% COP improvement was achieved. Many studies have proposed hybrid LDAC- VCS where the liquid desiccant has been used to dehumidify the supply air [101–103]. Mansuriya et al. [103] analyzed a modified liquid desiccant dehumidification incorporated vapor compression refrigeration system based on thermo-economic approach. The system is optimized based on the co-efficient of performance and the total annual cost of the system. The results show that 51.3% of the total cooling load can be handled by the desiccant dehumidifier alone. This significant sharing of heat duty by addition of liquid desiccant dehumidification to conventional vapor compression refrigeration system justifies this hybridization for humid and hotter climates. COP of optimized system shows 68.4% improve compared to coefficient of performance of stand-alone vapor compression refrigeration system for handling the same cooling load. Dai et al. [104] studies the integration of desiccant dehumidification, evaporative cooling and vapor compression air conditioning. In this system, latent cooling of the air is carried out in the dehumidifier, and air sensible cooling via the VCS cooling coil. Experimental investigation demonstrates significant increase (56%) in cooling production and COP of the new hybrid system compared with vapor compression system alone. Capozzoli et al. [105] has economically analyzed a case based on the climatic conditions of three cities in Italy. Their results show considerable reduction of electric energy demand as well as better control of thermal-hygrometric conditions were noted. A simple payback of about 1 year has been obtained. Researchers have also studied integration of solar driven hybrid liquid desiccant and VCS. Li et al. [106] analyzed this system for Hong Kong climate condition using EnergyPlus. The results showed that an annual operation energy saving of 6760kWh compared to conventional VCS and a payback period of 7 years for a 19kW cooling capacity design system. Su et al. [107] looks at driving vapor compression chiller by generated electricity from solar for cooling the desiccant solution for a two-stage dehumidification, and the released heat from the collector is used for the desiccant regeneration. Simulation results show the proposed system has a superior power saving ability of 55.65% comparing with the conventional one, besides the equivalent power generation efficiency reaches 8.7% in the base design condition. A comparative driven force analysis showed the two-stage

dehumidification has a better match of driven force compared with the single-stage liquid desiccant dehumidification, thus leading to a reduced irreversible loss of 65.43%. Sensitivity analysis indicated that the dehumidification temperature has a decisive effect on the system performance.

In heap pump driven systems, the cooling capacity from the evaporator is used to cool the liquid desiccant and exhaust heat from the condenser is used to regenerate the liquid desiccant. In this process, there are two air streams, one outdoor fresh air (a1) that will be cooled and dehumidifier, and the second one (a3), a stream air used to regenerate the liquid desiccant (a3). In this configuration there are three liquid desiccant circulation flow as shown in Figure 17: one in dehumidifier (S5-S6), one in regenerator (S7, S8), and one circulating between the heat exchanger (S1-S2, S3-S4). The flow rate in the latter one is one order of magnitude less than the other two flows [75].

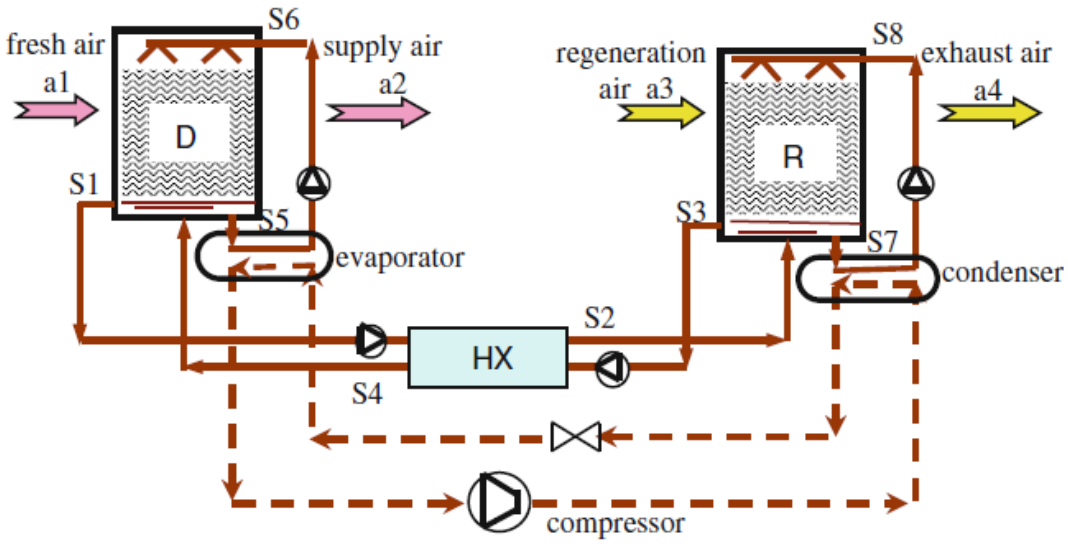

Figure 17. Heat pump driven liquid desiccant air handling devices [75].

Many studies have been conducted on combined heat pump desiccant dehumidifiers for different case studies, different configurations, and different desiccant solutions. All these studies have theoretically and experimentally shown improvement in COP and energy savings [108–118]. Sanaye et al. [117] modeled and optimized a hybrid liquid desiccant-heat pump system containing dehumidification and cooling section. The system was analyzed in four energy, exergy, economic and environmental aspects. Then, the system was optimized

for total annual cost and exergy efficiency. Results for our case study showed that the proposed optimized system decreased the electricity consumption for 33.2% in comparison with that for an electrical HP system during seven months of operation in a year (18.9% due to using desiccant dehumidifying system and 81.1% due to using a heat exchanger instead of an electrical heater). This amount of lower electricity consumption also provided 1.85e5kgCO_2/year lower CO_2 production (33.2%) in comparison with that for a conventional HP system. The COP of the system at the optimum point was also about 4.83 (in comparison with 2.74 for the conventional case in which heat pump and electrical heater were used). Jradi and Riffat [119] experimentally investigated a micro-scale tri-generation consisting of an organic Rankine-cycle, dehumidification and cooling unit. A scroll expander was used in the Rankine unit for heat and power generation. Cooling unit was a dew point evaporative cooler to provide the cooling capacity through air cooling. An experimental setup was built and the micro-scale tri-generation system was tested under different operational conditions using a wood pellet biomass boiler as a heating source. It is shown that the proposed system is capable of providing about 9.6kW heating power, 6.5kW cooling power and 500W electric power. The overall efficiency of the tri-generation system is about 85%. The dehumidification-cooling system has a thermal COP of 0.86 and electrical COP of 7.7.

Solar has been used as the heating source for solution regeneration. The solution temperature is usually below 80°C which fit well with solar provided temperature and solar radiation availability matches with cooling demand [120]. During recent years many researches have been investigating integration of LDAC with solar theoretically and experimentally. Katejanekam and Kumar [121] simulated a solar regenerated liquid desiccant ventilation pre-conditioning system for Thailand climate. In their proposed system, the solar energy is used for regeneration process and cooling water from a cooling tower for precooling. The effects of various parameters on the moisture removal rate and evaporation rate were analyzed theoretically. The results suggest that the solar radiation, ventilation rate, and desiccant solution concentration have the most influence on the system. They also suggested that balance between the water removed at the dehumidifier and that evaporated at the regenerator needs to be considered to maintain uniform performance during continuous operation. Similarly, Mohaisen and Ma [122] developed and simulated a

solar assisted liquid dehumidification air conditioning system using LiCl solution on Matlab Simulink platform. Their result has been validated with experimental results by Fumo and Goswami [123]. The simulation results based on three consecutive sunny summer days in Sydney show daily COP of 0.5-0.55 by the proposed system and 73.4% of thermal energy required for thermal regeneration was provided by the solar collectors. Croffot and Harrisson [124] experimentally evaluated the performance of a solar driven system installed in Canada. The system includes a low-flow parallel plate liquid desiccant air conditioner, and a 95m^2 evacuated tube solar collector array. Results from five test days have shown an overall solar collector efficiency of 56%, solar fraction of 63% and a thermal COP of 0.47. The average total cooling was 12.3kW and average latent cooling was 13.2kW. Peng et al. [125] studied a solar air pre-treatment collector/regenerator. Their simulation results showed that the storage capacity of proposed system could be improved by 50%, when the regeneration temperature was 60°C, and the inlet air specific humidity was 2.33kg/kg. In another study, Lychnos and Davies [113] performed experimental and theoretical simulation for a solar powered liquid desiccant system using $MgCl_2$. The theoretical model was developed and verified with the experimental results. Compared with conventional evaporative cooler, the proposed system could further lower the average daily maximum temperature by 5.5-7.5^oC. Alizadeh [126] fields tested implementing polymer plate heat exchanger into LDAC in Australia summer weather condition. Lithium chloride with 43% was used in the experiments and a scavenger air regenerator concentrates the dilute solution from the dehumidifier using hot water from flat plate solar. Alizadeh [126] experimentally analyzed the effects of various air flow rate and desiccant flow rate on the system performance. The experimentally obtained data was compared with a developed model. The comparison showed a good agreement between the experiments and model predictions. The results showed that the proposed system could provide cooling capacity up to 20kW with dehumidification efficiency up to 72%.

Qi et al. [127] simulated yearly system performance of solar assisted LDAC for commercial application in five cities (Singapore, Beijing, Huston, LA and Boulder). In this study, the effects of various solar collector areas and monthly solar radiations, ambient air conditions on the electricity consumption saving and monthly average COP were theoretically analyzed.

Results shows that for buildings located in humid areas with low sensible-total heat ratio, the electricity energy reduction of the system was high and about 450MWh in Houston and Singapore and payback was approximately 7 years. For building in dry climate, although the total cooling load was low, up to 45% of electricity of AC can be saved because of significant improve in chiller COP during more than 70% of operation time and the payback was around 22 years. However, for the buildings with mild outdoor humidity, such as those in Beijing and Los Angeles the electricity energy saved only around 100MWh and the cost payback period was more than 30 years, and the application of LDAC was not that suitable. Li and Zhang [128,129] investigated a solar energy driven hollow fiber membrane-based desalination system. The system consists of a membrane-based humidifier, a fin-and-tube type dehumidifier and a solar heating unit, which consists of a U-tube evacuated solar collector and a heat storage tank. The hollow fiber membrane-based humidifier is similar to a shell-and-tube heat mass exchanger. Through numerical modelling and experimental tests, they found that the COP of the system can reach about 0.75 and electric COP of 36.13 is achievable, which means electrical energy consumption is much less due to solar energy reclamation. Results show that solar accounts for 92.0% of the electric energy consumption by the entire system. Sensible heat losses account for most of the energy losses from the system. Chen et al. [130] proposes solar assisted liquid desiccant dehumidifier and regenerative indirect evaporative cooling (LDD- Regenerative Indirect Evaporative Cooling (RIEC)) system for fresh air treatment. The hot and humid fresh air is firstly dehumidified by LDD and then sensibly cooled by RIEC. The thermal energy captured by solar collectors is used for desiccant solution regeneration. In this study, they have looked into the influences of solar collector area and inlet air conditions and optimizing the extraction air ratio of RIEC. The energy saving ratio is quantitatively evaluated with respect to a conventional A/C system. Results shows that the energy saving ratio ranges from 22.4% to 53.2% under various inlet air conditions.

This characteristic of liquid desiccant dehumidification system that the dilute liquid desiccant can be regenerated by low grade heat makes it attractive option for integrating with thermal sources. Many studies have been done on integration of liquid desiccant system

with solar, vapor compression, heat pump, and CHPs. But only two research has been done integrating liquid desiccant with SOFCs.

2.3.3.1 Liquid desiccant integrated with SOFC system

The typical SOFC system exhaust temperature matches very well with the required temperature for liquid dehumidification [131]. Elmer [76] has looked into design, development and proof of concept combined generation of power, cooling and heating based on SOFC and Liquid desiccant air conditioning technology for building application. A 1.5kW SOFC integrated with liquid desiccant has been proposed for providing heating, cooling and electricity to low carbon buildings. Elmer et al. [132] used empirical SOFC and liquid desiccant component data for an energetic, economic and environmental analysis. They have used a simple 0D model in Engineering Equation Solver (EES) platform for regeneration, dehumidifier and fuel cell. The model is based on dimensionless vapor pressure and temperature difference ratio designed for packed bed liquid desiccant. The results show (1) the moisture removal of the supply rate is mainly controlled by desiccant temperature and cooling water temperature in constant flow rates. (2) The air inlet condition has a large effect on cooling output performance and the unit performs better in a hot and humid climate. (3) By increasing the regeneration heat source temperature more water vapor vaporizes from the weak solution. The model they used have limitation such as not including the effectiveness of heat and mass exchanger effectiveness, geometry of the contactor, and desiccant carry over [76]. For desiccant air conditioning system Elmer [61] developed an Integrated Desiccant air Conditioning System (IDCS). This system combines regenerator, dehumidifier and evaporative inter-cooler into a single membrane-based heat and mass exchanger to reduce the size, complexity and leakage. The IDCS operates with a KCOOH desiccant working fluid. The liquid desiccant is sprays through nozzle from the top where regenerator is located and flows downward due to gravity. In this design instead of preheating desiccant before regeneration and precooling it before dehumidification, thermal energy is supplied to the regenerator through airstream and an evaporative inter-cooler is designed. This is because all desiccant flow is contained within one complete Heat and Mass Exchanger (HMX) the solution cannot be extracted for prior heating and cooling. This feature is weakness of this design as precooling and preheating of liquid desiccant increases the

performance of the system [83] Their design was supposed to significantly reduces the number of heat exchangers, pipes, and ducting in liquid desiccant air conditioning systems. The main issue with this integrated system was imbalance between moisture removal rate in the dehumidifier and moisture addition rate in the regenerator. This mass imbalance is primarily due to the available surface area for heat and mass exchange in the regenerator being too small and an insufficient vapor pressure differential between the air and desiccant solution. In order to regenerate the desiccant solution back to its original condition following the dehumidification process, the regenerator needs to operate for extended time periods. Across the variables investigated there is a greater instantaneous moisture removal rate in the dehumidifier than moisture addition rate in the regenerator. Desiccant solution leakage/carry-over on the dehumidifier side of the HMX has been noticed during the experiment as well [89]. In response to the highlighted shortcomings of the novel IDCS Theo Elmer developed a Separated liquid Desiccant air Conditioning System (SDCS) for tri-generation system integration. SDCS consist of three separate cores including dehumidifier, regenerator, and an evaporative cooler. The SDCS uses a semi-permeable, microporous-membrane-based crossflow contactor, operating with KCOOH desiccant solution. The solution channel consists of polyethylene sheet, with fiber membrane attached on either side to allow diffusion of water but prevent the liquid desiccant entering the air side. In evaporative cooler, air and water come into contact in a crossflow HMX. Before liquid desiccant entering the dehumidifier, a plate heat exchanger is used to precool the desiccant to increase its potential. After dehumidifying the air, the weak solution enters the dehumidifier tank. The regenerator has a tank and pump which delivers weak desiccant to the top of regenerator. Desiccant is preheated before entering the dehumidifier. The strong desiccant flows to regenerator tank after regeneration. In this design, because the entire SDCS is placed within the environmental, the water for the evaporative cooler and desiccant for dehumidifier are at the ambient temperature which has an impact on moisture absorption capacity of the desiccant and the sensible cooling. This design causes little to no sensible cooling achievable. Also, the evaporative cooler only provides around 80–150W of cooling over their study range. As a result, the evaporative cooling provided is not enough to produce a sufficient solution temperature decrease and to provide sensible cooling to the supply air in the dehumidifier. Elmer et al. experimental results on SDCS show (1) effective

instantaneous balancing of the dehumidifier and regenerator across a range of environmental and operational values, (2) operation of the dehumidifier is dictated, to some degree by the available SOFC thermal exhaust, (3) COP values in the range of 0.4–0.66 are achievable with a low-grade thermal input (45–60°C) typical of an SOFC CHP system and (4) potential for non-synchronous operation in a tri-generation system context, bringing about improvements to peak cooling output and total system efficiency [133]. Elmer et al. used empirical SOFC and liquid desiccant component data for an energetic, economic and environmental analysis. The 1.5kW BlueGen SOFC systems is electrically connected to the grid to import or export as required. The waste heat recovery circuit is connected to a home's 300L hot water cylinder which also includes an auxiliary gas boiler. Experimental results shows that the electrical efficiency of SOFC system increases from 14% at 200W to maximum of 60% at 1500W and then decreases to 56% as 2000W capacity. Thermal output from fuel cells varies linearly from 320W_{th} at 200W_e to 540W_{th} at 1500W. The calculated water heat recovery temperature for 2l/min flow based varies between 47 C at 100W_e to 52°C at 2000W_e [134].

Be Power Tech, Inc. [80] developed BeCool, a natural gas-powered air-conditioning system that produced electricity as by product on the site. The innovative idea shifts some grid-powered electricity for cooling demand to natural gas which would substantially reduce peak summer power demand and help to reduce the need for costly peaking power plants. Their studies showed that their 5ton BeCool unit eliminates ~ 10kW of peak electricity demand, generates 43MWh/yr electricity and saves ~ 10MWh/yr compared to conventional air conditioning. They build a prototype and the test results showed that the electrical power efficiency was 45% to 60%. The primary potential energy saving is 4.1 Quads, and the technology has the potential to reduce 222 million metric tons of CO_2. Their analysis for California climate 7 and 14 shows 53% CO_2 reduction in a 50% electrical efficiency for fuel cell and 90% combined heat and power efficient fuel cell system is used.

BeCool uses exhaust heat from the fuel cell and heat from the burner to increase the concentration of LiCl to 42% mass fraction in the regeneration process. Be Power Tech designed and built an experimental prototype BeCool system integrating a 2.5kW SOFC system (EnGen system), a boost natural gas burner, and a custom-made liquid desiccant air

conditioner designed to produce from 2.5-tons (8.8kW thermal) to 4-tons (14.0kW thermal) of cooling. The system was tested under multiple outdoor air conditions. Their study showed that, in all cases the heat supplied by the fuel cell was not sufficient to provide the heat required for the air conditioning process, since these isolated tests could not rely on storage from daily continuous regeneration. For this reason, the supplemental natural gas burner was used to supply the heat required [80].

Integrated fuel cell dehumidification systems have never previously been studied for data center application. The only two studies that have looked at integration of SOFC with dehumidification systems were focused on building applications of the technology. The models that have been used in previous studies are simple steady state models for the fuel cell and liquid desiccant systems. In this study, I investigate the integration of rack and row level fuel cell powered servers with Liquid Desiccant Dehumidifier (LDD) technology that can be dynamically dispatched to produce electricity and cooling in various amounts to meet power and air conditioning demands of data centers. In addition, the storage capacity to meet the demand of data center for the entire year is evaluated. The objectives of this phase of the study focus on theoretically evaluating the integrated system concept and to assess the achievable air conditioning from SOFC waste heat. To explore the feasibility of thermally integrating SOFC with LDD, a spatially resolved physical model developed in MATLAB is used to simulate the operating characteristics of this SOFC system. A corresponding physical model is developed to simulate the liquid desiccant air conditioner for dehumidification. This study considers SOFC systems capable of powering single server rack (~12kW) and row of servers (~240kW) and the operation of an LDD for cooling and dehumidification of that same configuration. The small-scale LDD operation is based on distributed waste heat from each individual SOFC at the rack level. The analysis will indicate whether waste-heat based cooling and dehumidification can power the servers and maintaining server operating temperatures and humidity in the safe range for different weather conditions.

3 SOFC System Modeling

3.1 SOFC stack model

A spatially and temporally resolved fuel cell stack model has been developed based on the developed model in NFCRC using the MATLAB software [135]. The model is developed for one unit cell that describes the response of the entire stack. 51 unitary anode-supported (fuel electrode-supported) planar rectangular cells are assembled into one-unit SOFC stack. Figure 18 presents one crossflow cell geometry with its components as well as a depiction of two repeated cells in series. The planar rectangular cells are flexible, compact, easy to produce, and have lower manufacturing cost compared to tubular cells. The unit cell consists of five layers i.e., cathode flow, anode flow, Positive electrode, Electrolyte, Negative electrode (PEN), fuel bipolar plate and air bipolar plate.

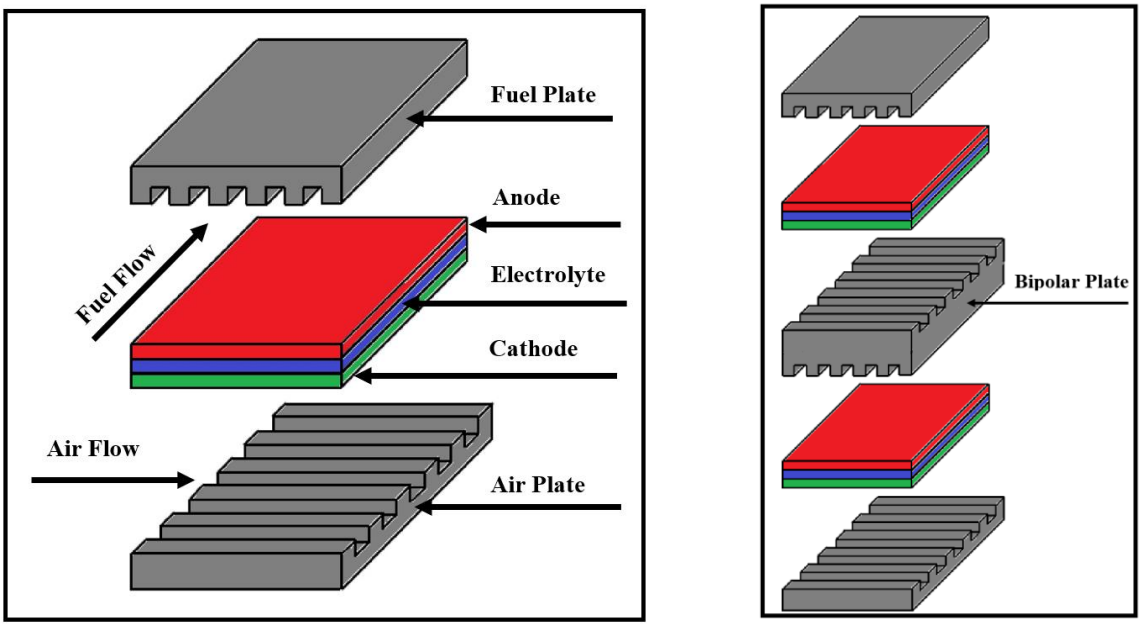

Figure 18. Planar fuel cell model.

The spatially and temporally resolved model uses different states to calculate parameters at different nodes of a cell. These nodal states are calculated at each time step among set of points in the time vector using the MATLAB Ordinary Differential Equation (ODE) solver. These nodal states are composed of nodal temperatures of fuel and air separator plates

(bipolar plates), temperature of fuel and air flows, nodal temperature of the PEN, nodal concentration of different species in both cathode and anode flow sides (methane, hydrogen, carbon monoxide, carbon dioxide, and steam species for anode side as well as oxygen and nitrogen species at cathode side), nodal current and cathode/anode flow inlet pressure. The evaluated parameters based on the mentioned states are nodal Nernst voltage, nodal voltage losses, nodal operating voltage (should be obtained constant across the cell in order to satisfy the equipotential surface condition), nodal molar flow rate of ions crossing the PEN, nodal heat generation in the PEN, nodal heat and mass transfers and many other parameters. A two-dimensional multi-layer approach is accomplished for both the electrochemical modeling and heat transfer modeling resulting in a quasi-3-D representation of an electrochemical cell. As an assumption, instantaneous electrochemical reactions are assumed, due to relatively fast electrochemical reactions compared to cell and stack thermal response dynamics. Using Faraday's law, the rate of electrochemical reactions is directly proportional to the cell current. Furthermore, it is considered that electrical current flows only in one direction from one electrode to the other one along the PEN, as the electrical potential is assumed constant on the electrode surfaces. In the developed model, gases behave as ideal gas due to high operating temperature of the SOFC.

In this study a 5×5 spatial resolution (number of rows and columns) is accomplished for all 5 layers (fuel plate, fuel flow, PEN, air flow, air plate). The solid oxide fuel cell has an active surface area of 139.24cm^2 (11.8cm × 11.8cm). Fuel cell module material properties are presented in Table 2 and geometry parameters are presented in Table 3. Figure 19 depicts schematically the geometric parameters of the fuel cell.

Table 2. Fuel cell material properties.

Material Properties[135]	
Anode (Fuel) Electrode Material	Ni/YSZ Cermet
Cathode (Air) Electrode Material	LSCF
Electrolyte Material	YSZ Composite
Conductivity of Electrolyte (W/m. K)	6.19
Density of Electrolyte (kg/m^3)	375
Specific Heat of Electrolyte (J/kg. K)	800
Conductivity of Bipolar Plate (W/m. K)	5
Density of Bipolar Plate (kg/m^3)	2000
Specific Heat of Bipolar Plate (J/kg. K)	600

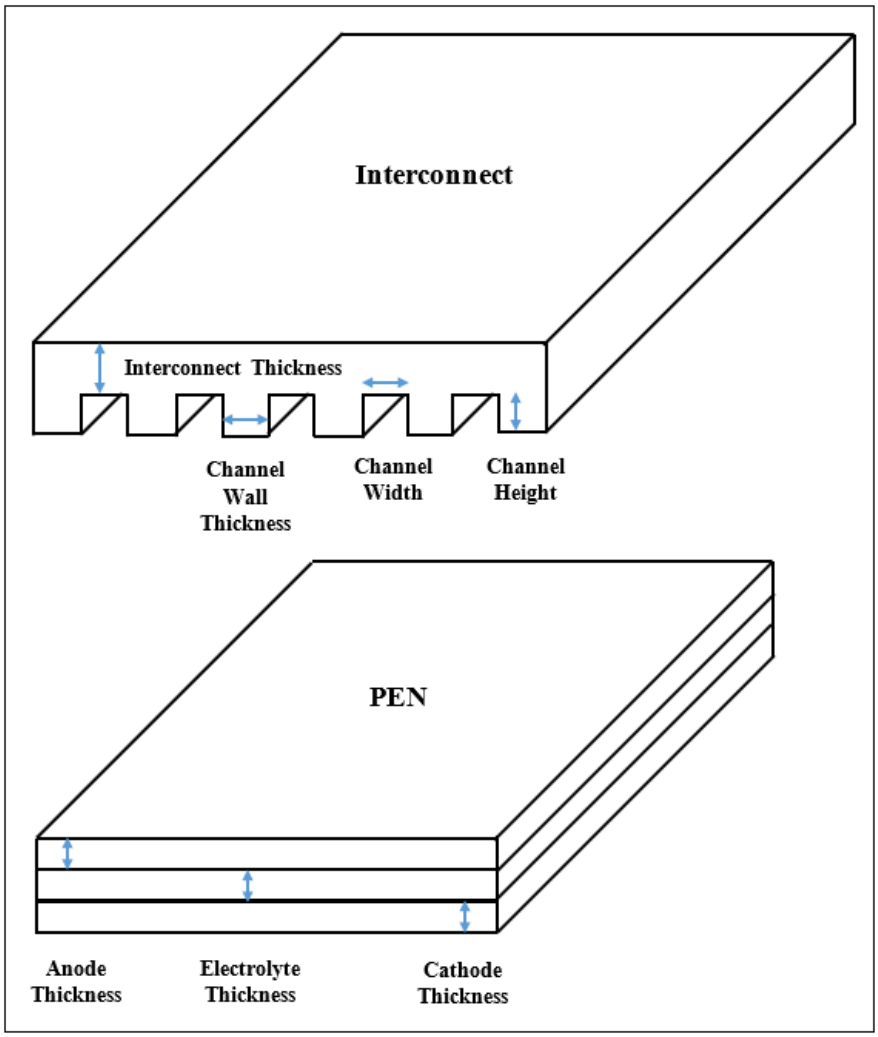

Figure 19. Geometric parameters of a fuel cell.

Table 3. Fuel cell geometrical parameters.

Geometrical Parameters	
Anode Thickness (m)	$800e^{-6}$
Cathode Thickness (m)	$50e^{-6}$
Electrolyte Thickness (m)	$18e^{-6}$
Bipolar Plate Thickness (m)	$6e^{-3}$
Plate Thickness (m)	$3e^{-3}$
Cell Length (m)	$11.8e^{-2}$
Cell Width (m)	$11.8e^{-2}$
Channel Height (Fuel Side) (m)	$2e^{-3}$
Channel Height (Air Side) (m)	$2e^{-3}$
Channel Width (Fuel Side) (m)	$5e^{-3}$
Channel Width (Air Side) (m)	$5e^{-3}$
Channel Wall Thickness (Fuel Side) (m)	$5e^{-3}$
Channel Wall Thickness (Air Side) (m)	$5e^{-3}$

3.1.1 Governing Equations

3.1.1.1 Energy balance

The developed model takes into account the conservation of energy within each node and energy transfer between control volumes to calculate the nodal temperature changes during dynamic operating conditions for all 5 layers which are fuel plate, air plate, cathode flow, anode flow and the PEN. Nodal energy balance equation for the cathode/anode stream includes convective heat transferred to the solid walls (PEN and bipolar plate), enthalpy flux due to the electrochemical reaction, mass transfer of oxygen ions from/to the PEN, and inlet/outlet enthalpy flux of the bulk flow from/to adjacent nodes. It is assumed that temperature in each control volume decreases/increases linearly along the control volume of each node (for anode/cathode streams). A nodal energy balance for the PEN includes convective heat transferred to the PEN from streams, conductive heat transferred to the PEN

from bipolar plate, conductive heat transferred to adjacent nodes in PEN and heat generation due to the electrochemical reactions and electrical resistances. Radiation heat transfer between PEN and bipolar plate is negligible. A nodal energy balance equation for the bipolar plate includes convective heat transferred to bipolar plate from streams, conductive heat transferred to bipolar plate from PEN and conductive heat transferred to adjacent nodes in bipolar plate. Adiabatic boundary condition is considered for all the nodes located at the beginning and at the end of the cell on PEN and bipolar plate, as the cell height is relatively thin compared to its length. Also, it is considered that the stack is well insulated such that heat loss to the environment is negligible. The nodal energy balance equation for cathode and anode flows, PEN and bipolar plate are presented below. Note that all nodal specific heat capacities are calculated at the node temperature. Also, for each cathode/anode node, inlet flow enthalpy is the outlet flow enthalpy of the previous node in the flow direction as follows [135].

$$(\rho_{B.P.} \times V_{B.P.} \times C_{B.P.})|_{Node} \times \frac{\partial T_{B.P.}}{\partial t}\Big|_{node} = \sum \dot{Q}_{conv_{B.P.,A,C}}\Big|_{node} + \sum \dot{Q}_{cond_{B.P.,PEN}}\Big|_{node} + \sum \dot{Q}_{cond_{B.P.,B.P.}}\Big|_{node} \quad \text{Equation 16}$$

$$(\rho_{PEN} \times V_{PEN} \times C_{PEN})|_{Node} \times \frac{\partial T_{PEN}}{\partial t}\Big|_{node} = \sum \dot{Q}_{conv_{PEN,A,C}}\Big|_{node} + \sum \dot{Q}_{cond_{PEN,B.P.}}\Big|_{node} + \sum \dot{Q}_{cond_{PEN,PEN}}\Big|_{node} - I|_{node} V|_{node} - \frac{I|_{node}}{n_e F}\left(h_{H_2O}\Big|_{Node} - h_{H_2}\Big|_{Node} - \frac{1}{2} h_{O_2}\Big|_{Node}\right) \quad \text{Equation 17}$$

$$\left(\frac{P_C \times V_C}{R \times T_C} \times \bar{C}_{P_C}\right)\Big|_{Node} \times \frac{\partial T_C}{\partial t}\Big|_{node} = \sum_{Species} \dot{H}_{In}\Big|_{node} - \sum_{Species} \dot{H}_{Out}\Big|_{node} + \sum \dot{Q}_{conv_{C,PEN}}\Big|_{node} + \sum \dot{Q}_{conv_{C,B.P.}}\Big|_{node} - \frac{I|_{node}}{2 n_e F}\left(h_{O_2}\Big|_{Node}\right) \quad \text{Equation 18}$$

$$\left(\frac{P_A \times V_A}{R \times T_A} \times \bar{C}_{P_A}\right)\Big|_{Node} \times \frac{\partial T_A}{\partial t}\Big|_{node} = \sum_{Species} \dot{H}_{In}|_{node} - \sum_{Species} \dot{H}_{Out}|_{node} + \sum \dot{Q}_{conv_{A,PEN}}|_{node} + \sum \dot{Q}_{conv_{A,B.P.}}|_{node} - \frac{I|_{node}}{n_e F}\left(h_{H_2}|_{Node} - h_{H_2O}|_{Node}\right) \quad \text{Equation 19}$$

Where $\dot{H}_{In}|_{node}\ \left(\frac{J}{s}\right)$ and $\dot{H}_{Out}|_{Node}\ \left(\frac{J}{s}\right)$ are the total enthalpy of inlet and outlet stream of each node along anode/cathode stream, $\bar{C}_{P_{\frac{A}{C}}}\Big|_{Node}\ \left(\frac{J}{mole.K}\right)$ is an average specific heat capacity of species in each node along anode/cathode stream, $C_{PEN}|_{Node}\ \left(\frac{J}{kg.K}\right)$ and $C_{BP}|_{Node}\ \left(\frac{J}{kg.K}\right)$ are specific heat capacities of each node on the PEN and interconnect plate, $\rho_{PEN}|_{Node}\ \left(\frac{kg}{m^3}\right)$ and $\rho_{BP}|_{Node}\ \left(\frac{kg}{m^3}\right)$ are densities of each node on the PEN and interconnect plate, $V_{PEN}|_{Node}\ (m^3)$ and $V_{BP}|_{Node}\ (m^3)$ are volume of each node on the PEN and interconnect plate and $T_{PEN}|_{Node}\ (K), T_{BP}|_{Node}\ (K)$ are temperature of each node on the PEN and interconnect plate and $\dot{Q}\big|_{Node}\ \left(\frac{J}{s}\right)$ is composed of convection and conduction heat transfer to each node on each of different layers.

In order to calculate convection heat transfer between flows and solid walls, a local convective heat transfer coefficient is required. Reynolds numbers of fuel and air flows in channels are much lower than the critical Reynolds number for turbulent flow because not only are the fuel and air channels' cross-sectional area typically small, but also mean velocities of fuel and air flow are not very high. In these conditions, a fully developed laminar flow and uniform surface temperature exist approximately within all control volumes. In laminar flow condition, with considering the aspect ratio of the interconnect channels, a constant Nusselt number of four is used to calculate local convection heat transfer coefficient as below:

$$h = \frac{Nu_D \times k}{D_h} \quad \text{Equation 20}$$

3.1.1.2 Mass balance

As flows move from inlets to the cathode and anode outlets, the composition of fuel in anode side and the composition of oxygen/nitrogen at cathode side will be changed. The developed model takes into account the conservation of mass within each node and mass transfer between control volumes to calculate the nodal species' concentration's changes (species concentration are considered as states). Mass balance in cathode/anode flow side includes inlet/outlet molar flow rates from/to adjacent nodes and variation due to the existing electrochemical reaction. The nodal dynamic mass balance equations for steam, hydrogen, carbon monoxide, carbon dioxide, methane, oxygen and nitrogen species are presented below. Note that for each node, the inlet molar flow rate is the outlet molar flow rate of the previous node in the flow direction as follows [135].

$$\frac{dX_{O_2}|_{Node}}{dt} = \frac{\dot{n}_{O_2,In}|_{Node} - \dot{n}_{O_2,Out}|_{Node} - \frac{I|_{Node}}{2 \times n_e \times F}}{\frac{P_C|_{Node} \times V_C|_{Node}}{R \times T_C|_{Node}}} \quad \text{Equation 21}$$

$$\frac{dX_{N_2}|_{Node}}{dt} = \frac{\dot{n}_{N_2,In}|_{Node} - \dot{n}_{N_2,Out}|_{Node}}{\frac{P_C|_{Node} \times V_C|_{Node}}{R \times T_C|_{Node}}} \quad \text{Equation 22}$$

$$\frac{dX_{H_2O}|_{Node}}{dt} = \frac{\dot{n}_{H_2O,In}|_{Node} - \dot{n}_{H_2O,Out}|_{Node} + \frac{I|_{Node}}{n_e \times F} - r_{SR}|_{Node} \times V_A|_{Node} - r_{WGS}|_{Node} \times V_A|_{Node}}{\frac{P_A|_{Node} \times V_A|_{Node}}{R \times T_A|_{Node}}} \quad \text{Equation 23}$$

$$\frac{dX_{H_2}|_{Node}}{dt} = \frac{\dot{n}_{H_2,In}|_{Node} - \dot{n}_{H_2,Out}|_{Node} - \frac{I|_{Node}}{n_e \times F} + 3 \times r_{SR}|_{Node} \times V_A|_{Node} + r_{WGS}|_{Node} \times V_A|_{Node}}{\frac{P_A|_{Node} \times V_A|_{Node}}{R \times T_A|_{Node}}} \quad \text{Equation 24}$$

$$\frac{dX_{CO}|_{Node}}{dt} = \frac{\dot{n}_{CO,In}|_{Node} - \dot{n}_{CO,Out}|_{Node} + r_{SR}|_{Node} \times V_A|_{Node} - r_{WGS}|_{Node} \times V_A|_{Node}}{\frac{P_A|_{Node} \times V_A|_{Node}}{R \times T_A|_{Node}}} \quad \text{Equation 25}$$

$$\frac{dX_{CO_2}|_{Node}}{dt} = \frac{\dot{n}_{CO_2,In}|_{Node} - \dot{n}_{CO_2,Out}|_{Node} + r_{WGS}|_{Node} \times V_A|_{Node}}{\frac{P_A|_{Node} \times V_A|_{Node}}{R \times T_A|_{Node}}} \quad \text{Equation 26}$$

$$\frac{dX_{CH_4}|_{Node}}{dt} = \frac{\dot{n}_{CH_4,In}|_{Node} - \dot{n}_{CH_4,Out}|_{Node} - r_{SR}|_{Node} \times V_A|_{Node}}{\frac{P_A|_{Node} \times V_A|_{Node}}{R \times T_A|_{Node}}} \quad \text{Equation 27}$$

Where $\dot{n}$ $\left(\frac{mole}{s}\right)$ is the species molar flow rate, $I|_{Node}$ (A) is current of each node, $T_{\frac{A}{C}}\Big|_{Node}$ (K) is temperature of each node along the anode/cathode stream, $P_{A/C}|_{Node}$ (Pa) is pressure of each node along the anode/cathode stream, $V_{A/C}|_{Node}$ (m^3) is volume of each node along the anode/cathode stream and $r_{SR/WGS}|_{Node}$. Are the reaction rates which are calculated below.

In this model, it is considered that Steam Methane Reforming (SMR) and Water Gas Shift (WGS) reaction take place in anode, but the actual direction and magnitude of the reaction rates depends on the operating conditions.

$$CO + H_2O \quad \leftrightarrow \quad CO_2 + H_2 \quad \text{(WGS)} \quad \text{Equation 28}$$

$$CH_4 + H_2O \quad \leftrightarrow \quad CO + 3H_2 \quad \text{(SMR)} \quad \text{Equation 29}$$

In the literature, the Haberman and Young's model [136] is widely used for calculating the water gas shift (WGS) and steam methane reforming (SMR) reaction rates; thus it is adopted in the present study. The following general formulations can be considered based on the quasi-homogeneous expression of the reaction kinetics.

$$r_{WGS}|_{Node} = K_{WGS}|_{Node}\left[P_{CO}|_{Node}P_{H_2O}|_{Node} - \frac{P_{CO_2}|_{Node}P_{H_2}|_{Node}}{K_{eq,WGS}|_{Node}}\right], \qquad K_{eq,WGS}|_{Node} = \frac{K_{WGS}|_{Node}}{K_{RWGS}|_{Node}} \quad \text{Equation 30}$$

$$r_{SR}|_{Node} = K_{SR}|_{Node}\left[P_{CH_4}\big|_{Node}P_{H_2O}\big|_{Node} - \frac{P_{CO}|_{Node}P_{H_2}^3\big|_{Node}}{K_{eq,SR}\big|_{Node}}\right], \qquad K_{eq,SR}\big|_{Node} = \frac{K_{SR}|_{Node}}{K_{Methanation}|_{Node}} \qquad \text{Equation 31}$$

Where K_{WGS} and K_{SR} show the rate of water gas shift reaction and steam reformation reaction. K_{eq} is also equilibrium constant of each reaction. Ordinarily, based upon the first order kinetic expression (Arrhenius form), the rates of forward steam reformation and water gas shift reactions are as below:

$$K_{WGS}|_{Node} = 0.0171\exp\left(\frac{-103191}{RT_F|_{Node}}\right) \qquad \text{Equation 32}$$

$$K_{SR}|_{Node} = 2395\exp(\frac{-231266}{RT_F|_{Node}}) \qquad \text{Equation 33}$$

The SMR and WGS equilibrium constants can be calculated as below:

$$K_{eq,WGS}\big|_{Node} = \exp(-0.2935Z^3 + 0.6351Z^2 + 4.1788Z + 0.3169) \qquad \text{Equation 34}$$

$$K_{eq,SR}\big|_{Node} = 1.0267 \times 10^{10}\exp(-0.2513Z^4 + 0.3665Z^3 + 0.581Z^2 - 27.134Z + 3.277) \qquad \text{Equation 35}$$

$$Z = \frac{1000}{T(K)} - 1 \qquad \text{Equation 36}$$

3.1.1.3 Polarization model

Nernst Voltage:

The Nernst potential is the electrical potential of each node which accounts for species concentration, operating temperature and pressure, and extent of reaction as well.

$$V_{Nernst}|_{Node} = E^0|_{Node} + \frac{R\ T_{PEN}|_{Node}}{n_e\ F} \times Ln\left(\frac{X_{H_2,b}\big|_{Node}\ X_{O_2,b}^{0.5}\big|_{Node}}{X_{H_2O,b}\big|_{Node}}\ P_A|_{Node}^{0.5}\right) \qquad \text{Equation 37}$$

Where $E^0|_{Node}\ (V)$ is a standard voltage of each node, R is a universal gas constant equal to $8.314\left(\frac{J}{mole.K}\right)$. $T_{PEN}|_{Node}\ (K)$ is temperature of each node on the PEN, n_e (mole of electron/moles of steam) is number of moles of electron transferred per unit mole of hydrogen equal to 2, $F\ \left(\frac{C}{mole}\right)$ is Faraday constant equal to 96485, X_i is species molar fraction and $P_A|_{Node}(atm)$ is pressure of each node along the anode stream.

The standard reversible voltage ($E^0|_{Node}$) of each node is calculated based upon the Gibbs energy change of reaction at the node temperature and standard pressure ($\Delta G|_{T_{PEN|_{Node}},P_{Amb}}(J/\ mole)$) according to Equation 38:

$$E^0|_{Node} = \frac{\Delta G\left(H_2 + \frac{1}{2}O_2 \rightarrow H_2O\right)\Big|_{T_{PEN|_{Node}},P_{Amb}}}{n_e\ F} \qquad \text{Equation 38}$$

When the current is non-zero in the fuel cell, the cell operating voltage is lower than the Nernst voltage due to the voltage losses. These voltage losses can be described as follows: ohmic loss governed by ohm's law, activation loss governed by Butler-Volmer equation and concentration loss.

Activation Loss:

The Butler-Volmer equation is typically employed to characterize electrochemical activation loss associated with sluggish charge transfer reactions at the operating conditions of the cell as follows for the cathode and anode interfaces.

$$J|_{Node} = J_{0,Ca}\big|_{Node} \times \left\{exp\left(\frac{\alpha\ n_e\ F\ \eta_{act,Ca}\big|_{Node}}{R\ T_{PEN}|_{Node}}\right) - exp\left(-\frac{(1-\alpha)\ n_e\ F\ \eta_{act,Ca}\big|_{Node}}{R\ T_{PEN}|_{Node}}\right)\right\} \qquad \text{Equation 39}$$

$$J|_{Node} = J_{0An}|_{Node} \times \left\{ exp\left(\frac{\alpha\, n_e\, F\, \eta_{act,An}\big|_{Node}}{R\, T_{PEN}|_{Node}} \right) - exp\left(-\frac{(1-\alpha)\, n_e\, F\, \eta_{act,An}\big|_{Node}}{R\, T_{PEN}|_{Node}} \right) \right\} \quad \text{Equation 40}$$

The exchange current density is a kinetic parameter measuring the local electrode current density at open circuit conditions i.e., at equilibrium conditions when no net current density is consumed or produced within the cell, and α is the symmetry factor or charge transfer coefficient. Equation 41 and Equation 42 are employed to calculate the exchange current density as a function of temperature.

$$J_{0,Ca}\big|_{Node} = (1.344 \times 10^{10}) \times exp\left(-\frac{1 \times 10^5}{R\, T_{PEN}|_{Node}} \right) \quad \text{Equation 41}$$

$$J_{0,An}\big|_{Node} = (2.051 \times 10^{9}) \times exp(-\frac{1.2 \times 10^5}{R\, T_{PEN}|_{Node}}) \quad \text{Equation 42}$$

The value of transfer coefficient is usually 0.5 for fuel cell applications [137]. With $\alpha = 0.5$, equations Equation 41 and Equation 42 can be expressed as:

$$\eta_{act,Ca}\big|_{Node} = \frac{R\, T_{PEN}|_{Node}}{F} \times sinh^{-1}\left(\frac{J|_{Node}}{2\, J_{0,Ca}\big|_{Node}} \right) \quad \text{Equation 43}$$

$$\eta_{act,An}\big|_{Node} = \frac{R\, T_{PEN}|_{Node}}{F} \times sinh^{-1}(\frac{J|_{Node}}{2\, J_{0,An}\big|_{Node}}) \quad \text{Equation 44}$$

Ohmic Loss:

Ohm's law is employed to evaluate the cell ohmic loss. Ohmic loss consists of cathode, anode and electrolyte ohmic losses as well as interconnect ohmic loss and contact ohmic loss which has the effect of ohmic resistance in the contact region between electrodes and interconnect plates. Equation 45 to Equation 50 describe the ohmic loss different components [135]:

$$\eta_{ohm,Cont}\big|_{Node} = 0.1 \times 10^{-4} \times (J|_{Node}) \quad \text{Equation 45}$$

$$\eta_{ohm,Ca}\big|_{Node} = (1.05 \times 10^{-8}) \times T_{PEN}|_{Node} \times exp(\frac{1150}{T_{PEN}|_{Node}}) \times \delta_{Ca} \times (J|_{Node}) \quad \text{Equation 46}$$

$$\eta_{ohm,An}\big|_{Node} = (2.38 \times 10^{-8}) \times T_{PEN}|_{Node} \times exp(\frac{1200}{T_{PEN}|_{Node}}) \times \delta_{An} \times (J|_{Node}) \quad \text{Equation 47}$$

$$\eta_{ohm,El}\big|_{Node} = (2.99 \times 10^{-5}) \times exp(\frac{10300}{T_{PEN}|_{Node}}) \times \delta_{El} \times (J|_{Node}) \quad \text{Equation 48}$$

$$\eta_{ohm,Ic}\big|_{Node} = (1.075 \times 10^{-7}) \times T_{IC}|_{Node} \times exp(\frac{1100}{T_{IC}|_{Node}}) \times \delta_{Ic} \times (J|_{Node}) \quad \text{Equation 49}$$

$$\eta_{ohm} = \sum \left(\frac{1}{A_{SOFC}}\right) \times T_{PEN}|_{Node} \times exp(\frac{\Delta G_{act}}{T_{PEN}|_{Node}}) \times \delta \times (J|_{Node}) \quad \text{Equation 50}$$

Concentration Loss:

Concentration losses come from a physical limitation of gaseous diffusion from the bulk fluid flow to and from the reaction sites. As the cell produces current it must be continually supplied with reactants at the TPB, however, at some rate the supply of reacting species cannot diffuse through the electrode quick enough which is called the limiting current density and will reduce the operating voltage all the way to zero. Concentration losses can be expressed with the following equation:

$$\eta_{conc}|_{Node} = \frac{R\, T_{PEN}|_{Node}}{nF} \ln \frac{j_L}{j_L - j} \quad \text{Equation 51}$$

where $j_L \left(\frac{amp}{cm^2}\right)$ is the limiting current, , R is a universal gas constant equal to $8.314\left(\frac{J}{mole.K}\right)$, $T_{PEN}|_{Node}\ (K)$ is temperature of each node on the PEN, n_e (mole of electron/moles of steam) is number of moles of electron transferred per unit mole of hydrogen equal to 2 and $F\ \left(\frac{C}{mole}\right)$ is Faraday constant.

3.2 SOFC stack results

Figure 20 to Figure 24 show the spatial distribution of temperature, Nernst voltage, losses, voltage, and current density in a unit SOFC. The temperature changes between 1000K-1040K. The temperature has its lowest amount at the corner close to the cathode and anode streams inlet where the air which is cooling stream has its lowest temperature (highest cooling potential) and the reformation which is endothermic is still occurring at the beginning of the cell. Temperature has the highest amount at the corner close to the cathode and anode streams outlet where air has its highest temperature (lowest cooling potential) and electrochemical reaction which is dominant at the end of cell generates heat due to its exothermicity.

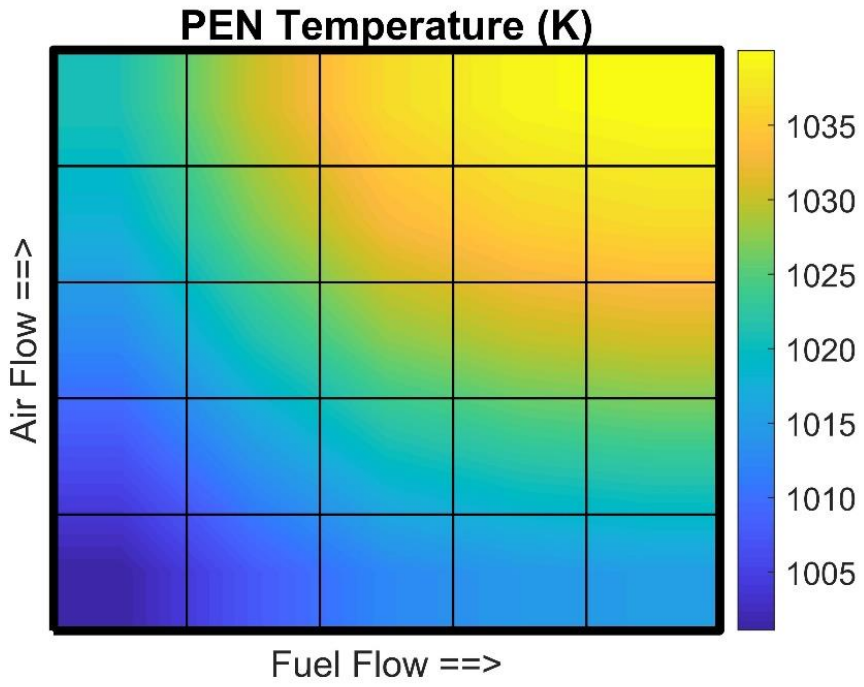

Figure 20. State spatial distribution of temperature.

The Nernst voltages are among 0.9V-0.98V. The Nernst voltage is highest at the corner close to the cathode and anode inlet streams where both fuel and oxidant partial pressures are high leading to high thermodynamic potential with the lowest Nernst potentials realized at the corner close to the cathode and anode streams outlet.

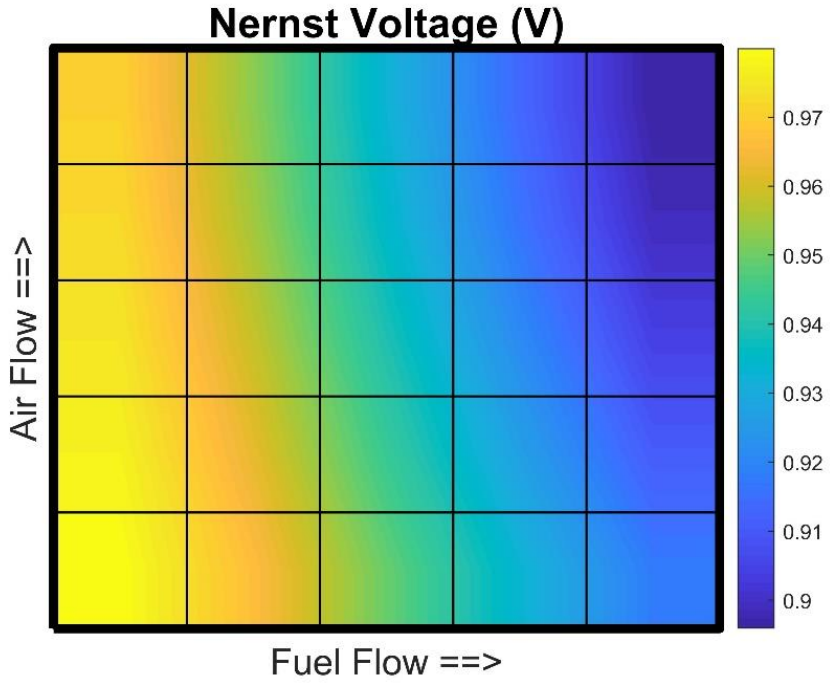

Figure 21. Steady-state spatial distribution of Nernst voltage.

The lowest amount of losses is 0.065V captured where the temperature is highest. High temperature increases the thermal energy available in the system, generally resulting in the fact that all the particles in the system now move and vibrate with increased intensity. This higher level of thermal activity will possess sufficient energy to overcome activation polarization and most importantly increases electrolyte ionic conductivity, which decreases the ohmic loss.

Figure 22 shows the spatial distribution of cell operating voltage which is uniform along the cell as expected due to the equipotential surface that is established by the good electronic conductivity of the electrodes and bipolar plates. The current density along the direction of fuel flow decreases as the fuel gets consumed and has less potential to produce current.

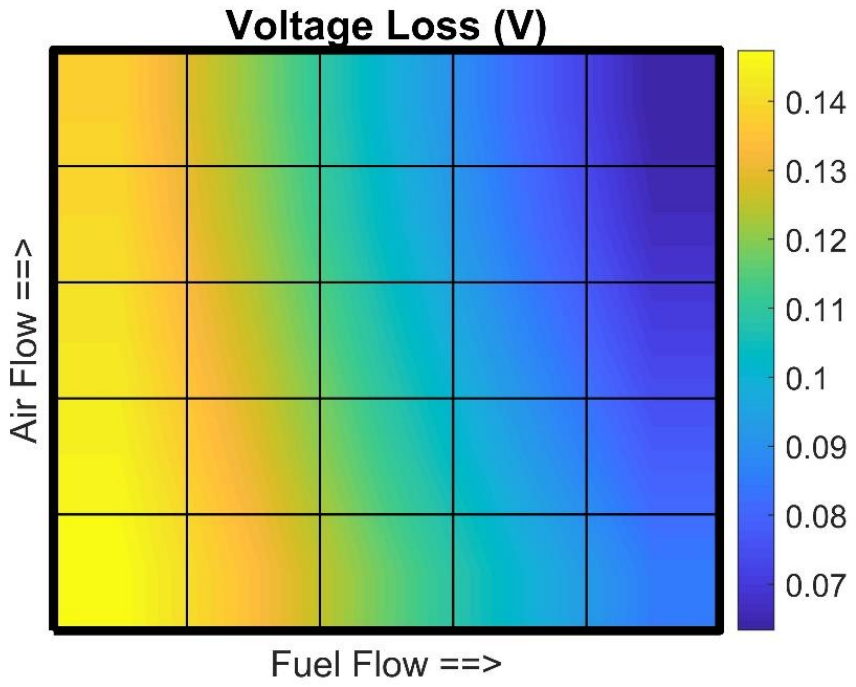

Figure 22. Steady-state spatial distribution of losses.

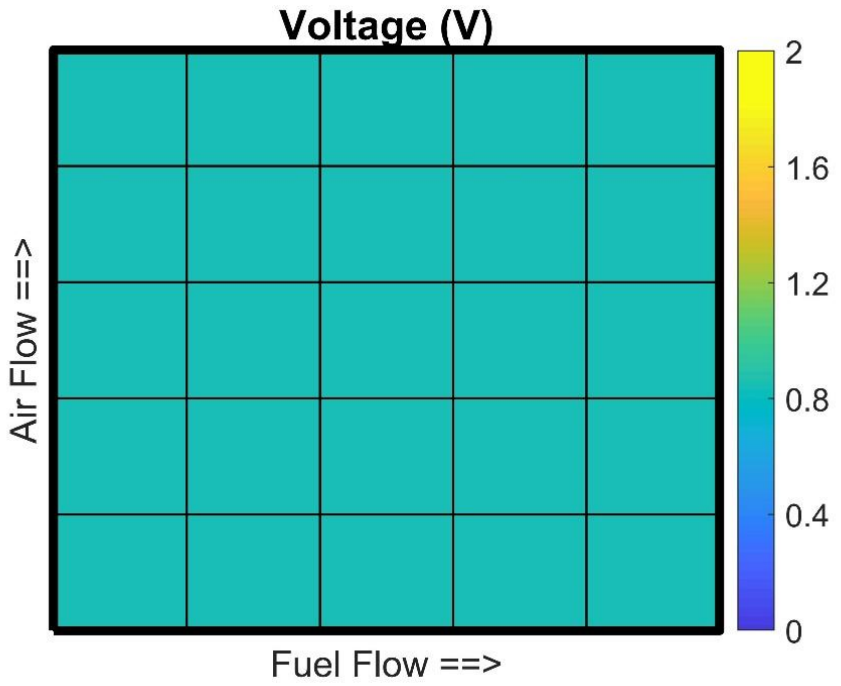

Figure 23. Steady-state spatial distribution of voltage.

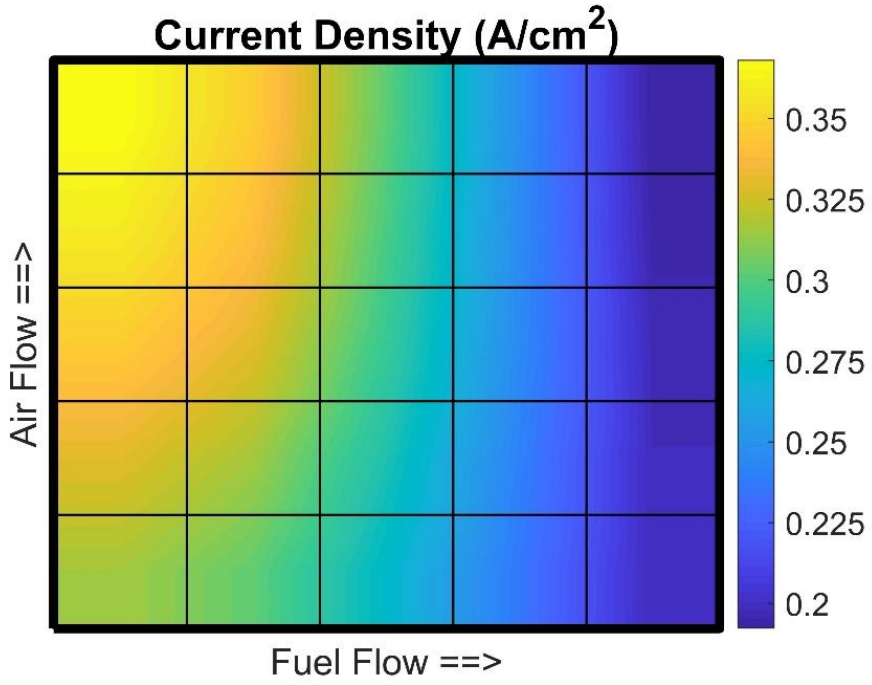

Figure 24. Steady-state spatial distribution of current density.

3.3 SOFC system design & control

The SOFC system model contains a fuel cell stack, an anode off-gas oxidizer, air preheating heat exchangers, recirculate valve, mixer, blower, and reformer. A system diagram is provided in Figure 25. The oxidizer outlet preheats air and fuel first, and then, the leftover heat from the SOFC exhaust is recovered for regenerating desiccant liquid in the LDD system.

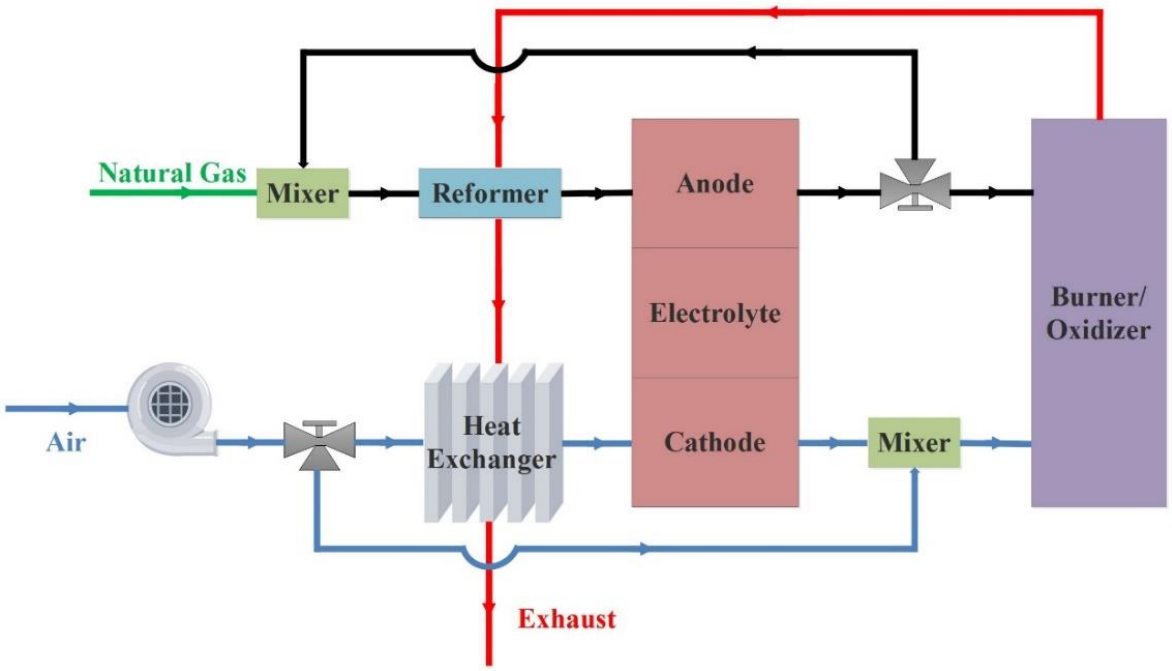

Figure 25. SOFC system configuration.

3.3.1 Balance of plant model

The balance of plant model is described below:

3.3.1.1 Blower

A variable-speed blower model, enabling simulation of the rotating moment of inertia of the blower, is implemented in this study. The blower supplies sufficient pressure head and air flow rate for controlling the cell temperature gradient, The implemented dynamic model for blower is shown in Equation 52 [138].

$$J \,.\, w \,.\frac{dw}{dt} = P_B - P_{Imp} \qquad \text{Equation 52}$$

Where w is rotational speed, J is the moment inertia, P_B is the electric power supplied to the blower and P_{Imp} is the impeller loss evaluated according to Equation 53.

$$P_{Imp} = \frac{\dot{V}_{Air} \cdot \Delta P_{ca}}{\eta_B}$$ Equation 53

where $\dot{V}_{Air}$ is the air volumetric flow rate, ΔP_{ca} is the pressure drop at cathode side and η is the blower mechanical efficiency.

3.3.1.2 Heat exchanger

Heat exchangers are modeled as one-dimensional counter flow plate heat exchangers comprised of three layers e.g., hot stream, metal separator plate and cold stream in order to capture the thermal inertia of the heat exchangers. The developed dynamic model for a heat exchanger is spatially discretized into nodes and control volumes. In each node, material and energy balances are implemented using Equation 54 and Equation 55.

$$\rho^{c,h} . V^{c,h} . c_p^{c,h} . \frac{dT^{c,h}}{dt} = \dot{Q}_{conv} + \dot{H}_{In}^{c,h} - \dot{H}_{Out}^{c,h}$$ Equation 54

$$\rho_{Plate} \cdot c_{Plate} \cdot V_{Plate} \cdot \frac{dT_{Plate}}{dt} = \dot{Q}_{conv} + \dot{Q}_{cond}$$ Equation 55

Where $\rho^{c,h} . V^{c,h} . c_p^{c,h} . \frac{dT^{c,h}}{dt} = \dot{Q}_{conv} + \dot{H}_{In}^{c,h} - \dot{H}_{Out}^{c,h} \dot{Q}_{conv}$ is convective heat transfer between solid and gaseous nodes, ρ is the density, V is volume and c_p , c are the specific heat capacity of gaseous and solid nodes.

3.3.1.3 Mixer

The following expressions can be used to find the composition of the mixed stream.

$$\dot{n}_{mix} = \sum_i (\dot{n}_1 . x_{1,i} + \dot{n}_2 . x_{2,i}$$ Equation 56

$$x_{mix,i} = \frac{\dot{n}_1 . x_{1,i} + \dot{n}_{mix} . x_{1,i}}{\dot{n}_{mix}}$$ Equation 57

$$n_{mix} C_p . \frac{dT_{mix}}{dt} = \dot{n}_1 . h_1 + \dot{n}_2 . h_2 + \dot{n}_{mix} . h_{mix}$$ Equation 58

3.3.1.4 Reformer

In this study both internal reforming and external reforming is considered. For external reforming, like internal reforming, SMR and WGS take place. The mass balance equation is the same as the one as explained in section 3.1.1.2 for fuel cell without electrochemical term ($I = 0$) and the energy balance is the same as heat exchanger which explained in 3.3.1.2.

3.3.1.5 Oxidizer

The combustion model accounts only for the same seven species as the remainder of the model. The following three reactions are considered in this combustor model.

Methane: $CH_4 + 2O_2 \rightarrow 2H_2O + CO_2$ Equation 59

Carbon Monoxide: $CO + \frac{1}{2} O_2 \rightarrow CO_2$ Equation 60

Hydrogen: $H_2 + \frac{1}{2} O_2 = H_2O$ Equation 61

Proper accounting of all the reacting species is necessary to find the resulting flow rate and composition post combustion. The energy conservation equation is as follows:

$$n_{com} C_p . \frac{dT_{comb}}{dt} = \dot{n}_1 . h_1 + \dot{n}_2 . h_2 - \dot{n}_{out} . h_{out}$$ Equation 62

3.3.2 Control strategy

3.3.2.1 Temperature control

Cell temperature control is one of the key issues involved in the dynamic operation of high temperature SOFC systems. In this study, the stack is thermally managed by manipulating one actuator, which controls the blower power. A variable speed blower enables control of blower dynamics that consider the inertia of the blower as described above. Increasing the blower power ultimately increases the blower speed, which in-turn increases the air flow rate introduced to the stack. The air flow rate has two functions in the proposed system, i.e., providing the oxygen for the electrochemical reactions and providing cooling or heating to the stack. The temperature control strategy consists of two parts. Stack temperature gradient is controlled with blower power. If the temperature gradient goes higher than the set point, the blower power increases which increases the air flow rate which cools the stack. To control stack average temperature, the valve position changes to increase or decrease the air flow to oxidizer which affects the cell inlet air flow temperature. To decrease the cell average temperature, the valve opens more, to decrease the hot flow temperature in the air heat exchanger. In this study, the controller set-point temperature difference constraint is 50K. Also, the inlet temperature of both anode and cathode temperature are controlled to the set point of 1023K.

3.3.2.2 Stack power management

During dynamic operating condition, the stack power is controlled by manipulating the current in feed-forward controller. At each time among set of points in time vector, the current is calculated based upon the operating voltage and the stack power as below:

$$I|_{Cell} = \frac{P_{Stack}}{\overline{V}_{Op} \times N_{Cell}} \qquad \text{Equation 63}$$

3.3.2.3 Fuel utilization

In controller model, fuel flow rate is controlled by manipulating cell current and system fuel utilization in feed-forward controller as below:

$$\dot{n}_{CH_4}\big|_{System} = \frac{I|_{Cell}}{4 \times F \times FU|_{System}} \times N_{Cell}$$ Equation 64

where FU is SOFC system fuel utilization defined as the ratio between stoichiometric fuel flow required for the electrochemical reactions at a given current and the actual inlet fuel flow introduced to the system. It should be noticed that the controller keeps the fuel utilization constant at a nominal value for a wide range of operating conditions except for very low powers control of very low flow rates could lead to the possibility of concentration loss increases.

3.3.2.4 Steam-to-carbon ratio

To prevent carbon deposition in the stack the molar ratio of steam-to-carbon is set to 2.02 in this study. The anode recirculation valve is manipulated to control the amount of recirculated flow to keep the steam-to-carbon ratio at this set point.

3.4 Steady state results

The system model is based on a commercially available SOFC systems called BlueGEN. BlueGEN CHP unit, originally manufactured by Ceramic Fuel Cells Ltd (CFCL). BlueGEN is a commercially available SOFC CHP system, now built and sold by SOLIDpower, designed for small- to medium-scale building applications. Operating on natural gas, the unit can produce power modulated from 500W_e (25%) to 2kW_e (100%); however, it achieves its highest net electrical efficiency of 60% at a 1.5kWe output. The BlueGEN SOFC unit consists of 51 planar type Yttria Stabilized Zirconia (YSZ) electrolyte-supported cell layer sets (each layer consists of 4 cells) and operates at around 750°C. Hydrogen is produced from natural gas by external and internal steam reforming.

The polarization curve data from the BlueGEN SOFC system tested at the NFCRC and the developed model results are presented in Figure 26. Note that the V-j curve obtained from the test covers only the operating envelope of the SOFC system. The results show that the MATLAB model simulates the BlueGEN system V-j curve accurately.

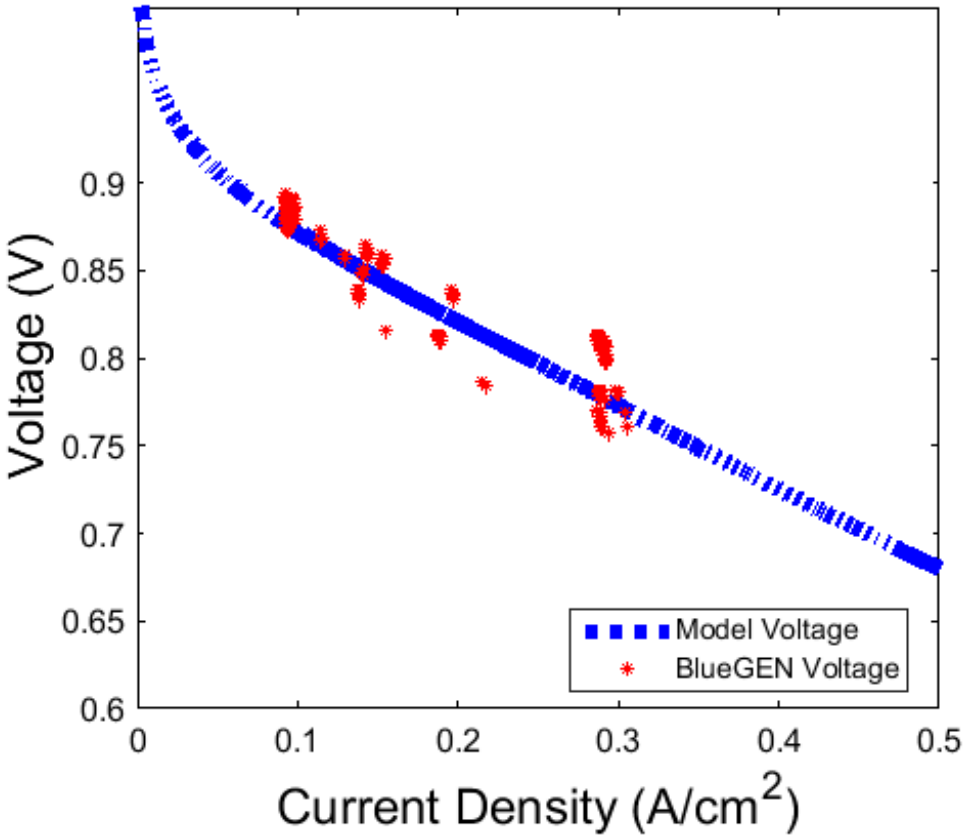

Figure 26. SOFC polarization curve for the BlueGEN data compared to the current physical SOFC system model.

The steady state performance of the system was calculated under the standard operating conditions of the BlueGEN at 85% fuel utilization and cathode outlet temperature of 750˚C. The SOFC system is controlled to keep the stack temperature difference at 50˚C. The SOFC parameter and standard operating conditions are presented in Table 4. The electrical efficiency of the stack is over 61% under standard operating conditions. The steady state performance parameters of the model for 1.5kW SOFC system and experiment values are compared in Table 5. Note that experimental values well match those of the model. Note also that the exhaust gas temperature and flow rate were not measured during the experiment.

Table 4. SOFC Parameters and Design Operating Conditions.

Parameters	Value
Fuel Utilization	0.85
Steam to Carbon Ratio	2.02
Cell Area	139.24cm^2
Power Density	233mW/cm^2
Stack Temperature Change	50°C
SOFC Stack Average Temperature	1023K

The particular SOFC system that was evaluated in this study was designed for CHP, and thus produces more heat than would be used for preheating the SOFC inlet air and fuel. The heat produced from the SOFC system in the current case is then used for producing hot water for LiCl regeneration purposes. This model indicates that a nominal 1.5kW system would produce 0.0104kg/s of exhaust gas and that the temperature of the exhaust would be 100˚C.

Table 5. SOFC steady state performance parameters.

Parameters	Model Value	Experiment Value
Net Power Output	1.49kW	1.5kW
Voltage	42.5V	42.5V
Current	38.94A/cm^2	38.94A/cm^2
Electrical Efficiency	61.1%	61.27%
Exhaust Gas Temperature	373K	-
Exhaust Gas Mass Flow Rate	0.0104kg/s	-

3.5 SOFC dynamic result

Electricity demand for a single residential unit is used as a desired demand applied to the spatially resolved dynamic SOFC model. SOFC model results (Figure 27) that generated output power follows the desired demand quite closely except for very short periods of high ramp rate operating conditions. Figure 28 shows the electrical efficiency of the system

during the dynamic operation. The average efficiency during dynamic operation is 71%. The high efficiency is due to high fuel utilization (85%) and part load operation of the system which also lead to a lower exhaust temperature.

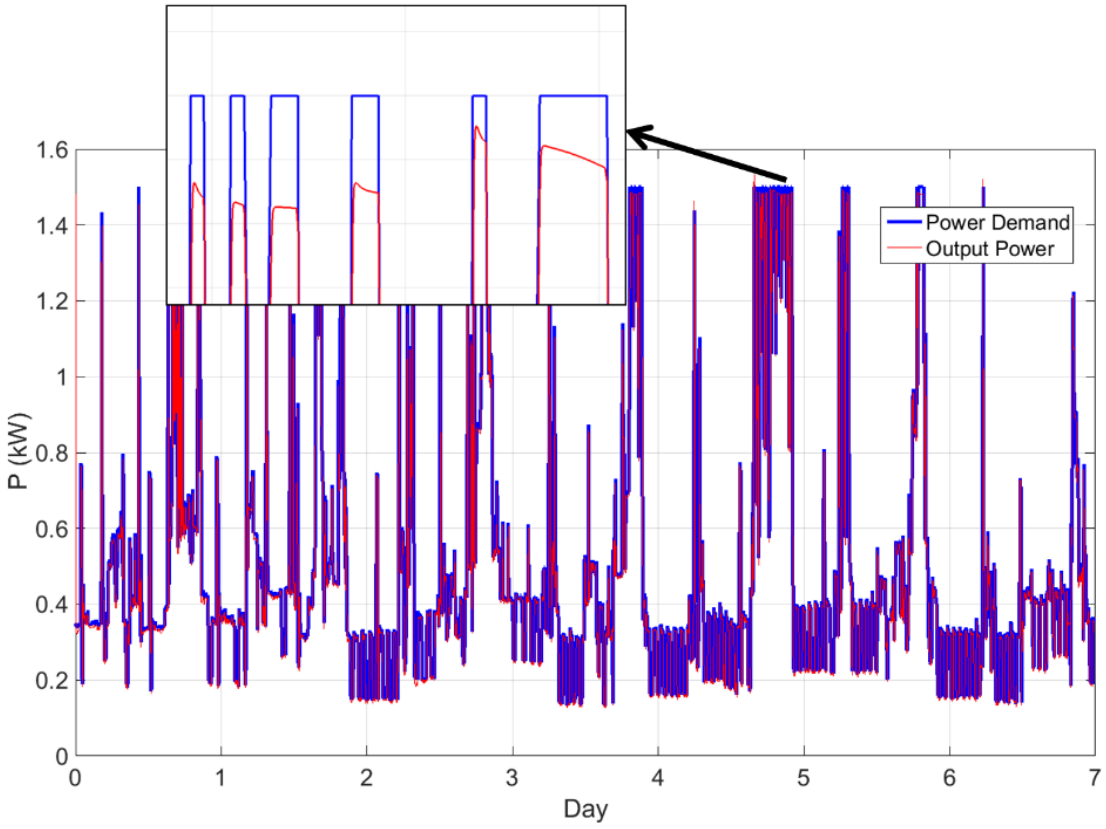

Figure 27. SOFC model power output following the residential electricity demand

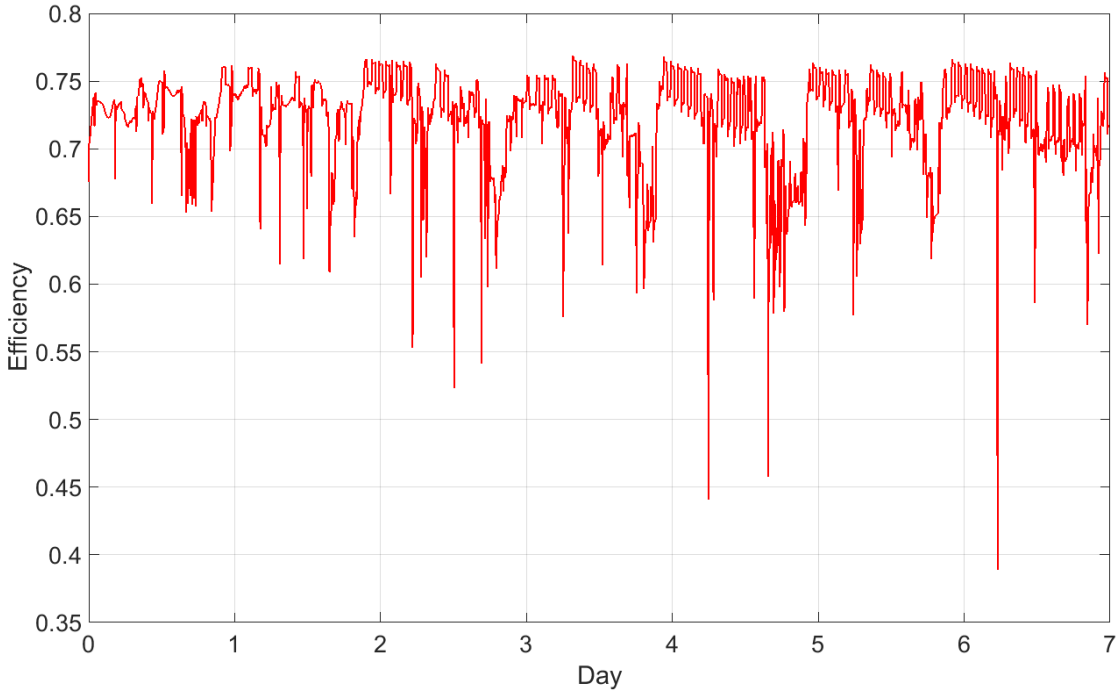

Figure 28. Variation of electrical efficiency versus time.

Temperature and mass flow rate of SOFC exhaust gas versus time are presented in Figure 29 and Figure 30, respectively. As shown in Figure 25, the oxidizer output is used for preheating fuel and air and then leaves the system as exhaust. This SOFC system exhaust is used to produce hot water for regenerating LiCl in liquid desiccant regenerator.

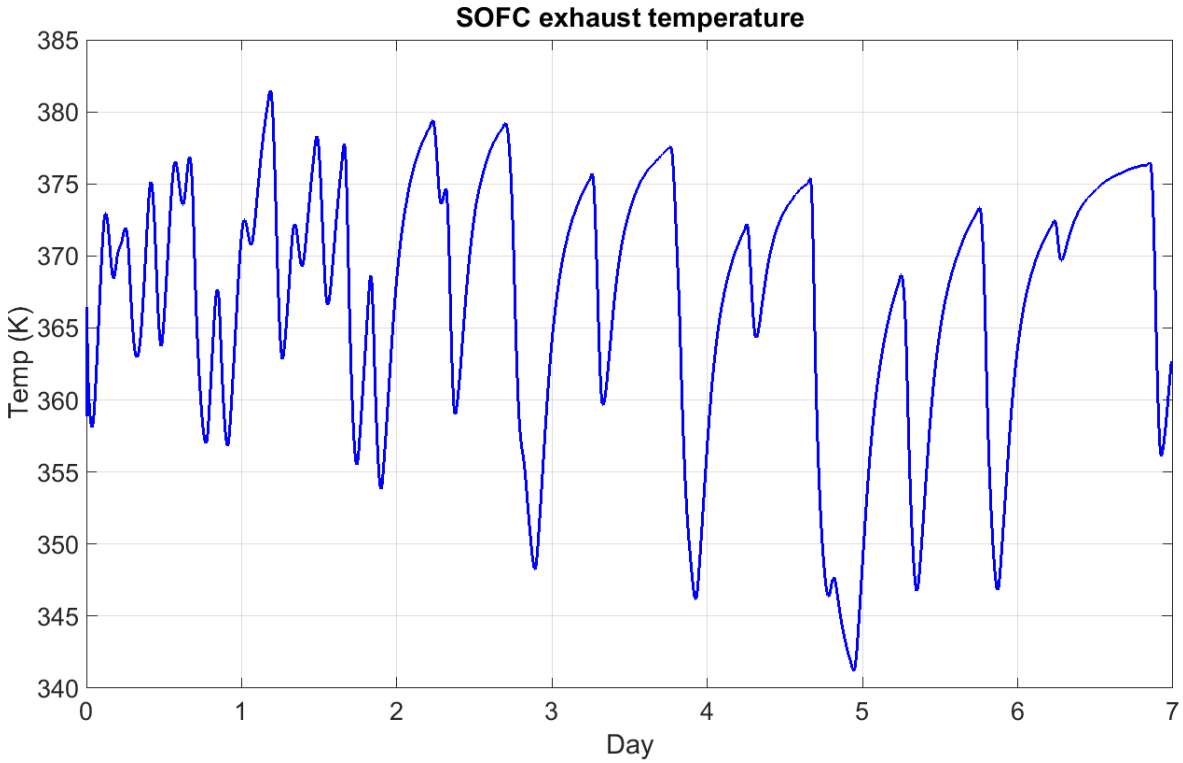

Figure 29. Exhaust gas temperature of the SOFC system.

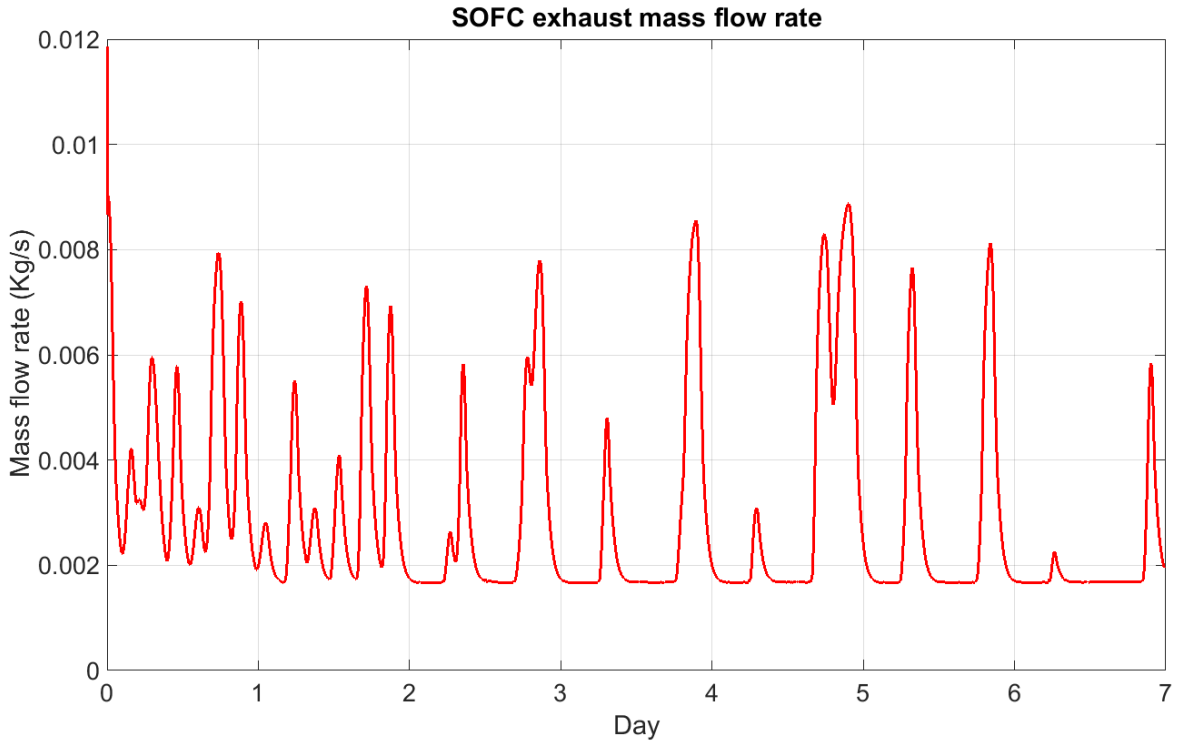

Figure 30. Exhaust gas mass flow rate of the SOFC system.

Figure 31 and Figure 32 show the PEN average temperature and stack temperature difference during the dynamic operation, respectively. The set point for PEN average temperature is 1023K and for stack temperature difference is 50K, due to very high dynamic load the controller is not able to keep the cell at the desired temperature. PEN average temperature goes as high as 1078K and stack temperature difference changes up to 94K.

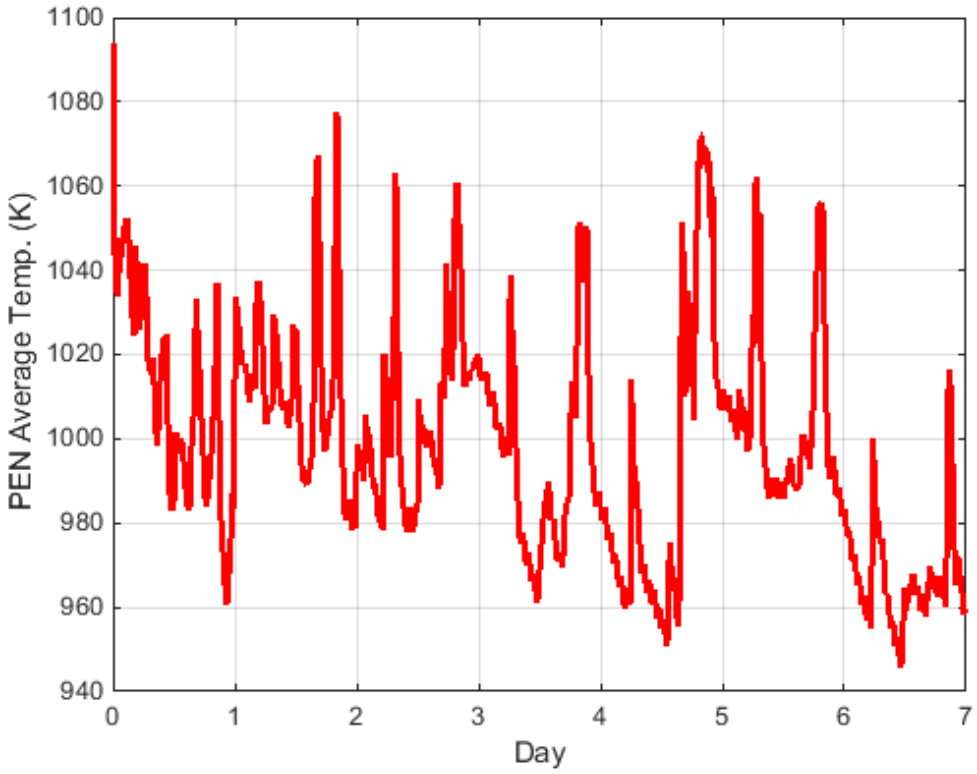

Figure 31. PEN average temperature.

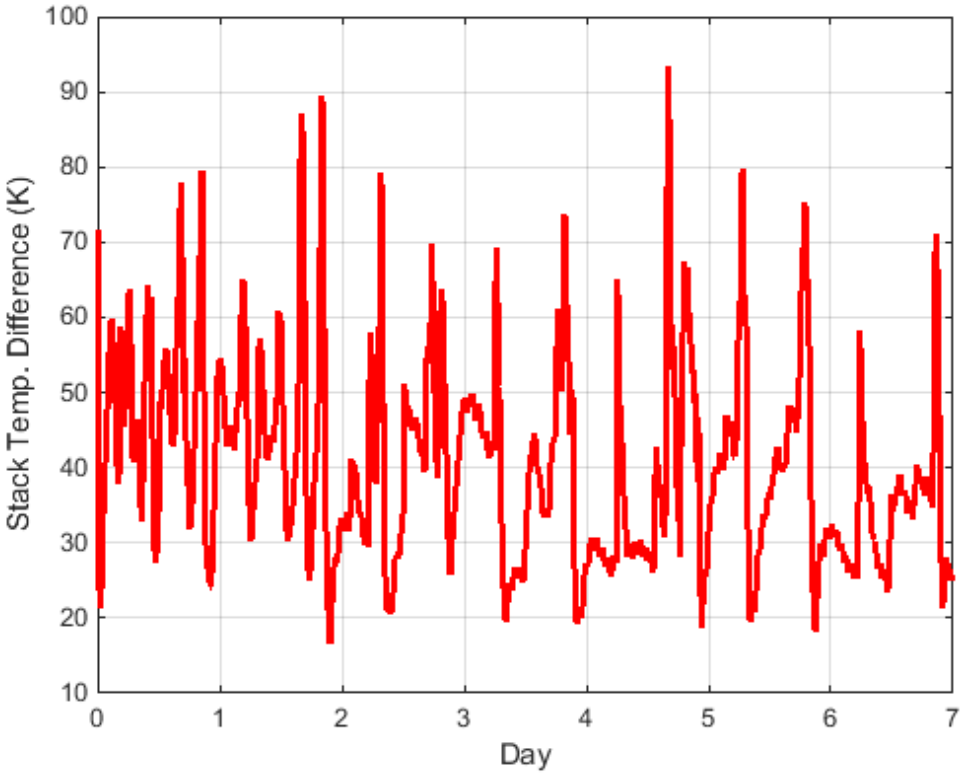

Figure 32. Stack temperature difference.

3.6 Summary

This chapter has focused on developing a spatially and temporally resolved dynamic physical SOFC model. It also focused on designing the SOFC system components and balance of plant based upon the commercially used SOFC in this research experiment. Additionally, it has focused on the control strategies for the SOFC system. This chapter has included the steady state stack spatially distribution results, and verification of developed model with experimental tests. Finally, SOFC results under dynamic operation of a residential load have been presented.

4 Liquid Desiccant Dehumidifier Modeling

4.1 Liquid desiccant component modeling

The LDD system model is based upon a similar DEVap concept developed by NREL [83] The current physical model is developed to simulate the DEVAP components including regenerator, dehumidifier and indirect evaporative cooler. LiCl solution is the working fluid used is this system. Figure 33 shows the LLD system diagram.

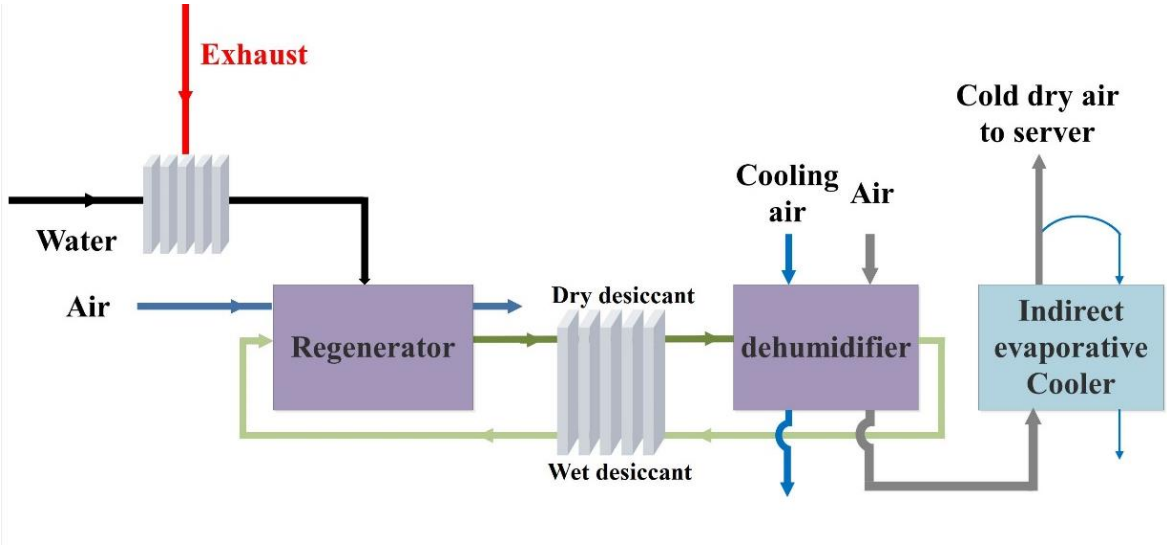

Figure 33. Configuration of the LLD system.

Energy balance, and mass balance equations were applied to the LDD model. For the air and water properties EES [139] has been used, whereas for LiCl properties a library has been developed based on literature experimental results. MATLAB was used to simulate the operation of the LDD system under different SOFC exhaust and weather conditions. The detailed model for each component is explained in the next section.

4.1.1 Dehumidifier modeling

During the dehumidification process, the liquid desiccant is in contact with air through a permeable membrane that allows water vapor interaction but prevents the flow of LiCl into the air. LiCl absorbs the water vapor in the air until it reaches water vapor pressure

equilibrium with the air. This process is exothermic. The desiccant is kept cool by the evaporation of water to the exhaust heat stream. Figure 34 shows the dehumidifier unit schematic.

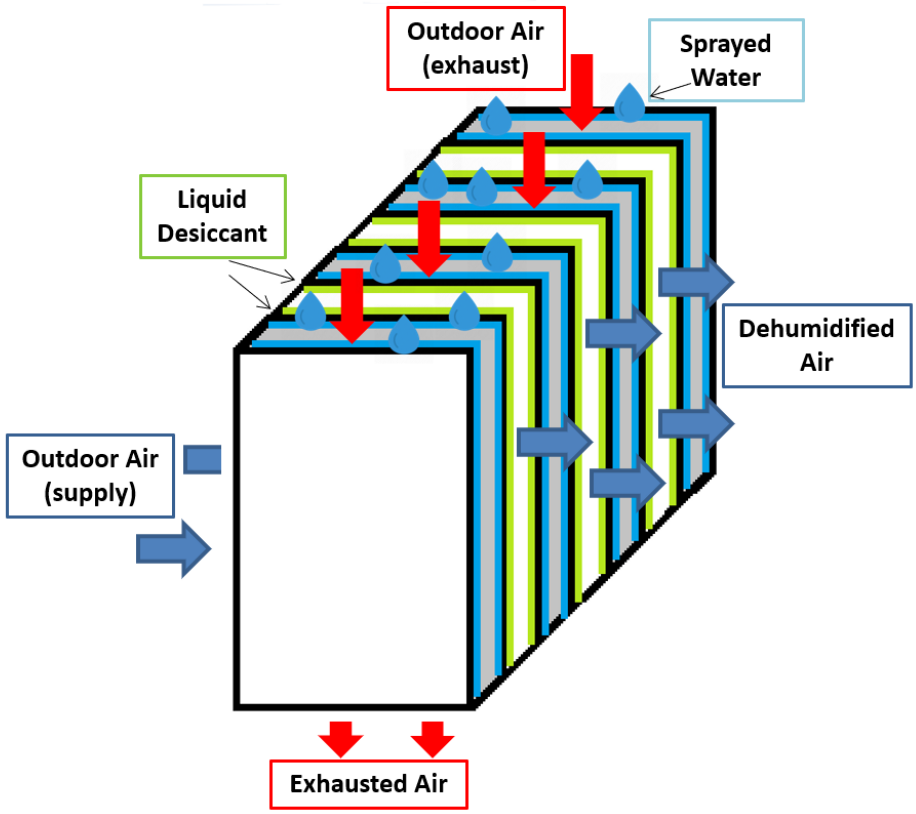

Figure 34. Dehumidifier unit schematic.

Equations for each stream are presented below. Mass transfer is driven by a vapor pressure differential between the air and desiccant solution as shown in Equation 66. The supply air side heat transfer for the dehumidifier is given by Equation 68. The heat transferred to the solution includes the sensible heat due to the temperature difference between the desiccant and air, and desiccant and water, plus the latent heat of absorption and enthalpy of dilution, given by Equation 72 [75,97].

Supply air side:

$$(\dot{m}\omega)_{sa,e} - (\dot{m}\omega)_{sa,i} = -J_{sa}dA$$ Equation 65

$$J_{sa} = \frac{P_a - P_{sol}}{R_w T_a \left(\frac{1}{h_{ma}} + \frac{\delta_{mem}}{D_{mem}}\right)}$$ Equation 66

$$\left(\dot{m}C_pT\right)_{sa,e} - \left(\dot{m}C_pT\right)_{sa,i} = q_{sa}dA$$ Equation 67

$$q_{sa} = \frac{T_{LD} - T_{sa}}{\left(\frac{1}{h_{sa}}\right) + \left(\frac{\delta}{k}\right)_{mem} + \left(\frac{\delta}{2k}\right)_{sol}}$$ Equation 68

Liquid desiccant side:

$$(\dot{m})_{LD,e} - (\dot{m})_{LD,i} = J_{sa}dA$$ Equation 69

$$(\dot{m}C)_{LD,e} - (\dot{m}C)_{LD,i} = 0$$ Equation 70

$$\left(\dot{m}C_pT\right)_{LD,e} - \left(\dot{m}C_pT\right)_{LD,i} = q_{LD}dA$$ Equation 71

$$q_{LD} = q_{lat_{sa}} - q_{sa} - q_{plate}$$ Equation 72

$$q_{lat_{sa}} = L_{sa}(h_{fg} + h_{mix})$$ Equation 73

$$q_{plate} = \frac{T_{LD} - T_w}{\left(\frac{\delta}{k}\right)_w + \left(\frac{\delta}{k}\right)_p + \left(\frac{\delta}{2k}\right)_{sol}}$$ Equation 74

Exhaust air side:

$$(\dot{m}\omega)_{ea,e} - (\dot{m}\omega)_{ea,i} = J_{ea}dA$$ Equation 75

$$J_e = h_{me}(\omega_w - \omega_e)$$ Equation 76

$$\left(\dot{m}C_pT\right)_{ea,e} - \left(\dot{m}C_pT\right)_{ea,i} = -q_{ea}dA$$ Equation 77

$$q_{ea} = q_{lat} - q_{plate}$$ Equation 78

$$q_{lat} = J_e h_{fg}$$ Equation 79

$$q_{ea} = h_{ea}(T_{ea} - T_w)$$ Equation 80

Where P_a and P_{sol} are the inlet equivalent vapor pressure of the air and liquid desiccant solution respectively in P_a. h_{ma} ($\frac{kg}{m^2.s}$) and h_{as} ($\frac{k}{m^2K}$)are the respective convective mass transfer and heat transfer coefficients of the air. R_w is the molar gas constant for water ($461.5\frac{J}{kg.K}$).

4.1.2 Indirect evaporative cooling modeling

The dehumidified air goes to an indirect evaporative cooler after the dehumidifier where it is cooled indirectly by water evaporating into a separate airstream in counter flow. A portion of cold dehumidified supply air is recirculated to the counter flow direction as the second stream to cool the primary air stream. Figure 35 shows the indirect evaporative cooler schematic.

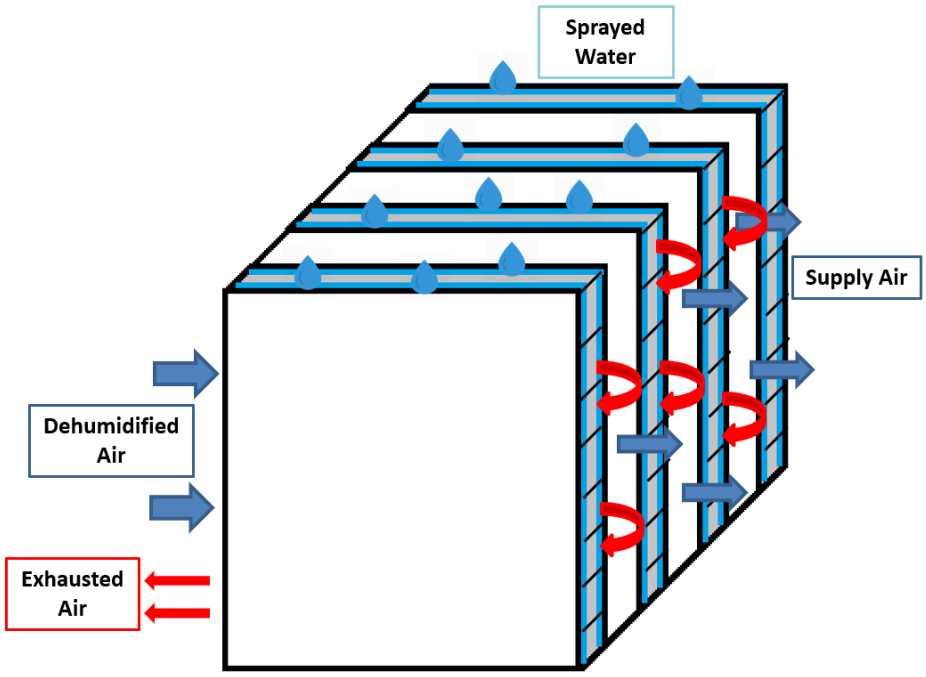

Figure 35. Indirect evaporative cooler schematic.

Supply air stream and cooling air stream energy and mass balance equations are presented in Equation 81 to Equation 90.

Supply air:

$$(\dot{m}\omega)_{sa,e} - (\dot{m}\omega)_{sa,i} = 0 \qquad \text{Equation 81}$$

$$\left(\dot{m}C_pT\right)_{sa,e} - \left(\dot{m}C_pT\right)_{sa,i} = -q_{sa}dA$$ Equation 82

$$q_{sa} = h_{sa}(T_{sa} - T_p)$$ Equation 83

Exhaust air:

$$(\dot{m}\omega)_{ea,e} - (\dot{m}\omega)_{ea,i} = J_e dA$$ Equation 84

$$J_e = h_{me}(\omega_w - \omega_e)$$ Equation 85

$$\left(\dot{m}C_pT\right)_{ea,e} - \left(\dot{m}C_pT\right)_{ea,i} = -q_{ea}dA$$ Equation 86

$$q_{ea} = q_{lat} - q_{plate}$$ Equation 87

$$q_{lat} = J_e h_{fg}$$ Equation 88

$$q_{plate} = \frac{T_p - T_w}{\left(\frac{\delta}{k}\right)_p + \left(\frac{\delta}{k}\right)_w}$$ Equation 89

$$q_{ea} = h_{ea}(T_{ea} - T_w)$$ Equation 90

4.1.3 Regenerator modeling

Absorption process weakens the desiccant solution and reduce its ability to absorb water vapor. To desorb water vapor from LiCl, the desiccant is heated to have equilibrium water vapor pressure that is higher than that of the air. This regeneration process is the reverse of dehumidification and can use low grade heat sources. In this study, the SOFC system exhaust heat is used in this regeneration process to increase the concentration of LiCl in solution. Then, the concentrated liquid desiccant solution is stored. When moisture must be removed, the high concentration solution is used to dehumidify the outside air. Figure 36 shows the regenerator schematic.

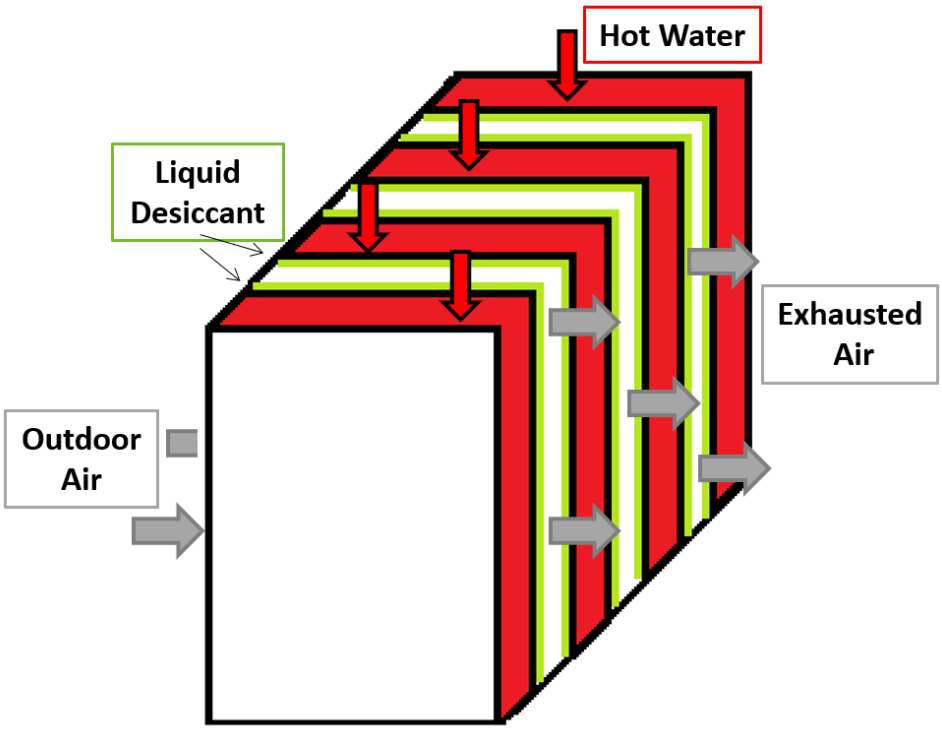

Figure 36. Regenerator unit schematic.

Supply air:

$$(\dot{m}\omega)_{sa,e} - (\dot{m}\omega)_{sa,i} = -J_{sa}dA \qquad \text{Equation 91}$$

$$J_{sa} = \frac{P_a - P_{sol}}{R_w T_a \left(\frac{1}{h_{ma}} + \frac{\delta_{mem}}{D_{mem}}\right)}$$ Equation 92

$$\left(\dot{m} C_p T\right)_{sa,e} - \left(\dot{m} C_p T\right)_{sa,i} = q_{sa} dA$$ Equation 93

$$q_{sa} = \frac{T_{LD} - T_{sa}}{\left(\frac{1}{hsa}\right) + \left(\frac{\delta}{k}\right)_{mem} + \left(\frac{\delta}{2k}\right)_{sol}}$$ Equation 94

Liquid desiccant:

$$(\dot{m})_{LD,e} - (\dot{m})_{LD,i} = J_{sa} dA$$ Equation 95

$$(\dot{m} C)_{LD,e} - (\dot{m} C)_{LD,i} = 0$$ Equation 96

$$\left(\dot{m} C_p T\right)_{LD,e} - \left(\dot{m} C_p T\right)_{LD,i} = q_{LD} dA$$ Equation 97

$$q_{LD} = q_{lat_{sa}} - q_{sa} - q_{plate}$$ Equation 98

$$q_{lat_{sa}} = L_{sa}(h_{fg} + h_{mix})$$ Equation 99

$$q_{plate} = \frac{T_{LD} - T_w}{\left(\frac{\delta}{2k}\right)_w + \left(\frac{\delta}{k}\right)_p + \left(\frac{\delta}{2k}\right)_{sol}}$$ Equation 100

Exhaust air:

$$\left(\dot{m}C_pT\right)_{w,e} - \left(\dot{m}C_pT\right)_{w,i} = q_w dA \qquad \text{Equation 101}$$

$$q_w = q_{plate} \qquad \text{Equation 102}$$

4.2 Control strategy for the liquid desiccant system

The dehumidifier's model inlet parameters are the weather conditions, the return air condition, desiccant temperature and concentration, and cold water temperature and flow. The model output is supply air temperature, desiccant outlet temperature and exhaust air temperature. In order to keep the humidity of the air cooling the servers below the allowable limits, the air humidity in the dehumidifier is controlled by manipulating the percentage of return air. In this model, the desiccant outlet concentration is also controlled by the desiccant flow rate.

In the regenerator system the inputs of the model are weather condition, desiccant inlet temperature and concentration, and hot water temperature and flow. The outlets are air (exhaust air) temperature, desiccant temperature, and hot water temperature. To use the desiccant for dehumidification purposes, it is required to regenerate it to a certain concentration. In this model the manipulating parameter to control the desiccant concentration is the desiccant flow rate.

4.3 Liquid desiccant system model verification

The validity of the model can be assessed by comparing its predicted supply conditions to the measured supply conditions. These comparisons are done for each stage independently: the first-stage dehumidifier and the second-stage Indirect Evaporative Cooler (IEC). Experimental data [140] from DEVap prototype testing is used to verify the dehumidifier and indirect evaporative cooler in the next two section, respectively.

4.3.1 Dehumidifier verification

5 different cases from [140] have been used to verify the dehumidifier model. Table 6 shows the input conditions used in all the cased to as well as experimental outcome and model output for supply air temperature and relative humidity. Figure 37 compares the model predictions (x-axis) and the experiments (y-axis) of the relative temperature of the first-stage supply-side air. The ±10% lines in Figure 37 show that the model and the experiments match within 10%.

Table 6. Dehumidifier unit verification input and output parameter.

Input Data											**Experiment Output**		**Model Output**	
	P_{atm} (kPa)	**$\dot{m}_{sa}$ (kg/s)**	**$\dot{m}_{ea}$ (kg/s)**	**$\dot{V}_{LD}$ (LPM)**	**C_{LD}**	**T_{LD}** (℃)	**T_{sa}** (℃)	**T_{ea}** (℃)	**RH_{sa}** (g/kg)	**RH_{ea}** (g/kg)	**T_{sa}** (℃)	**RH_{sa} (g/kg)**	**T_{sa}** (℃)	**RH_{sa}** (g/kg)
1	82.8	0.154	0.615	0.337	0.373	27.4	26.7	35	53.26	41.31	27.2	35.45	27.85	34.15
2	82.7	0.154	0.0308	0.337	0.376	28.3	26.7	35	53.30	42.31	28.2	35.07	28.61	34.3
3	81.7	0.154	0.0616	0.299	0.424	35.2	35	35	42.16	42.31	32.6	26.74	35.5	27.4
4	82.9	0.154	0.0615	0.360	0.379	28.7	26.7	26.7	52.08	67.96	26.3	34.32	28.14	34.77
5	100	0.152	0.061	0.337	0.38	32.9	26.7	28	50.1	45.02	29.1	29.1	28.4	29.58

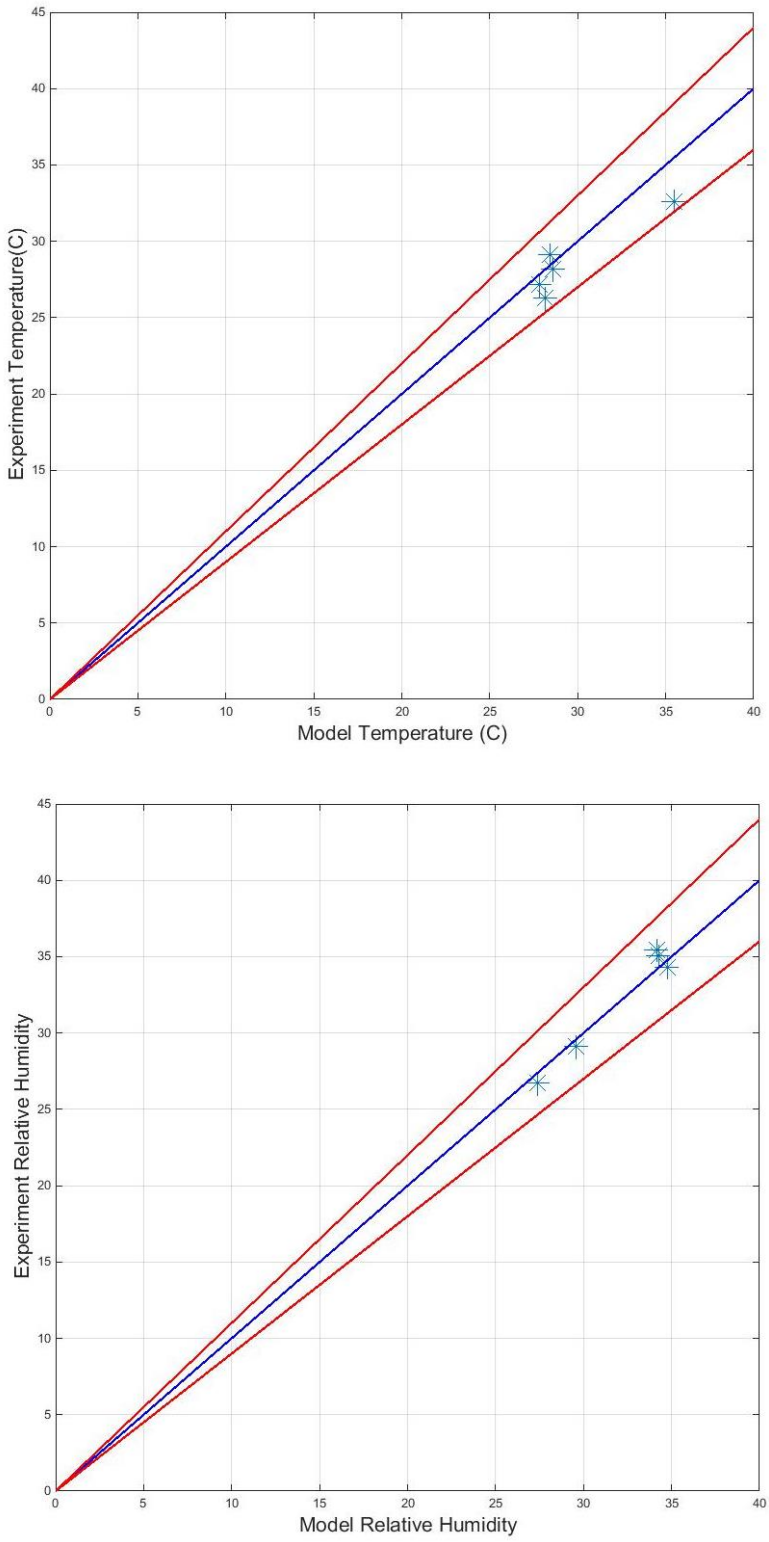

Figure 37. Model-experiment comparison of dehumidifier. (top) Change in supply-side air, temperature (bottom) change in relative humidity.

4.3.2 Indirect evaporative cooler verification

For indirect evaporative cooler, 5 different cases from [140] have been used to verify the model. Table 7 shows the input conditions as well as experimental outcome and model output for supply air temperature and relative humidity. Figure 38 compares the model predictions (x-axis) and the experiments (y-axis) of the relative temperature of the supply-side air. For the Indirect evaporative cooler, the measured supply-side temperature change predicted by the model matches the experiments within 10% except for test number 3. In case 3 the temperature difference is higher and has low mass flow which shows the weakness of bulk model to predict the result and the need for a discretized model.

Table 7. Indirect evaporative cooler verification input and output parameter.

	Input Data					**Experiment Output**			**Model Output**		
	P_{atm} (kPa)	$\dot{m}_{sa}$ (kg/s)	$\dot{m}_{ea}$ (kg/s)	T_{sa} (℃)	RH_{sa} (g/kg)	T_{sa} (℃)	RH_{sa} (g/kg)	T_{ea} (℃)	T_{sa} (℃)	RH_{sa} (g/kg)	T_{ea} (℃)
1	81	0.154	0.031	35	21.8	18	59.4	-	19.01	58.55	24.9
2	83.2	0.150	0.014	25	44.24	21.01	56.33	-	20.11	58.96	21.84
3	81	0.062	0.018	35	21.79	14.1	76.21	-	12.61	84.03	27.37
4	81.1	0.154	0.046	35	35.78	19.3	89.97	-	22.6	74.07	24.93
5	81	0.108	0.032	35	21.56	14.2	74.99	-	14.8	74.04	24.75

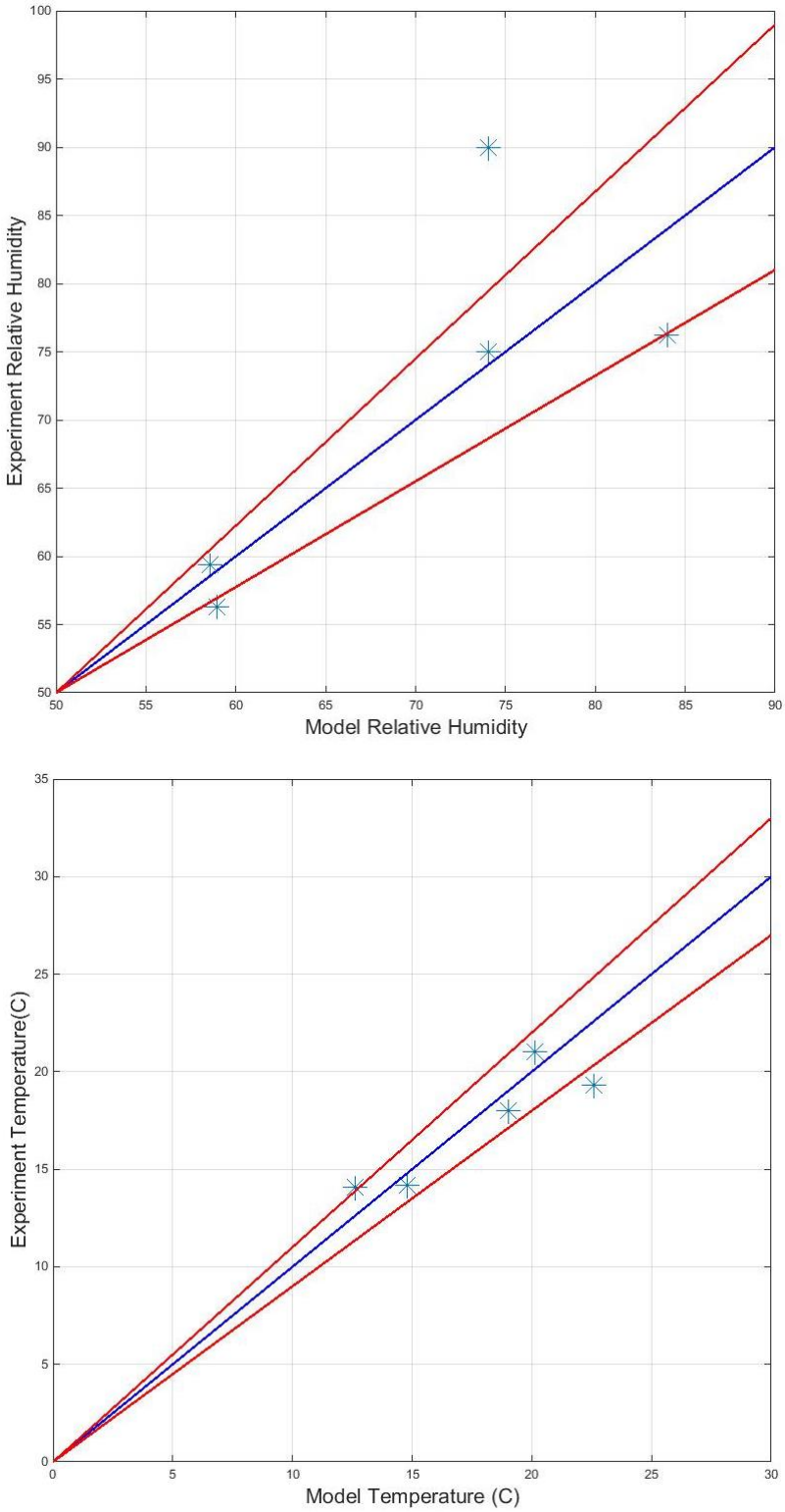

Figure 38. Model-experiment comparison of indirect evaporative cooler. (top) Change in supply-side air, temperature (bottom) change in relative humidity.

4.4 Summary

In this chapter, a physical model has been developed to simulate the DEVap components including liquid desiccant dehumidifier, regenerator, and indirect evaporative cooler. In addition, the control strategy for each component has been explained. The developed models have been also verified and compared to the experimental data from literatures.

5 Data Center Cooling Demand Model

Modern data centers try to use adiabatic cooling whenever the weather condition allows. However, adiabatic cooling is not possible in all locations at all times. Different types of common data center cooling systems were presented in chapter 2. This chapter presents the method for calculating the cooling demand of data center at various locations. Also, the cooling demand for seven different data center locations that are used as case studies of this research are analyzed.

In order to calculate the amount of cooling required for data center a MATLAB data center model has been developed which calculates the amount of cooling required by a data center. The inputs of the model are weather data associated with data center locations including temperature, pressure, and relative humidity. The weather data are obtained on an hourly basis from Typical Meteorological Year (TMY) data from 2006 to 2016. The model takes this data and contains multiple functions that have been developed for calculating thermodynamic parameters such as saturated temperature, wet bulb, and dew point temperatures based upon the knowns weather data.

In order to calculate the load, the acceptable operating conditions for servers within a data center are required. ASHRAE is the association that updates and releases an industry standard for data center operations every couple of years, based upon industry technology improvements. Table 8 shows the boundaries that define the ASHRAE recommended and allowable environmental envelope from the 2016 standard [17].

Table 8. ASHRAE 2016 Thermal Guidelines [17].

	Recommended Envelope	**Allowable Envelope**
Max Dry Bulb	27℃	32℃
Dew Point	5.5 − 15℃	5.5 − 18℃
Relative Humidity	60%	80%

Based on outside weather data, cooling zones for data center is defined in 4 regions based upon ASHRAE recommendations [141,142] as presented in Table 9. The model calculates the

number of hours that the system needs mechanical cooling for each of the locations using the weather data.

Table 9. Zone Boundaries for Recommended Environmental Envelope for IT Equipment.

	Zone 1	**Zone 2**	**Zone 3**	**Zone 4**
Cooling Strategy	Economizer	Economizer+ Evap. Cooling	Evap. Cooling	Mechanical Cooling
Low end Temperature	NA	NA	If DP< 5.5°C DP Then 10.8°C WB (51.4°F)and 18°C DP (64.4°F) Else 32°C	18.7°C WB
High end Temperature	32°C WB	10.8°C WB	18.7°C WB (65.6°F)	NA
Low end Moisture	5.5°C DP	NA	Na	18°C DP
High end Moisture	18°C DP	5.5°C DP	If DB < 32°C DB Then DB < 5.5°C DP Else 18°C DP	NA

5.1 Data Center modeling

In order to calculate the power consumption of the data center first the IT equipment's power consumption is calculated by the model presented by [143]. For a homogeneous server cluster:

$$U = 1/N \sum_{i=1}^{N} u_i \qquad \text{Equation 103}$$

Where U is utilization, N number of servers, u_i each server utilization. The server utilization can be given to the model either as a constant number or utilization profile if available. Servers use half of the rated power in idle model and linearly increase with utilization [143], server power consumption is calculated by:

$$P_i = P_i^{idle} + \left(p_i^{peak} - P_i^{idle}\right).u_i \qquad \text{Equation 104}$$

The total power consumption is:

$$P = \sum_{i=1}^{N} p_i$$ Equation 105

It is not practical to measure the actual power consumption of each server rack continuously. As a result, the impact of task consolidation (L) for the running servers is modelled as:

L=0: perfect consolidation, meaning that workload is packed onto the minimum number of running servers.

L=1: workload is distributed uniformly so $U = u_i$

$$u_i = \frac{U}{L(1-U)+U}$$ Equation 106

The main components of power loss are the UPS and the Power Distribution Unit (PDU) which can be calculated as follows:

$$P_{PDU} = P_{PDU}^{idle} + \lambda_{PDY}\left(\sum_{i=1}^{N} p_i\right)^2$$ Equation 107

$$P_{UPS} = P_{UPS}^{idle} + \lambda_{UPS}\sum_{PDUs} P_{PDU}$$ Equation 108

Where λ_{PDY} and λ_{PDY} are the loss coefficients for UPS and PDU systems, respectively. In power supply equipment of a data center the power loss can be up to 15% of the total power consumption at peak [143]. The air flow needed for server cooling is calculated based on the following equation:

$$F_{air} = \frac{DC_{size} \times Util}{C_{p_{air}} \times \Delta T \times \eta_{heat}}$$ Equation 109

DC_{size} represents the capacity of data center, $Util$ is utilization factor for data center, $C_{P_{air}}$ is the air specific heat, ΔT is the temperature difference for the air inlet and outlet from the server, and η_{heat} is the efficiency of heat removal.

Data center total power demand is defined in the following equation. Miscellaneous power is around 4% of data center designed capacity.

$$P_{tot} = P_{cooling} + P_{server} + P_{PDU} + P_{UPS} + P_{fans} + P_{miscellaneous} \quad \text{Equation 110}$$

In cooling zone 4, cooling power can be calculated either for a water-cooled chiller or an air-cooled chiller. For air cooled chiller, the chiller presented at [144] is used as the reference chiller for calculating the chiller's power demand. Table 10 shows the effect of dry bulb temperature on the chiller efficiency.

Table 10. effect of dry bulb temperature on air cooled chillers efficiency.

DB [°F]	75	85	95	105
Efficiency [kW/Ton]	0.952	1.069	1.208	1.384

For the water cooled chiller, the chiller presented in [145] is used as the reference chiller for calculating the chiller's power demand. The effect of wet bulb temperature on the chiller efficiency is shown on the Table 11 below [146].

Table 11. effect of dry bulb temperature on water cooled chillers efficiency.

WB [°F]	60	65	70	75
Efficiency [kW/Ton]	0.502	0.518	0.574	0.592

5.2 Data Center cooling demand results

In order to calculate the number of hours that the data centers in each location need mechanical cooling, TMY data for seven locations in the United States that are home to Microsoft data centers have been used as the input for the code. The number of hours of each cooling type that is required in each location based on both allowable and recommended

envelope is shown in Figure 39. As expected, by expanding the range of temperature and humidity, the number of hours that mechanical cooling is required decreases. For data centers located in California, Seattle, and Wyoming a mechanical cooling system is barely required, while economizer and evaporative cooling will be sufficient throughout the year to keep the servers in acceptable range. However, Illinois, Iowa, Virginia and Texas require between 1000hr to 4500hr of mechanical cooling based on the location and ASHRAE requirements.

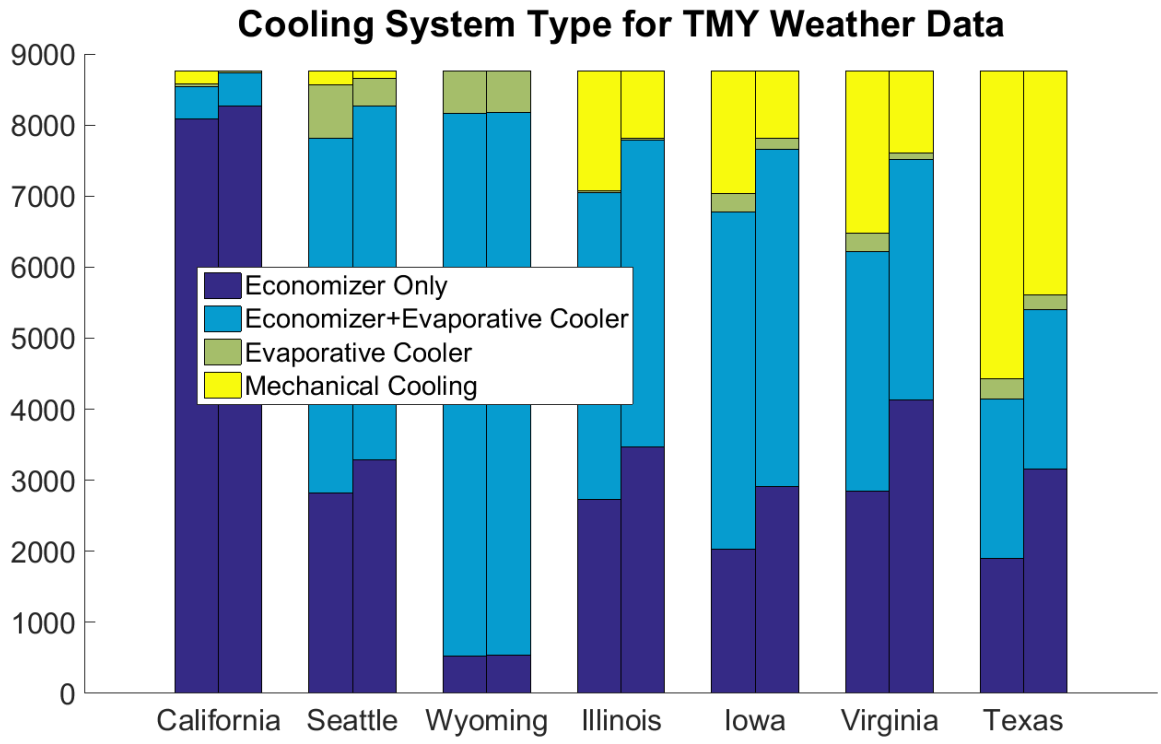

Figure 39. Cooling system type for 7 locations based on ASHRAE recommended (left bar) & allowable (right bar) range.

Server load profiles tend to be confidential information that are rarely published. However, the profile is roughly constant and utilization changes between 60% to 80%. For the current work and data center simulation results, either NREL published server load profiles as shown in Figure 40 [141] are used by scaling it to the size of the targeted data center, or it is assumed that the utilization is constant at 70% throughout the entire operating period.

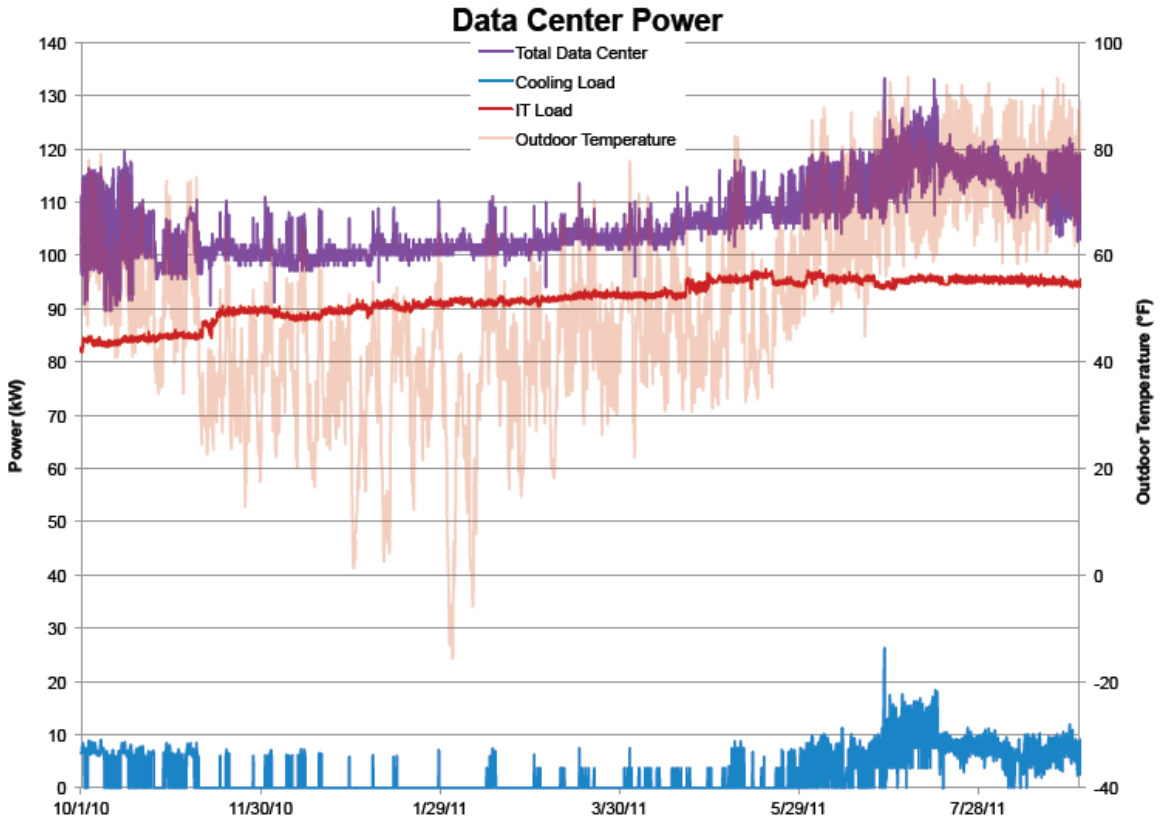

Figure 40. Load profile for the RSF data center over the first 11 months of operations Illustration by Chad Lobato, NREL[141].

The following data center simulation results for each location are based upon the assumption of a 50MW designed data center that follows the load demand of [141]. The designed temperature difference of air entering and leaving the servers is 15°C. The number of cooling hours and cooling device correspondent to that is based on ASHRAE recommended envelope. The mechanical cooling system in these results is assumed air cooled chiller. Figure 41 to Figure 44 show the results for California and Texas which are the two ends of the spectrum with California being the location with the lowest overall energy use and Texas the highest.

Figure 41 shows the TMY (average data from 2006 to 2016) dry bulb and wet bult temperature for California and Texas which are the parameters that determine what type of cooling is required for the data center. California and Texas average dry bulb temperature are 14°C and 20.2°C and wet bulb temperature are 11.6°C and 15°C, respectively. California

has the least variation in temperature throughout the year while Texas temperature changes more than 40°C during the year which has a significant impact on change in the cooling required for Texas.

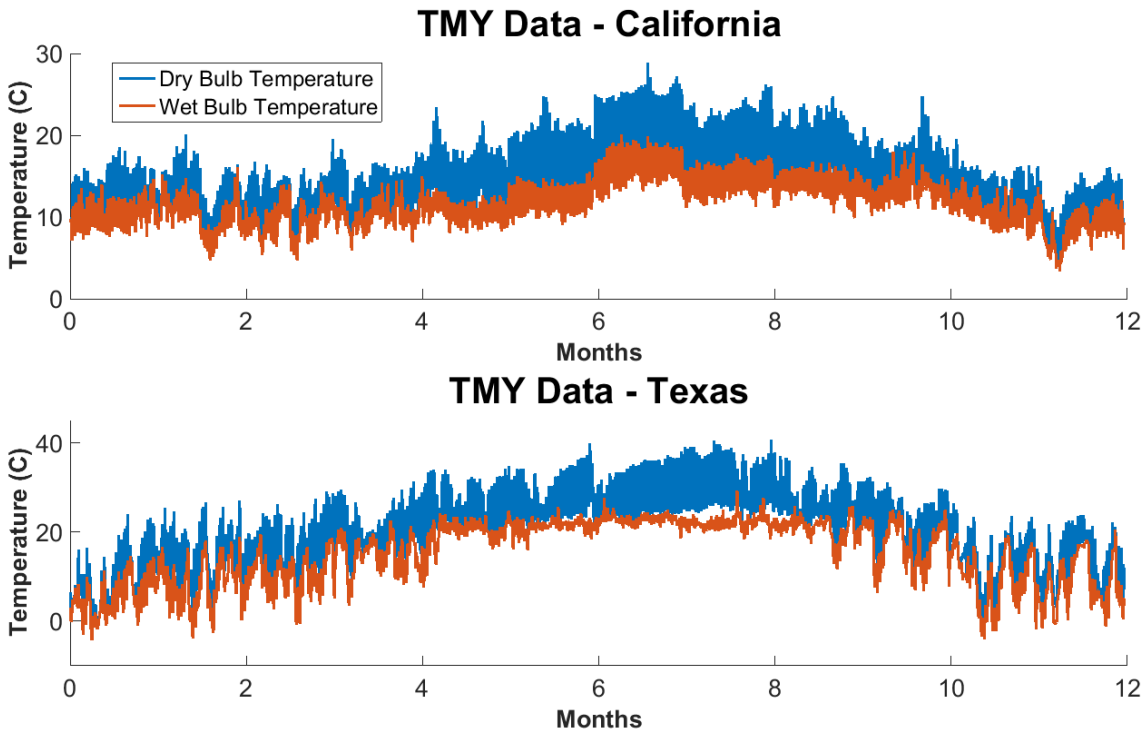

Figure 41. TMY data for California and Texas throughout the year.

Figure 42 and Figure 43 show the power demand breakdown and percentage of each category for California and Texas, respectively. As expected, for Texas half of the year mechanical cooling is required to keep the servers in the range, however for California the number of hour that mechanical cooling is required 186hr. As a result, 9% of power consumed by data centers is dedicated to mechanical cooling device for this scenario in Texas, while for California the number is 1%.

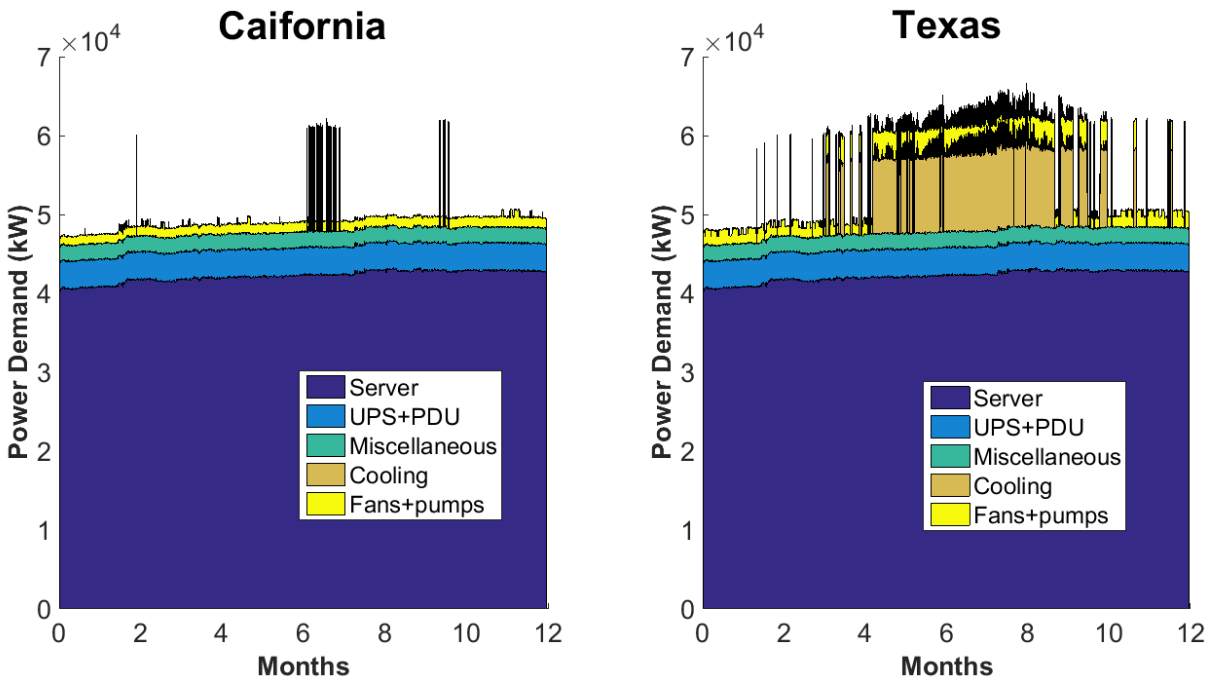

Figure 42. Data Center power demand breakdown throughout a year for California and Texas.

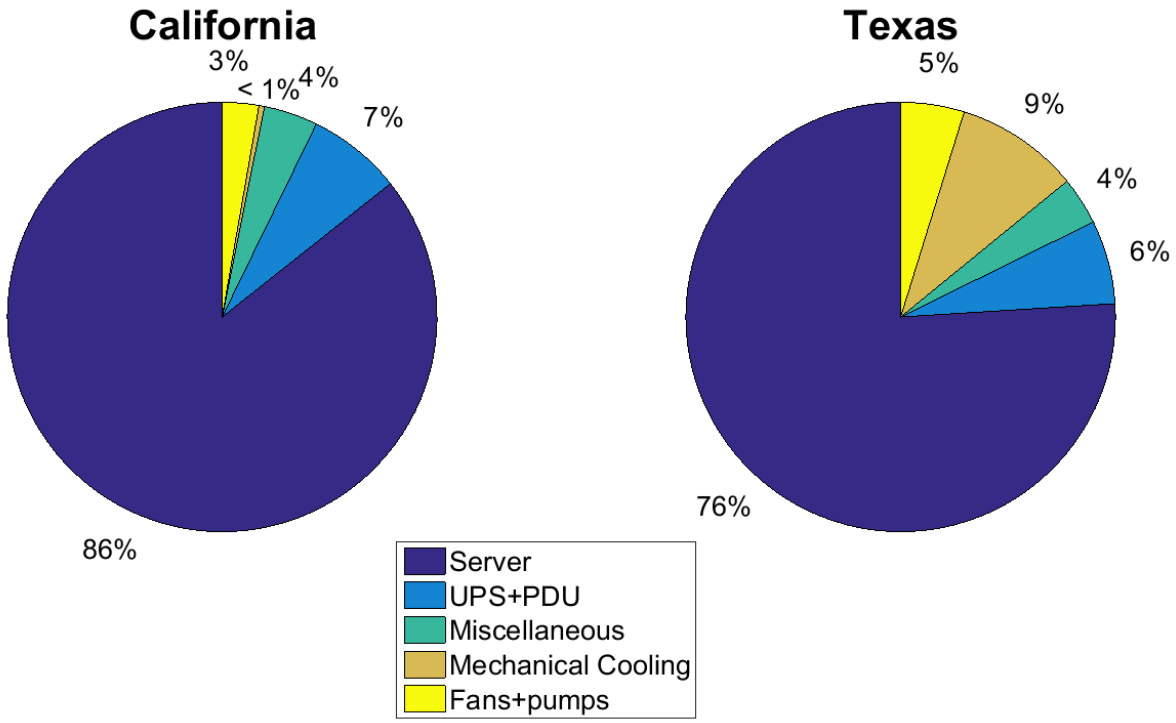

Figure 43. Data Center power demand percentage for California and Texas.

PUE is the ratio of total energy used by facility to energy used by the serves. This parameter shows how effectively a data center uses energy. As the number gets closer to 1 it means that the facility becomes very efficient, with most of the energy being directly converted in the servers for the computational demands of the data center. The following two graphs shows the PUE for the entire year. The spikes that bring PUE up to the 1.4- 1.5 range are because of energy being consumed by mechanical coolers. The average PUE for California and Texas for the whole year as simulated with the current model are 1.16 and 1.32, respectively.

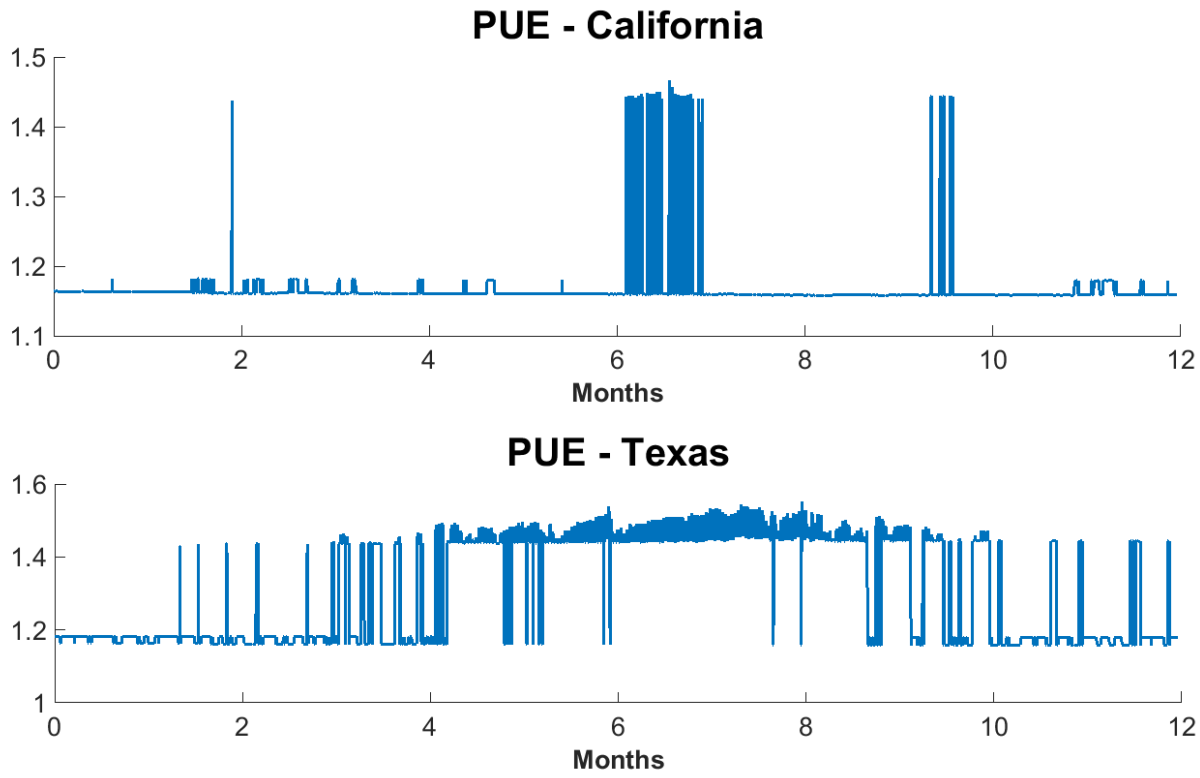

Figure 44. PUE for California and Texas for the entire year.

The results for the TMY data, Power usage breakdown, percentage of energy usage, and PUE for the other 5 locations are presented in APPENDIX A.

Figure 45 shows energy use for each location for a 50MW designed data center following Figure 40 load demand. The air temperature difference is 15°C and ASHRAE 2016 standards is followed for temperature and humidity limits. Table 12 shows the average PUE for all the locations with California having the lowest PUE at 1.167 and Texas the highest at 1.315.

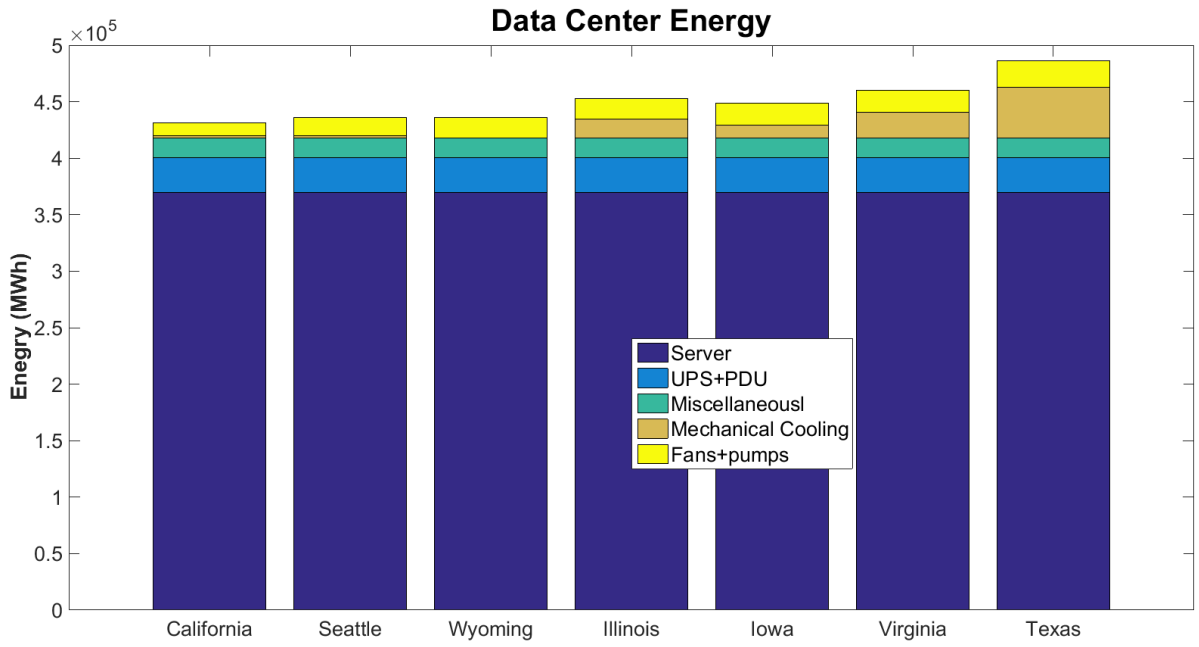

Figure 45. Data center energy usage for a 50MW data center.

Table 12. Average PUE for 7 data center target location.

Location	California	Seattle	Wyoming	Illinois	Iowa	Virginia	Texas
PUE	1.167	1.18	1.179	1.225	1.23	1.244	1.315

The type of cooling system, designed temperature difference, and changing allowable range has a significant effect on the amount of energy that data center consumes. For example, as the technology is rising IT manufacturers are pushing the boundaries on safe temperature that IT equipment's can tolerate. Figure 46 and Table 13 show the energy used and percentage consumed by different part of data center for various combinations. Water cooled system use less energy than air cooled system. Increasing the temperature difference for the air entering and leaving the server room means less flow of air is required, which leads to less energy required for cooling the air. As the IT technology progresses, the IT equipment can tolerate higher temperature which leads to higher range of acceptable temperature and humidity. This means wider range of outside temperature is acceptable for cooling the server, leading to lower energy usage.

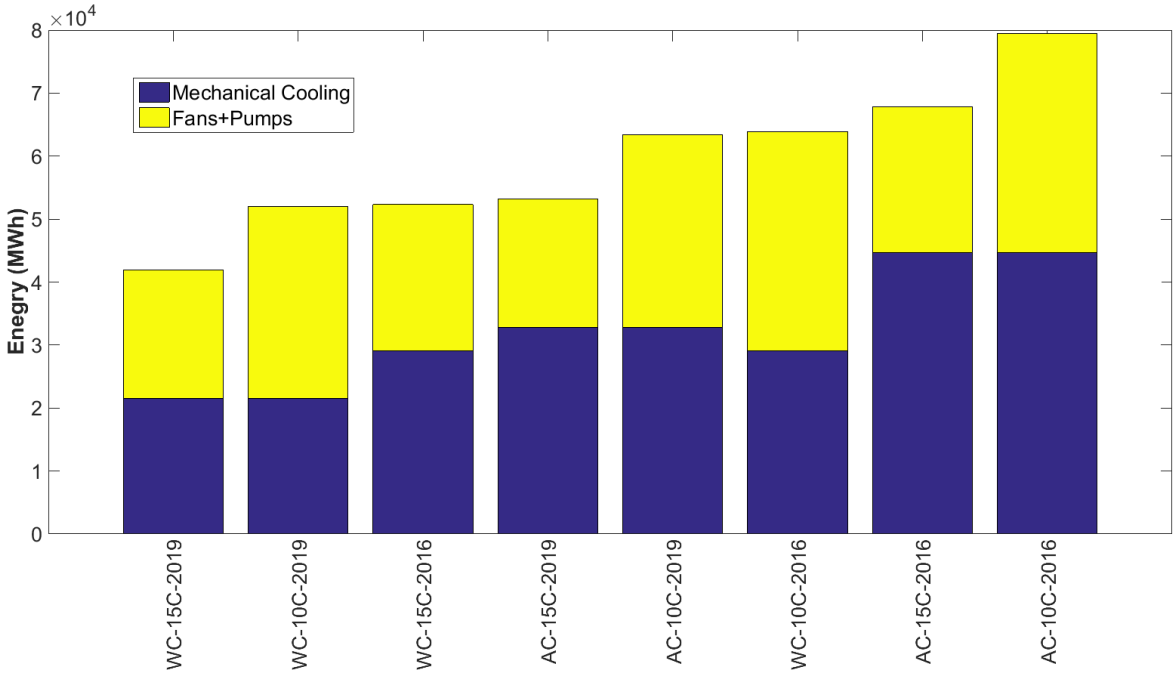

Figure 46. Energy consumed by different part of data center for various combinations.

Table 13. percentage of energy consumed by different part of data center for various combinations.

PUE	1.244	1.271	1.272	1.274	1.302	1.303	1.314	1.345
Energy (*e8 MWh)	4.6	4.699	4.70	4.71	4.81	4.82	4.86	4.97
Fan+Pump (%)	4	6	5	4	6	7	5	7
Mechanical Cooling (%)	5	5	6	7	7	6	9	9
Server (%)	80	79	79	78	77	77	76	74

5.3 Summary

In this chapter, a data center cooling model has been developed to calculate the amount of cooling required by a data center. The model takes the weather data for each location and acceptable range of temperature and humidity for data center to calculate the load. In addition, the cooling demand for California, Seattle, Wyoming, Illinois, Iowa, Virginia, and Texas have been calculated and analyzes. Texas had the highest cooling demand with a PUE of 1.315 and California had the lowest with a PUE of 1.167. Energy usage of data center based

on different types of cooling device (water cooled, air cooled) and at different designed temperature difference has been compared. Results showed that higher temperature difference and water-cooled system lead to less energy consumed by the cooling system.

6 Integrated System Analysis

6.1 Integrated system design

In this section, the possibility of using a highly efficient, zero emission SOFC system to produce electricity and cooling in various amounts to meet electricity and cooling demands of a data center is investigated. In this configuration each fuel cell powers one server rack and heat from each individual SOFC system in used in a small-scale LDD to produce cooling for one server. Figure 47 shows the integrated system configuration for rack level power and cooling.

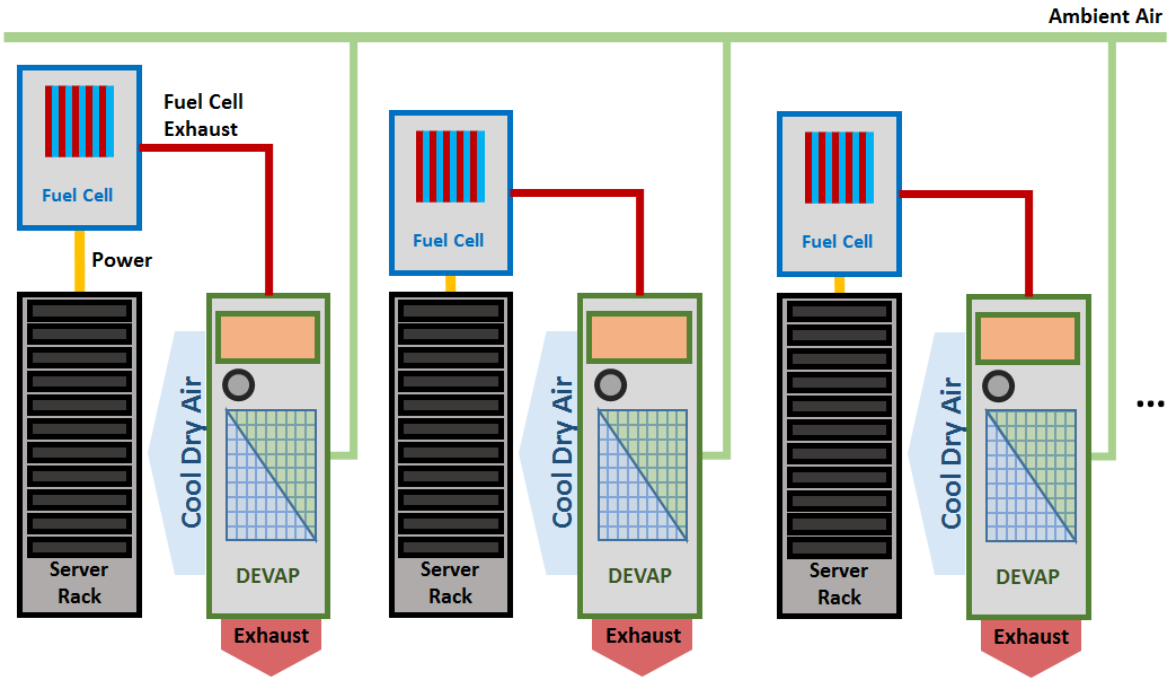

Figure 47. System configuration for server rack level power and cooling.

Server rack average power density can start as low as 6kW and go to above 20kW per rack. For this analysis, each server rack power is considered nominally 12kW. We assume that a fuel cell equivalent to eight 1.5kW BlueGEN SOFC systems is used to meet the server electrical demand (note that some above nominal power conditions can usually be provided by SOFC systems, e.g., to periodically achieve peak demands in the 20kW range). The exhaust

of the SOFC is used to regenerate LiCl liquid desiccant to provide 1400CFM cold and dehumidified air for each server rack.

6.2 Spontaneous integrated system performance

Figure 48 shows the integrated SOFC-LDD system. The SOFC exhaust gas produces hot water that will supply the heat demand for regenerating the liquid desiccant. The regeneration process occurs within a heat and mass exchanger where the vapor desorbs from the desiccant and is carried away by an air stream due to desiccant solution that has higher water vapor pressure than the air. The high concentration LiCl is stored in a tank. When air conditioning is required, the high concentration LiCl is used to dehumidify the air. As mentioned before the ASHRAE recommended suitable range of temperature and humidity for all environmental classes inside the data centers is 18˚C to 28˚C dry bulb temperature and 9˚C to15˚C dew point and 60% RH [17].

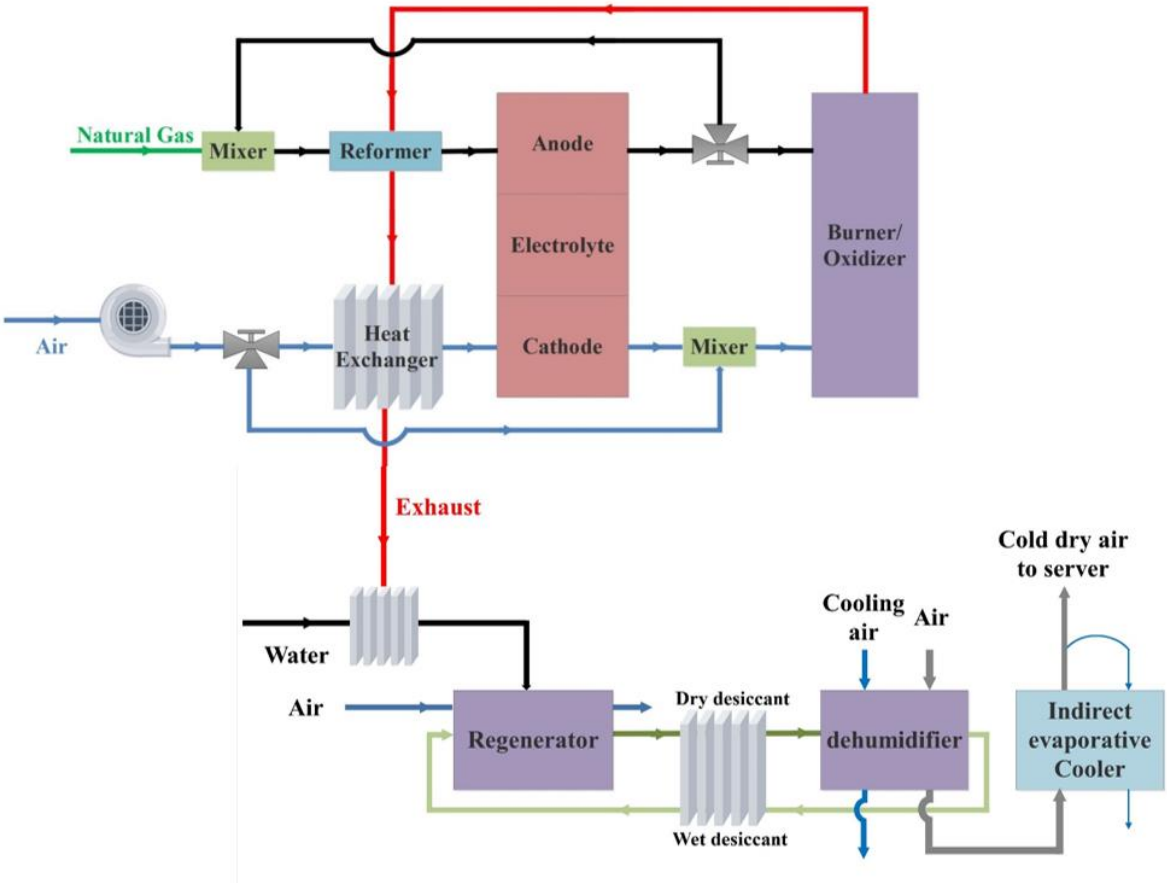

Figure 48. Integrated SOFC-LDD system model schematic.

For this section, the integrated system is tested for spontaneous load for three different weather conditions to analyze whether SOFC system exhaust-heat based cooling and dehumidification can maintain server operating temperatures and humidity in the safe range for different weather conditions. Table 14,

Table 15 and Table 16 show the inlet and outlet condition for each of the three scenarios. The weather conditions studied are warm and humid air (25˚C, 70% RH), hot and moderate humidity air (35˚C, 45% RH) and hot and dry air (40˚C, 20% RH).

Table 14. Inlet and outlet conditions of the regenerator stage.

$T_{air,in}$ (˚C)	$RH_{air,in}$	$\dot{m}_{air}$ (kg/s)	$T_{w,in}$ (˚C)	$T_{w,out}$ (˚C)	$\dot{m}_{w}$ (kg/s)	$T_{LiCl,out}$ (˚C)	$X_{LiCl,out}$
35	40%	0.02	60	35	0.055	48.5	34.5%
35	45%	0.035	60	55	0.055	46	35%

Table 15. Inlet and outlet conditions of the dehumidifier stage.

$T_{air,in}$ (˚C)	$RH_{air,in}$	$T_{LiCl,in}$ (˚C)	$X_{LiCl,in}$	$X_{LiCl,out}$	$\dot{m}_{LiCl}$ (kg/s)	$\dot{m}_{air}$ (kg/s)	$T_{air,out}$ (˚C)	$RH_{air,out}$
25	70%	35.2	34.5%	33%	0.25	0.045	30.5	33.9%
35	45%	35.2	35%	33%	0.25	0.06	34.9	31.2%
40	20%	-	-	-	-	-	40	20%

Table 16. Inlet and outlet conditions of the IEC stage.

$T_{air,in}$ (˚C)	$RH_{air,in}$	$T_{w,in}$ (˚C)	$T_{Cair,in}$ (˚C)	$\dot{m}_{Cair}$ (kg/s)	$T_{Sair,out}$ (˚C)	$w_{Sair,out}$ (kg/kg)	$DP_{Sair,out}$ (˚C)
30.5	33.9%	20	19.8	0.038	19.8	0.0093	12.5
34.9	31.2%	20	21	0.051	21	0.0109	15
40	20%	20	20		20	0.009	12.4

Figure 49 shows the model results of the first test on a psychrometric chart. The green line labeled 'LiCl – 35%' shows the humidity ratio of the air in equilibrium with the liquid desiccant at a mass fraction of 0.35 LiCl and at each of the temperatures considered. Line black shows the first stage dehumidification process for supply air and then the cooling air

process. The dehumidification process is internally cooled by evaporation of water to exhaust air to keep the desiccant cooler and increase its dehumidification potential. Then, the supply air is cooled by indirect evaporative cooling at constant humidity ratio. Horizontal black line shows the second stage process for supply air, which goes through indirect evaporative cooling at constant humidity ratio. Under these conditions the integrated system was able to produce cold and dehumified air that is in the safe range for server racks. In this case the return air from server is considered for first stage cooling air which has lower relative humidity and higher potential for evaporative cooling.

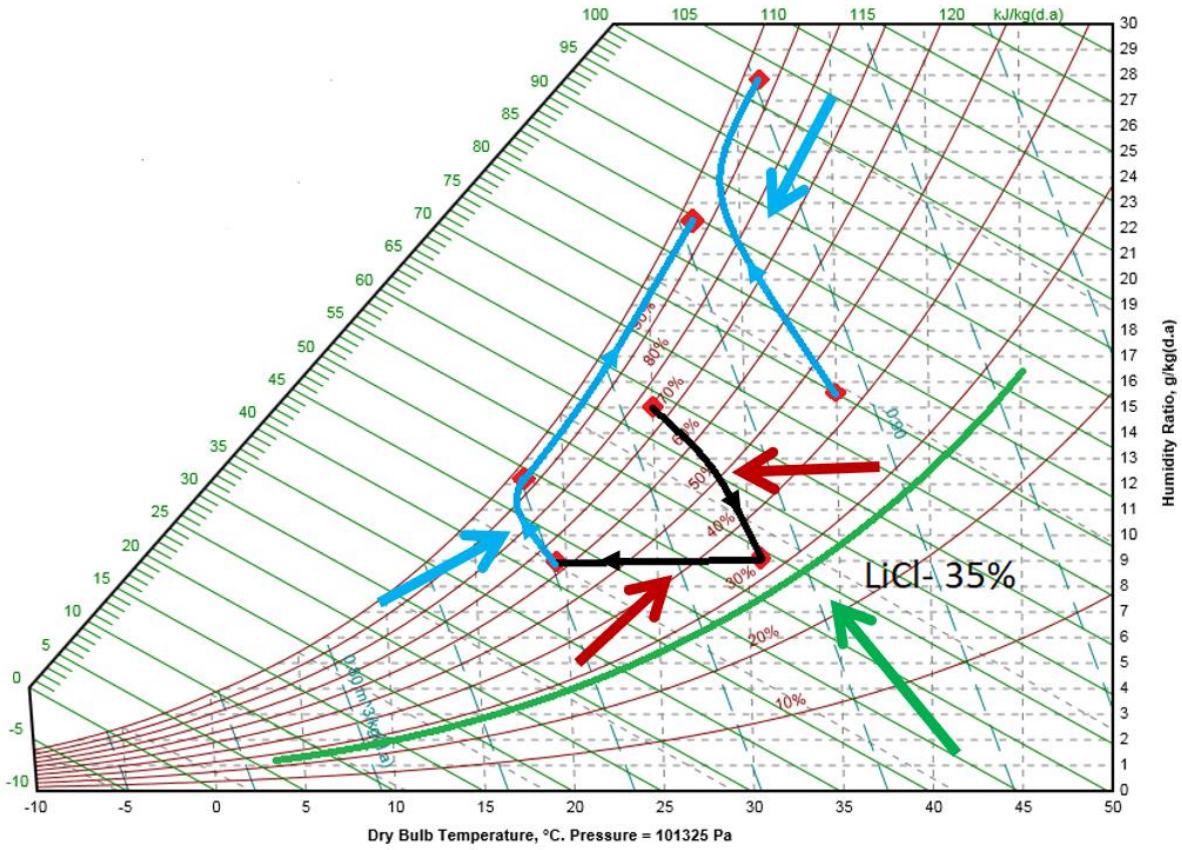

Figure 49. Airstream at 25˚C and 70% RH with simulated LDD processes on a psychrometric chart at 100kPa.

However, the system is able to provide only 97CFM of air flow under these conditions, which is less than the maximum air flow demand (almost 7%) for each server rack. This suggests that the current integrated SOFC-LDD system cannot continuously provide all the power and cooling required for the server rack if it is operated continuously at 12kW. However, both the server demand dynamics and day-night weather variations, could lead to dynamic

conditions that with some storage of the concentrated solution (at times when cooling and dehumidification are not needed) could be well-matched to the server demands for power and for cooling and dehumidification. Next step will consider these dynamics for several real-world weather (temperature and relative humidity) and server power.

For the second weather condition with 35˚C and 45%RH (Figure 50) the system can produce 96CFM cold and dry air for each server rack. In this case the outside air is considered for the first stage cooling air. Please note that the SOFC system is running based upon design operating conditions for the system. Further investigation is needed to evaluate the SOFC system available heat under different operating conditions that could produce higher quality exhaust heat (e.g., operation at lower fuel utilization) likely at the expense of electrical efficiency.

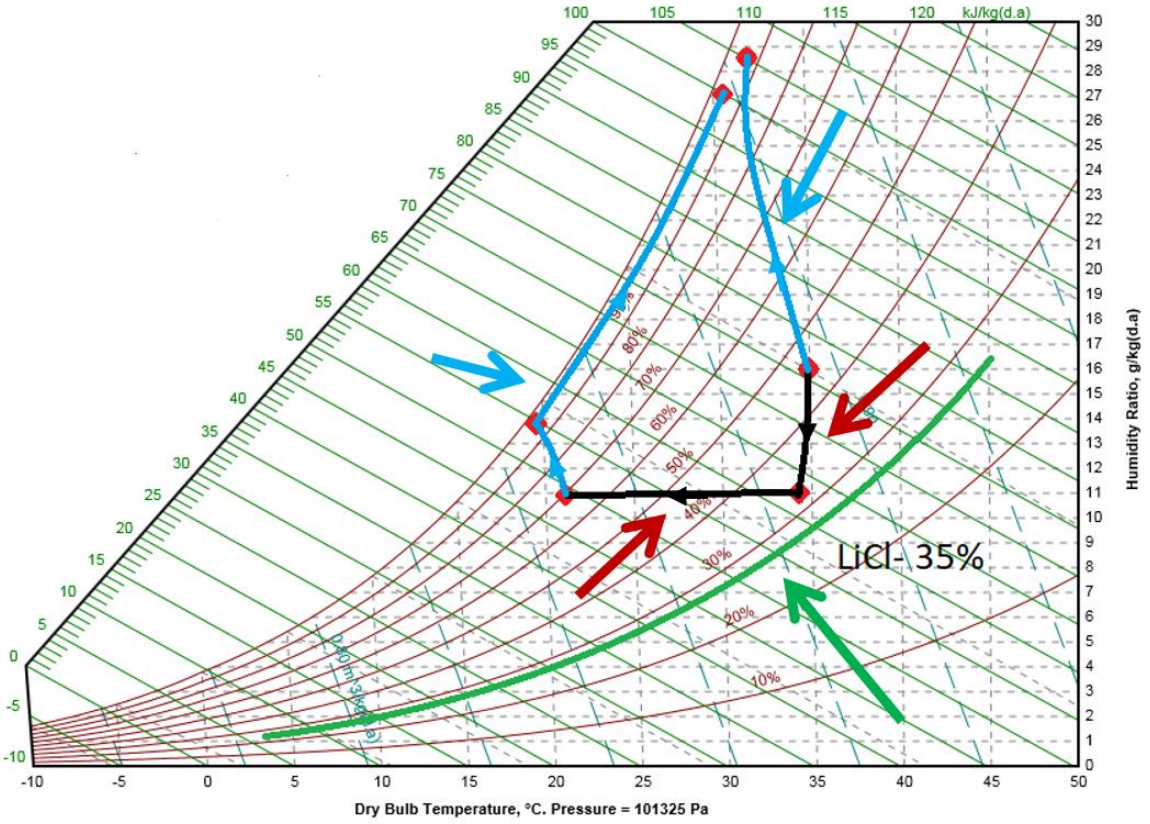

Figure 50. Airstream at 35˚C and 45%RH with simulated LDD processes on a psychrometric chart at 100kPa.

Figure 51 presents the results of hot and dry air (40˚C, 20% RH) conditions on a psychrometric chart. In this scenario dehumidification is not needed for the supply air entering the server rack. The incoming air only goes through the second stage and gets

cooled through indirect evaporation. The mass flow rate of air in this condition is independent of SOFC heat.

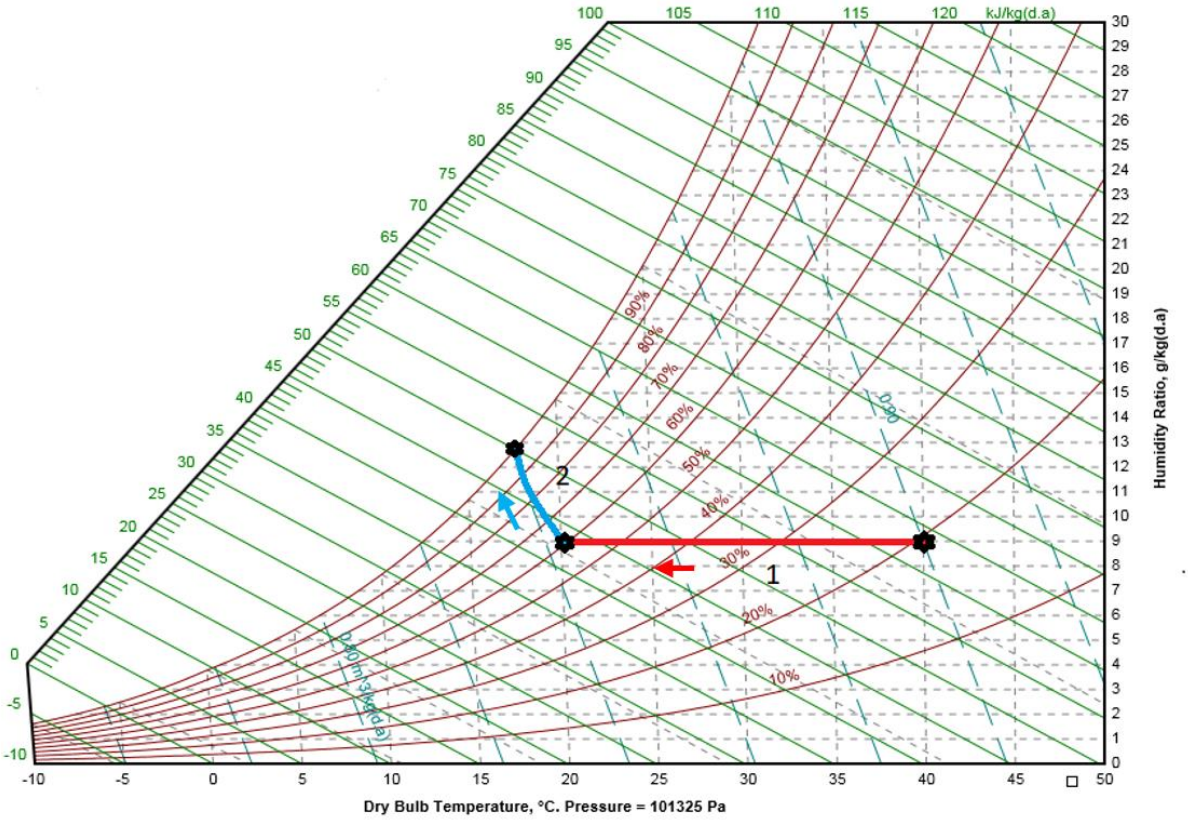

Figure 51. Airstream at 40˚C and 20% RH process on a psychrometric chart at 100kPa.

6.3 LiCl daily storage

Microsoft has 7 different locations in the States for data centers which is shown at Figure 52. The locations are in Washington, California, Texas, Wyoming, Iowa, Illinois, and Virginia. For this study, 24-hour weather data on July 20, 2018 is considered. Figure 53 shows the temperature variation during 24 hours on July 20th.

Figure 52. Microsoft data center location in the US.

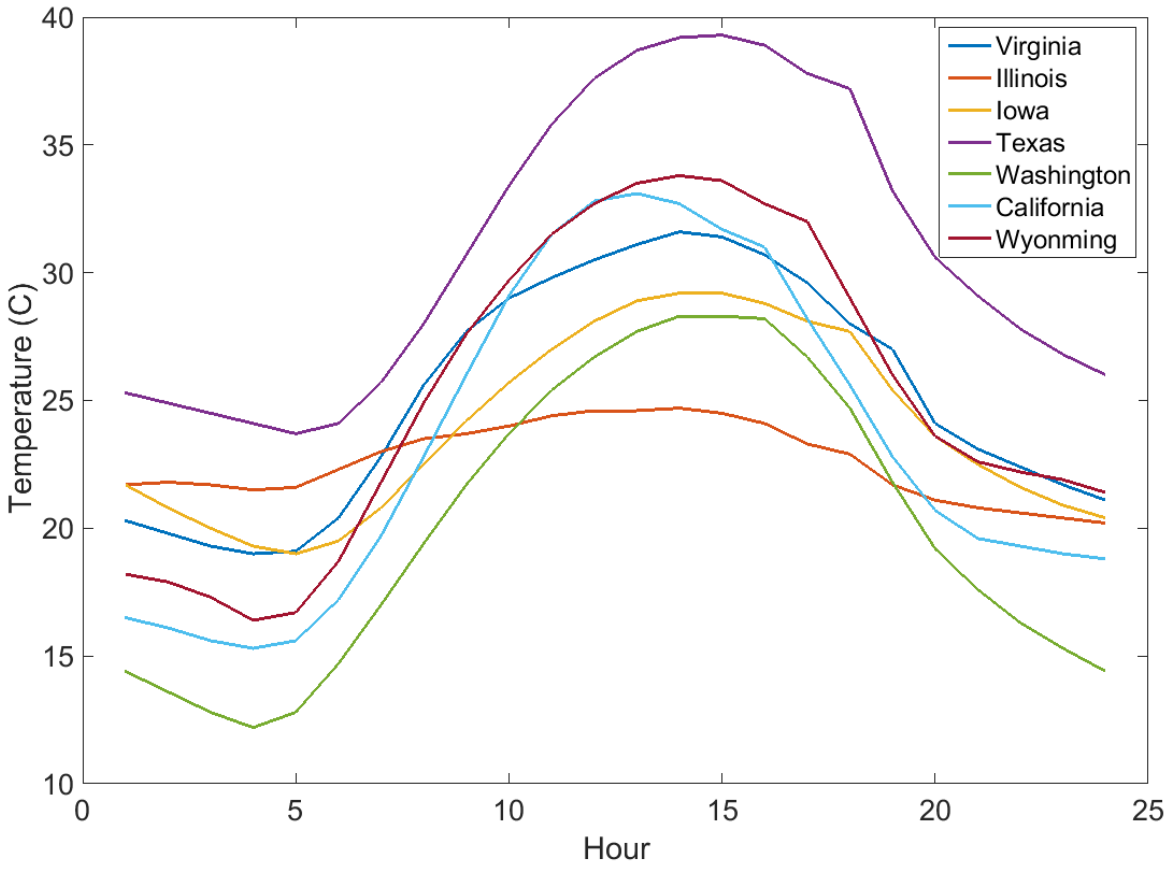

Figure 53. Temperature of 7 different location for 24 hours on July 20, 2018.

Figure 54 shows the dew point for each hour during one day for 7 different locations. In this part, only latent load is considered. As it is shown in Figure 54, Washington, California, and Wyoming dew point are below the higher limit for data centers (15°C) during the 24 hours which means that these three locations do not have any latent heat during this day. For the other 4 locations, Virginia, Illinois, Iowa, and Texas, the dew pint is almost always above the limit. Table 17 shows the average temperature, relative humidity, and Dew point for all locations. Illinois and Texas have the highest latent load for 24 hours.

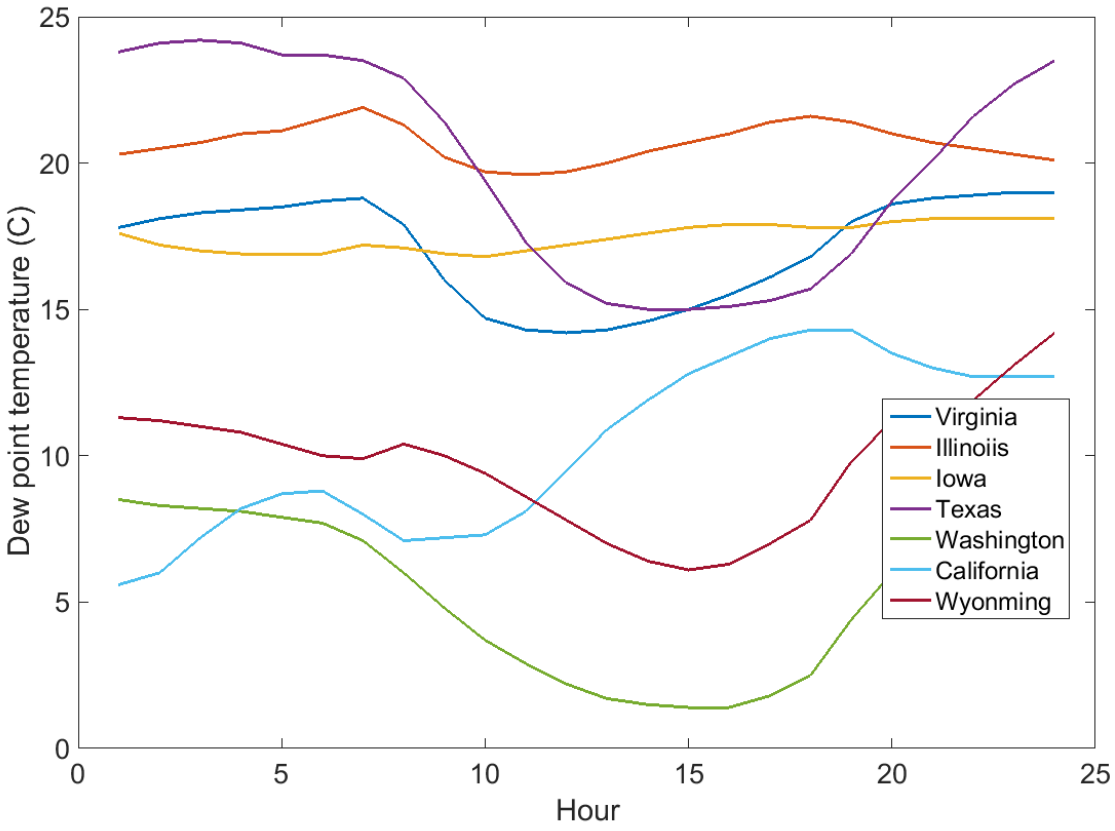

Figure 54. Dew point temperature of 7 different locations for 24 hours on July 20, 2018.

Figure 55 shows the schematic of the system for the case that the dehumidification is impendent from regeneration. The regenerator will produce strong desiccant spontaneously as the fuel cell is working all day 24 hours, then this strong LiCl will be stored and when the dehumidification is needed will be used.

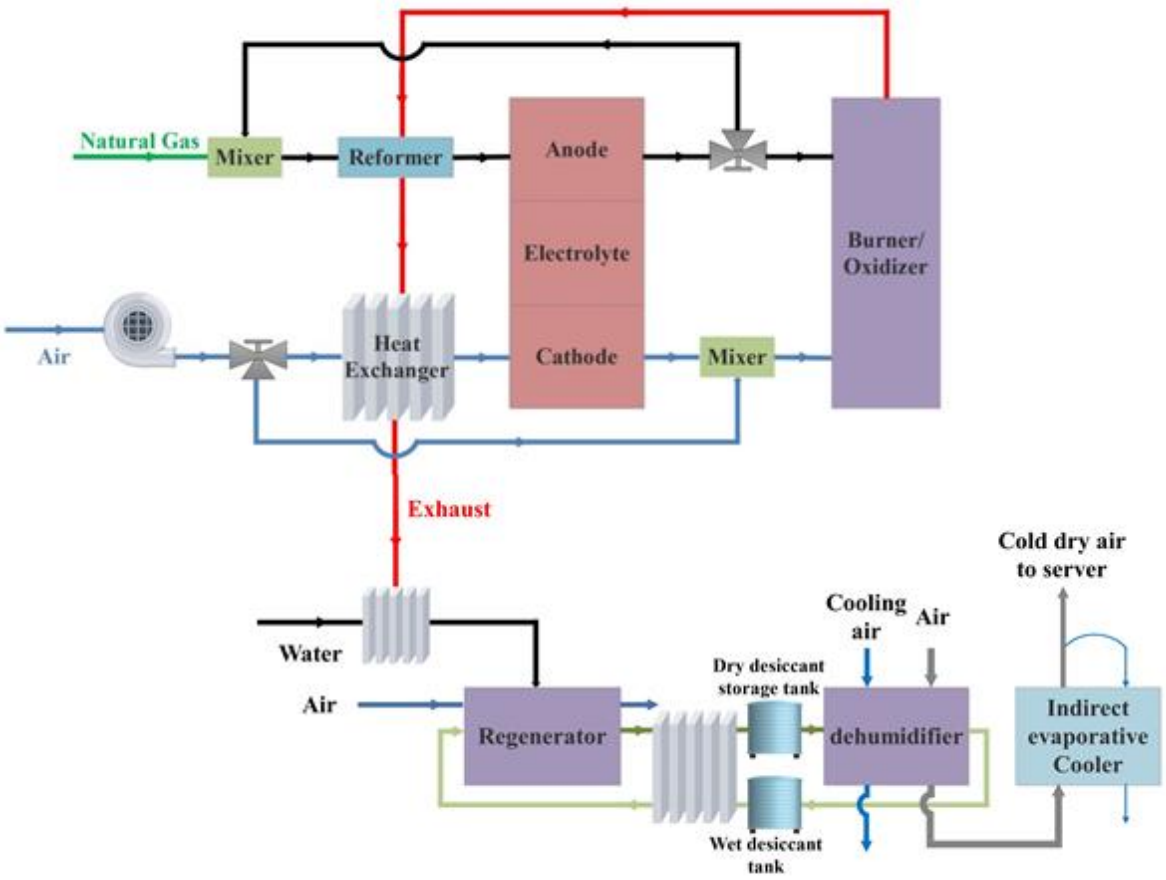

Figure 55. SOFC-LDD schematic for considering storage capacity.

Table 17. 24-hour average weather data on July 20, 2018.

Location	Temperature (°C)	Relative Humidity	Dew Point (°C)
Virginia	25.21	65.08	17.09
Illinois	22.61	89.43	20.69
Iowa	23.95	68.7	17.47
Texas	30.93	59.88	19.95
Washington	20.12	37.46	5.18
California	23.36	43.66	10.32
Wyoming	25.23	37.44	9.7

Table 18 shows the result for the four locations that need dehumidification on July 24th, the results show that fuel cell will be able to produce almost 10% of the daily storage for these cases. This is because during this day all these 4 locations need dehumidification all day long, so there won't be time during the day/night that regeneration can store extra amount of

storing desiccant for later use. For storage capacity I need to look into the yearly capacity which during some months there won't be any latent load and the regenerator can produce and store LiCl for months that dehumidification is needed.

Table 18. Daily storage capacity for 7 data center locations during July 20th.

Location	Temperature (℃)	Humidity ratio (g/kg)	Relative humidity	Pressure (kPa)	Outlet Temperature (℃)	Outlet Humidity ratio	Required LiCl capacity	Fuel Cell LiCl Capacity
Virginia	25.21	12.41	79.8	100	7.84	11	2.31	0.173
Illinois	22.61	15.94	88.97	98	25.93	11	2.35	0.173
Iowa	23.95	13.12	67.07	97	28.43	11	2.3	0.202
Texas	30.93	15.06	52.04	99	30.99	11	2.31	0.194

6.4 LiCl yearly storage

Figure 56 shows dew point temperatures for the seven locations of the study for the entire year. As we can see Virginia, Iowa, Illinois, and Texas are the four locations that have significant number of hours with dew point higher than 15°C, which is the limit for acceptable humidity level of the servers. In this section, I investigate the amount of liquid desiccant that is required to dehumidify the air in these locations, as well as the storage capacity for each of these four locations.

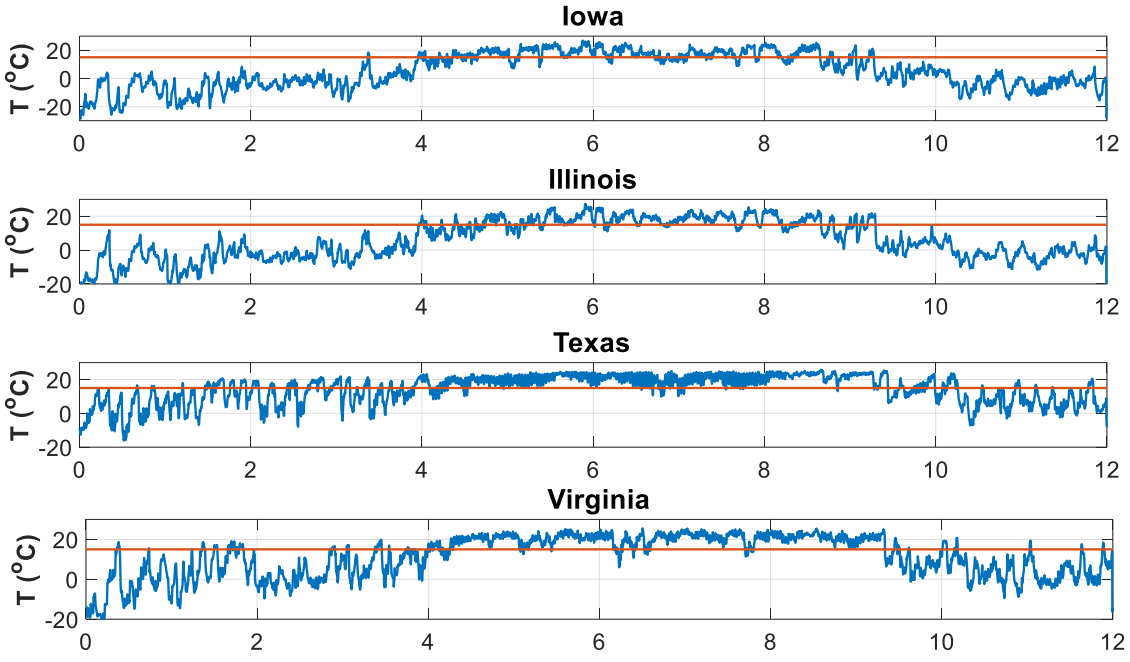

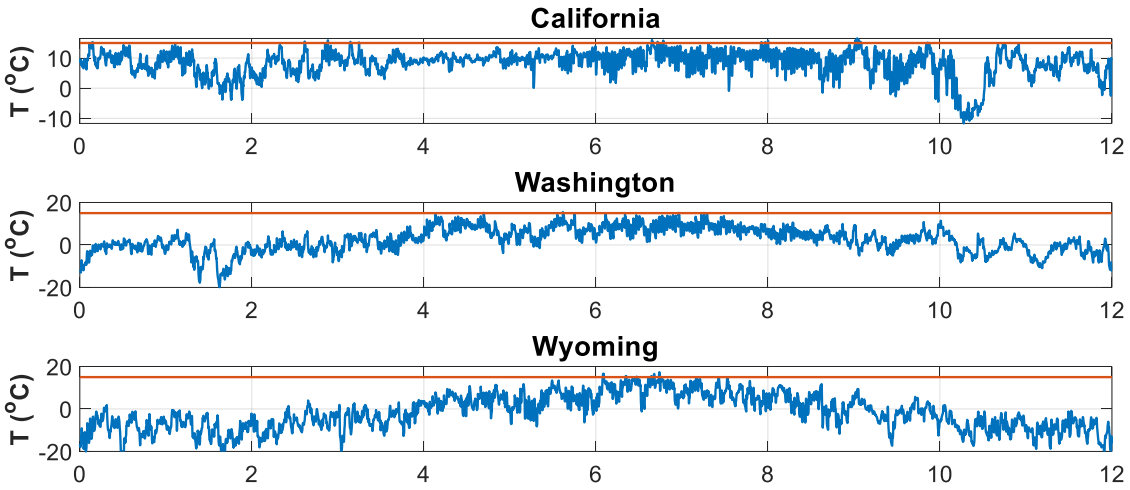

Figure 56. Dew point for the seven locations of the study for the entire year.

For this section's results, the assumptions are as follow:

1. Each single server rack is 12kW.

2. The space is designed so that each row of servers contains 10 server racks. (Figure 57 shows the schematic of row level server cooling.)

3. The temperature difference of the air entering and leaving the servers is 15°C. The humidity ratio of the air cooling the server is kept below $11\frac{g}{kg}$ (ASHRAE recommendation);

4. Each fuel cell powering the servers is equivalent to 8 BlueGEN (12kW).

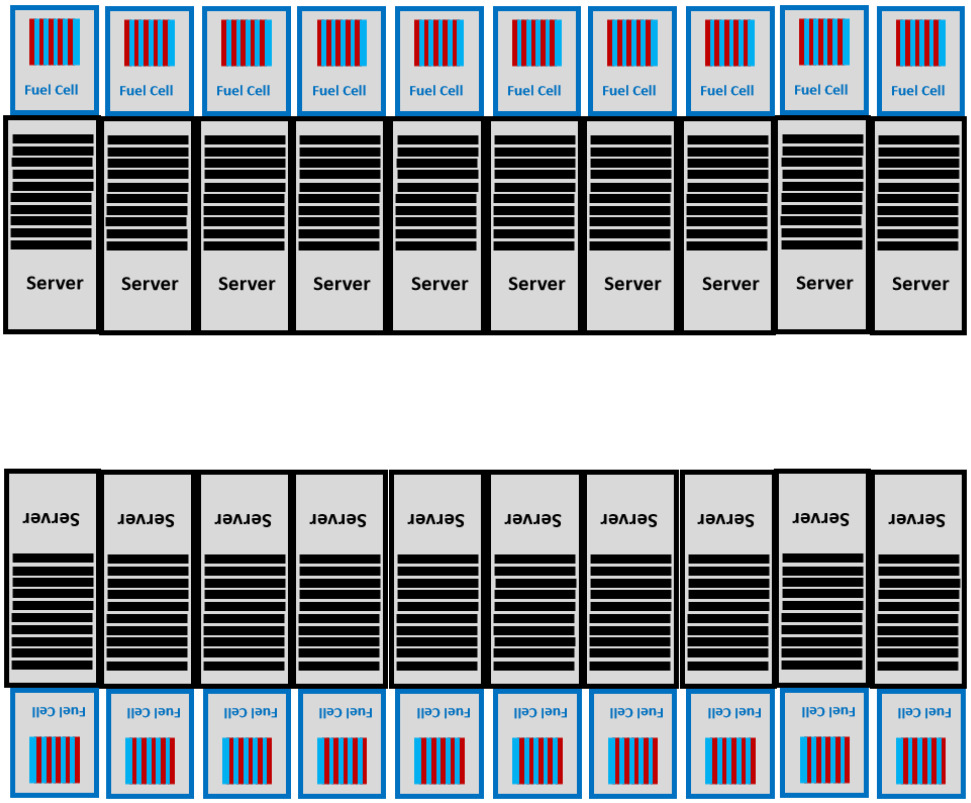

Figure 57. Schematic of row level server cooling.

The results are presented for two scenarios; in first scenario, liquid desiccant provides dehumidified air for one single server rack for the entire year, the fuel cell runs at full load, and the dehumidifier is sized based on server rack, and the regenerator is sized based on FC exhaust. In second scenario, liquid desiccant provides dehumidified air for two rows (20 server racks), Fuel cell runs at 70% load, dehumidifier is sized based on cooling required for two rows, and regenerator is sized based on equivalent of two rows fuel cell exhaust. The reason for row level fuel cells running at 70% and in rack level running at 100% is that when fuel cell provides power for only one rack, it is more likely that the single server rack runs at full load, however, when several fuel cells provide power for 20 racks, the load of serves will be balanced to the data center overall utilization (between 60 to 80%).

6.4.1 First scenario: Rack level regenerator and dehumidifier results

In the rack level scenario, each server rack is 12kW and the server load is at 100%, which results in the 12-kW fuel cell running at full load. The efficiency of the fuel cell is 60% at full

load and the exhaust leaves the fuel cell at 100°C and $0.0832\frac{\text{Kg}}{\text{s}}$. The dehumidifier capacity is 3 tons, sized based on worst case scenario for one single server. The regenerator is sized one ton based on the available heat from fuel cell exhaust. Figure 58 to Figure 63 shows the regenerators results for Illinois for the entire year.

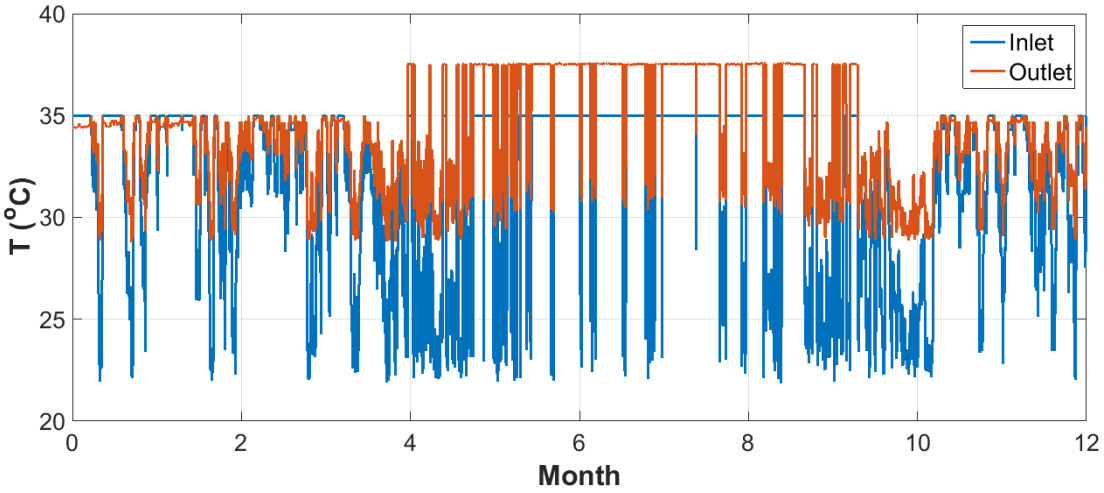

Figure 58. Mixture air temperature before and after regeneration process for the entire year at Illinois location.

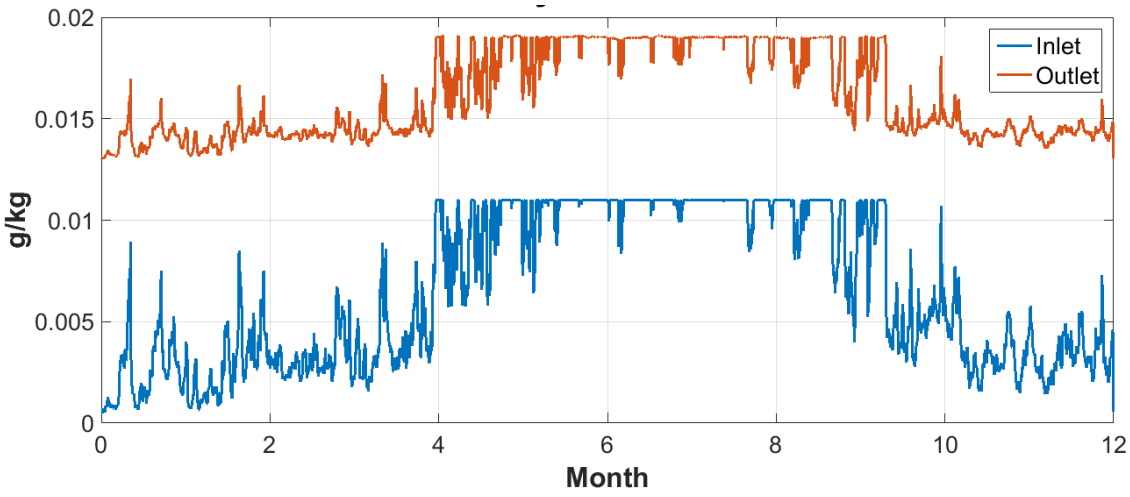

Figure 59. Mixture air humidity ratio before and after regeneration process for the entire year at Illinois location.

In the regenerator, as shown in Figure 36 a mixture of outside air and return air is sent to the regenerator. When outside air temperature is hot and humid, more return air is mixed with outside air, and when the outside air humidity is more than $11\frac{g}{kg}$, 100% return air is

used for regeneration process. This is because the return air from servers has lower humidity and higher capacity to absorb water from desiccant. Figure 58 and Figure 59 show the mixture air temperature and humidity before and after regeneration process respectively. As expected, during the regeneration process, the air humidity increases as it absorbs the humidity of the desiccant and while the hot water facilitates the regeneration process it also causes the increase in air temperature. Figure 60 shows the return air percentages.

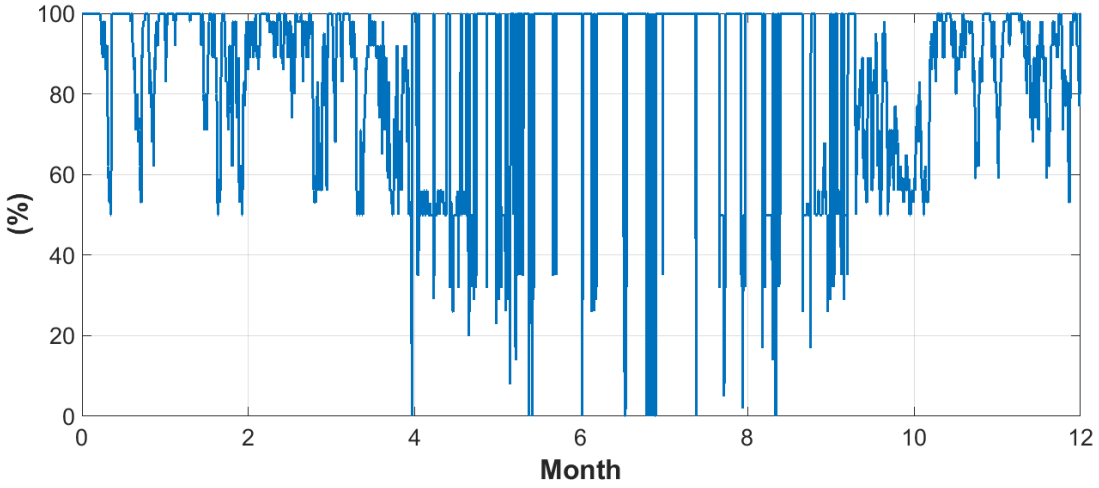

Figure 60. Return air percentages for regeneration process at Illinois location.

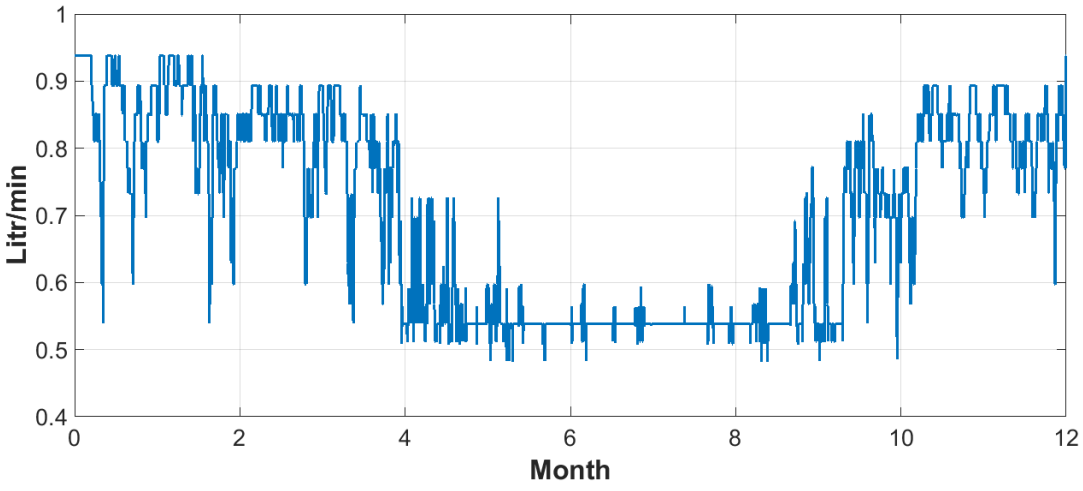

Figure 61. Rate of regenerated desiccant flow for the entire year at Illinois location.

Figure 61 shows the flow rate of desiccant than is being regenerated throughout the year. The model controller keeps the desiccant concentration in a constant range, changing from 32% to 35% as shown in Figure 62. To keep the concentration at constant it manipulates the

amount of desiccant in can regenerate at a time. During the month that the air inlet humidity is high and has less capability to absorb the humidity of desiccant, less desiccant is regenerated as it is seen in Figure 61 during the summer months. The hot water produced from the exhaust of fuel cell enters the regenerator at 60°C and leaves at between 44°C to 47°C shown in Figure 63.

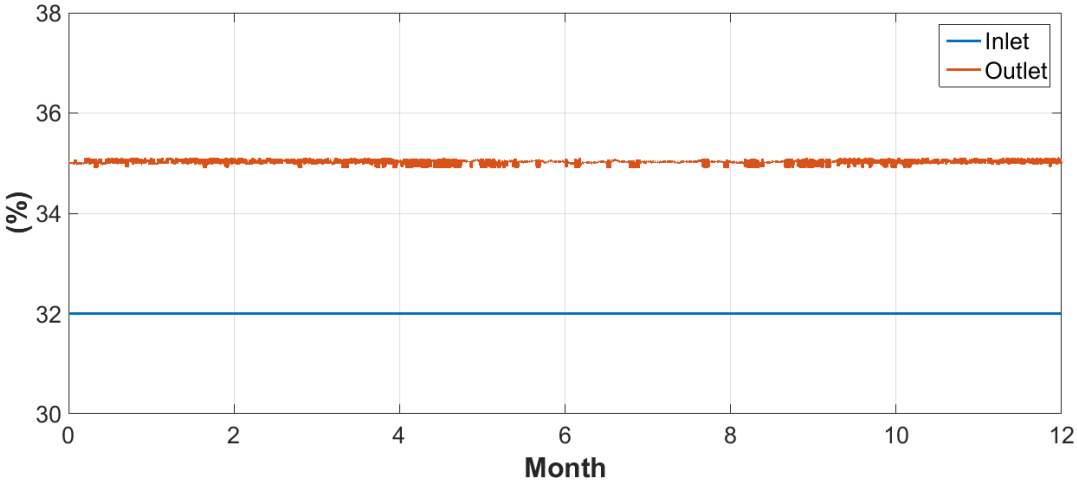

Figure 62. Desiccant inlet and outlet concentration in regenerator at Illinois location.

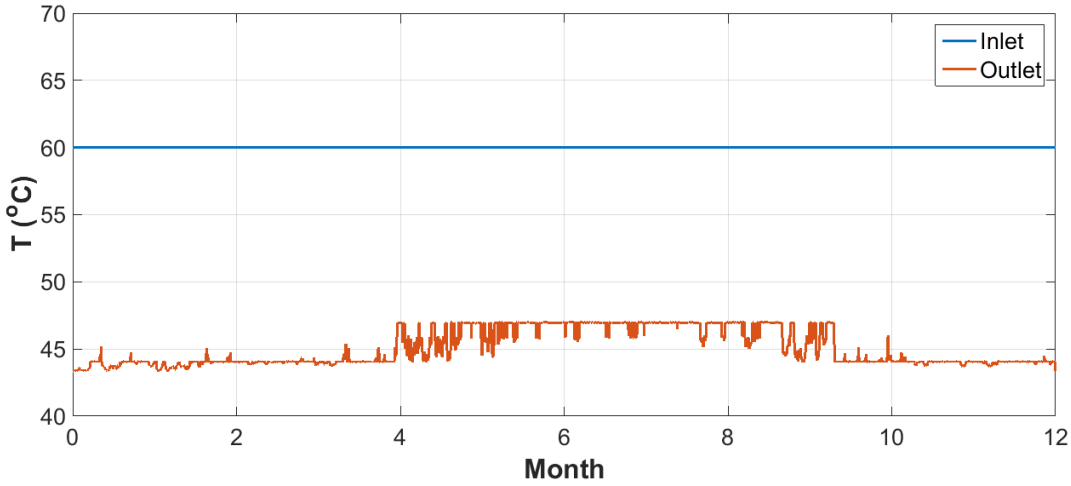

Figure 63. Hot water inlet and outlet from regenerator at Illinois location.

Figure 64 to Figure 69 show dehumidifier results for Illinois. In dehumidifier, two air streams are send to the system, one is the supply air which is a mixture of outside air and return air and the second stream is the cooling air that is send to the dehumidifier to keep the temperature constant by evaporative cooling. Figure 64 and Figure 65 show the supply air

and cooling air inlet and outlet temperature. The temperature of the streams stays almost the same even though the dehumidification is an exothermic process, which is due to the indirect evaporation of water to the second air stream. Figure 66 shows the amount of return air. For Illinois during May to September dehumidification is needed. Other time of the year the humidity of supply air is within the acceptable range. As the outside air humidity is higher the use of return air increases due to its lower humidity compared to outdoor air. However, the return air percentages depend both on temperature and humidity of outdoor air and return air to keep the supply air humidity within the acceptable range for servers. Figure 67 shows the humidity ratio of inlet and outlet supply air.

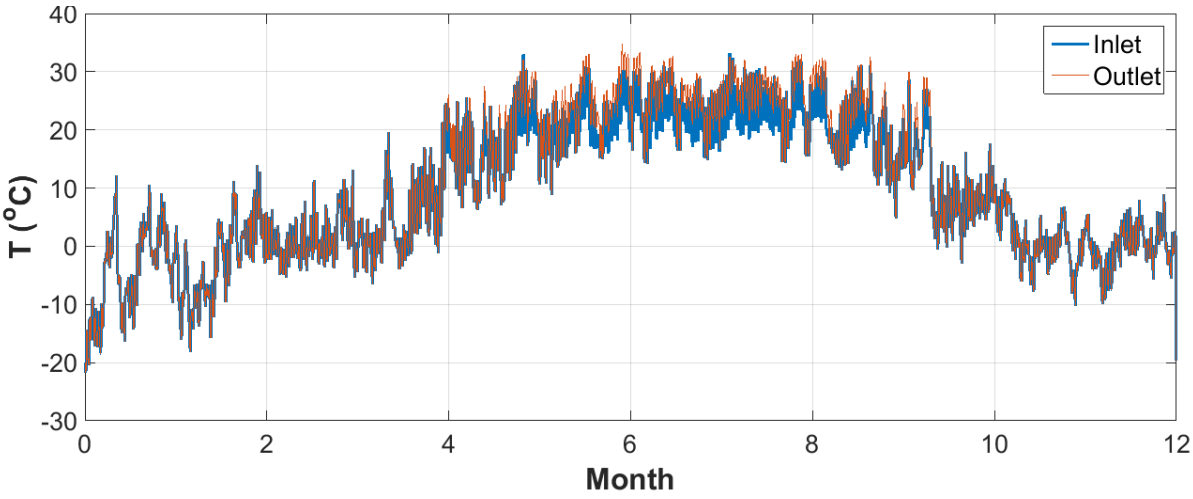

Figure 64. Supply air inlet and outlet temperature in dehumidifier for the entire year at Illinois location.

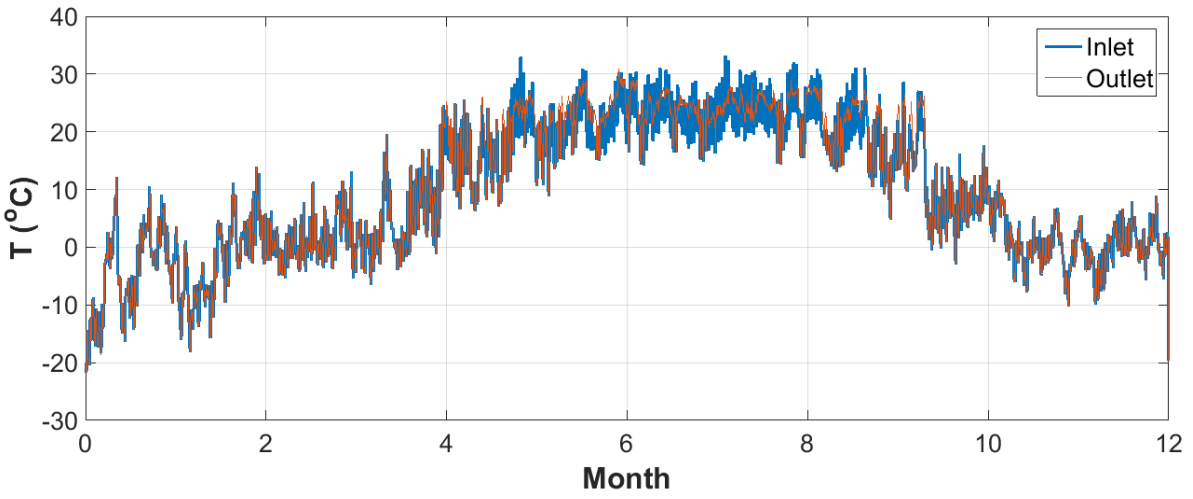

Figure 65. Cooling air inlet and outlet temperature in dehumidifier for the entire year at Illinois location.

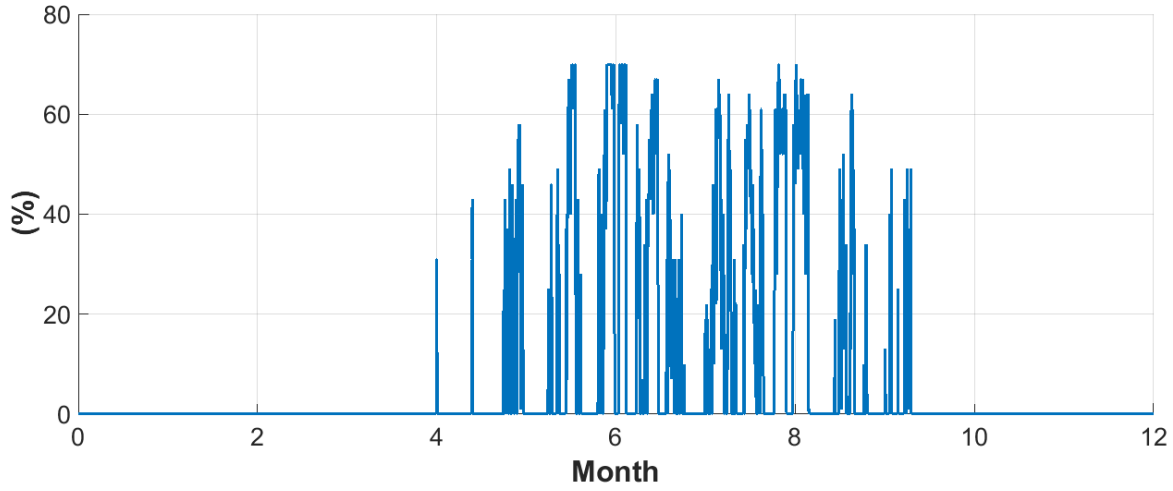

Figure 66. Return air percentages for dehumidifier process for the entire year at Illinois location.

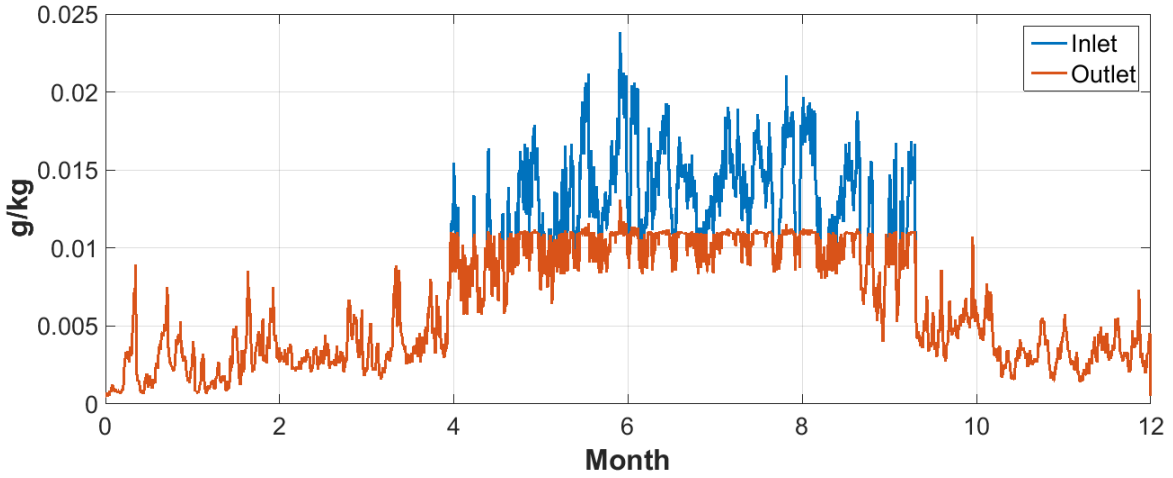

Figure 67. Humidity ratio of inlet and outlet supply air for the entire year at Illinois location.

Figure 68 shows the desiccant flow that is needed for the entire year to dehumidify the air for the server while keeping the desiccant concentration between 35% to 32%. The desiccant concentration changes are shown at Figure 69. For Illinois the strong desiccant is used during May to September and the rest of the year is stored.

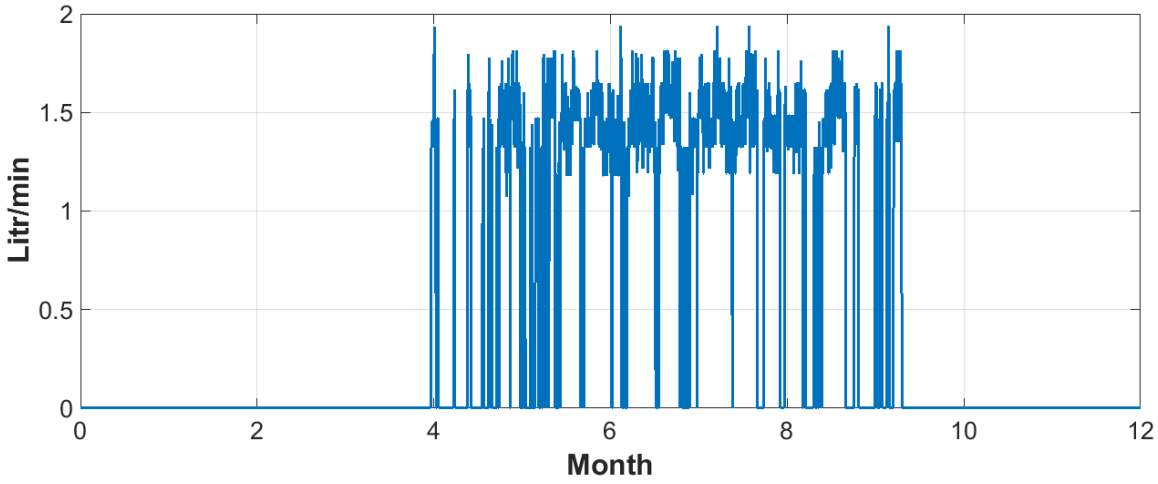

Figure 68. Desiccant flow that is needed for the entire year to dehumidify the air for the servers at Illinois location.

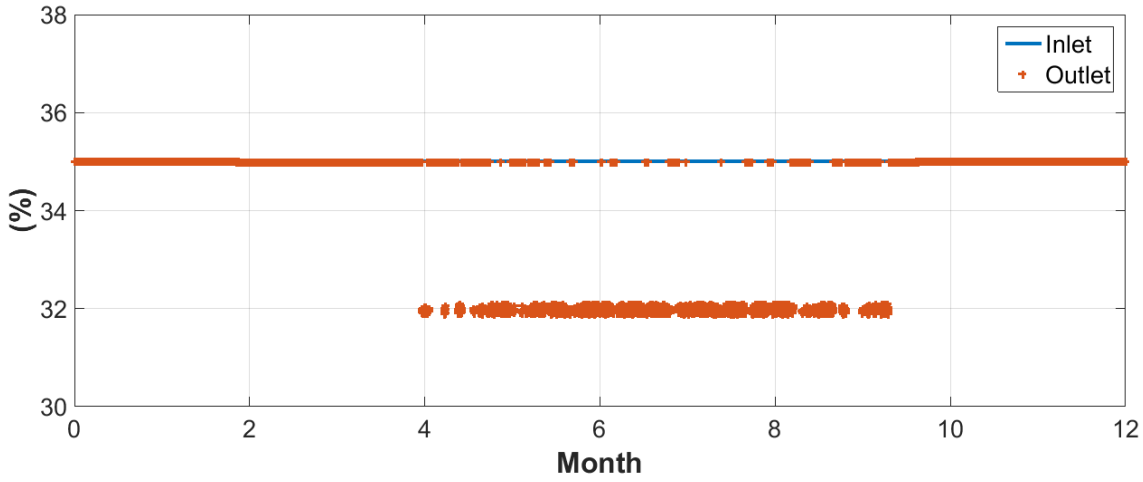

Figure 69. Desiccant inlet and outlet concentration in dehumidifier at Illinois location.

The dehumidifier and regenerator rack level results for Iowa, Texas, and Virginia can be found in Appendix B.1.

6.4.2 First scenario: Rack level storage

Figure 70 shows the net desiccant consumption and production for the entire year for Virginia, Texas, Iowa, and Illinois. The positive bar (blue lines) shows the time that the strong desiccant produced is being stored, and the negative bar (orange lines) are when the consumption of strong desiccant is higher than the amount that is being produces and as a result is a desiccant deficit. The areas with higher temperature and humidity level such as

Texas has more deficit periods during the year. At rack level, the stored desiccant goes as high as 58lit, and the deficit goes as high as 86lit at a time.

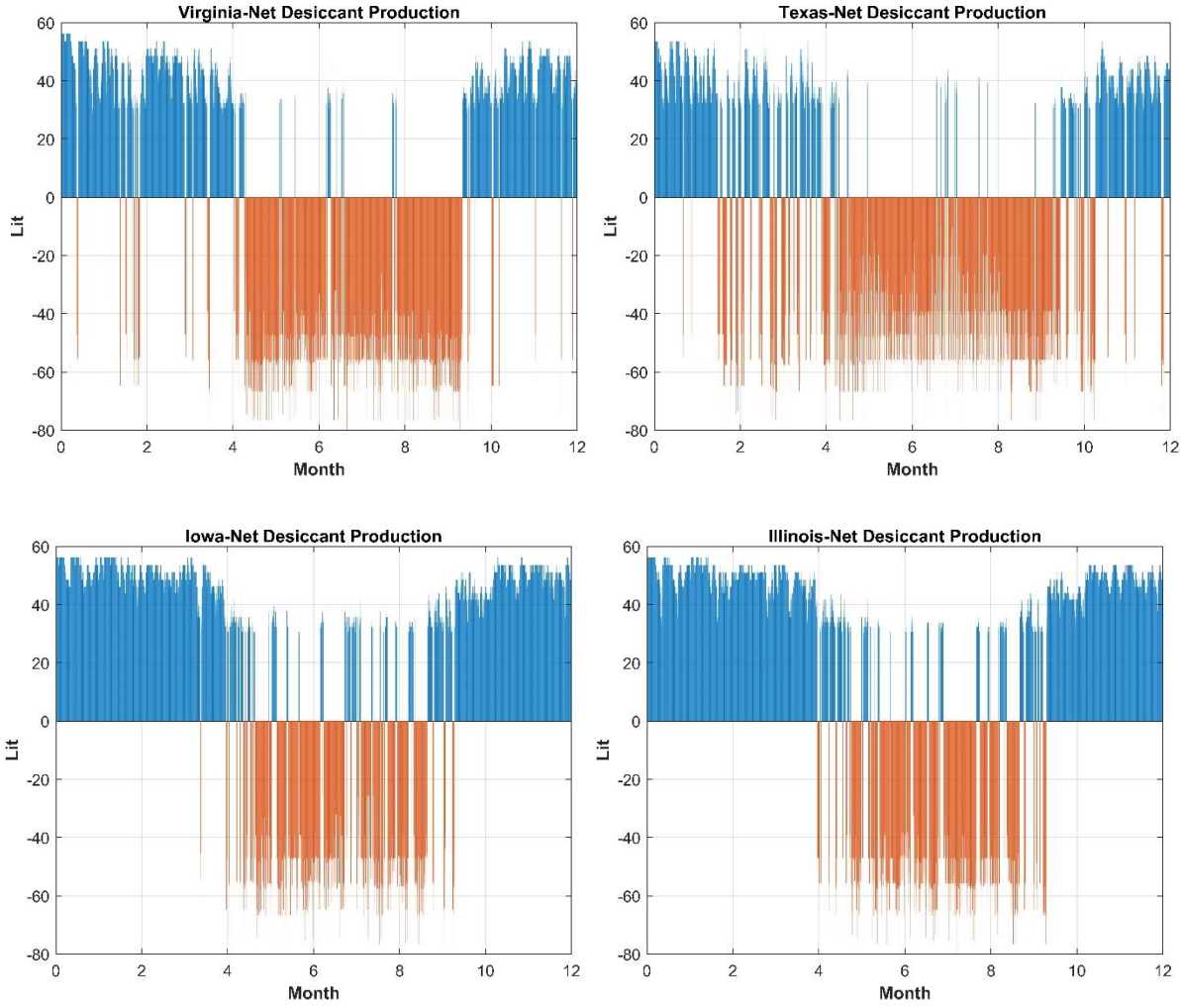

Figure 70. Net desiccant consumption and production for the entire year for Virginia, Texas, Iowa, and Illinois.

Figure 71 shows the state of storage (charge) of strong desiccant for all four locations. Considering starting at zero state in January. During the first couple of months most of the strong desiccant that is produced gets stored and fills the tank, as the usage of strong desiccants increases during spring and summer, the tank gets empty and a deficit is observed, and then again during fall the tank gets filled with strong desiccant. For Texas, there is a time period between Feb to April that the rate of production and consumption of the strong desiccants is more or less similar which keeps the tank as constant state.

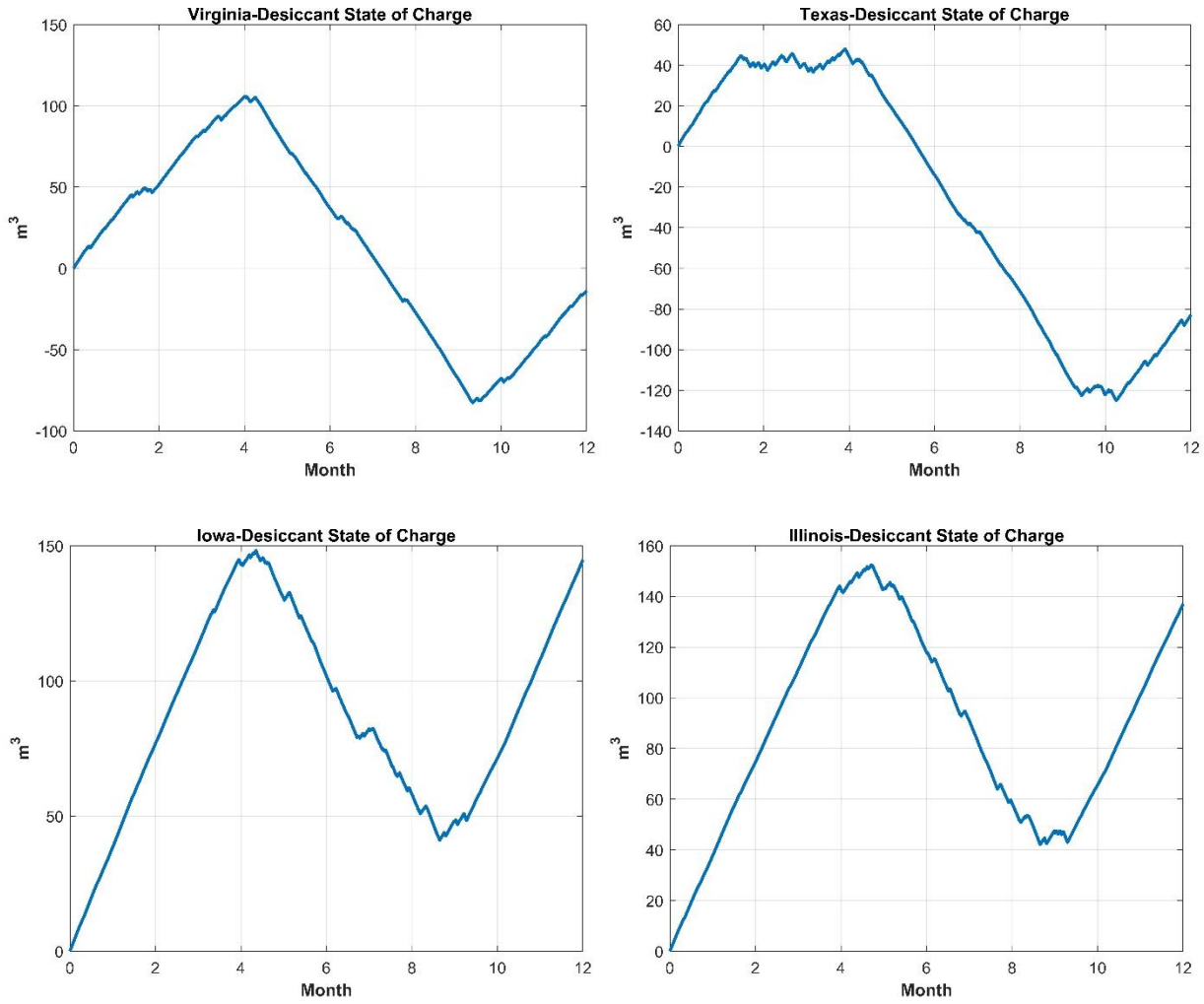

Figure 71. State of storage (charge) of strong desiccant for all four locations.

Table 19 shows the row level results for Virginia, Texas, Iowa, and Illinois. The net production to consumption ratio without storage shows what percentages of the demand of data center cooling in each location can be met by simultaneous production and consumption of strong desiccant in regenerator and dehumidifier respectively. For all four locations this ratio is below 40%. However, with storage only 60% and 44% of annual production is enough to meet the entire years demand for Illinois and Iowa respectively. For Virginia, with storage there is only 4% deficit for Virginia and for Texas the deficit decreases from 60% to 20% with storage. For row level results, the annual production and consumption of strong desiccant is shown for each location. Virginia needs the biggest tank size with 187m^3, which is due to the unbalance between production season and

consumption. For Virginia, the first couple of months the year the cooling system is mainly producing strong desiccant without the consumption (unlike Texas) which leads to need for a bigger size storage tank.

Table 19. Rack level storage results for Virginia, Texas, Iowa, and Illinois.

	Illinois	Iowa	Texas	Virginia
Net Production to Consumption Ratio (Without storage) (%)	36.94	38.14	39.65	36.73
Annual Production (m^3)	366	372	314	333
Annual Consumption (m^3)	229	227	397	347
Excess production (m^3)	137	145	-82.9	-13.8
Tank size (m^3)	110	107	173	187
Annual Net Production to Consumption Ratio (%)	59.8	63.9	-20.9	-3.9

6.4.3 Second scenario: Row level regenerator and dehumidifier results

In the row level scenario, each row has 10 server racks, and two rows are cooled by one dehumidifier system. Each server rack is 12kW and the server load is at average 70%, which results in the equivalent of 240kW fuel cell running at 70% capacity. The efficiency of the fuel cell is 64% and the exhaust leaves the fuel cell at 86℃ and $0.0635\frac{\mathrm{Kg}}{\mathrm{s}}$. The dehumidifier capacity is 42 tons, sized based on the cooling required for worst case weather condition for 20 servers. The regenerator is sized to 15 tons based on the available heat from fuel cell exhaust. Figure 72 to Figure 77 show the regenerator results for Illinois for the entire year. The process is similar to the rack level regeneration, more return air is used for the mixture when outside air temperature is hot and humid. Then the outside air humidity exceeds the $11\frac{g}{kg}$, the air used in regeneration process is 100% return air.

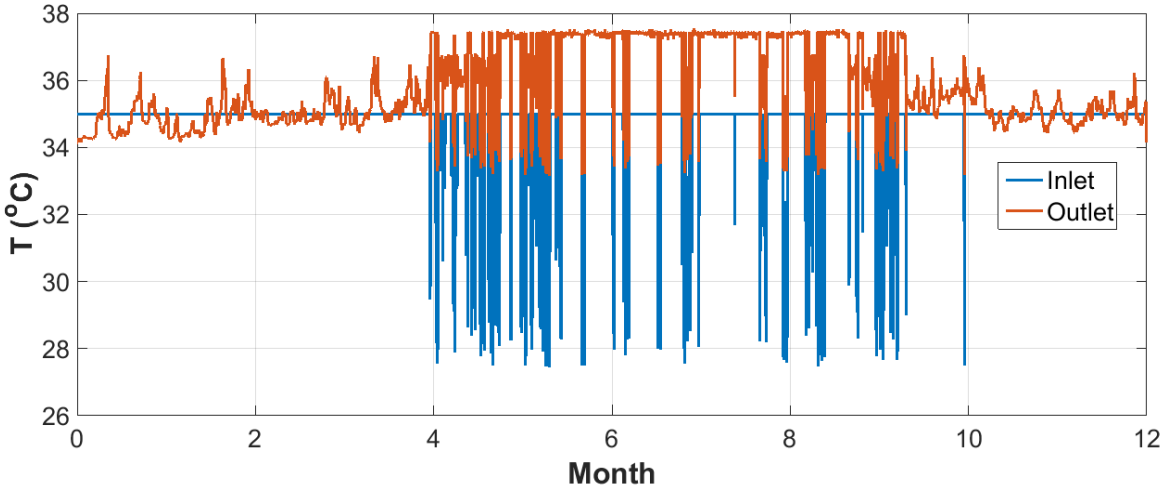

Figure 72. Mixture air temperature before and after the regeneration process at Illinois location.

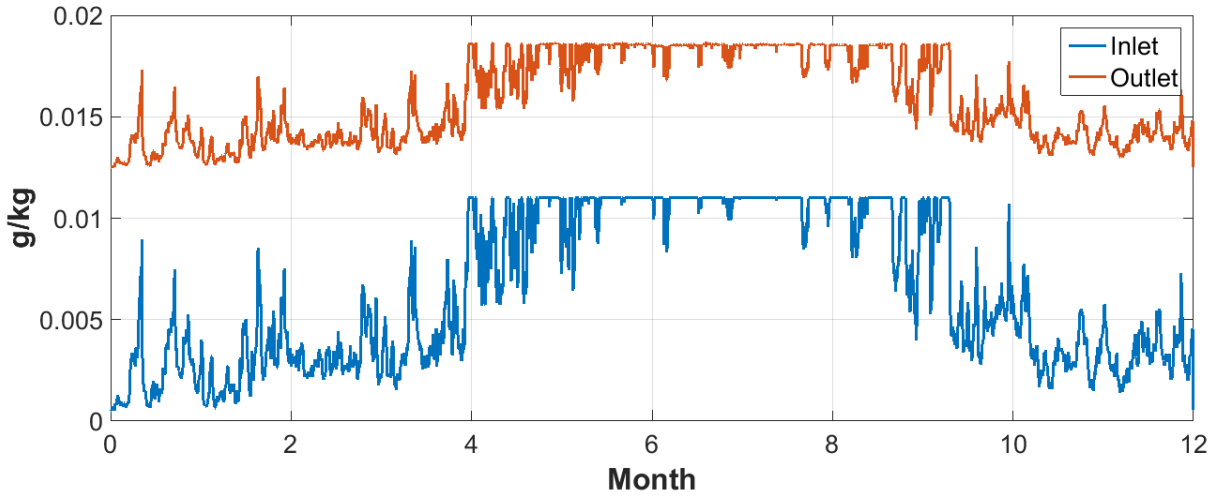

Figure 73. Mixture air humidity before and after the regeneration process at Illinois location.

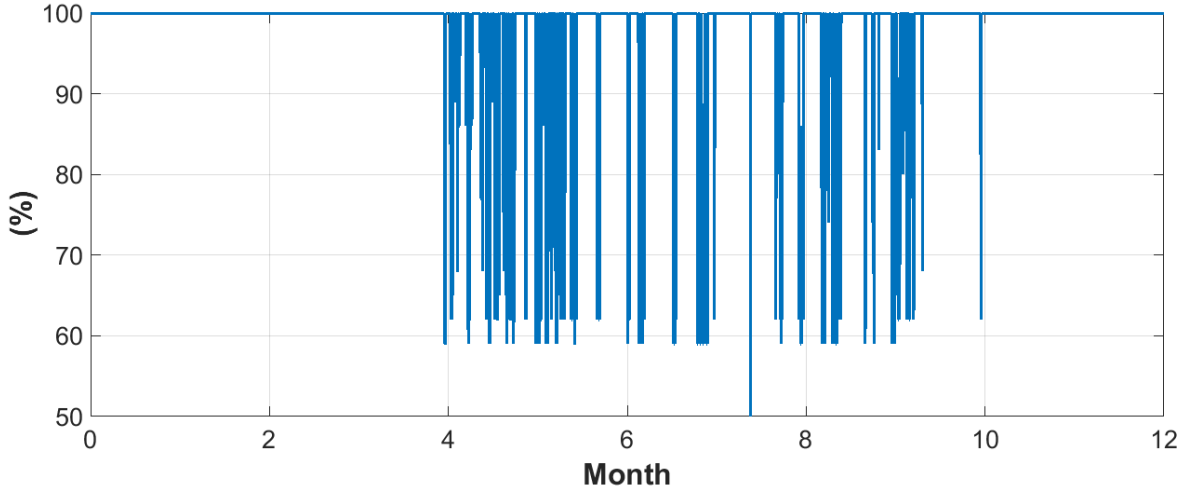

Figure 74. Return air percentage for regenerator at Illinois location.

Figure 72 and Figure 73 show the mixture air temperature and humidity before and after regeneration process respectively. The humidity of the air mixture increases as it absorbs the water from weak desiccant. The regeneration process is endothermic, while the hot water from fuel cell exhaust provides the heat required for this process, it also causes the increase in the mixture temperature. Figure 74 shows the return air percentages.

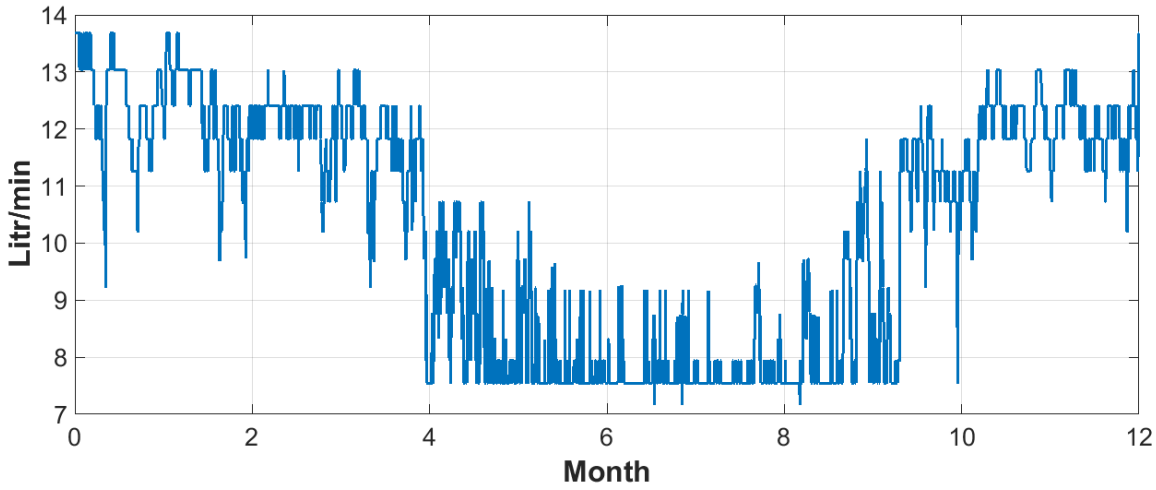

Figure 75. Regenerated desiccant flow rate throughout the year at Illinois location.

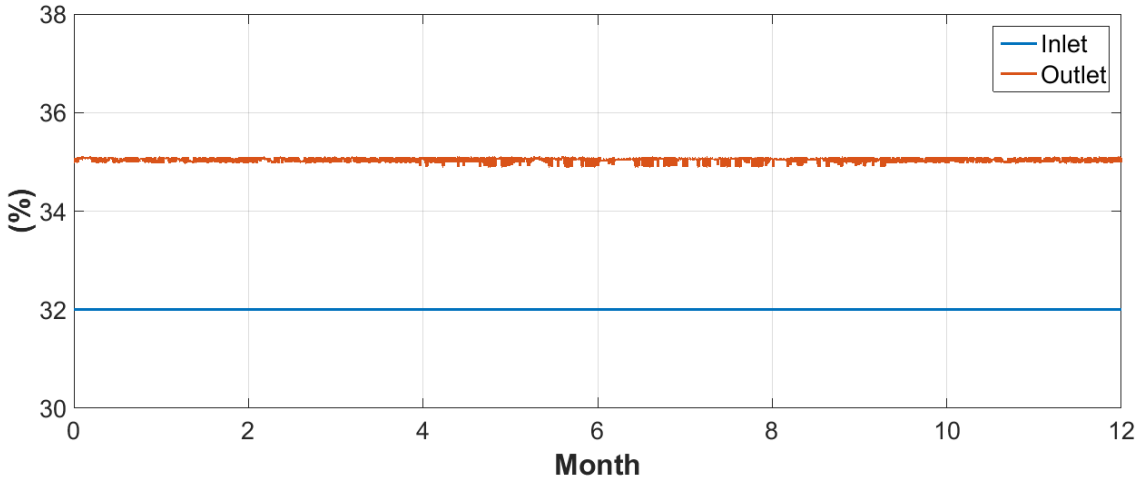

Figure 76. Desiccant concentration inlet and outlet in regenerator at Illinois location.

Figure 75 shows the flow rate of desiccant than is being regenerated throughout the year. The model controller keeps the desiccant concentration in a constant range, changing from 32% to 35% as shown in Figure 76. The hot water produced from the exhaust of fuel cell enters the regenerator at 60°C and leaves at between 40°C to 45°C as shown in Figure 77.

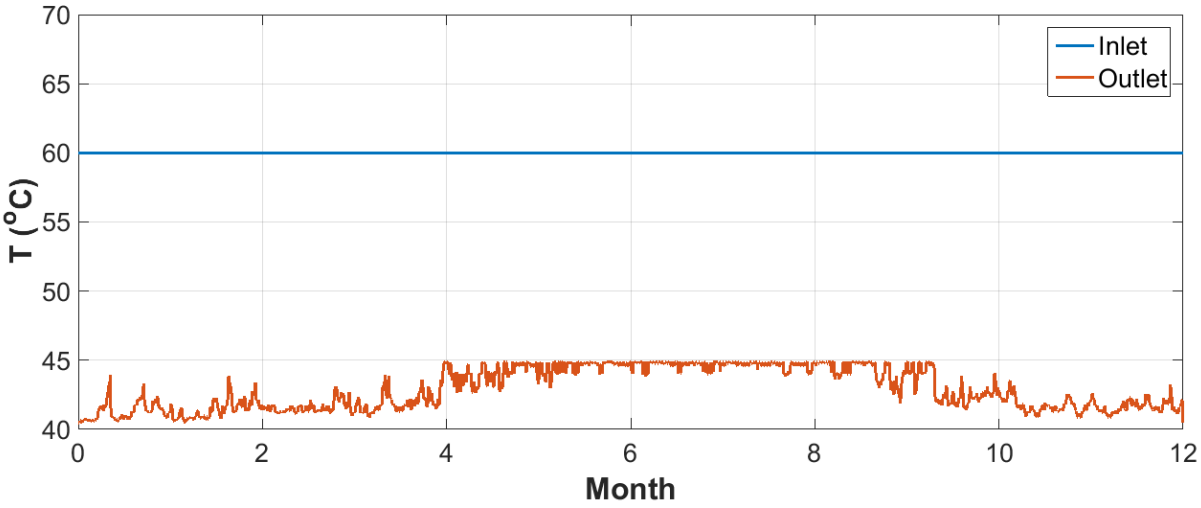

Figure 77. Hot water inlet and outlet temperature before and after regenerator at Illinois location.

Figure 78 to Figure 83 show the dehumidifier row level results for Illinois. Figure 78 and Figure 79 show the supply air and cooling air inlet and outlet temperature. Supply air stream is a mixture of outside air and return air that gets dehumidified to cool the servers and the cooling air is sent to the dehumidifier to keep the temperature constant by evaporative cooling. Figure 80 shows the amount of return air. Figure 81 show the humidity ratio of inlet and outlet supply air.

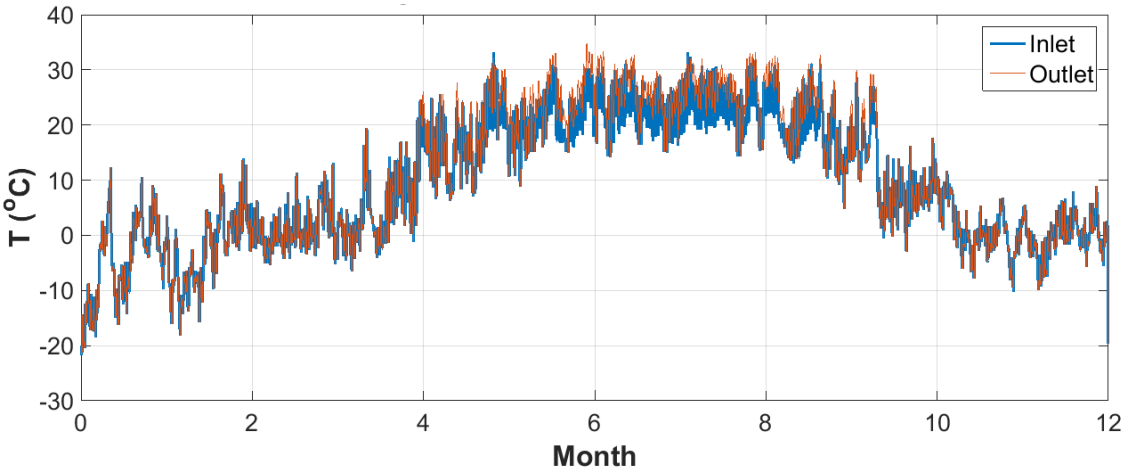

Figure 78. Supply air inlet and outlet temperature in dehumidifier at Illinois location.

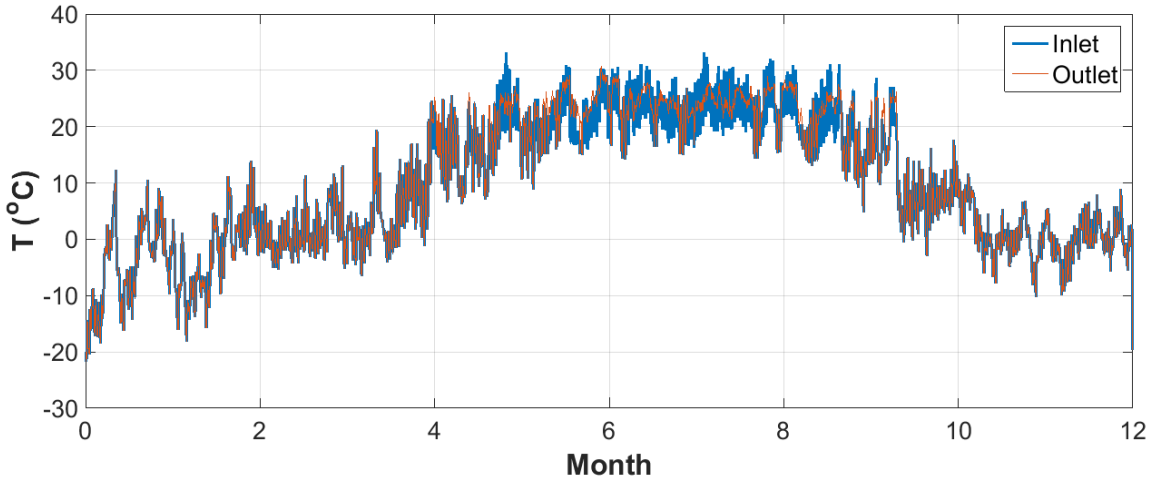

Figure 79. Cooling air inlet and outlet temperature in dehumidifier at Illinois location.

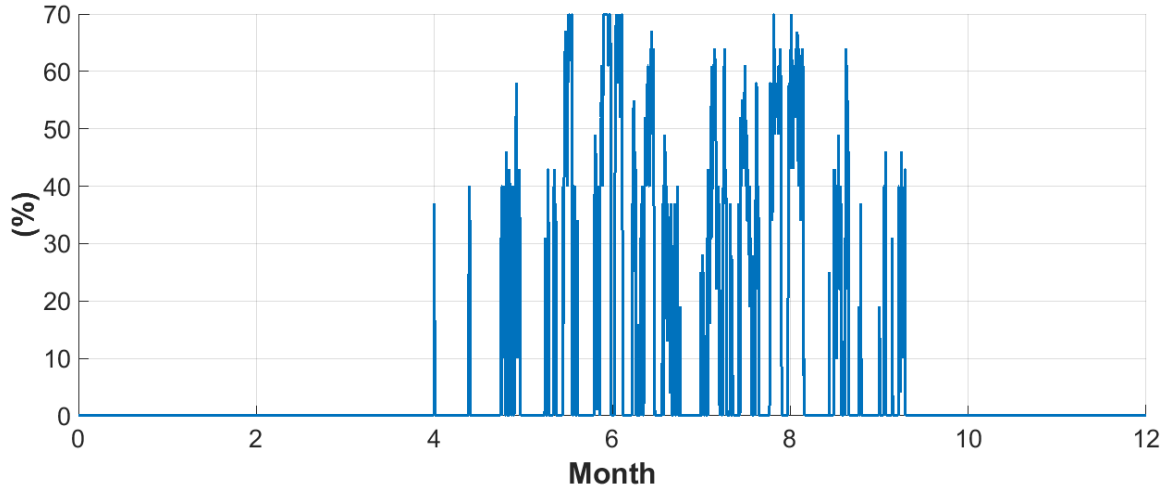

Figure 80. Return air percentage in dehumidifier at Illinois location.

Figure 82 shows the desiccant flow that is needed for the entire year to dehumidify the air for 20 servers while keeping the desiccant concentration between 35% to 32%. The desiccant concentration changes are shown at Figure 83.

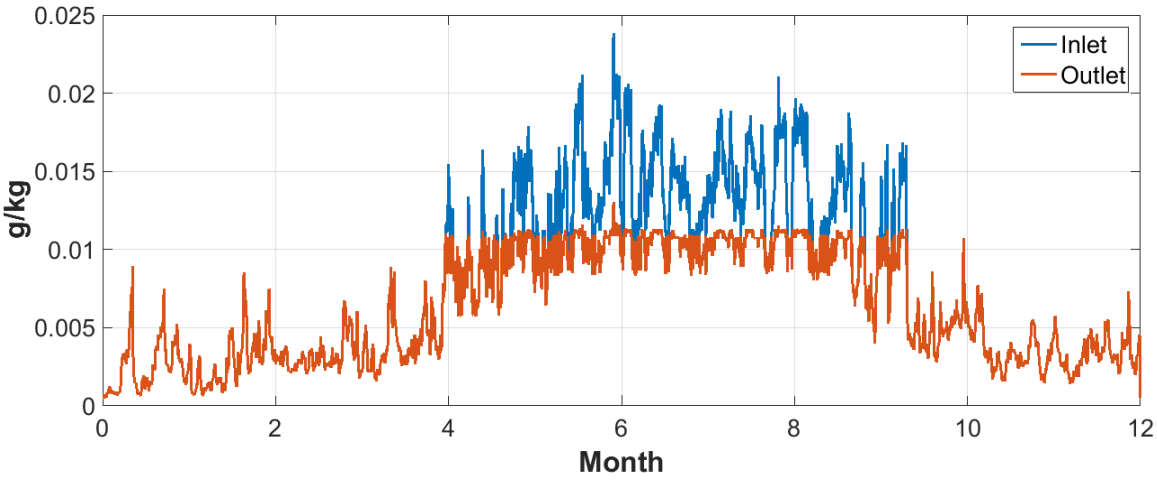

Figure 81. Cooling air inlet and outlet humidity ratio in dehumidifier at Illinois location.

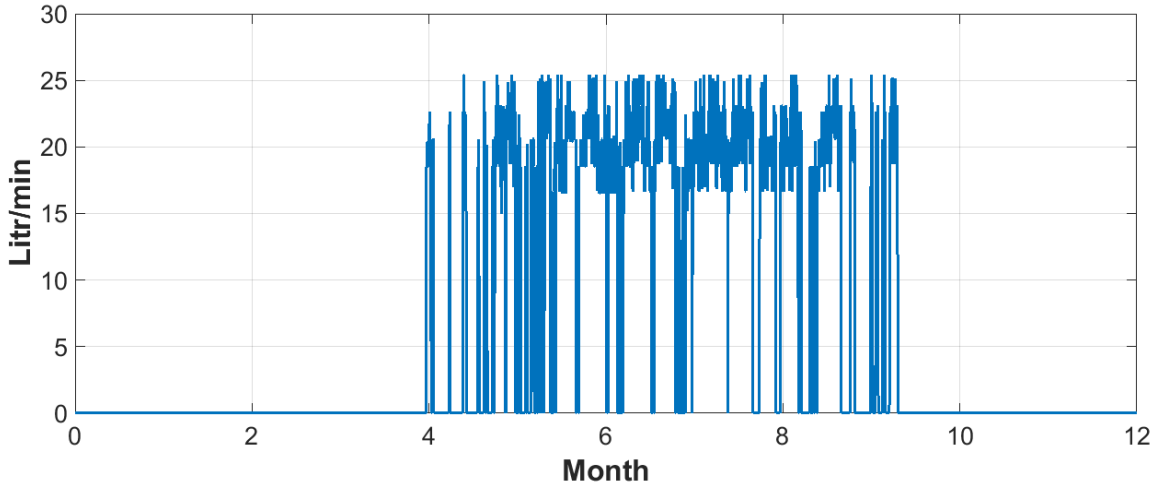

Figure 82. Desiccant flow rate in dehumidifier for the entire rate at Illinois location.

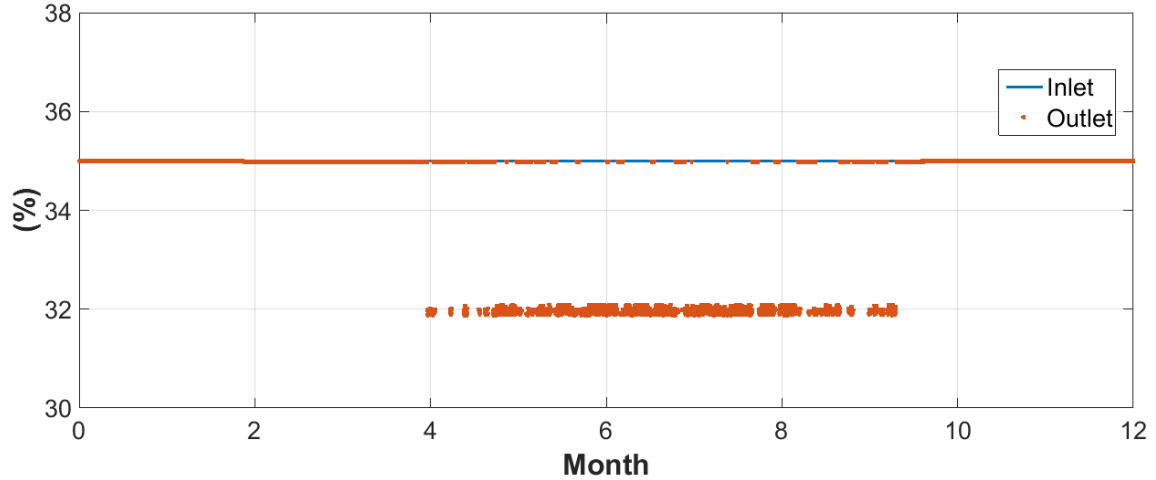

Figure 83. Desiccant inlet and outlet desiccant concentration at Illinois location.

The dehumidifier and regenerator row level results for Iowa, Texas, and Virginia can be found in Appendix B.2.

6.4.4 Second scenario: Row level storage

Figure 84 shows the net desiccant consumption and production for the entire year for Virginia, Texas, Iowa, and Illinois in row level storage. The positive blue data indicate periods of the time in which excess strong desiccant is produced, while the negative orange data show the desiccant being used to dehumidify, especially during summer months. At the row level, the requirements for storing the desiccant are found to be as large as 822 liters while the deficit amount is found to be as large as high as 1200 liters that are required over the year. So, in some of the regions, insufficient desiccant is produced in the fall, winter, and spring to meet the dehumidification requirements in the summer.

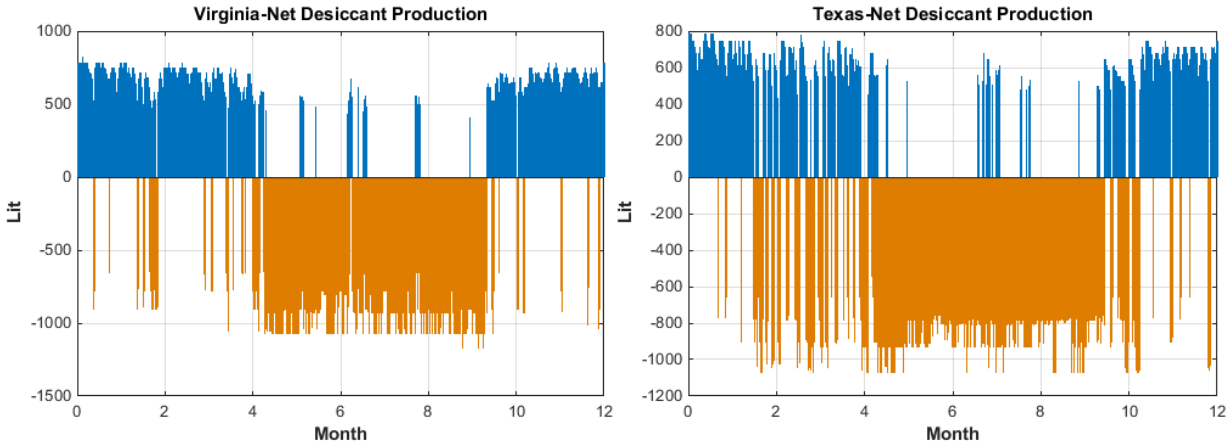

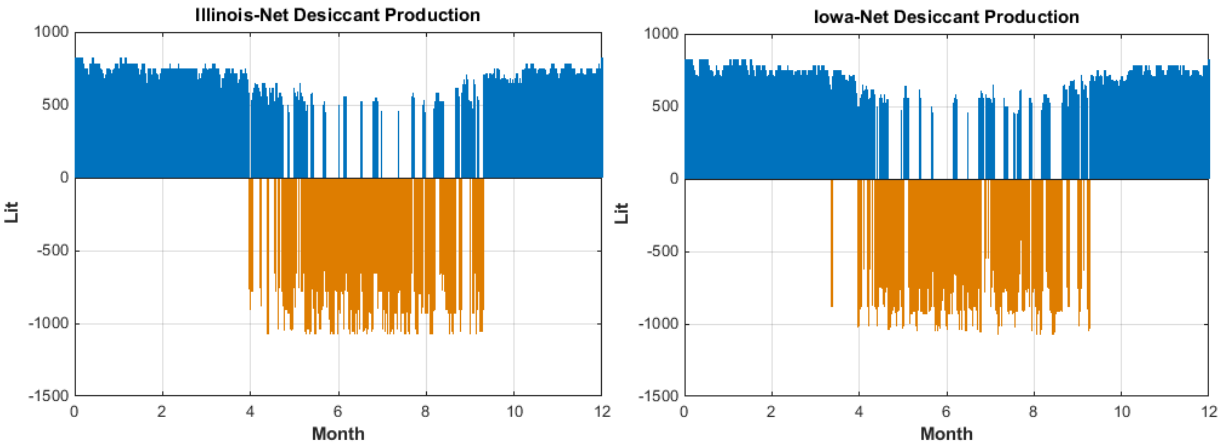

Figure 84. Net desiccant consumption and production for Virginia, Texas, Iowa, and Illinois in row level storage.

Figure 85 shows the state of storage (charge) of strong desiccant for all four locations, considering starting at zero state in January. Table 20 shows the rack level results for the four locations. For all three locations this ratio is below 40% the same as rack level results. However, with storage 80% and 72% annual production meets the entire years demand for Illinois and Iowa respectively. For Virginia, with storage, the strong desiccant production is equivalent to demand and for Texas the deficit decreases from 20% to 16% compared to rack level. For row level results, the annual production and consumption of strong desiccant is shown for each location. Virginia needs the biggest size of tank (2600m^3) due to the high humidity level and unbalanced strong desiccant production and consumption.

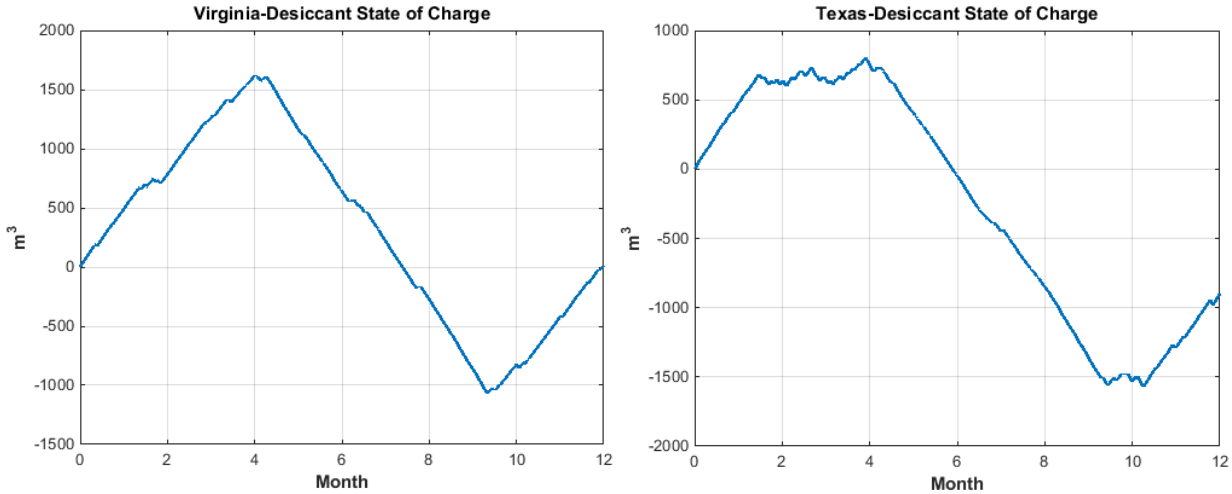

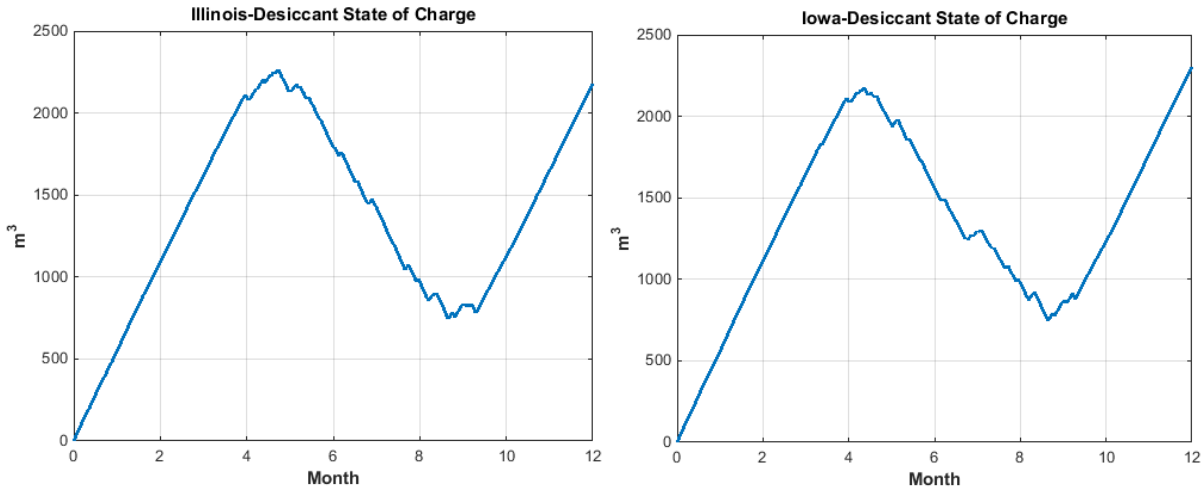

Figure 85. the state of storage of strong desiccant for Virginia, Texas, Iowa, and Illinois in row level storage.

Table 20. Rack level storage results for the four locations.

	Illinois	**Iowa**	**Texas**	**Virginia**
Net production to consumption (Without storage) (%)	37	39	40	36
Annual production (m^3)	5400	5400	4600	4920
Annual Consumption (m^3)	3220	3190	5500	4910
Excess production (m^3)	2180	2300	-900	13
Tank size (m^3)	1516	1550	2360	2600
Annual net production to consumption (%)	67.7	72.1	-16.4	0.26

6.4.5 Rack and Row level Comparison:

To compare the two scenarios, it is assumed that the cooling and power system is designed for a 240MW data center in Illinois. Table 21 shows a comparison of the two scenarios. Each server is 12kW and requires 1400CFM cold air entering the servers at 20°C and leaving the servers at 35°C. The humidity ratio is kept below $11\frac{g}{kg}$. Fuel cells are used to power the servers. Each fuel cell is equivalent to the 8 BlueGEN system tested in the laboratory. The hot water loop temperature change is between 45°C to 60°C and the maximum recirculated air in the IEC is 20%. The results show that designing the server cooling is row level instead of

rack level can decrease the size of storage needed for servers between 26 to 32% in different weather conditions. This design gives the opportunity to run the fuel cell at partial load with higher efficiency and decreases the infrastructure needed for server cooling.

Table 21. Rack and Row level storage comparison.

Rack					**Row**				
• Fuel cell runs full load • FC efficiency 60% • FC exhaust at 100°C, 0.0832kg/s • Server load 100% • Dehumidifier: 3ton • Regenerator 1ton					• Fuel cell runs at 70% load • FC efficiency 64.5% • FC exhaust at 86.3°C, 0.0635kg/s • Server load 70% • Dehumidifier: 42ton • Regenerator 15ton				
	Illinois	**Iowa**	**Texas**	**Virginia**		**Illinois**	**Iowa**	**Texas**	**Virginia**
Tank size ($10^6 m^3$)	2.2	2.1	3.4	3.7	**Tank size ($10^6 m^3$)**	1.5	1.55	2.3	2.6

6.5 Summary

In this chapter, the integrated system behavior has been analyzed to meet server power and cooling demands in a data center setting for both the spontaneous case and the case with storage. The SOFC system could produce enough power for a single server rack. The SOFC system exhaust heat has been predicted to leave the 12kW SOFC system at 100˚C temperature and 0.832kg/s flow rate. The exhaust of the SOFC system can produces hot water at 0.044kg/s at 60˚C. The results showed that the SOFC exhaust heat was able to continuously provide 8% of server rack required supply air in the safe range of temperature and dehumidification under these conditions. Results showed that for daily storage in a summer day, that needed dehumidification all 24 hours, the integrated system did not provide the server required cooling demand. In the second section the yearly storage requirements and annual dynamic operation have been analyzed for 4 different locations in the US: Illinois, Iowa, Virginia, and Texas. Two scenarios are investigated: (1) rack level server with 12kW demand, and (2) row level servers with 240kW demand. Yearly storage results showed that in the rack level design was only able to produce 60% and 44% of annual desiccant requirements to meet the entire annual demand for Illinois and Iowa, respectively.

In Virginia there is only a 4% deficit (96% of demand was met), while in Texas the deficit is 20%. In the row level design, Virginia's annual production balances the demand, while Texas still has deficit, but one that is decreased from 20% to 16% compared to rack level design. Comparison between row level scenario and rack level scenario shows that the row level design cooling system decreases the size of storage needed for servers between 26 to 32% in different weather conditions. The main reason for this improvement is that the row level design gives the opportunity to run the servers at partial load and store the desiccant based on the load of overall server rows rather than one server which also decreases the infrastructure needed for server cooling.

7 SOFC experimental and degradation analysis

7.1 Integrated system experimental setup

Figure 86 shows the experimental schematic of the integrated system which consists of eight BlueGEN SOFC systems, the dehumidification unit, server, waste heat recovery unit and a heater. The system includes a heater for the cases that the fuel cell is not able to produce enough heat for the regeneration system and for startup of the system. The eight BlueGEN exhaust gas streams are combined in one duct, and then go through the heater (if needed) and then produce hot water in the water heat recovery loop. The hot water is then pumped to the regenerator. Preconditioned air goes through the dehumidifier to produce dehumidified air, which then goes through the indirect evaporative cooler to cool the air sensibly before it goes to cool the server rack.

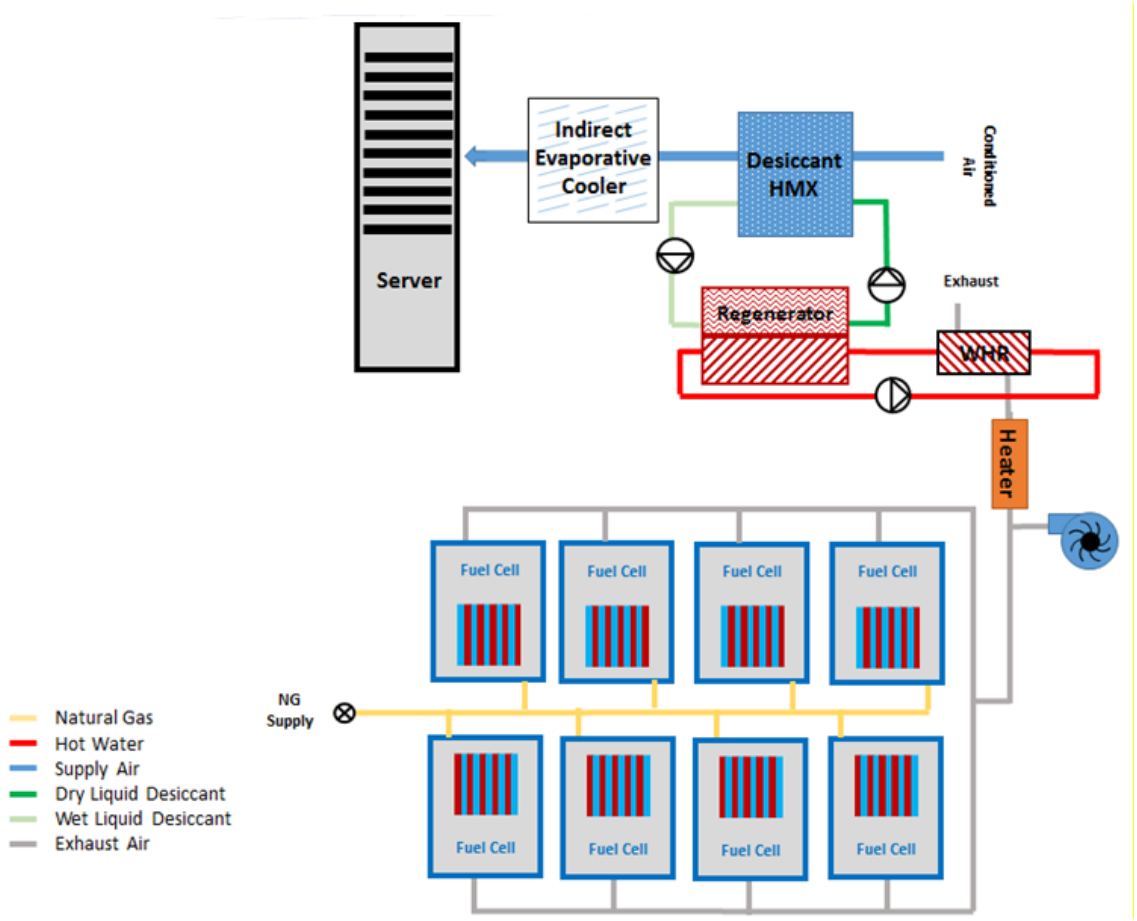

Figure 86. Experiment set-up concept schematic.

7.1.1 SOFC system

The SOFC systems installed at NFCRC are BlueGEN cogeneration systems. BlueGEN is a commercially available CHP unit, built and sold by SOLIDpower. Figure 87 shows the eight BlueGEN units as installed in the NFCRC laboratory. Operating on natural gas, each unit can produce power modulated from 500We (25%) to 2kWe (100%); however, it achieves its highest net electrical efficiency of 62% at a 1.5kWe output. The BlueGEN systems are typically operated and controlled remotely by SOLIDpower. However, through an online human machine interface, the power output profile and as a result fuel utilization are controllable by the user. To be able to install the BlueGEN we need to provide six connections: fuel (natural gas), electrical, flue gas, internet, water, and drain connections.

Figure 87. BlueGEN systems in the NFCRC laboratory.

Natural gas connection:

BlueGEN requires an uninterrupted supply of natural gas, and it only operates on the second family of gases (methane-based gases). Gas supply pressure to the BlueGEN appliance must be 9–20mbar (0.9–2kPa) so an Elster Jeavons (model J78R) gas pressure regulator is used to avoid fluctuations due to variations in the main gas supply pressure.

Electrical connection:

The BlueGEN systems require an electrical connection to successfully operate during startup and to export the electricity produced during normal operation. For electrical connection the grid availability is 208VAC 3 phase, 60 hertz. Each fuel cell needs 120VAC 1 phase, 60 hertz. 3 transformers are used where two of them provide electrical connection needed for six BlueGENs and one of them runs two BlueGENs.

Water and drain connection:

The main water supply pressure must be at least 1bar (100kPa) and no more than 10bar (1000kPa). During operation, the appliance can consume up to 30litres of water per day, depending on heat and condensate recovery. The BlueGEN appliance has an internal water storage tank for the process water and this tank will fill from the main water supply intermittently. The water consumption rate may be up to 1 liter per minute when this tank is filling. Operation of water needs to be uninterrupted. Wastewater is ejected from the BlueGEN appliance under pressure (0–1bar or 0–100 kPa).

The main water supply connection, drain, and overflow rejection connection configuration can be seen in Figure 88. Water is distributed in a manifold to each fuel cell line and each fuel cell has its own valve for water shut down. For water rejection line, overflow and wastewater will be collected in a tank through a sloped pipe and then will be pumped to the drain. Figure 89 and Figure 90 show the pump used for fuel cell water rejection connection, manifold, and valves for fuel cell supply water, respectively.

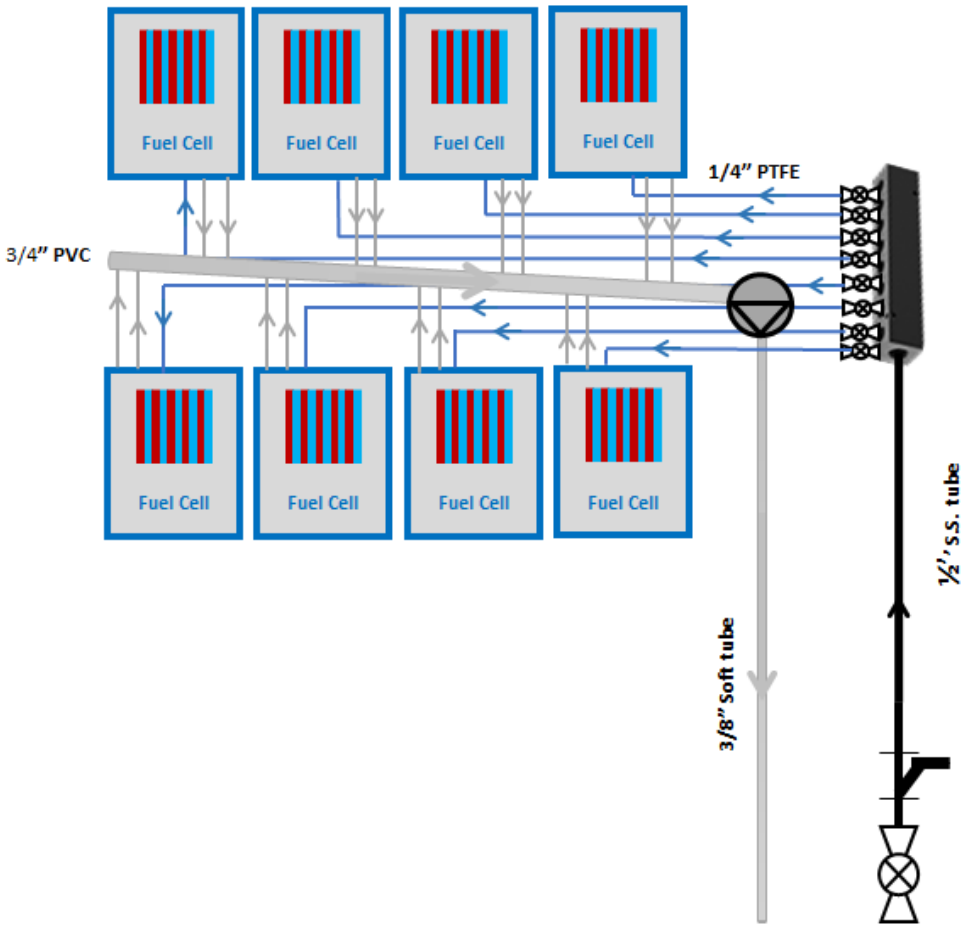

Figure 88. Water connections schematic.

Figure 89. Pump used for fuel cell water rejection connection.

Figure 90. Manifold and valves for fuel cell supply water.

Exhaust connection:

The air pipe material can be aluminum, stainless steel, galvanized steel, or polypropylene pipes. It is not allowed to use PVC or any glue for the air pipe. The maximum exhaust temperature can go up to be 200°C. The exhaust connections are made on the top of the BlueGEN systems and are connected via double-walled 4inch ducting as shown in Figure 91. The laboratory facility runs a dedicated exhaust port available in the lab space which maintains a constant negative pressure, ensuring continuous flow. Shows the exhaust duct manifold infrastructure.

Figure 91. BlueGEN exhaust manifold.

6.1.5. Internet connection:

BlueGEN systems must be connected to an appropriate uninterrupted and reliable internet connection. To facilitate this connection, a micro network was setup within the laboratory which includes all the eight BlueGEN systems as well as the servers within the server rack. The network is connected behind a Sonic Wall which provides the connectivity and the protection for the systems.

7.1.2 Server rack

Figure 92 shows the server rack in the NFCRC provided by Microsoft. The server rack consists of twenty-one HP 380E servers and during the full load needs up to 15kW power. Each server has 2 CPU and each of them has 6 cores. Each server has 96GB RAM and 25 hard drive with each 600k bite. A 24 port ethernet switch has been mounted on the server rack for the network connection.

Figure 92. Server rack at NFCRC laboratory

7.2 SOFC system experimental analysis

7.2.1 SOFC system dynamic results

Following several months of steady-states tests, several dynamic tests were run to characterize performance of SOFC system over dynamic operation. One of the BlueGEN systems ran over the dynamic power profile shown in Figure 93 and Figure 94 for 10 days.

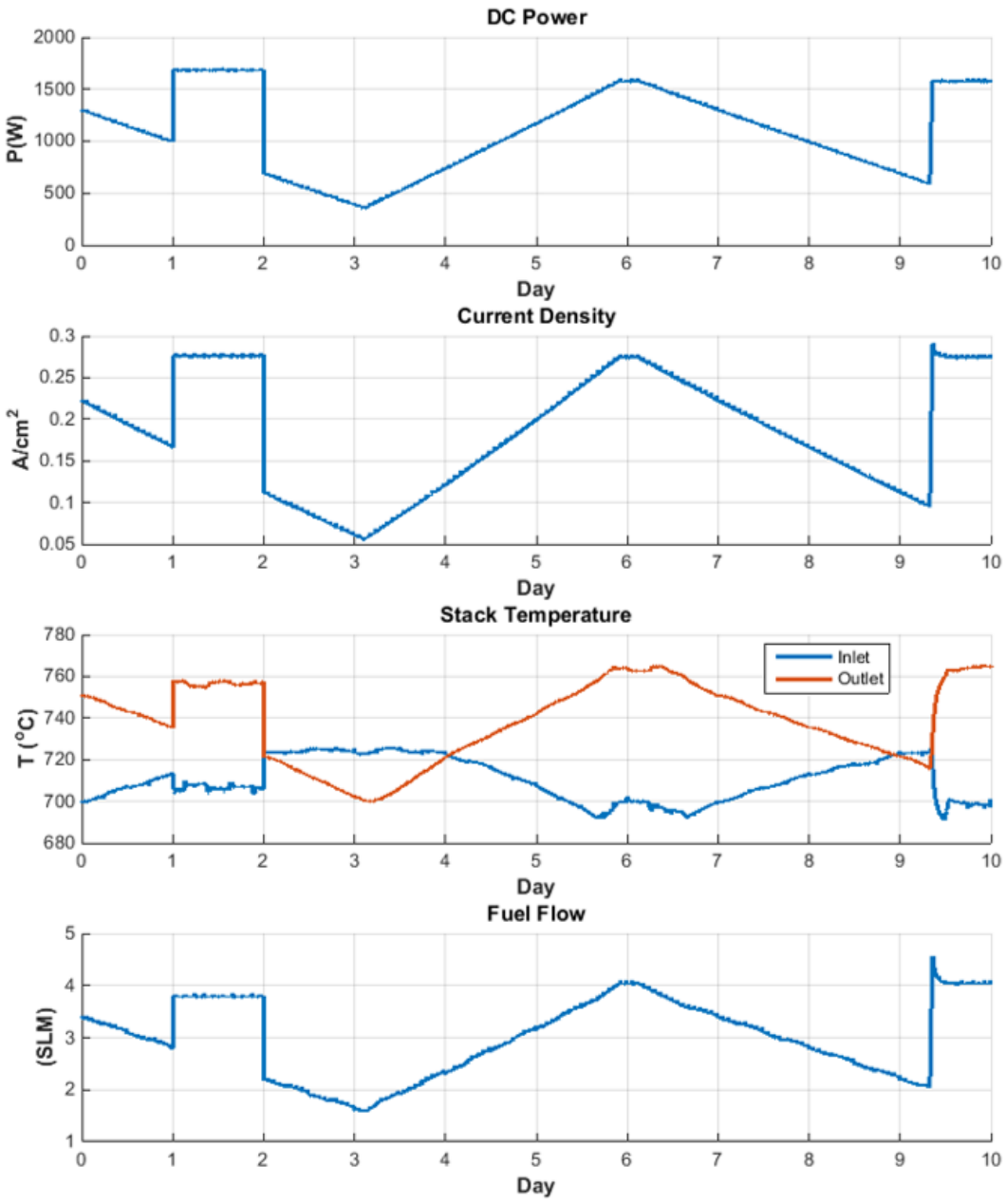

Figure 93. BlueGEN dynamic operation data.

Looking at SOFC dynamic data, it is observed that BlueGEN electrical efficiency is the highest, roughly 64%, at full load. BlueGEN efficiency is the lowest at 30% at 300W of output (the lowest output considered in this dynamic operating test). The BlueGEN system is recommended to run between 1500W and 500W. At the lowest recommended power, the efficiency is roughly 43%. As expected, at loads lower than the nominal power current density drops, and because of lower polarization, voltage increases. Experimental results

show that BlueGEN control system is designed to keep air flow constant and that it changes the fuel utilization and fuel flow proportional to the output power. BlueGEN stack temperature difference is designed to stay at 50°C at full load. The experimental results show that by reducing the load, the temperature difference decreases. The exit temperature drops below the inlet temperature at 700W. At low current density the endothermicity of reformation reaction is higher that exothermicity of electrochemical reaction which causes temperature drop along the cell. Note that while electrochemical efficiency (as indicated by voltage) increases at part-load, fuel utilization is lowered to maintain the overall thermal balance (self-sustaining operation) so that the overall system efficiency drops at part-load conditions. At these part-load conditions the fuel cell stack operates at overall endothermic conditions, which must be matched by heat from the thermal oxidizer that converts the unspent fuel at the lower fuel utilization conditions.

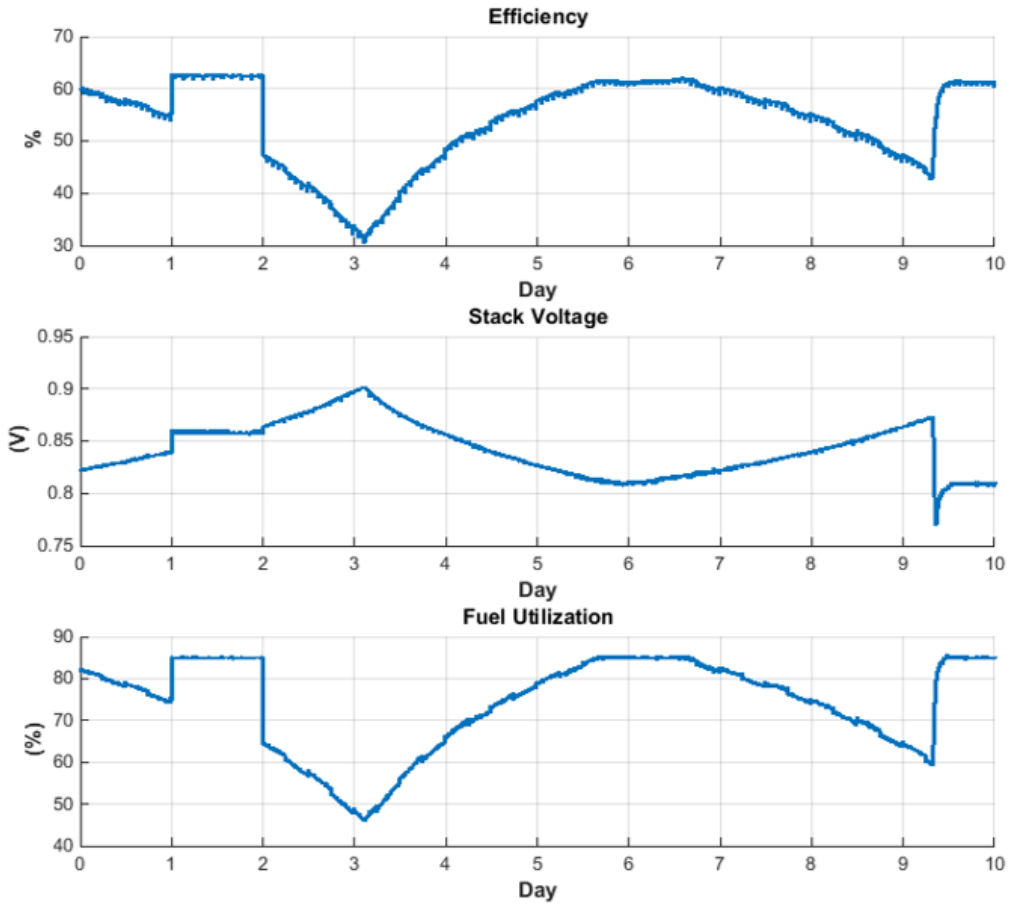

Figure 94. BlueGEN dynamic operation data.

In another dynamic test, the BlueGEN system was tested through the following profile shown in Figure 95 in 24h for 42 days. During this cycle, the power decreases between 1500W to 500W with 100W increments. In each power step the system is given 1 hour to reach to steady state and then it has 15 minutes to ramp down (or up) to the next power level.

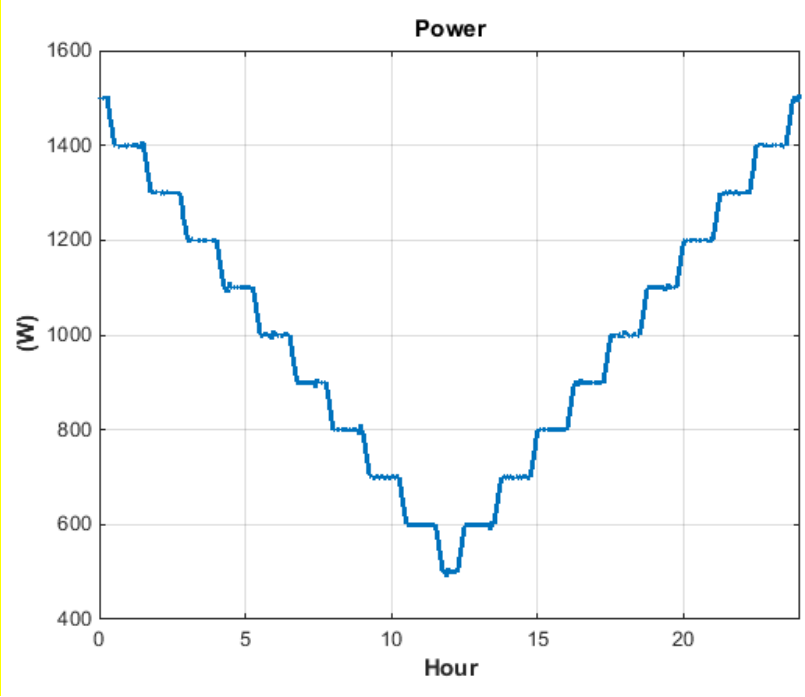

Figure 95. BlueGEN stack power cycle- 24h.

Figure 96 shows the current density and voltage change during the introduced power cycle over the 24hr period. As expected, the current density changes proportional to power profile. Looking at voltage profile in each power step, voltage does not reach to a steady-state and is constantly changing in the 1-hour periods. Stack temperature data in Figure 97 shows that one hour is not enough for the system to reach steady-state temperature due to high thermal inertia of the system which results in the observed voltage changes. Note that during the power decrement dynamics the voltage starts higher than would be expected for steady-state conditions because average stack temperature remains high from the previous higher power conditions. This is expected due to the fact that ohmic losses, which are highly dependent upon temperature, are the dominant polarizations for this SOFC stack. Note that the opposite effect (voltage that is initially lower than steady-state voltage) occurs for the initial response to a power increase dynamic.

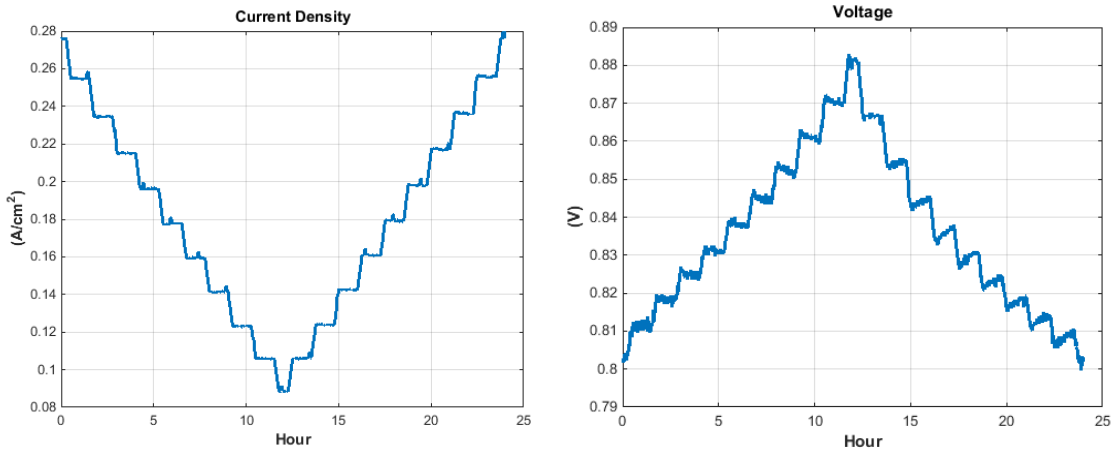

Figure 96. BlueGEN current density and voltage on a 24h cycle.

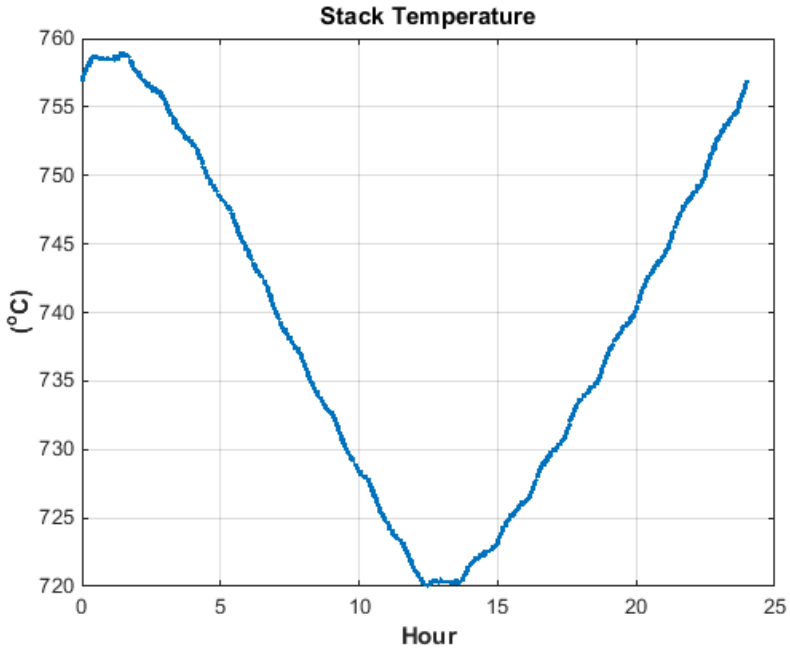

Figure 97. BlueGEN stack temperature on a 24h cycle.

Figure 98 and Figure 99 show BlueGEN performance parameters, temperatures, and flows during ramp up from 500W to 1500W in solid lines and ramp down in dashed line. The hysteresis effect was observed because the system did not reach to steady state during this power cycle in each step.

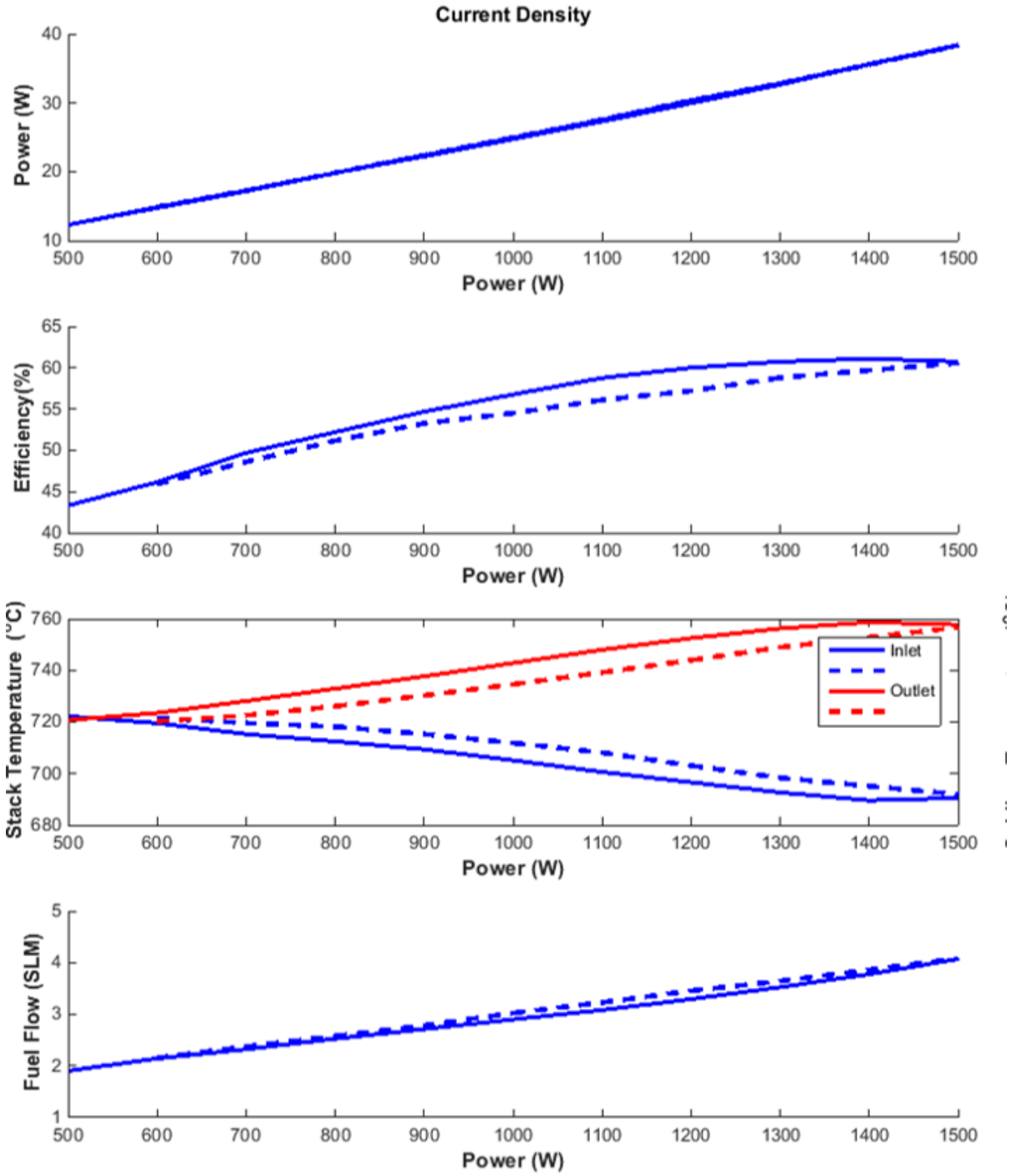

Figure 98. BlueGEN performance under ramp test.

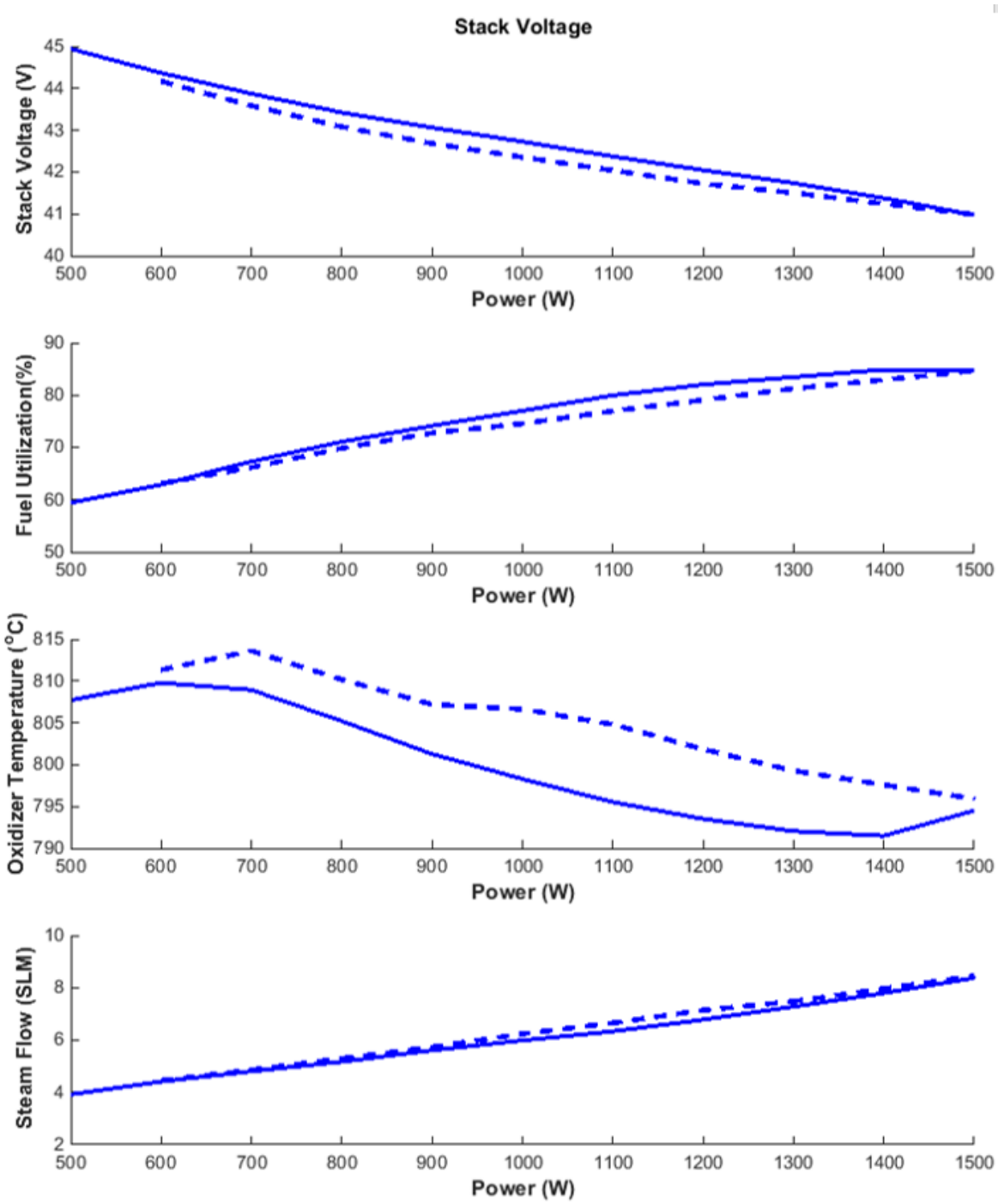

Figure 99. BlueGEN performance under ramp test.

Another set of experiment was conducted to test how long it would take for the BlueGEN to reach steady states. In the new test as it is shown in Figure 100, the BlueGEN runs the same cycle as before, however, in each power step it has 8 hours to reach to steady states. It takes a week for the BlueGEN to go through the new cycle.

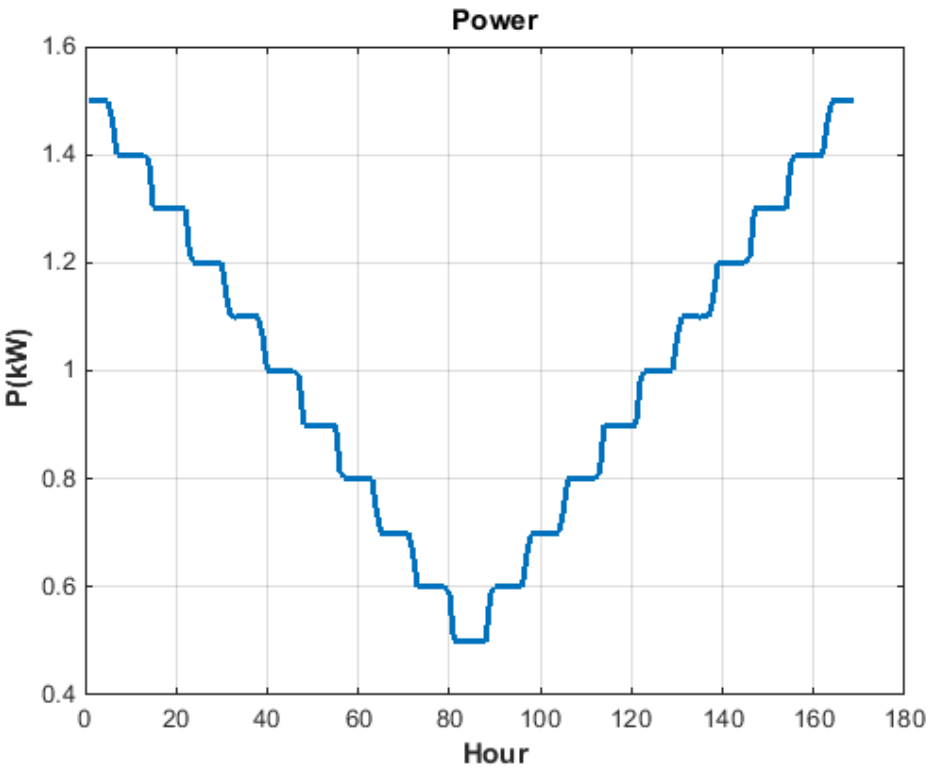

Figure 100. BlueGEN stack power cycle- one week.

Figure 101 and Figure 102 show the voltage and the stack temperature, respectively over a week. Each color is representative of one day data. Looking closer to each power step data, it shows that voltage and temperature changed during the first couple of hours sharply and the BlueGEN system reached to steady states after 5 to 6 hours.

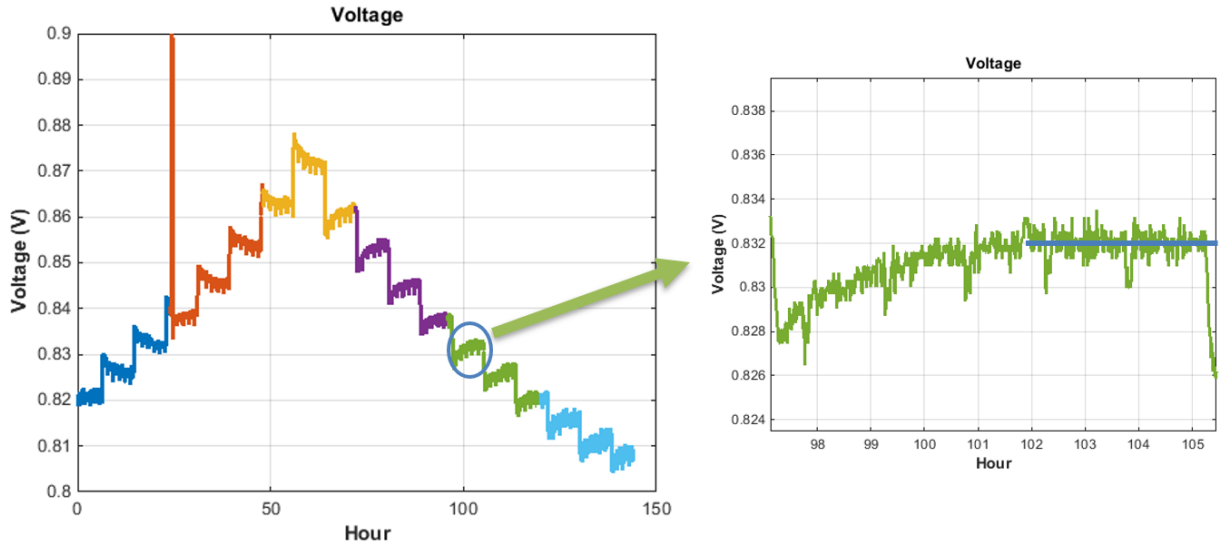

Figure 101. BlueGEN voltage on a one-week cycle.

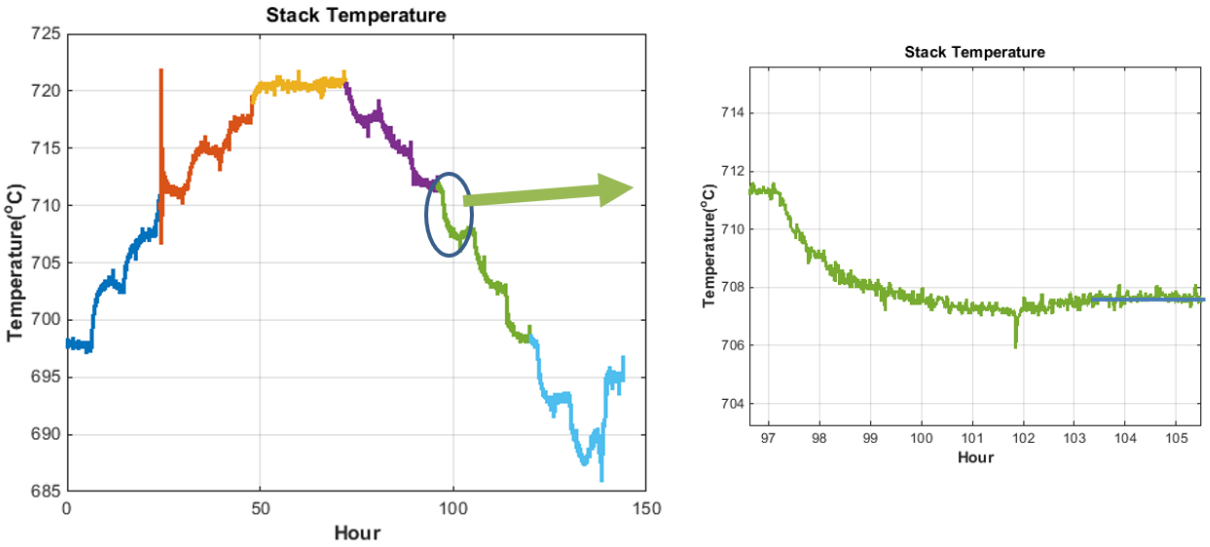

Figure 102. BlueGEN stack temperature on a one-week cycle.

7.3 SOFC Degradation Results

BlueGEN system was tested on power cycle presented on Figure 95 for 42 days. Figure 103 shows the VJ curve for the system on the first day and last day of test. As expected, the hysteresis effect is observed due to not reaching to steady-state at each power step. Results shows that the BlueGEN system degraded by 0.58% for the 42 days of operation (1000h) on

a very highly dynamic set of operating conditions. This degradation is equivalent to 4.7mV/cell.

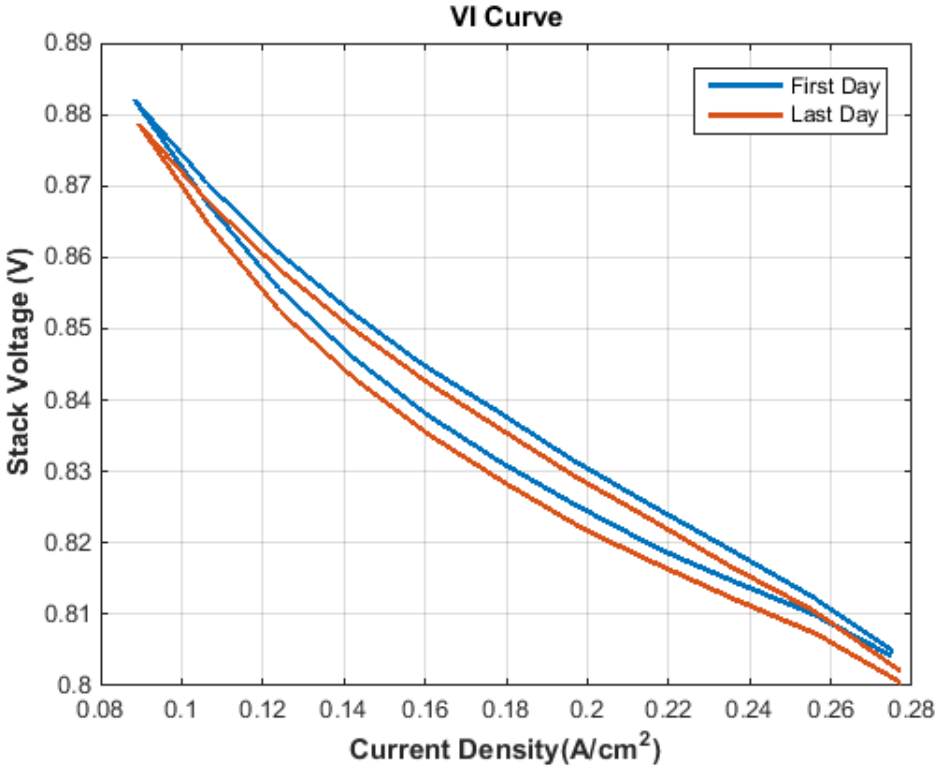

Figure 103. BlueGEN V-J characteristics curve for a 24h power cycle for 42 days

At this writing the BlueGEN system has been running for more than 6000hr from the time of installation at the NFCRC. Figure 104 shows the power profile of BlueGEN system over this 6000h operating period. After 4000 hours of steady-state operation the system runs the first dynamic load Figure 93, then after a couple of days of steady operation it goes through the 24h dynamic load cycles for 1000hr followed by the one-week dynamic cycle. Figure 105 shows the voltage change over the 600hr operation. The system operation is divided to three region and Table 22 shows the degradation results for each of the regions of operation. The BlueGEN degradation rate is 0.25% per 1000hr for the first region of steady-state operation. During the first 1000hr of operation as the system is new the degradation rate is twice that of the regular steady-state operation. Also, the system degrades twice as fast as steady-state operation while operating under highly dynamic operating conditions. As the system degrades, the fuel consumption increases and as a result the overall system efficiency drops.

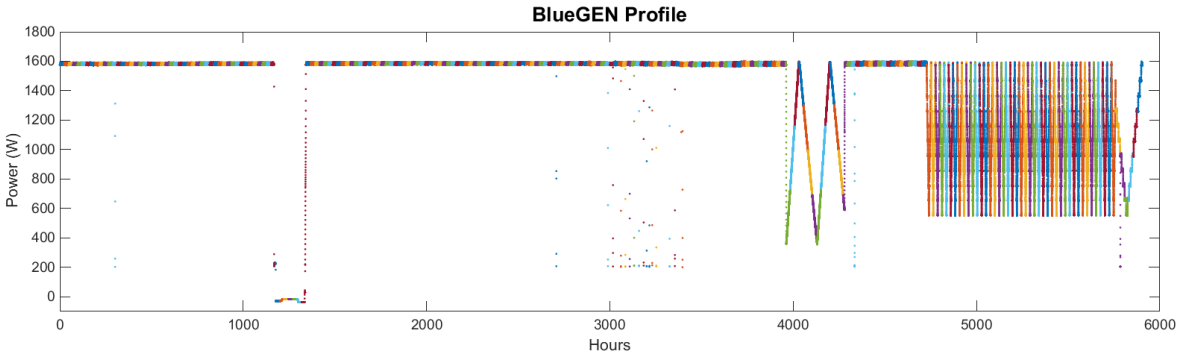

Figure 104. BlueGEN power profile over 6000h operation.

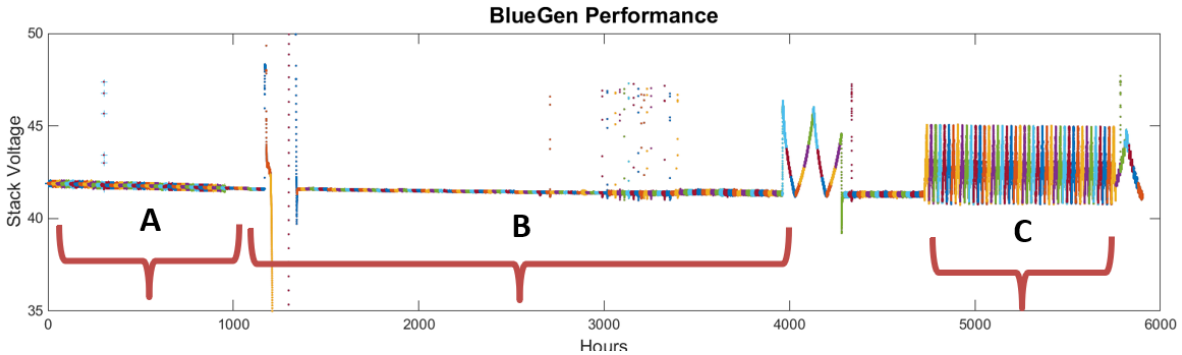

Figure 105. BlueGEN stack voltage (V) during 6000h operation.

Table 22. BlueGEN degradation analysis.

Parameter	A, initial steady-state operation 1000h	B, steady-state operation 3000h	C, dynamic operation 1000h
Degradation per 1000h	0.58%	0.025%	0.59%
Degradation per cell	4.8mV	2mV	4.7mV
Efficiency decrease	0.59%	0.3%	0.58%
Fuel consumption increase	0.6%	0.3%	0.5%

7.4 SOFC cell experimental analysis

For cell level tests, experiments were carried out using a commercial anode supported solid oxide cell. The cell anode side consists of two layers, a thick Ni-YSZ anode support (250-400μm) acting as the mechanical support, current collector and gas diffusion layer, and the other is the functional layer with a more dense structure near the electrode-electrolyte interface (≈10μm thick). The electrolyte consists of 8% mol Y_2O_3-ZrO_2 (YSZ, 5μm thick) on which Gadolinium Doped Ceria oxide (GDC) barrier layer (3μm) is deposited to prevent the formation of insulating $SrZrO_3$. The cathode active layer (15μm thick) was made up of

lanthanum strontium cobalt ferric oxide ($La_{1-x}Sr_xCo_yFe_{1-y}O_{3-\delta}$) in contact with the cathode current collector of similar thermal expansion. The cell had an active area of 12.6cm^2 (cathode diameter of 40mm).

7.4.1 SOFC Cell experimental setup

Figure 106 shows the procedures of mounting a cell. A proper gas tightness and electrical connection is required during this procedure. Insulation and sealing material (Mica) is used alongside glass seals for this purpose (Figure 106.a). Nickel mesh and gold meshes with gold leads are used as the current collectors on the anode (fuel side) and cathode (air side), respectively. The first layer is nickel mesh surrounded with Mica (Figure 106.b). Between the mica and nickel mesh a layer of glass seals is injected (Figure 106.b). The single cell is placed on top of nickel mesh with a layer of glass seals touching the anode side (Figure 106.c). The first layer of alumina felt is placed on top of the cell, and the gold mesh is placed on top of the cathode (Figure 106.d). Gold is used due to lesser reactivity at high temperature in air. The last layer is the alumina felt (Figure 106.e). The porosity of alumina felt helps in distributing the air uniformly over the cathode.

(a)

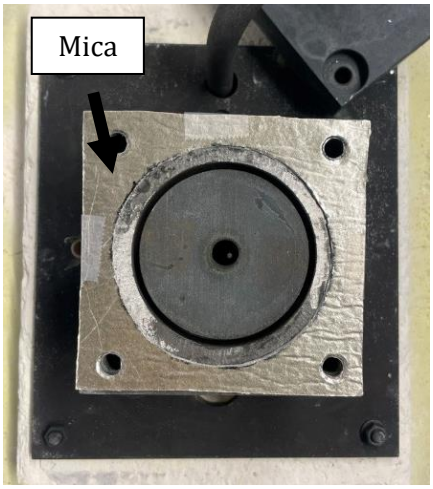

(b)

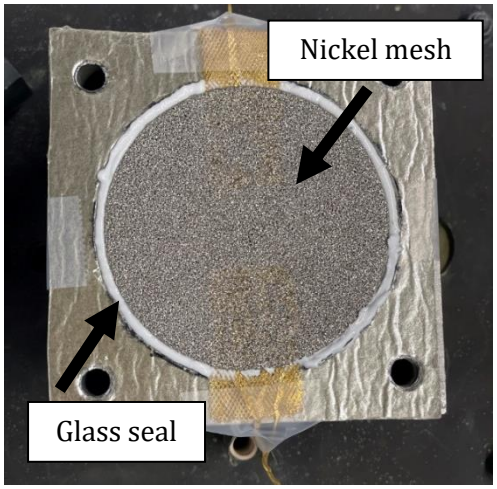

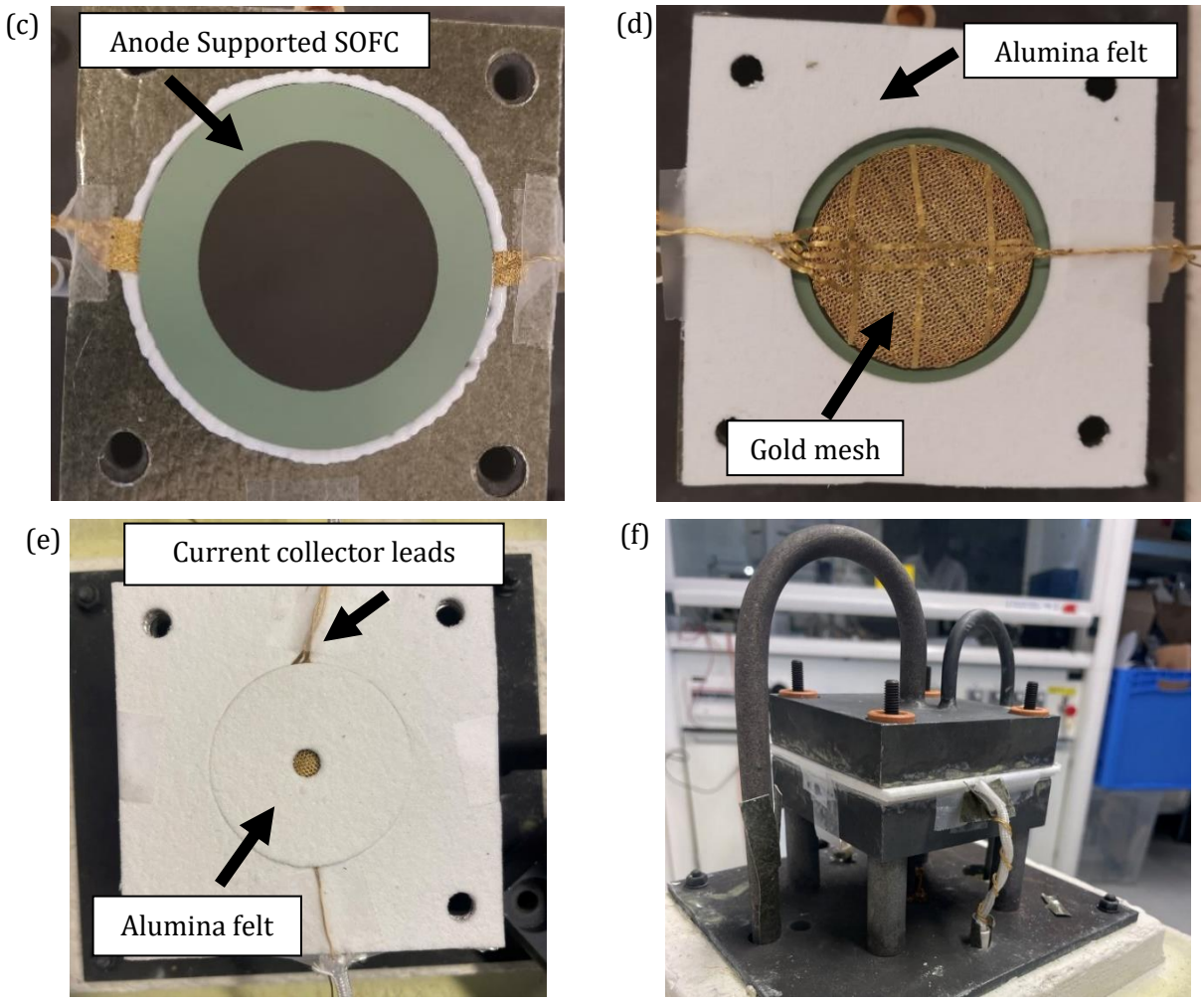

Figure 106. a) 1st layer of mica on the setup b) Nickel mesh along with mica and glass seals (c) Anode supported SOFC placed on the nickel mesh and the glass seal, (d) first layer of alumina felt and gold mesh (e) Alumina felt layer on top of the gold mesh and current collector lead (f) The single cell SOFC subsystem upon closing the top plate.

The experimental setup of the single cell used for each of the three 1000hr tests is shown in Figure 107. The furnace keeps the temperature at constant. The JV scan and EIS measurements were performed with a Zahner Zennium impedence analyzer. Zanher positive terminal connects to the cathode and the negative terminal to anode. The voltage response is also measured via the same system. During EIS measurements constant loads of 0.1, 0.5, and 0.9A/cm^2 were applied to the cell. For applying constant loas of 0.5A/cm^2 during the 1000hr polarization a load box (Elektro Automatik Gmbh) is connected to the setup. The fuel cell air and fuels are supplied by Voegtlin Red-y smart series mass flow controllers. The purity level of hydrogen, nitrogen and ammonia used in the experiments are 99.999%,

99.999% and 99.99% respectively. Nitrogen and hydrogen are stored as compressed gases while ammonia is stored in liquid form in commercial cylinders.

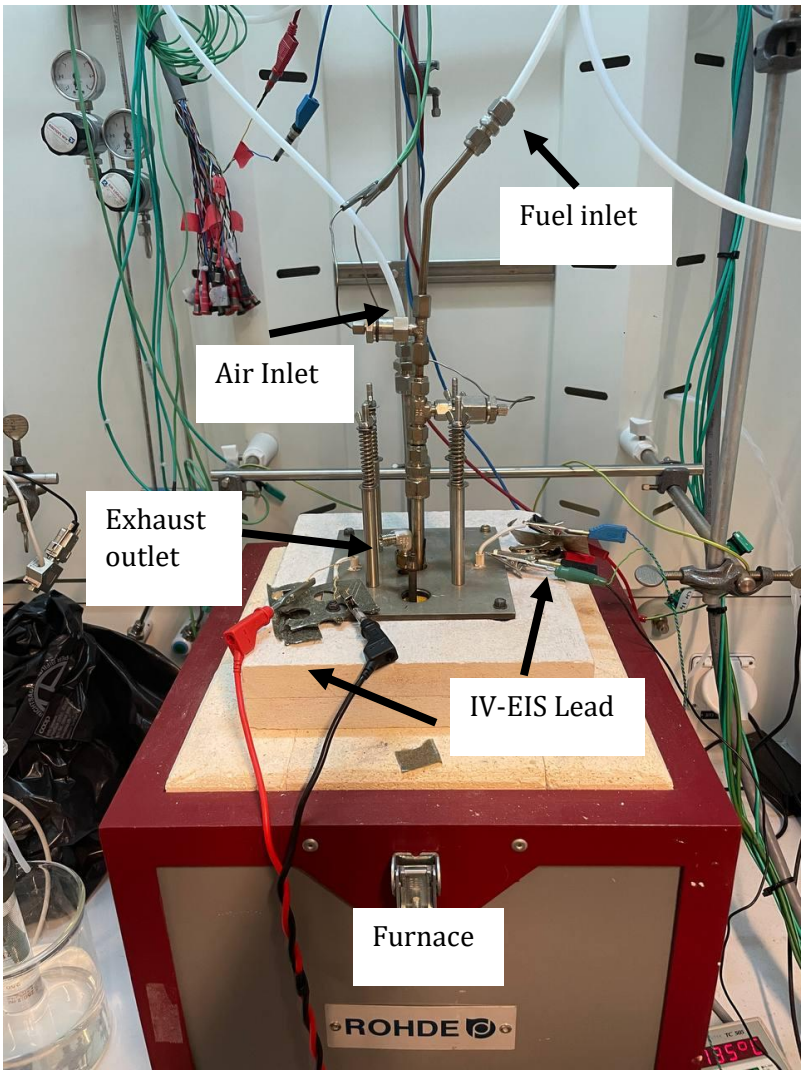

Figure 107. Experimental setup of single cell SOFC system.

7.4.2 Test conditions

The single-cells were tested with three different fuel composition as shown in Each test runs on a pristine single cell SOFC. Cell 1 on pure H2, cell 2 on H2-N2 (simulating the External Ammonia Decomposition Reaction (Ext ADR) case), and cell 3 on NH3 directly, which includes the internal decomposition reaction (Int ADR). A nominal operating temperature of 750°C is chosen for the tests. After mounting each cell, each SOFC cell is reduced in H2 and N2 atmosphere. Each cell runs for 1000hr at 0.5A/cm2 to compare long term effect of

different fuel on SOFC degradation. Dynamic current density (J)- Voltage (V) scans were performed every 100hr from Open Circuit Voltage (OCV) to 700mV at 5mV/s with 1mV resolution. The JV scans are followed by three EIS measurements at 0.1, 0.5, and 0.9A/cm2 and 200mA perturbation signal for a frequency range of 1KHz to 200KHz. The quality of EIS spectra was verified using the Kramer Kronig's (KK) test. The overall test duration of test for each cell was 47 days.

Table 23 to compare the degradation effects between in-situ and ex-situ ammonia reforming with that of pure hydrogen for a duration of 1000h. Each test runs on a pristine single cell SOFC. Cell 1 on pure H_2, cell 2 on H_2-N_2 (simulating the External Ammonia Decomposition Reaction (Ext ADR) case), and cell 3 on NH_3 directly, which includes the internal decomposition reaction (Int ADR). A nominal operating temperature of 750°C is chosen for the tests. After mounting each cell, each SOFC cell is reduced in H_2 and N_2 atmosphere. Each cell runs for 1000hr at 0.5A/cm^2 to compare long term effect of different fuel on SOFC degradation. Dynamic current density (J)- Voltage (V) scans were performed every 100hr from Open Circuit Voltage (OCV) to 700mV at 5mV/s with 1mV resolution. The JV scans are followed by three EIS measurements at 0.1, 0.5, and 0.9A/cm^2 and 200mA perturbation signal for a frequency range of 1KHz to 200KHz. The quality of EIS spectra was verified using the Kramer Kronig's (KK) test. The overall test duration of test for each cell was 47 days.

Table 23. Fuel conditions related to each cell.

Cell number	**Fuel Type**	**N_2 (ml/min)**	**H_2 (ml/min)**	**NH_3 (ml/min)**	**Air (ml/min)**
1	Pure Hydrogen	0	120	0	500
2	External-ADR	40	120	0	500
3	Internal-ADR	0	0	80	500

7.5 SOFC cell experimental results

7.5.1 Voltage degradation

Each cell was subjected to steady state testing for 1000 hours at 0.5A/cm^2 as shown in Figure 108. Figure 109 show the temperature change during these tests. The cell operating on H_2-

N_2 failed at 850hr. A sudden increase in cell temperature was likely the cause of failure. Consequently, the degradation rate for all cells is calculated based on voltage data from time 0 to 850hr. The degradation rate is calculated based on the slope of best linear fit to voltage over time with R^2 value of 98%, 97%, and 93% for H_2, N_2-H_2, and NH_3 respectively. The degradation rate observed for H_2 case is 2.51%kh^{-1}, for NH_3 case is 1.04%kh^{-1} and for N_2-H_2 case is 2.6%kh^{-1}. The cell tested with ammonia shows almost 60% less voltage degradation over time than the other two cases.

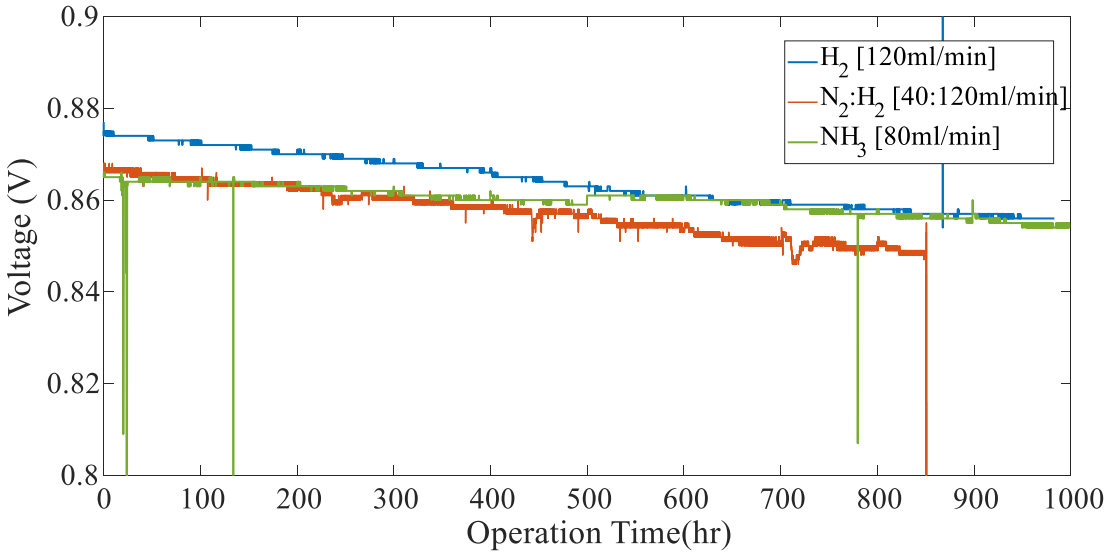

Figure 108. Voltage versus time characteristics of the 3 SOFC cells for the duration of 1000h.

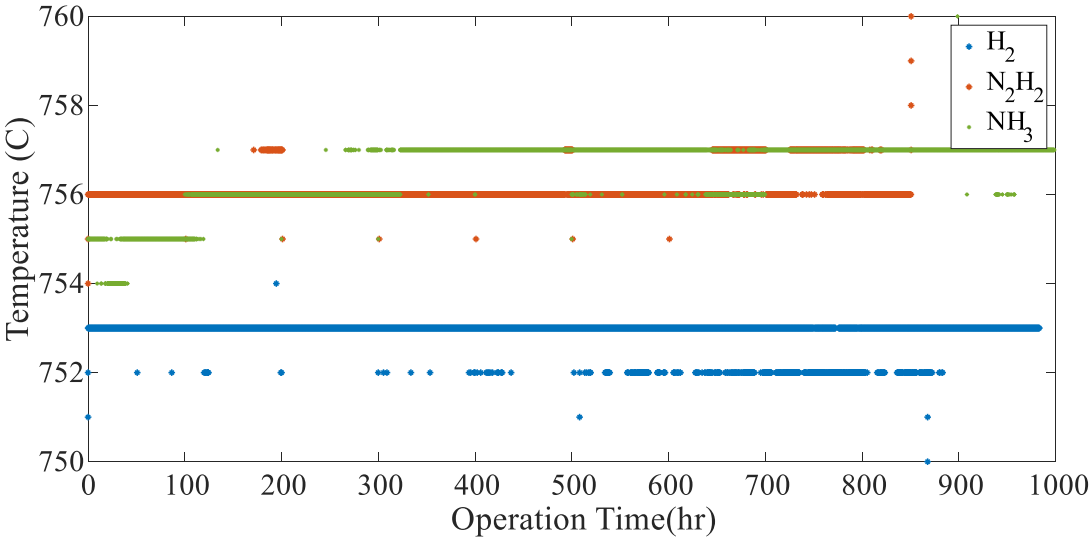

Figure 109. Temperature versus time of the three SOFC cells for the duration of 1000h.

Figure 110 shows the JV characteristics of the three fuel compositions at the beginning of the test and after 800h of test. The results show comparable performance for all three cases. The highest OCV was reached at NH_3 case with 1.228V, suggesting endothermal cracking, while the maximum current density reached was for H_2 at1.06A/cm^2. The OCV achieved for N_2-H_2 and H_2 was slightly lower that NH_3 at 1.199V and 1.215V respectively. The current density reached at 0.7V for N_2-H_2 was 1.02A/cm^2 and for NH_3 was .995A/cm^2. The similarity of OCVs measured proves that hydrogen is electrochemically oxidized after the initial decomposition of ammonia. If ammonia was directly utilized the OCV value should have been significantly higher [147]. Please note that the cell performance as a function of current density is similar operating all on ammonia, hydrogen, and hydrogen/nitrogen. Although power density is slightly lower in the case of NH_3 and N_2-H_2 fuel which could be due to the lower partial pressure of hydrogen.

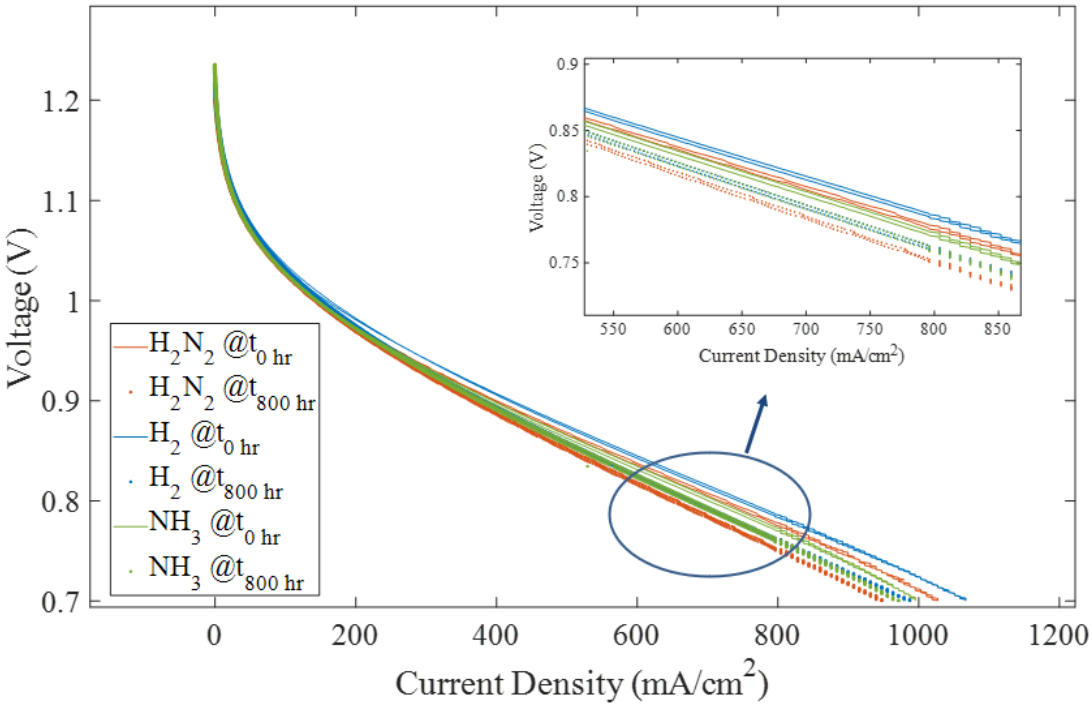

Figure 110. J-V characteristic curve for N_2-H_2, H_2 and NH_3 fuel composition at 750C.

7.5.2 Fuel Composition effect

The inductance and capacitance corrected Nyquist plot of the EIS spectra for different flows at the beginning of the test (t=0hr) and after 800hr at 1.256A are shown in Figure 111(a)

and (b), respectively. The residuals from KK tests were between ±1%. The results show a constant ohmic resistance at the beginning of the test however after 800hr test N_2-H_2 and H_2 case have slightly higher ohmic resistance, while polarization resistance is the highest for ammonia case. The ohmic and polarization resistance are presented at Table 24. It is evident that the increase in total resistance after 800hr test is due to the increase in ohmic resistance. The similarity in EIS between NH_3 and N_2-H_2 proves the two-step utilization of Ammonia as found in literature [64,65,73]. The inductance and capacitance corrected Bode plots (Figure 111(c) and (d)) shows that the NH_3 and H_2-N_2 have similar trends compared to H_2. The charge transfer region (10^1 to 10^3Hz) had lower resistance for H_2 while the gas diffusion resistance was higher for H_2 than the NH_3 and H_2-N_2 cases. This is likely due to higher hydrogen partial pressure in pure hydrogen case, since mass transport losses through the thick anode support may contribute to concentration polarization. These results are consistent with findings in literature [148].

Table 24. Effect of changing different fuel composition (N_2-H_2, NH_3, H_2) on resistance.

Fuel	**Ohmic Resistance (Ωcm^2)**		**Polarization Resistance (Ωcm^2)**	
	t=0hr	T=800hr	t=0hr	T=800hr
H_2	0.1673	0.1878	0.5065	0.5283
N_2H_2	0.1623	0.1920	0.5084	0.5142
NH_3	0.1638	0.1775	0.5213	0.5295

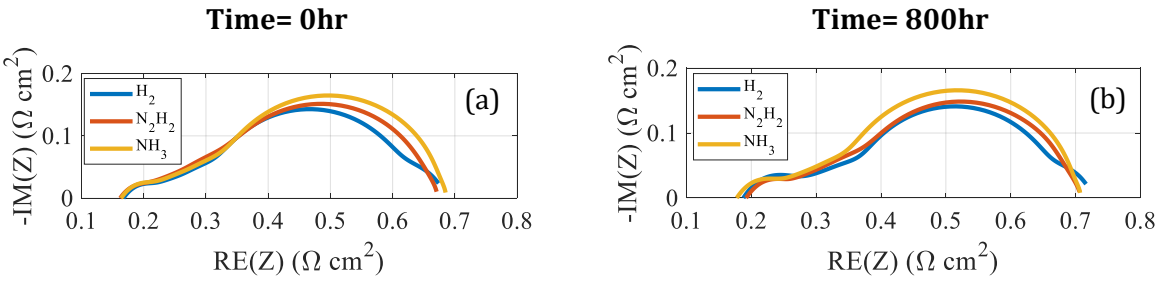

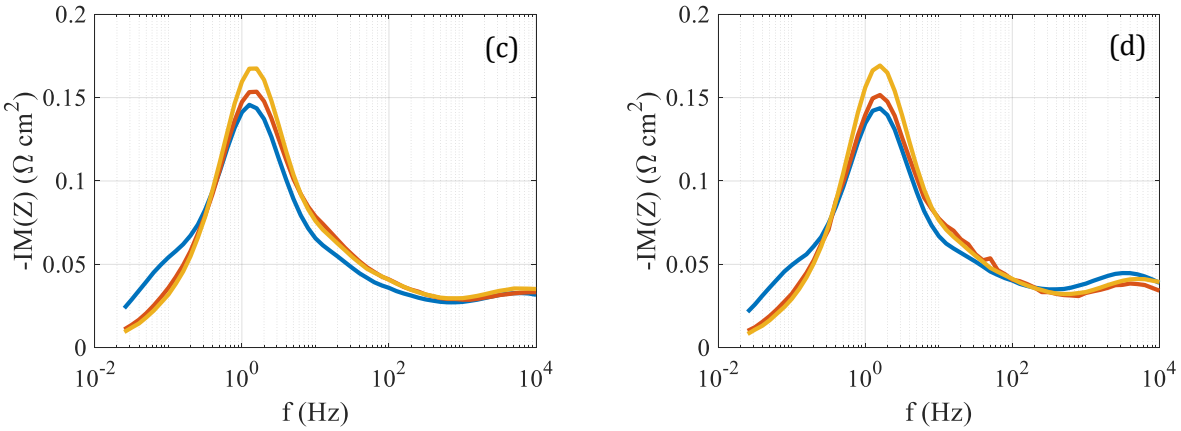

Figure 111. Effect of changing different fuel composition (N_2-H_2, NH_3, H_2) at t=0 and t=800hr. (a) Inductance and capacitance corrected EIS spectra at t=0hr, (b) Inductance and capacitance corrected EIS spectra at =800, (c) Inductance corrected Bode plot at t=0, (d) Inductance corrected Bode plot at t=800.

7.5.3 Effect of time on different fuel for SOFC

Figure 112 shows the effect of time on three cells fueled by H_2, N_2-H_2, and NH_3. The Nyquist plot corresponding to the EIS spectra reveals that in all three cases the ohmic resistance increases as the operating duration increases (12% for H_2, 18% for N_2-H_2 8% for NH_3). The N_2-H_2 case has the highest increase in ohmic resistance over time while the ammonia case has the lowest. The polarization resistance stays almost constant and the increase in total resistance over time is due to the increase in ohmic resistance. The inductance and capacitance corrected Bode plots revealed that the charge transfer frequency region increased in resistance while the gas conversion peaks stay the same as shown in Figure 112.

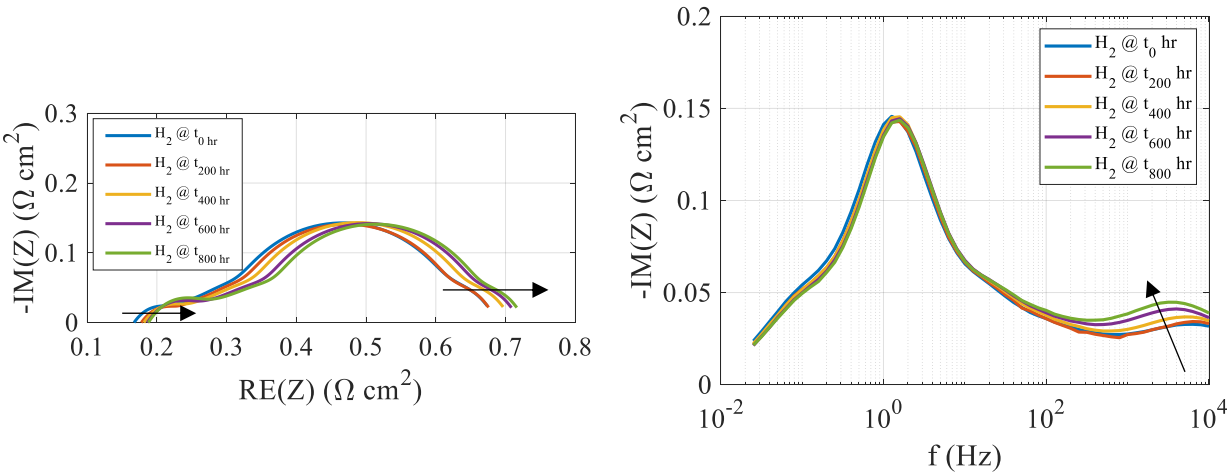

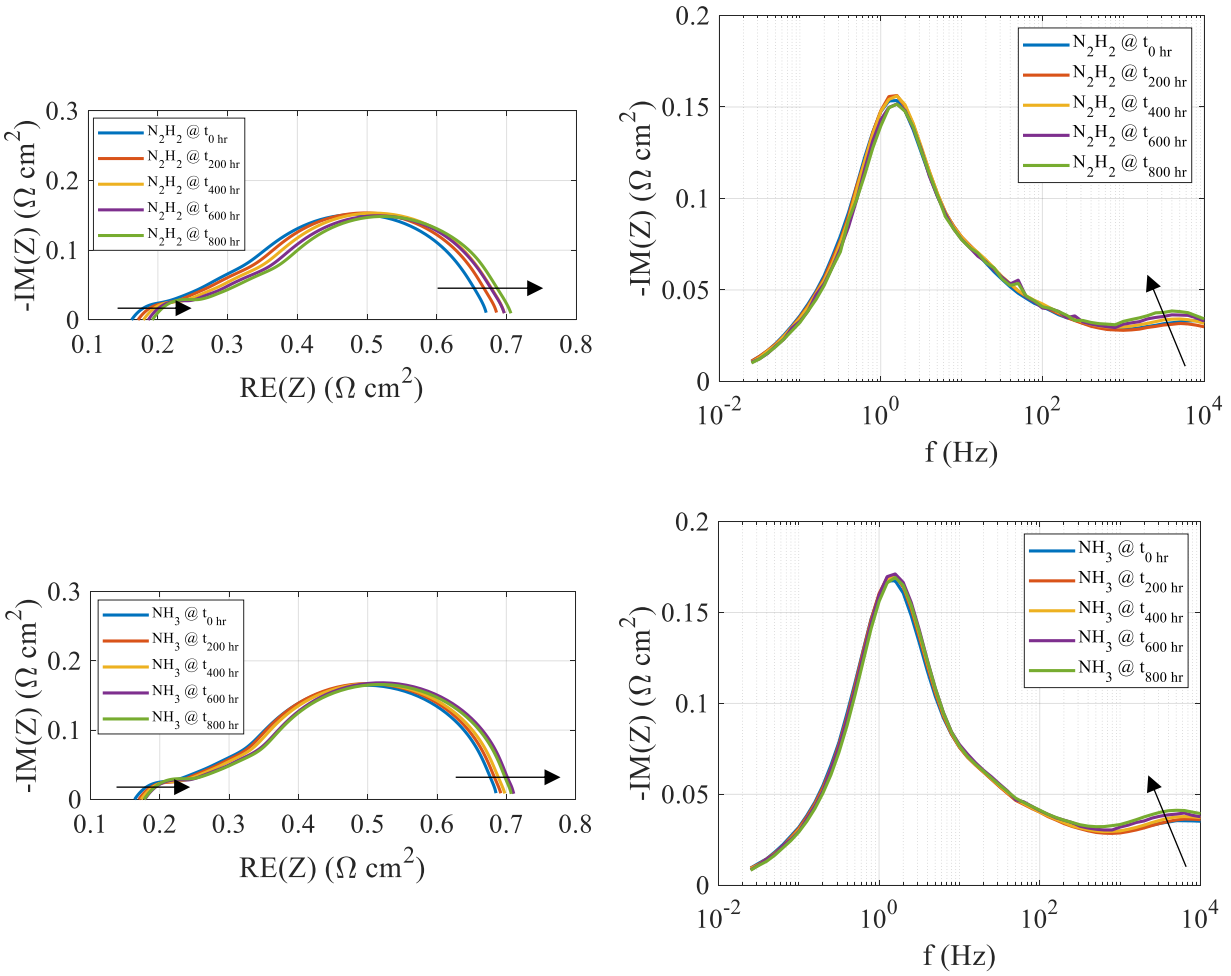

Figure 112. Effect of time on inductance and capacitance corrected EIS on left side and Bode plot on right side for H_2, N_2-H_2, and NH_3.

7.5.4 Microstructural analysis

SEM and EDX investigations were carried out on the anode surface to evaluate the effect of operating NH_3, N_2-H_2, and H_2 on SOFC cell. Figure 113(a) shows the SEM image of an anode after being purges with N_2-H_2 and reduced which is used as the reference cell. Figure 113(b) and (c) shows the anode microstructure inlet and outlet after operating on N_2-H_2. Please note that this cell failed after 850hr of operation therefore the SEM images are taken after 850hr of operation while for NH_3 and H_2 cases the images are taken after 1000hr of operation. As it can be seen, there is no significant changes to microstructure of anode inlet and outlet compared to reference cell. Looking at the SEM image of gas outlet region for H_2 performed cell (Figure 113(e)) signs of potential enlargement of Ni particle is apparent at the surface

level which can be starting for nickel migration; however, the effect is not magnificent enough to effect on quantifications Table 25. The anode microstructures are nearly the same without any crack for NH_3 case as it is shown in Figure 113(f) and (g). Further, the nickel particles are not enlarged suggesting that no significant degradation of the cell anode microstructure occurs after the ammonia exposure for over 1000h operation time. The findings are consistent with findings at [65]. Although no remarkable microstructure degradation signs were observed at SEM imaging, analysis of cross section SEM/EDX image is necessary for further investigation of degradation.

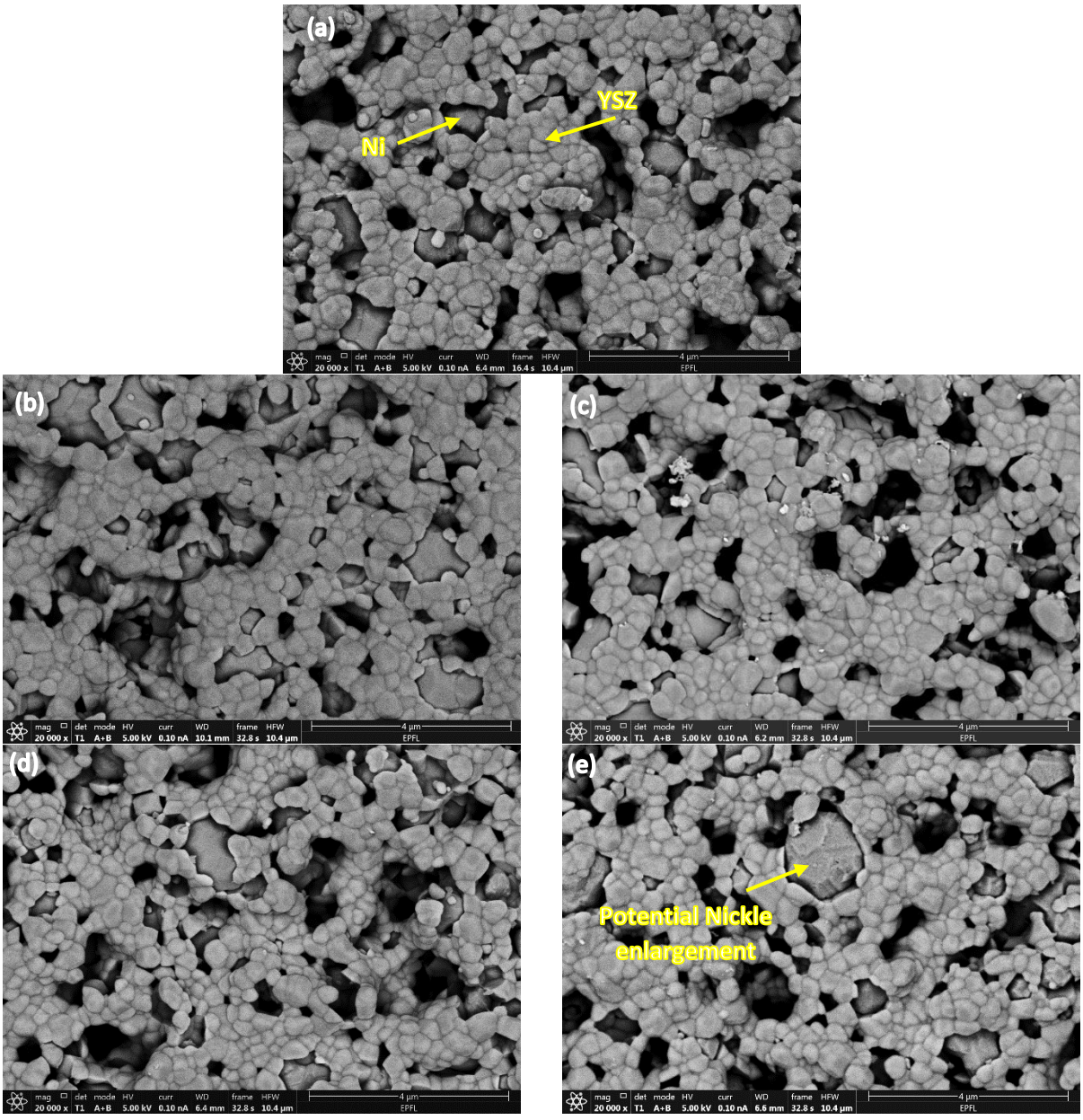

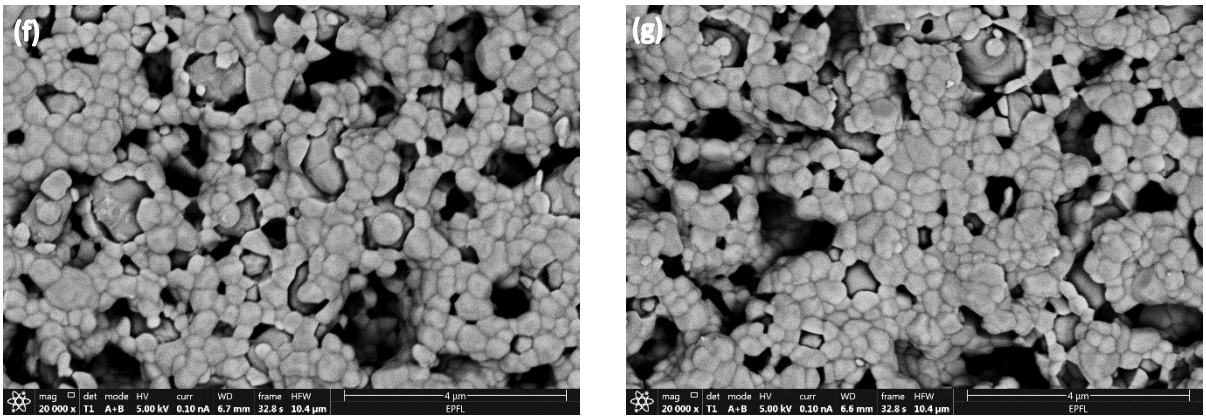

Figure 113. SEM-images taken of the anode surface at fuel inlet (left) and fuel outlet (right) region for (a) reference cell, (b, c) after operation with H_2-N_2 (d, e) after operation with H_2 (f, g) after operation with NH_3.

The aforesaid SEM observations are substantiated by the corresponding EDX quantification, and the data of the element atomic percentages. EDX quantification was done based on three different areas on each sample and the average is reported in Table 25. The nickel, oxygen, and zirconium atomic percentages after the tests with H_2-N_2 and NH_3 did not change significantly compared to the reference cell. The decrease of the nickel percentage is less than 5% as compared to the reference cell. Furthermore, it seems that there is no formation of Ni_3N on the anode surfaces for the 1000h operation time. For N_2-H_2 case there is a significant lower atomic percentage of Ni (20%) and higher percentage of Zr (~12%). The changes are due to the presence of ZrO_2 agglomeration on the surface of anode as shown in Figure 114 which came from the sintering process on zirconia refractories and, as such, are not relevant to degradation processes.

Table 25. EDX quantification analysis for reference cell and after operating on H_2, NH_3, N_2-H_2.

Cell	**Ni**		**Zr**		**Y**		**O**	
	inlet	**outlet**	**inlet**	**outlet**	**inlet**	**outlet**	**inlet**	**outlet**
Reference	28.3		28.8		4.5		38.3	
H2	25.5	23.3	29.4	33.2	5.1	6.3	40.1	37.2
N2-H2	10	9.0	40.3	41.1	7.7	7.8	41.9	42.1
NH3	25.3	24.1	30.5	31.2	5.6	5.8	38.5	38.89

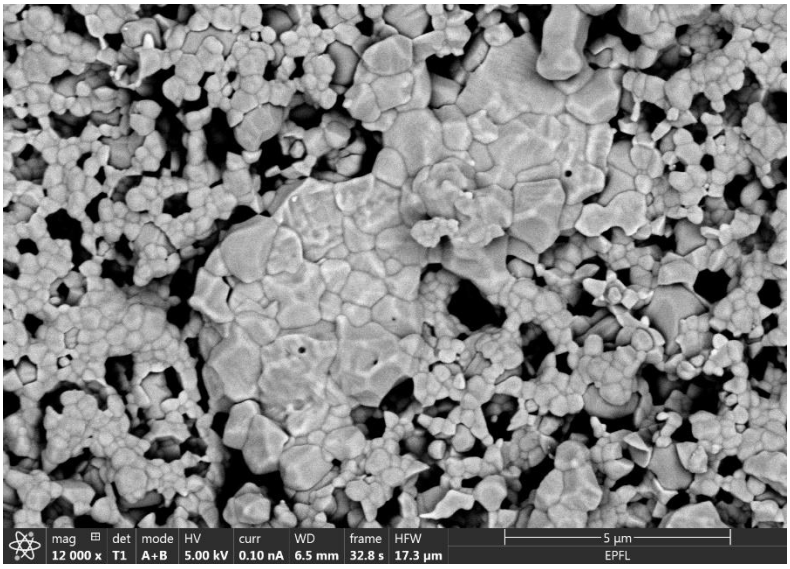

Figure 114. ZrO_2 agglomeration on the surface of anode at N_2-H_2 cell.

7.6 Summary

In this chapter degradation of SOFC was analyzed in various conditions. First the SOFC system degradation was evaluated while operating under steady states and dynamic loads. In order to do so, BlueGEN system was installed at APEP laboratory, and the system first operated under steady state at nominal condition for over 4000hr, and then operated under ramp up and ramp down dynamic load for 1000hr. Results showed that the BlueGEN system degraded 0.59%kh-1 under dynamic operation while depredating 0.025%kh^{-1} under steady state load. In the second part, the degradation of single cell SOFC directly fed with ammonia (NH_3) was analyzed and compared with externally reformed ammonia (N_2-H_2) and pure hydrogen (H_2). The voltage degradation rate observed for H_2 case was 2.51%kh^{-1}, for NH_3 case was 1.04%kh^{-1} and for N_2-H_2 case was 2.6%kh^{-1}. Also, the SEM investigation showed no sign of degradation on the cell anode microstructure occurs after the ammonia exposure.

8 Summary and Conclusions

8.1 Summary

The goal of this research was to first evaluate the integration of an SOFC system with liquid desiccant air conditioning for efficient and reliable data center power and cooling. The second goal was to evaluate the durability of the proposed technology under different dynamic and steady state operation and with different fuels. The goals were achieved by 1. extensive literature review on SOFC technology, degradation, and fuels as well as data center power and cooling and liquid desiccant technology, 2. Developing a dynamic model for BlueGEN SOFC based on EAGERS and validating the model with experimental results, 3. Developing a physical model for liquid desiccant air conditioning and validating the results with literature data, 4. Calculating data center cooling demand based upon cooling type and weather conditions in various locations, 5. Analysis of the integrated system for different weather conditions and determining the storage capacity to meet the annual demand of data centers, 6. experimental set up and long-term test and evaluation of the SOFC system degradation under steady-state and dynamic operation and SOFC cell degradation operating on different fuels. Findings showed that integrated SOFC-AC system coupled with seasonal storage is a great candidate for powering data centers and keeping the server racks in a safe range of temperature and humidity in hot and humid regions. Also, the SOFC technology used in this integrated system can be designed for robust dynamic operation over many years and can likely be fed by ammonia without any negative effect on durability of the system.

8.2 Conclusions

8.2.1 Integrated SOFC-AC for data center

A spatially and temporally resolved physical SOFC system model and a corresponding physical model for liquid desiccant dehumidification were developed and successfully verified by comparison with experimental data and literature data respectively. To simulate the integrated system behavior to meet server power and cooling demand in a data center, first the data center demand was modeled based on weather data. The developed model was

used to simulate the power and cooling for scenario cases with and without storage. The SOFC system could produce enough power for servers in all cases. For a single server case with no storage, the results showed that the SOFC exhaust heat was able to continuously provide almost 25% of server rack required supply air in the safe range of temperature and dehumidification under these conditions. This result showed that to provide enough cooling required for data centers seasonal storage is required. Results from simulating integrated SOFC-AC with seasonal storage showed that for three of the studied locations (Illinois, Iowa, and Virginia) the integrated system can provide enough cold and dehumidified air throughout the entire year, and for the extreme weather condition in Texas it meets up to 85% of the demand in a row level design. The analysis showed that the row level design gives the opportunity to run the fuel cell at partial load with higher efficiency and decreases the infrastructure needed for server cooling. Providing the required cooling for servers through liquid desiccant dehumidification using the high-quality heat of the SOFC exhaust will significantly decrease data center electric power consumption. This configuration offers the potential for high energy efficiency (up to XX% for electricity and YY% for electricity and cooling annually), environmental (up to ZZ% less carbon dioxide emissions) and economic benefits (up to XX% annual energy cost reduction) to data center applications, reducing both greenhouse gas and criteria pollutant emissions.

8.2.2 SOFC experimental and degradation analysis

First, the BlueGEN system was successfully installed and tested for observed degradation under both steady-state and dynamic operating conditions. To evaluate the degradation of BlueGEN system first the system ran under nominal conditions and then under dynamic load cycling conditions for 4000hr and 1000hr respectively. Findings showed that the system degrades twice as fast compared to steady-state operation while operating at a highly dynamic condition. As the system degrades, the fuel consumption increases and as a result the efficiency drops. Even though the SOFC system degrades twice faster in dynamic operation mode, the degradation rate is within the range of SOFC stack healthy lifetime which makes the BlueGEN SOFC technology a great candidate for large scale installation at data centers. Secondly, the objective was to evaluate the influence that ammonia fuel has on anode supported Ni/YSZ single cell compared to externally decomposed ammonia (N_2-H_2)

and pure hydrogen cases. Results showed that the cell voltage and power density were similar for all three cases (degradation of 1.04%kh^{-1}, 2.6%kh^{-1}, and 2.51%kh^{-1} for operation on ammonia, N_2-H_2, and H_2, respectively) and the voltage degradation was lower for ammonia compared to the other two cases. No changes were observed on anode surface for ammonia fed cell within the scale of SEM observation. EDX quantification showed no significant changes in atomic percentage of Ni meaning that there were no signs of nickel nitrite formation. Findings suggests that ammonia has a great potential as a substitute fuel for natural gas or H_2 in SOFCs.

8.3 Future Work

8.3.1 Integrated SOFC-AC for data center

In this dissertation the economic and environmental effects and benefits of this integrated system and comparison to other conventional and competing technologies were not thoroughly evaluated. Also looking into optimizing the integrated system design to minimize the cost and maximize the desiccant storage capacity could be another interesting area to research.

8.3.2 SOFC experimental and degradation analysis

Even though in this dissertation no sign of microstructural degradation was observed within SEM imaging range for NH_3 fed SOFC, a great area for further analysis is investigation of cross-sectional area which enables analysis of ammonia exposure to other cell layers. Also, to study the origin of degradation mechanisms and hence performance losses during the operation, the Distribution of Relaxation Times (DRT) analysis can be the potential next step based upon findings of this research. Also, longer duration operation of SOFC under dynamic operating conditions and with ammonia fuel would help to determine possible degradation impacts.

REFERENCES

[1] Jones N. The information factories. Nature 2018;561:163–6.

[2] Andrae ASG, Edler T. On global electricity usage of communication technology: trends to 2030. Challenges 2015;6:117–57.

[3] Strategy A. SMARTer2030: ICT solutions for 21st century challenges. The Global ESustainability Initiative (GeSI), Brussels, Brussels-Capital Region, Belgium, Tech Rep 2015;3.

[4] Goiri Í, Haque ME, Le K, Beauchea R, Nguyen TD, Guitart J, et al. Matching renewable energy supply and demand in green datacenters. Ad Hoc Networks 2015;25:520–34.

[5] Oró E, Depoorter V, Garcia A, Salom J. Energy efficiency and renewable energy integration in data centres. Strategies and modelling review. Renewable and Sustainable Energy Reviews 2015;42:429–45.

[6] Electric Power Annual 2020. Https://WwwEiaGov/Electricity/Annual/Pdf/EpaPdf n.d.

[7] Zhao L, Brouwer J, Liu J, James S, Siegler J, Kansal A, et al. Fuel cells for data centers: Power generation inches from the server. Microsoft Research, Tech Rep MSR-TR-2014–37 2014.

[8] Rong H, Zhang H, Xiao S, Li C, Hu C. Optimizing energy consumption for data centers. Renewable and Sustainable Energy Reviews 2016;58:674–91.

[9] Data Center Outages are Common, Costly, and Preventable. Https://UptimeinstituteCom/Data-Center-Outages-Are-Common-Costly-and-Preventable n.d.

[10] Mike DeCamp. Eaton's Blackout Tracker Annual Report shows 36.7 million people affected by more than 3,500 power outages in 2017. Https://WwwEatonCom/Us/En-Us/Company/News-Insights/News-Releases/2018/Eaton_s-Blackout-Tracker-Annual-Report-Shows-36-7-Million-PeopleHtml n.d.

[11] Tom Krazit. Microsoft releases details on last week's big Azure outage, during which servers were damaged but no data was lost. Https://WwwGeekwireCom/2018/Microsoft-Releases-Details-Last-Weeks-Big-Azure-Outage-Servers-Damaged-No-Data-Lost/ 2018.

[12] New Thinking on Data Center Power Security. Https://WwwBloomenergyCom/Blog/Category/Data-Center/ n.d.

[13] What is a Data Center? Https://WwwPaloaltonetworksCom/Cyberpedia/What-Is-a-Data-Center n.d.

[14] Data Center Power Design and Features. Data Center Power Https://WwwDigitalrealtyCom/Data-Center-Powerand Features n.d.

[15] Ascierto R. Uptime institute global data center survey. Seattle: Uptime Insitute Https://Uptimeinstitute Com/Uptime_assets/F7bb01a900c060cc9abe42bb084609f 63f02e448f5df1ca7ba7fdebb746cd1c4-2018-Data-Center-Industry-Survey Pdf 2018.

[16] Bob West. Understanding the Interplay Between Data Center Power Consumption/Data Center Energy Consumption and Power Density. Https://WwwDatacentersCom/News/Understanding-the-Interplay-between-Data-Center-Power-Consumption-Data-Center-En 2018.

[17] TC A. Data center power equipment thermal guidelines and Best practices. ASHRAE TC 99, ASHRAE, USA 2016.

[18] Salim RI, Noura H, Nabag M, Fardoun A. Modeling and temperature analysis of the nexa 1.2 kw fuel cell system. Journal of Fuel Cell Science and Technology 2015;12.

[19] Stephen J. Bigelow. Fee Cooling. Https://WwwTechtargetCom/Searchdatacenter/Definition/Free-Cooling?_gl=1*1i5xvc9*_ga*NzE0NzE4MDM1LjE2MTExNjk1OTk*_ga_RRBYR9CGB9*MTYxMjgwNTk5OC4yLjEuMTYxMjgwNjk5MC4w&_ga=2973131191364078739161280599 9-714718035161116959 9 n.d.

[20] Adam Meyer. Adiabatic cooling: best of both worlds. Https://WwwDatacenterdynamicsCom/En/Opinions/Adiabatic-Cooling-Best-of-Both-Worlds/ n.d.

[21] Hans Vreeburg. Indirect Adiabatic Data Center Cooling. Https://DatacenterCom/News_and_insight/Indirect-Adiabatic-Data-Center-Cooling/ n.d.

[22] Saito M, Yoshida H, Iwamoto Y, Ueda A. An analysis of a micro cogeneration system composed of solid oxide fuel cell, microturbine, and h2o/libr absorption refrigerator. Journal of Thermal Science and Technology 2007;2:168–79.

[23] Chan SH, Ho HK, Tian Y. Modelling of simple hybrid solid oxide fuel cell and gas turbine power plant. J Power Sources 2002;109:111–20.

[24] Yi Y, Rao AD, Brouwer J, Samuelsen GS. Analysis and optimization of a solid oxide fuel cell and intercooled gas turbine (SOFC–ICGT) hybrid cycle. Journal of Power Sources 2004;132:77–85.

[25] Zhang X, Li J, Li G, Feng Z. Cycle analysis of an integrated solid oxide fuel cell and recuperative gas turbine with an air reheating system. J Power Sources 2007;164:752–60.

[26] Burbank Jr W, Witmer D, Holcomb F. Model of a novel pressurized solid oxide fuel cell gas turbine hybrid engine. Journal of Power Sources 2009;193:656–64.

[27] Haseli Y, Dincer I, Naterer GF. Thermodynamic modeling of a gas turbine cycle combined with a solid oxide fuel cell. Int J Hydrogen Energy 2008;33:5811–22.

[28] Bao C, Cai N, Croiset E. A multi-level simulation platform of natural gas internal reforming solid oxide fuel cell–gas turbine hybrid generation system–Part II. Balancing units model library and system simulation. Journal of Power Sources 2011;196:8424–34.

[29] Bao C, Shi Y, Li C, Cai N, Su Q. Multi-level simulation platform of SOFC–GT hybrid generation system. International Journal of Hydrogen Energy 2010;35:2894–9.

[30] Hirschenhofer JH SDERKM. Fuel Cell Handbook. 4th ed. EG&G Services Parsons, Inc. Science Applications International Corporation; 1998.

[31] Mueller F, Gaynor R, Auld AE, Brouwer J, Jabbari F, Samuelsen GS. Synergistic integration of a gas turbine and solid oxide fuel cell for improved transient capability. Journal of Power Sources 2008;176:229–39.

[32] Akkaya AV, Sahin B. A study on performance of solid oxide fuel cell-organic Rankine cycle combined system. International Journal of Energy Research 2009;33:553–64.

[33] Al-Sulaiman FA, Dincer I, Hamdullahpur F. Energy analysis of a trigeneration plant based on solid oxide fuel cell and organic Rankine cycle. International Journal of Hydrogen Energy 2010;35:5104–13.

[34] Ghirardo F, Santin M, Traverso A, Massardo A. Heat recovery options for onboard fuel cell systems. International Journal of Hydrogen Energy 2011;36:8134–42.

[35] Al-Sulaiman FA, Hamdullahpur F, Dincer I. Efficiency and environmental impact assessments of a trigeneration plant using sofc and orc. Proceedings of the Global Conference on Global Warming, Istanbul, Turkey, vol. 11, 2009.

[36] Al-Sulaiman FA, Dincer I, Hamdullahpur F. Exergy analysis of an integrated solid oxide fuel cell and organic Rankine cycle for cooling, heating and power production. J Power Sources 2010;195:2346–54.

[37] Al-Sulaiman FA, Hamdullahpur F, Dincer I. Greenhouse gas emission and exergy assessments of an integrated organic Rankine cycle with a biomass combustor for combined cooling, heating and power production. Applied Thermal Engineering 2011;31:439–46.

[38] Pierobon L, Rokni M, Larsen U, Haglind F. Thermodynamic analysis of an integrated gasification solid oxide fuel cell plant combined with an organic Rankine cycle. Renewable Energy 2013;60:226–34.

[39] Al-Sulaiman FA, Hamdullahpur F, Dincer I. Performance comparison of three trigeneration systems using organic rankine cycles. Energy 2011;36:5741–54.

[40] Margalef P, Samuelsen S. Integration of a molten carbonate fuel cell with a direct exhaust absorption chiller. Journal of Power Sources 2010;195:5674–85.

[41] Silveira JL, Leal EM, Ragonha Jr LF. Analysis of a molten carbonate fuel cell: cogeneration to produce electricity and cold water. Energy 2001;26:891–904.

[42] Leal EM, Silveira JL. Study of fuel cell co-generation systems applied to a dairy industry. Journal of Power Sources 2002;106:102–8.

[43] Liu Y, Leong KC. Numerical study of an internal-reforming solid oxide fuel cell and adsorption chiller co-generation system. J Power Sources 2006;159:501–8.

[44] Yu Z, Han J, Cao X, Chen W, Zhang B. Analysis of total energy system based on solid oxide fuel cell for combined cooling and power applications. International Journal of Hydrogen Energy 2010;35:2703–7.

[45] Zink F, Lu Y, Schaefer L. A solid oxide fuel cell system for buildings. Energy Conversion and Management 2007;48:809–18.

[46] Yu Z, Han J, Cao X. Investigation on performance of an integrated solid oxide fuel cell and absorption chiller tri-generation system. Int J Hydrogen Energy 2011;36:12561–73.

[47] Asghari M, Brouwer J. Integration of a solid oxide fuel cell with an organic rankine cycle and absorption chiller for dynamic generation of power and cooling for a residential application. Fuel Cells 2019;19:361–73.

[48] Mehrpooya M, Dehghani H, Moosavian SMA. Optimal design of solid oxide fuel cell, ammonia-water single effect absorption cycle and Rankine steam cycle hybrid system. J Power Sources 2016;306:107–23.

[49] Rokni M. Design and analysis of a waste gasification energy system with solid oxide fuel cells and absorption chillers. International Journal of Hydrogen Energy 2018;43:5922–38.

[50] Tian M, Yu Z, Zhao H, Yin J. Thermodynamic analysis of an integrated solid oxide fuel cell, Organic Rankine Cycle and absorption chiller trigeneration system with CO2 capture. Energy Conversion and Management 2018;171:350–60.

[51] de Arespacochaga N, Valderrama C, Mesa C, Bouchy L, Cortina JL. Biogas deep clean-up based on adsorption technologies for Solid Oxide Fuel Cell applications. Chemical Engineering Journal 2014;255:593–603.

[52] Palomba V, Ferraro M, Frazzica A, Vasta S, Sergi F, Antonucci V. Dynamic simulation of a multi-generation system, for electric and cooling energy provision, employing a SOFC cogenerator and an adsorption chiller. Energy Procedia 2017;143:416–23.

[53] Palomba V, Ferraro M, Frazzica A, Vasta S, Sergi F, Antonucci V. Experimental and numerical analysis of a SOFC-CHP system with adsorption and hybrid chillers for telecommunication applications. Applied Energy 2018;216:620–33.

[54] Wu C-C, Chen T-L. Design and dynamics simulations of small scale solid oxide fuel cell tri-generation system. Energy Conversion and Management: X 2019;1:100001.

[55] eBay plans for 6 MW of Bloom SOFCs to power new data centre. Fuel Cells Bulletin 2012;2012:5. https://doi.org/https://doi.org/10.1016/S1464-2859(12)70196-7.

[56] Apple doubles fuel cell capacity at NC data centre with Bloom. Fuel Cells Bulletin 2013;2013:5. https://doi.org/https://doi.org/10.1016/S1464-2859(13)70011-7.

[57] Bloom to power 12 Equinix data centres in US. Fuel Cells Bulletin 2017;2017:1. https://doi.org/https://doi.org/10.1016/S1464-2859(17)30276-6.

[58] Zhao L, Brouwer J, James S, Peterson E, Wang D, Liu J. Fuel cell powered data centers: In-rack dc generation. ECS Transactions 2016;71:131.

[59] Etemadieh AA. Verification of a Solid Oxide Fuel Cell System for In-Rack Server Power Generation in Data Centers. University of California, Irvine; 2016.

[60] Cummins, McKinstry, Microsoft open energy lab in Seattle to test fuel cells in data centres. Fuel Cells Bulletin 2017;2017:1. https://doi.org/https://doi.org/10.1016/S1464-2859(17)30309-7.

[61] Ritchie AJ, Brouwer J. Design of fuel cell powered data centers for sufficient reliability and availability. Journal of Power Sources 2018;384:196–206.

[62] Saur G, Hammond SW, Kurtz JM, Cader T, Thoss D, Ecker S, et al. Radical Re-Envisioning of Data Centers with Row-Integrated Fuel Cells. National Renewable Energy Lab.(NREL), Golden, CO (United States); 2020.

[63] Afif A, Radenahmad N, Cheok Q, Shams S, Kim JH, Azad AK. Ammonia-fed fuel cells: a comprehensive review. Renewable and Sustainable Energy Reviews 2016;60:822–35.

[64] Yang J, Molouk AFS, Okanishi T, Muroyama H, Matsui T, Eguchi K. A stability study of Ni/Yttria-stabilized zirconia anode for direct ammonia solid oxide fuel cells. ACS Appl Mater Interfaces 2015;7:28701–7.

[65] Fuerte A, Valenzuela RX, Escudero MJ, Daza L. Ammonia as efficient fuel for SOFC. Journal of Power Sources 2009;192:170–4.

[66] Cinti G, Desideri U, Penchini D, Discepoli G. Experimental analysis of SOFC fuelled by ammonia. Fuel Cells 2014;14:221–30.

[67] Dekker NJJ, Rietveld G. Highly efficient conversion of ammonia in electricity by solid oxide fuel cells 2006.

[68] Wojcik A, Middleton H, Damopoulos I. Ammonia as a fuel in solid oxide fuel cells. Journal of Power Sources 2003;118:342–8.

[69] Fournier GGM, Cumming IW, Hellgardt K. High performance direct ammonia solid oxide fuel cell. J Power Sources 2006;162:198–206.

[70] Ma Q, Ma J, Zhou S, Yan R, Gao J, Meng G. A high-performance ammonia-fueled SOFC based on a YSZ thin-film electrolyte. Journal of Power Sources 2007;164:86–9.

[71] ZHANG L, You C, Weishen Y, Liwu LIN. A direct ammonia tubular solid oxide fuel cell. Chinese Journal of Catalysis 2007;28:749–51.

[72] Meng G, Jiang C, Ma J, Ma Q, Liu X. Comparative study on the performance of a SDC-based SOFC fueled by ammonia and hydrogen. Journal of Power Sources 2007;173:189–93.

[73] Stoeckl B, Subotić V, Preininger M, Schwaiger M, Evic N, Schroettner H, et al. Characterization and performance evaluation of ammonia as fuel for solid oxide fuel cells with Ni/YSZ anodes. Electrochim Acta 2019;298:874–83.

[74] Hung YT, Shy SS. A pressurized ammonia-fed planar anode-supported solid oxide fuel cell at 1–5 atm and 750–850° C and its loaded short stability test. International Journal of Hydrogen Energy 2020;45:27597–610.

[75] Nóbrega CEL, Brum NCL. Desiccant-assisted cooling: fundamentals and applications. Springer; 2013.

[76] Elmer T. A novel SOFC tri-generation system for building applications. Springer; 2016.

[77] Welch T, Carwarardine H, Butcher K. CIBSE Knowledge Series: KS13-Refrigeration 2008.

[78] Ouazia B, Barhoun H, Haddad K, Armstrong M, Marchand RG, Szadkowski F. Desiccant-evaporative cooling system for residential buildings. 12th Canadian Conference on Building Science and Technology, Institute for Research in Construction; 2009, p. 1–12.

[79] Liquid Desiccants. Http://AilrCom/Liquid-Desiccant/Ld-Tutorial/ n.d.

[80] Betts D, Ally MR, Mudiraj S, Tilghman M, Graham M. Small Business Voucher CRADA Report: Natural Gas Powered HVAC System for Commercial and Residential Buildings. Oak Ridge National Lab.(ORNL), Oak Ridge, TN (United States). Building …; 2017.

[81] Mei L, Dai YJ. A technical review on use of liquid-desiccant dehumidification for air-conditioning application. Renewable and Sustainable Energy Reviews 2008;12:662–89.

[82] Liu X, Jiang Y, Liu S, Chen X. Research progress in liquid desiccant air-conditioning devices and systems. Frontiers of Energy and Power Engineering in China 2010;4:55–65.

[83] Kozubal E, Woods J, Burch J, Boranian A, Merrigan T. Desiccant enhanced evaporative air-conditioning (DEVap): evaluation of a new concept in ultra efficient air conditioning. National Renewable Energy Lab.(NREL), Golden, CO (United States); 2011.

[84] Chen X, Riffat S, Bai H, Zheng X, Reay D. Recent progress in liquid desiccant dehumidification and air-conditioning: A review. Energy and Built Environment 2020;1:106–30.

[85] Liu XH, Jiang Y, Yi XQ. Effect of regeneration mode on the performance of liquid desiccant packed bed regenerator. Renewable Energy 2009;34:209–16.

[86] Zuber A, Checoni RF, Mathew R, Santos JPL, Tavares FW, Castier M. Thermodynamic properties of 1: 1 salt aqueous solutions with the electrolattice equation of state. Oil & Gas Science and Technology–Revue d'IFP Energies Nouvelles 2013;68:255–70.

[87] Sun J, Gong XL, Shi MH. Study on vapor pressure of liquid desiccants solution. J Refrig 2004;25:28–30.

[88] Ahmed SY, Gandhidasan P, Al-Farayedhi AA. Thermodynamic analysis of liquid desiccants. Solar Energy 1998;62:11–8.

[89] Elmer T, Worall M, Wu S, Riffat S. An experimental study of a novel integrated desiccant air conditioning system for building applications. Energy and Buildings 2016;111:434–45.

[90] Longo GA, Gasparella A. Experimental and theoretical analysis of heat and mass transfer in a packed column dehumidifier/regenerator with liquid desiccant. International Journal of Heat and Mass Transfer 2005;48:5240–54.

[91] Liu XH, Zhang Y, Qu KY, Jiang Y. Experimental study on mass transfer performances of cross flow dehumidifier using liquid desiccant. Energy Conversion and Management 2006;47:2682–92.

[92] Gao WZ, Shi YR, Cheng YP, Sun WZ. Experimental study on partially internally cooled dehumidification in liquid desiccant air conditioning system. Energy Build 2013;61:202–9.

[93] Bansal P, Jain S, Moon C. Performance comparison of an adiabatic and an internally cooled structured packed-bed dehumidifier. Applied Thermal Engineering 2011;31:14–9.

[94] Abdel-Salam AH, Simonson CJ. State-of-the-art in liquid desiccant air conditioning equipment and systems. Renewable and Sustainable Energy Reviews 2016;58:1152–83.

[95] Bansal P, Jain S, Moon C. Performance comparison of an adiabatic and an internally cooled structured packed-bed dehumidifier. Applied Thermal Engineering 2011;31:14–9.

[96] Liu XH, Jiang Y. Handling zone dividing method in packed bed liquid desiccant dehumidification/regeneration process. Energy Convers Manag 2009;50:3024–34.

[97] Woods J, Kozubal E. A desiccant-enhanced evaporative air conditioner: Numerical model and experiments. Energy Conversion and Management 2013;65:208–20.

[98] She X, Yin Y, Zhang X. Thermodynamic analysis of a novel energy-efficient refrigeration system subcooled by liquid desiccant dehumidification and evaporation. Energy Convers Manag 2014;78:286–96.

[99] Khalil A. An experimental study on multi-purpose desiccant integrated vapor-compression air-conditioning system. Int J Energy Res 2012;36:535–44.

[100] Bassuoni MM. Experimental performance study of a proposed desiccant based air conditioning system. Journal of Advanced Research 2014;5:87–95.

[101] Mohan BS, Maiya MP, Tiwari S. Performance characterisation of liquid desiccant columns for a hybrid air-conditioner. Applied Thermal Engineering 2008;28:1342–55.

[102] Mucke L, Fleig D, Vajen K, Jordan U. Hybrid liquid desiccant air-conditioning systems: A conceptual study with respect to energy saving potentials. International Journal of Refrigeration 2016;69:64–73.

[103] Mansuriya K, Patel VK, Raja BD, Mudgal A. Assessment of liquid desiccant dehumidification aided vapor-compression refrigeration system based on thermo-economic approach. Applied Thermal Engineering 2020;164:114542.

[104] Dai YJ, Wang RZ, Zhang HF, Yu JD. Use of liquid desiccant cooling to improve the performance of vapor compression air conditioning. Applied Thermal Engineering 2001;21:1185–202.

[105] Capozzoli A, Mazzei P, Minichiello F, Palma D. Hybrid HVAC systems with chemical dehumidification for supermarket applications. Applied Thermal Engineering 2006;26:795–805.

[106] Li Y, Lu L, Yang H. Energy and economic performance analysis of an open cycle solar desiccant dehumidification air-conditioning system for application in Hong Kong. Solar Energy 2010;84:2085–95.

[107] Su B, Qu W, Han W, Jin H. Feasibility of a hybrid photovoltaic/thermal and liquid desiccant system for deep dehumidification. Energy Conversion and Management 2018;163:457–67.

[108] Tu M, Ren C-Q, Zhang L-A, Shao J-W. Simulation and analysis of a novel liquid desiccant air-conditioning system. Applied Thermal Engineering 2009;29:2417–25.

[109] Lazzarin RM, Castellotti F. A new heat pump desiccant dehumidifier for supermarket application. Energy and Buildings 2007;39:59–65.

[110] Niu X, Xiao F, Ma Z. Investigation on capacity matching in liquid desiccant and heat pump hybrid air-conditioning systems. International Journal of Refrigeration 2012;35:160–70.

[111] Zhao K, Liu X-H, Zhang T, Jiang Y. Performance of temperature and humidity independent control air-conditioning system in an office building. Energy and Buildings 2011;43:1895–903.

[112] Chen Y, Yin Y, Zhang X. Performance analysis of a hybrid air-conditioning system dehumidified by liquid desiccant with low temperature and low concentration. Energy and Buildings 2014;77:91–102.

[113] Zhang L, Hihara E, Saikawa M. Combination of air-source heat pumps with liquid desiccant dehumidification of air. Energy Convers Manag 2012;57:107–16.

[114] Zhang L, Dang C, Hihara E. Performance analysis of a no-frost hybrid air conditioning system with integrated liquid desiccant dehumidification. International Journal of Refrigeration 2010;33:116–24.

[115] Gasparella A, Longo GA, Marra R. Combination of ground source heat pumps with chemical dehumidification of air. Applied Thermal Engineering 2005;25:295–308.

[116] Shen S, Cai W, Wang X, Wu Q, Yon H. Hybrid model for heat recovery heat pipe system in Liquid Desiccant Dehumidification System. Applied Energy 2016;182:383–93.

[117] Sanaye S, Taheri M. Modeling and multi-objective optimization of a modified hybrid liquid desiccant heat pump (LD-HP) system for hot and humid regions. Applied Thermal Engineering 2018;129:212–29.

[118] Abdel-Salam AH, Simonson CJ. Optimal design, sizing and operation of heat-pump liquid desiccant air conditioning systems. Science and Technology for the Built Environment 2020;26:161–76.

[119] Jradi M, Riffat S. Experimental investigation of a biomass-fuelled micro-scale tri-generation system with an organic Rankine cycle and liquid desiccant cooling unit. Energy 2014;71:80–93.

[120] Gommed K, Grossman G. Experimental investigation of a liquid desiccant system for solar cooling and dehumidification. Solar Energy 2007;81:131–8.

[121] Katejanekarn T, Kumar S. Performance of a solar-regenerated liquid desiccant ventilation pre-conditioning system. Energy and Buildings 2008;40:1252–67.

[122] Mohaisen AK, Ma Z. Development and modelling of a solar assisted liquid desiccant dehumidification air-conditioning system. Building Simulation, vol. 8, Springer; 2015, p. 123–35.

[123] Fumo N, Goswami DY. Study of an aqueous lithium chloride desiccant system: air dehumidification and desiccant regeneration. Solar Energy 2002;72:351–61.

[124] Crofoot L, Harrison S. Performance evaluation of a liquid desiccant solar air conditioning system. Energy Procedia 2012;30:542–50.

[125] Peng D, Zhang X, Yin Y. Theoretical storage capacity for solar air pretreatment liquid collector/regenerator. Applied Thermal Engineering 2008;28:1259–66.

[126] Alizadeh S. Performance of a solar liquid desiccant air conditioner–An experimental and theoretical approach. Solar Energy 2008;82:563–72.

[127] Qi R, Lu L, Huang Y. Energy performance of solar-assisted liquid desiccant air-conditioning system for commercial building in main climate zones. Energy Conversion and Management 2014;88:749–57.

[128] Li G-P, Zhang L-Z. Investigation of a solar energy driven and hollow fiber membrane-based humidification–dehumidification desalination system. Appl Energy 2016;177:393–408.

[129] Zhang L-Z, Li G-P. Energy and economic analysis of a hollow fiber membrane-based desalination system driven by solar energy. Desalination 2017;404:200–14.

[130] Chen Y, Yang H, Luo Y. Investigation on solar assisted liquid desiccant dehumidifier and evaporative cooling system for fresh air treatment. Energy 2018;143:114–27.

[131] Hawkes A, Staffell I, Brett D, Brandon N. Fuel cells for micro-combined heat and power generation. Energy & Environmental Science 2009;2:729–44.

[132] Elmer T, Worall M, Wu S, Riffat S. Assessment of a novel solid oxide fuel cell tri-generation system for building applications. Energy Conversion and Management 2016;124:29–41.

[133] Elmer T, Worall M, Wu S, Riffat S. Experimental evaluation of a liquid desiccant air conditioning system for tri-generation/waste-heat-driven applications. International Journal of Low-Carbon Technologies 2017;12:110–25.

[134] Elmer T, Worall M, Wu S. A novel solid oxide fuel cell tri-generation system for low carbon buildings. 12th International Conference on Sustainable Energy Technologies (SET 2013), 2013.

[135] McLarty D, Brouwer J, Samuelsen S. A spatially resolved physical model for transient system analysis of high temperature fuel cells. International Journal of Hydrogen Energy 2013;38:7935–46.

[136] Haberman BA, Young JB. Three-dimensional simulation of chemically reacting gas flows in the porous support structure of an integrated-planar solid oxide fuel cell. International Journal of Heat and Mass Transfer 2004;47:3617–29.

[137] Kazempoor P, Dorer V, Ommi F. Modelling and Performance Evaluation of Solid Oxide Fuel Cell for Building Integrated Co-and Polygeneration. Fuel Cells 2010;10:1074–94.

[138] Reineh MS, Fardadi M, Jabbari F. Thermal control of SOFC: An anti-windup approach for maximizing usable power. 2017 IEEE Conference on Control Technology and Applications (CCTA), IEEE; 2017, p. 311–6.

[139] Klein SA, Alvarado FL. Engineering Equation Solver (EES), FChart Software 2011.

[140] Kozubal E, Woods J, Judkoff R. Development and analysis of desiccant enhanced evaporative air conditioner prototype. National Renewable Energy Lab.(NREL), Golden, CO (United States); 2012.

[141] Sheppy M, Lobato C, van Geet O, Pless S, Donovan K, Powers C. Reducing Data Center Loads for a Large-Scale, Low-Energy Office Building: NREL's Research Support Facility (Book). National Renewable Energy Lab.(NREL), Golden, CO (United States); 2011.

[142] Metzger I, Dean J, Kurnik C. Psychrometric bin analysis for alternative cooling strategies in data centers. ASHRAE Transactions 2011;117:254.

[143] Rahmani R, Moser I, Seyedmahmoudian M. A complete model for modular simulation of data centre power load. ArXiv Preprint ArXiv:180400703 2018.

[144] Cartier Corporation. commercial HVAC chiller equipment: air cooled chiller. 2005.

[145] Stephen G. Kline. Energy Water Nexus: Balancing Two Precious Resources in HVAC Systems 2016.

[146] Ian Seaton. Cooling Efficiency Algorithms: Condensers and Temperature Differentials 2019.

[147] Yang J, Akagi T, Okanishi T, Muroyama H, Matsui T, Eguchi K. Catalytic Influence of Oxide Component in Ni-Based Cermet Anodes for Ammonia-Fueled Solid Oxide Fuel Cells. Fuel Cells 2015;15:390–7.

[148] Sampathkumar SN, Sun X, Joris S, van Herle J, Middleton PH, Frandsen HL. Performance Analysis of Ammonia in Solid Oxide Fuel Cells. ECS Transactions 2021;103:185.

APPENDIX A

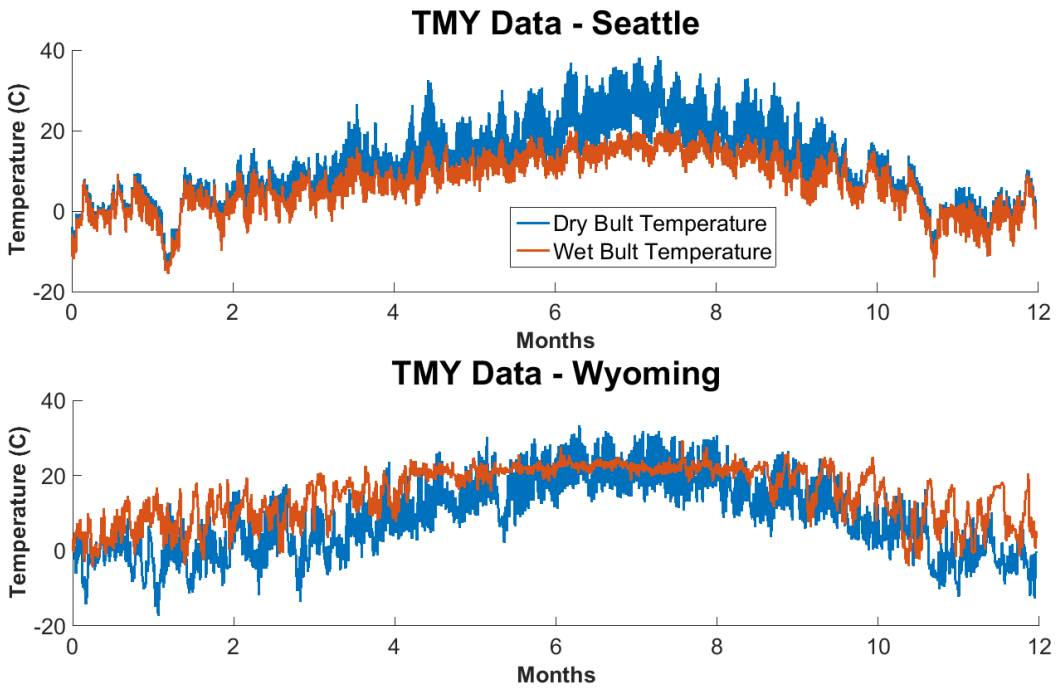
TMY Data - Seattle
Temperature (C)
Months
Dry Bult Temperature
Wet Bult Temperature
TMY Data - Wyoming
Temperature (C)
Months

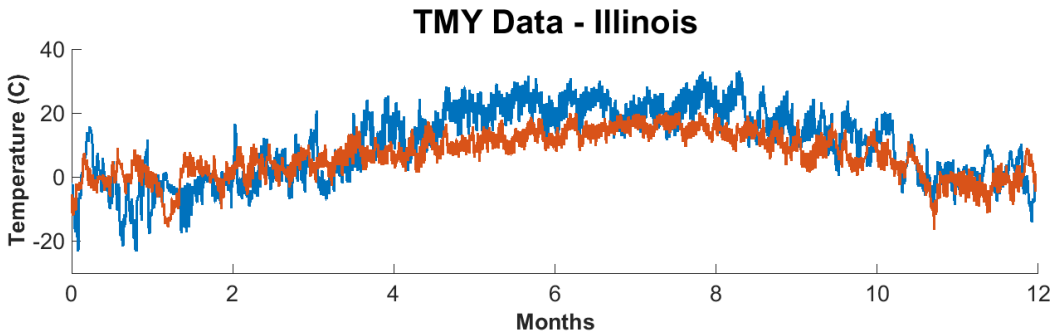
TMY Data - Illinois
Temperature (C)
40
20
0
-20
0
2
4
6
8
10
12
Months

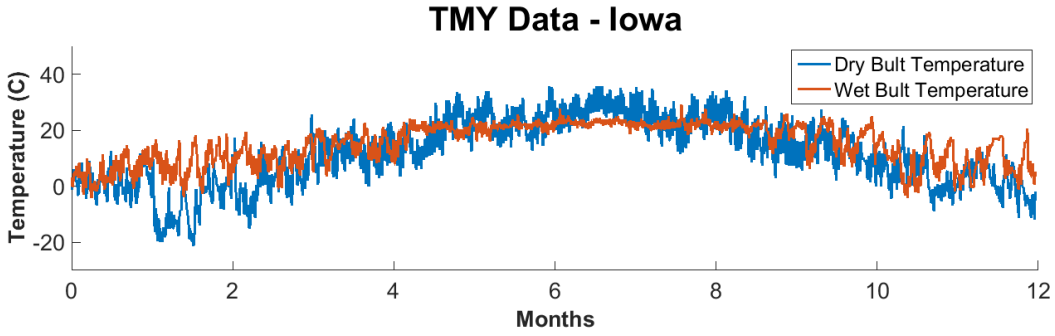
TMY Data - Iowa
Dry Bult Temperature
Wet Bult Temperature
Temperature (C)
40
20
0
-20
0
2
4
6
8
10
12
Months

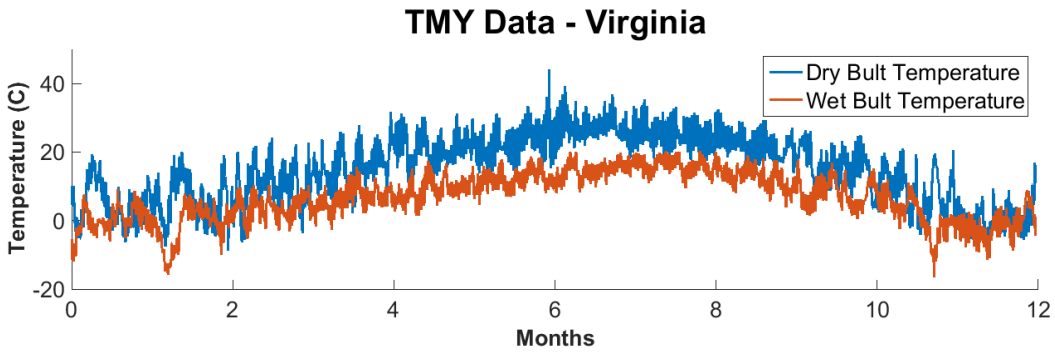
TMY Data - Virginia
Dry Bult Temperature
Wet Bult Temperature
Temperature (C)
40
20
0
-20
0
2
4
6
8
10
12
Months

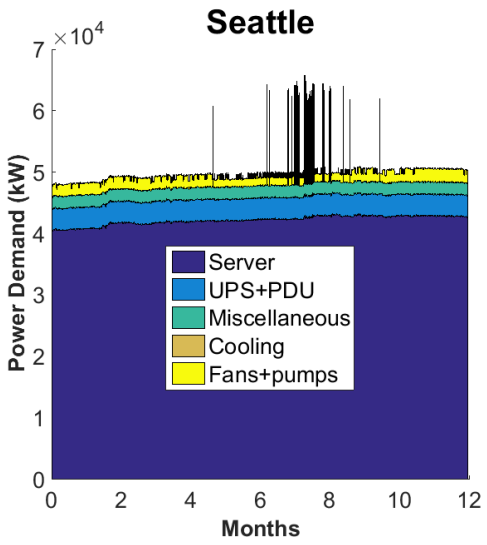
Seattle
×10^4
Power Demand (kW)
Months
Server
UPS+PDU
Miscellaneous
Cooling
Fans+pumps

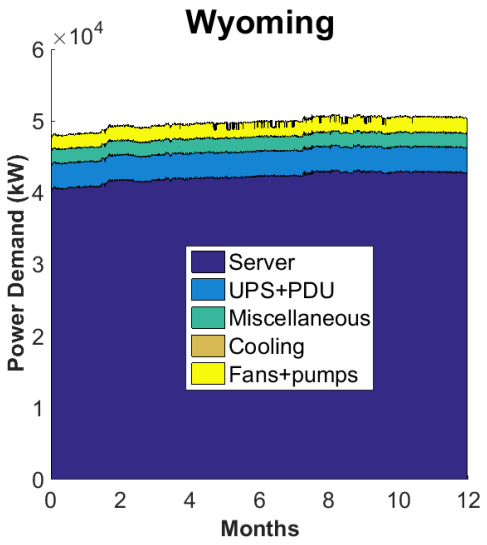
Wyoming
×10^4
Power Demand (kW)
Months
Server
UPS+PDU
Miscellaneous
Cooling
Fans+pumps

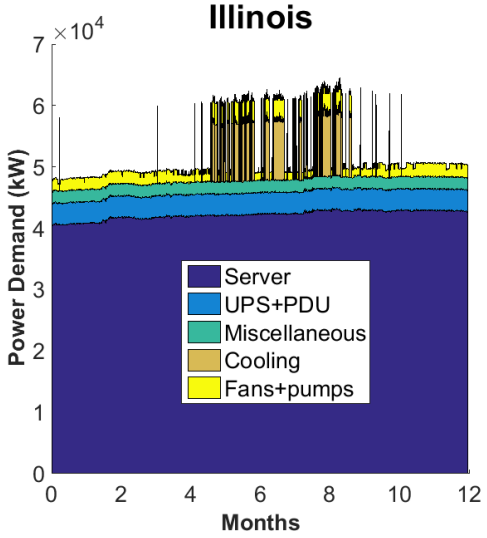
Illinois
×10^4
Power Demand (kW)
Months
Server
UPS+PDU
Miscellaneous
Cooling
Fans+pumps

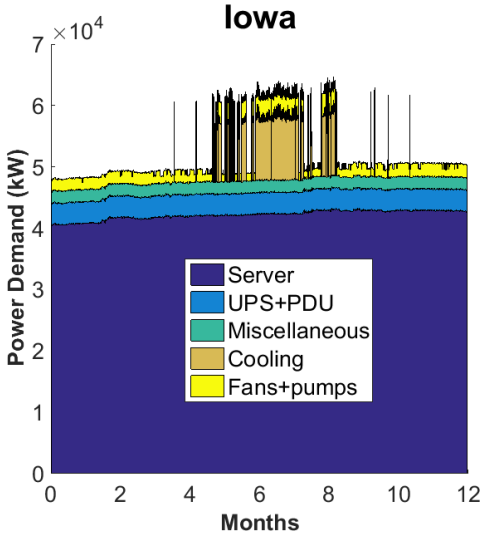
Iowa
×10^4
Power Demand (kW)
Months
Server
UPS+PDU
Miscellaneous
Cooling
Fans+pumps

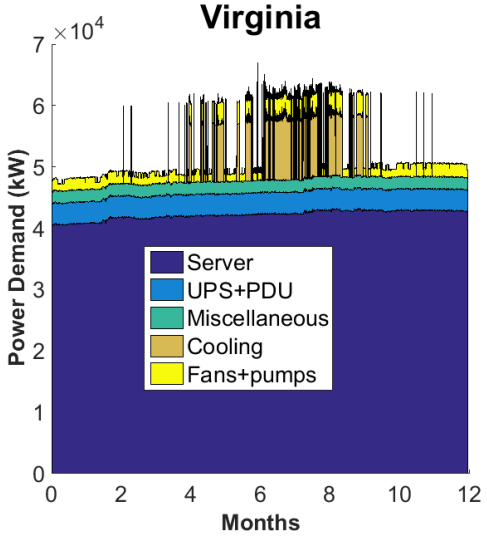
Virginia
×10^4
Power Demand (kW)
Months
Server
UPS+PDU
Miscellaneous
Cooling
Fans+pumps

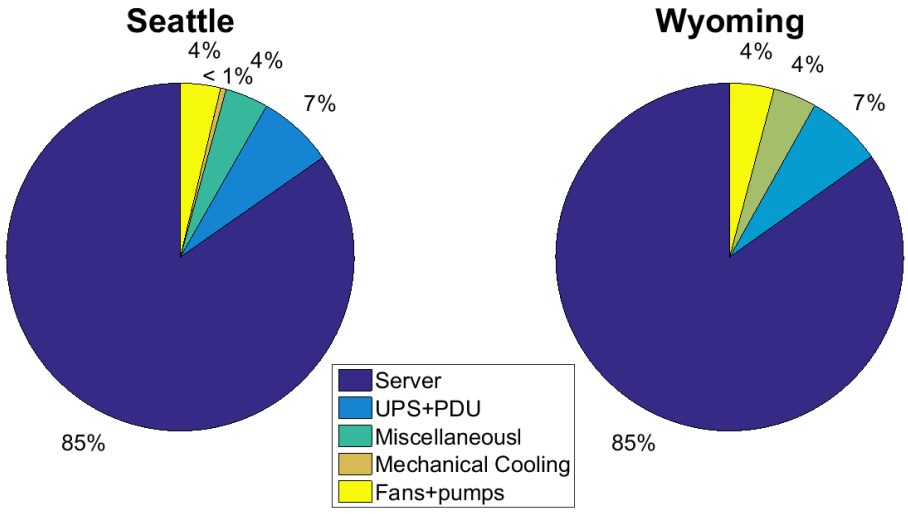
Seattle
4%
< 1%
4%
7%
85%
Wyoming
4%
4%
7%
85%
Server
UPS+PDU
Miscellaneousl
Mechanical Cooling
Fans+pumps

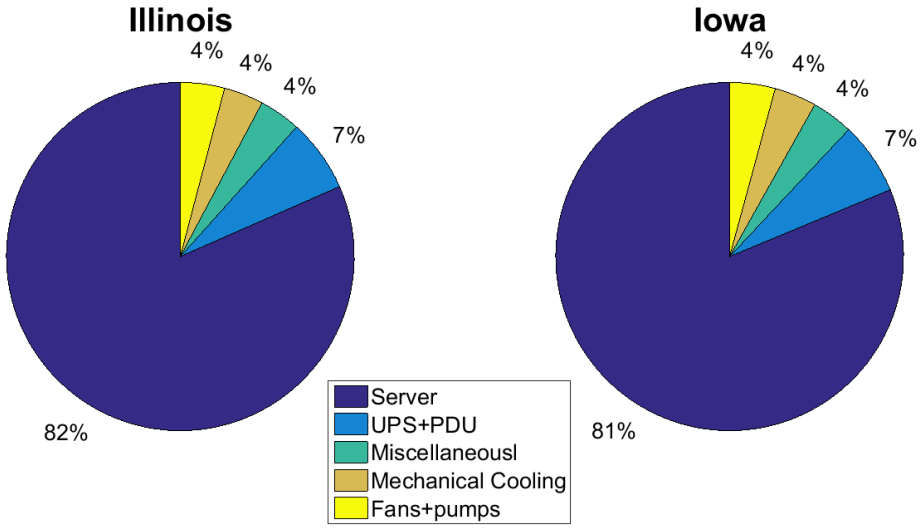
Illinois
4%
4%
4%
7%
82%
Iowa
4%
4%
4%
7%
81%
Server
UPS+PDU
Miscellaneousl
Mechanical Cooling
Fans+pumps

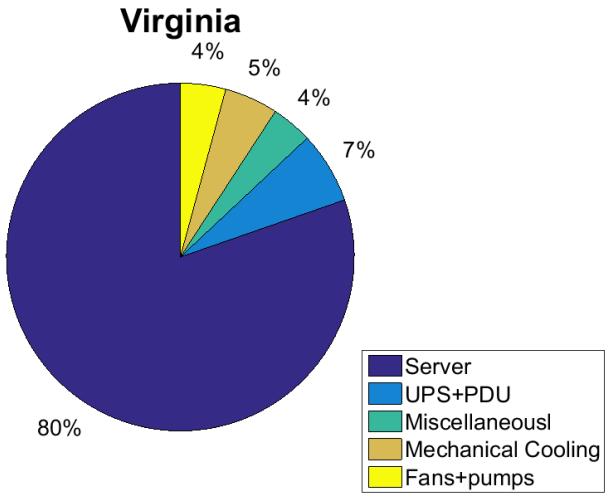
Virginia
4%
5%
4%
7%
80%
Server
UPS+PDU
Miscellaneousl
Mechanical Cooling
Fans+pumps

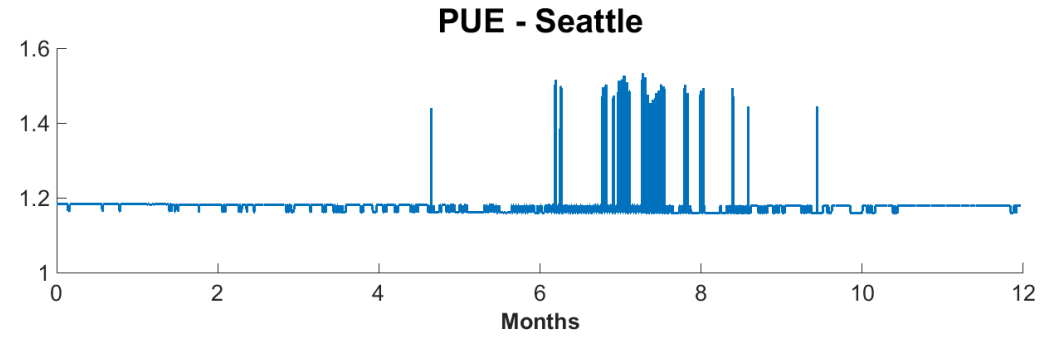
PUE - Seattle
1.6
1.4
1.2
1
0
2
4
6
8
10
12
Months

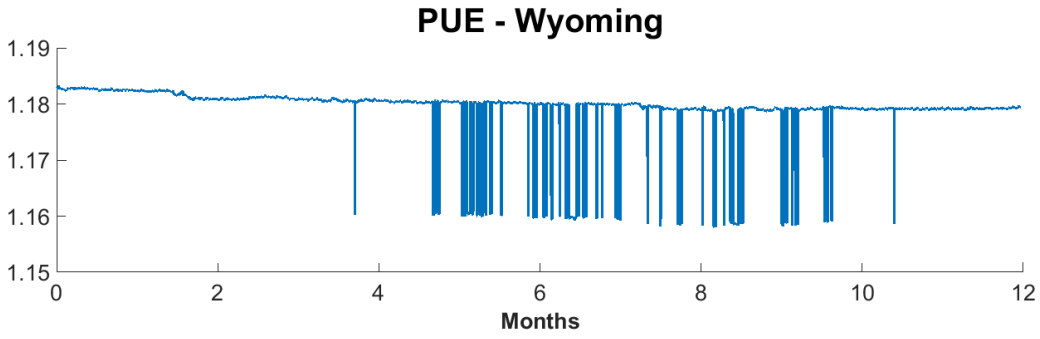
PUE - Wyoming
1.19
1.18
1.17
1.16
1.15
0
2
4
6
8
10
12
Months

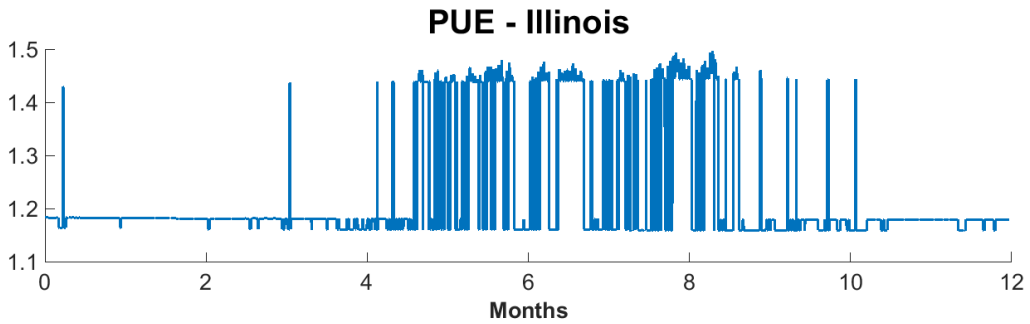
PUE - Illinois
1.5
1.4
1.3
1.2
1.1
0
2
4
6
8
10
12
Months

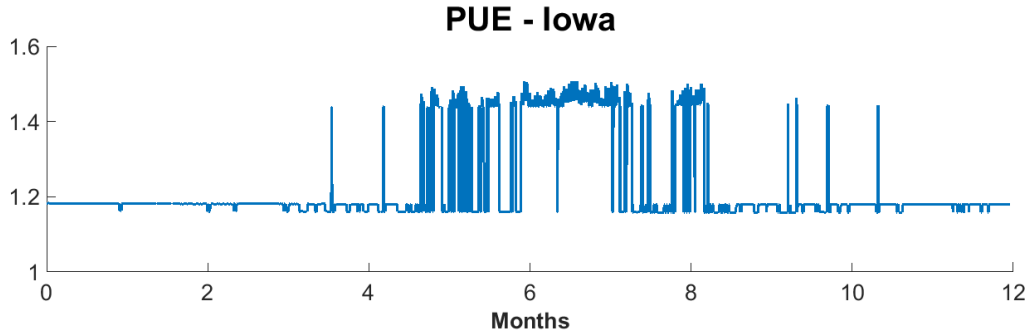
PUE - Iowa
1.6
1.4
1.2
1
0
2
4
6
8
10
12
Months

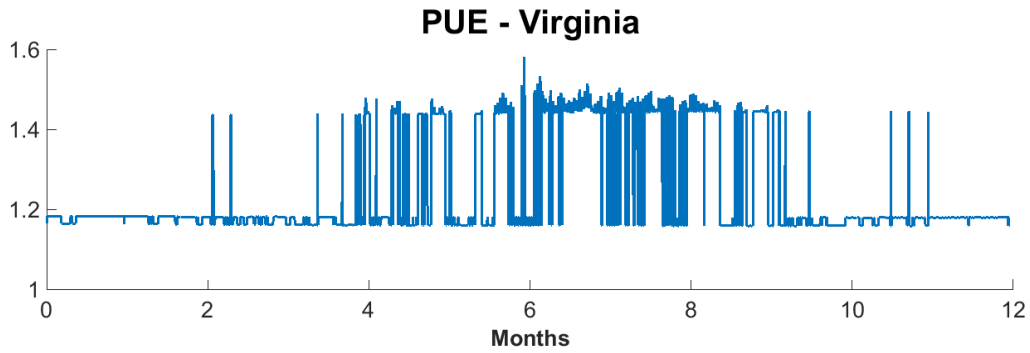
PUE - Virginia
1.6
1.4
1.2
1
0
2
4
6
8
10
12
Months

APPENDIX B

B.1. Rack level results

Virginia Regenerator:

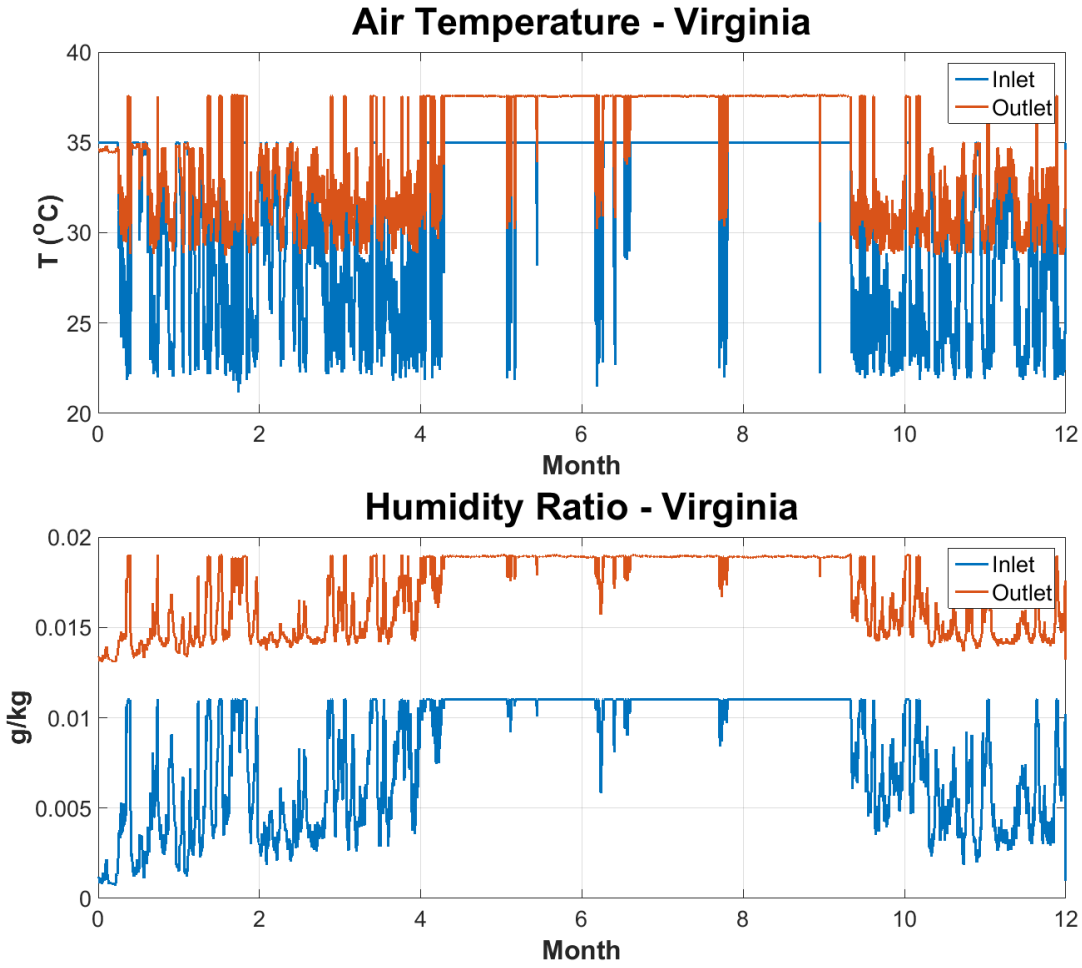

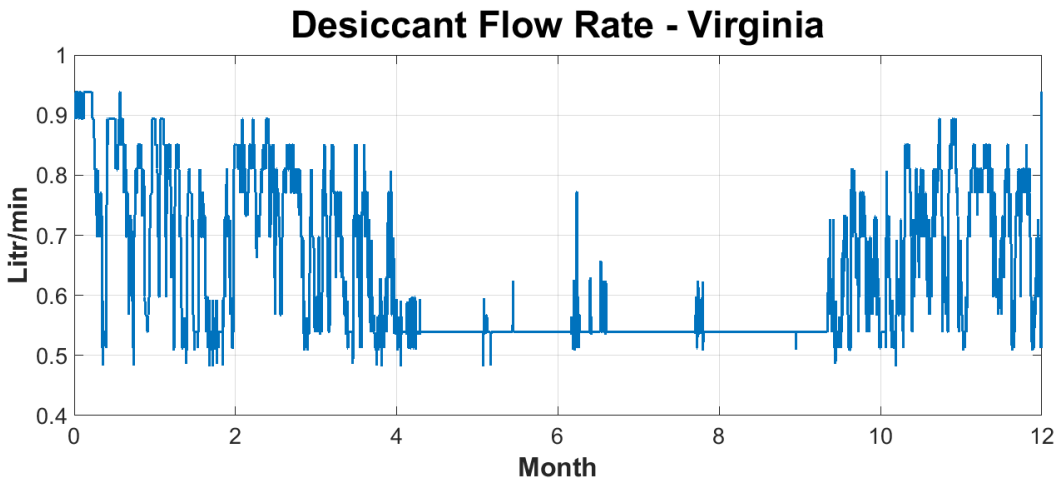
Desiccant Flow Rate - Virginia
Litr/min
Month

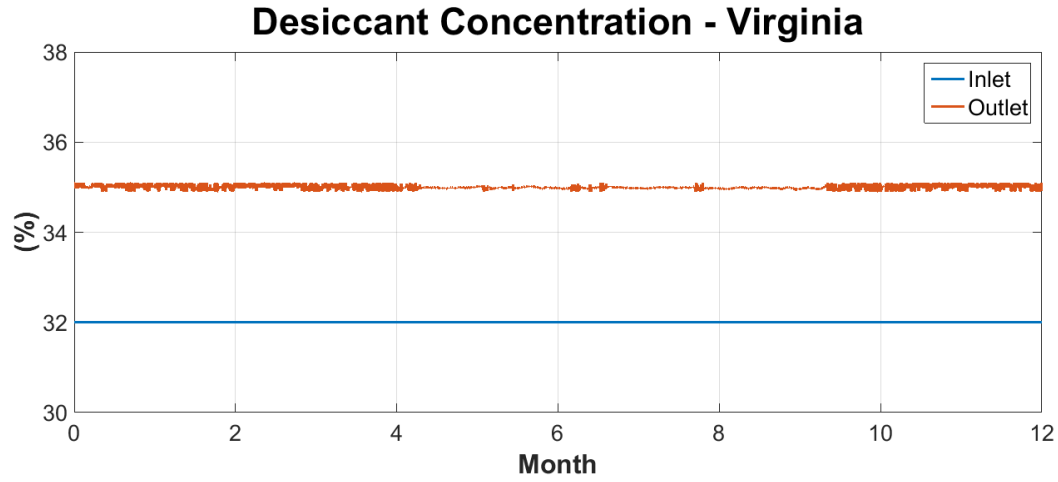
Desiccant Concentration - Virginia
Inlet
Outlet
(%)
Month

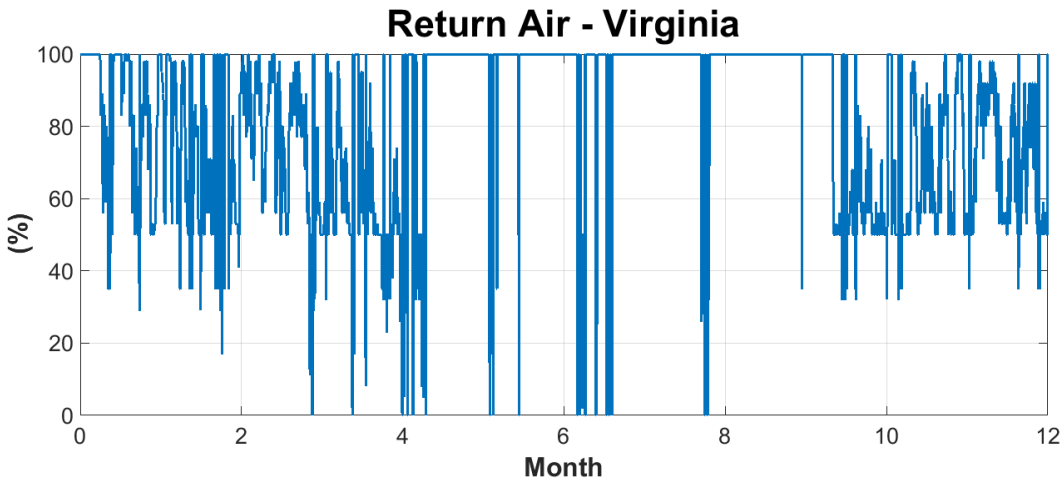
Return Air - Virginia
(%)
Month

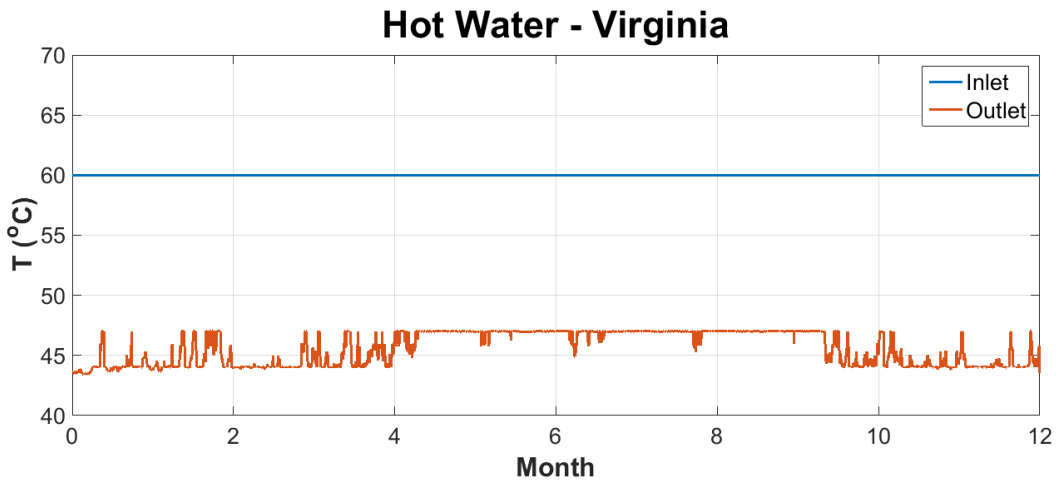

Virginia Dehumidifier:

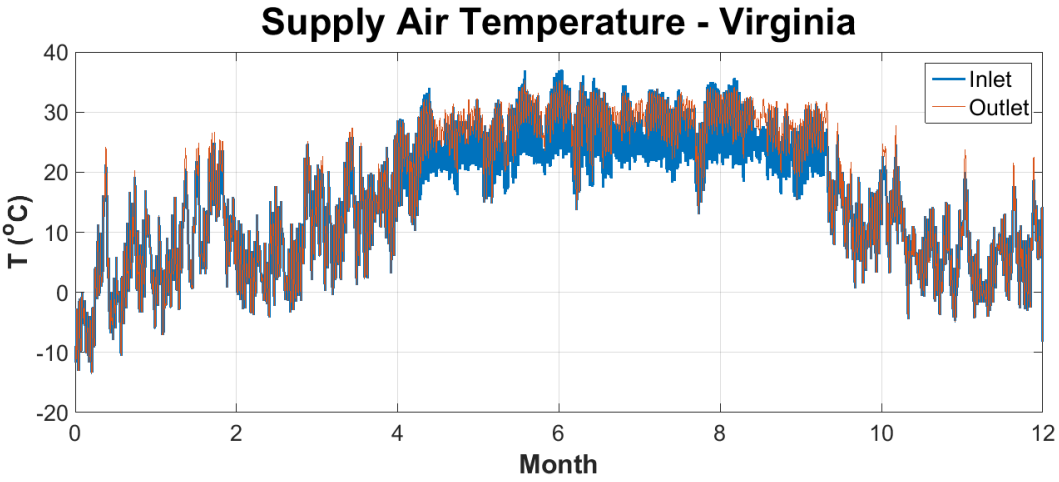

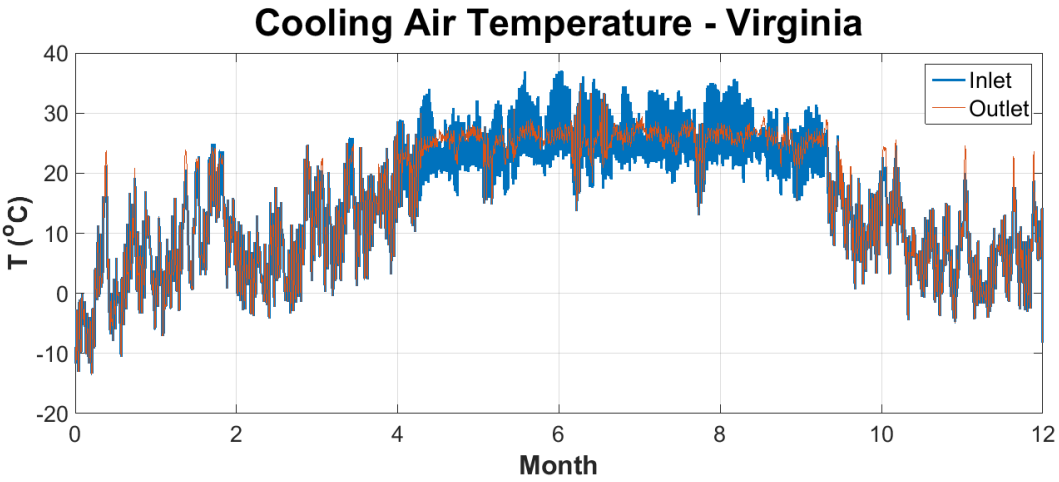
Cooling Air Temperature - Virginia
Inlet
Outlet
T (°C)
Month

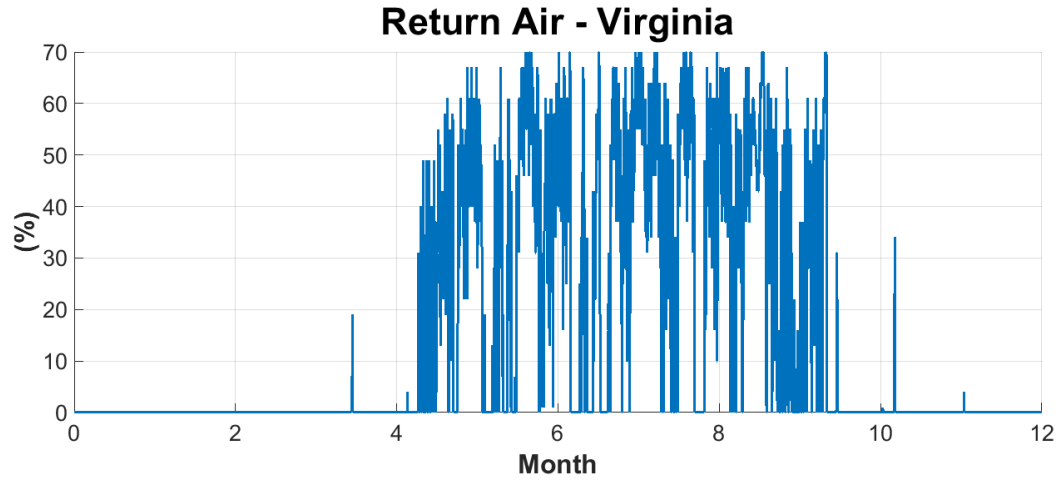
Return Air - Virginia
(%)
Month

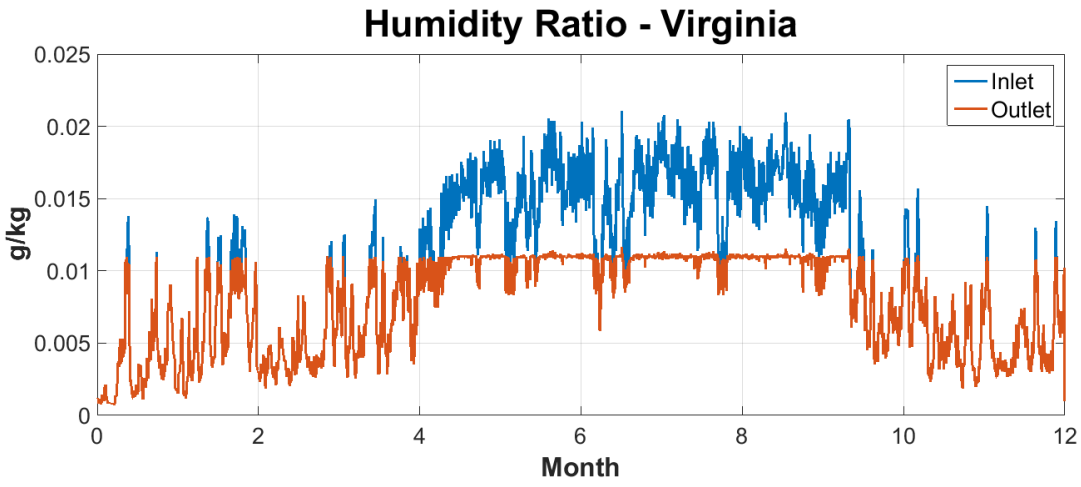
Humidity Ratio - Virginia
Inlet
Outlet
g/kg
Month

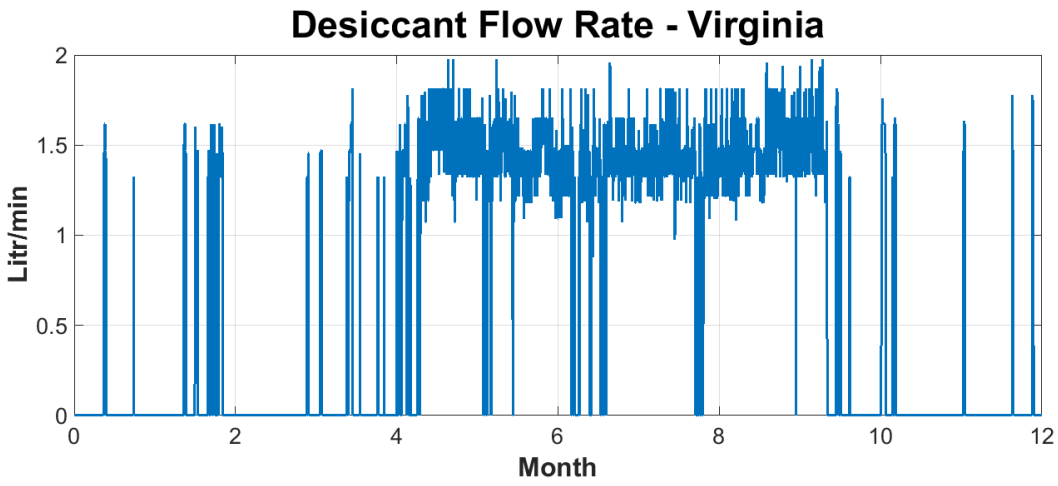

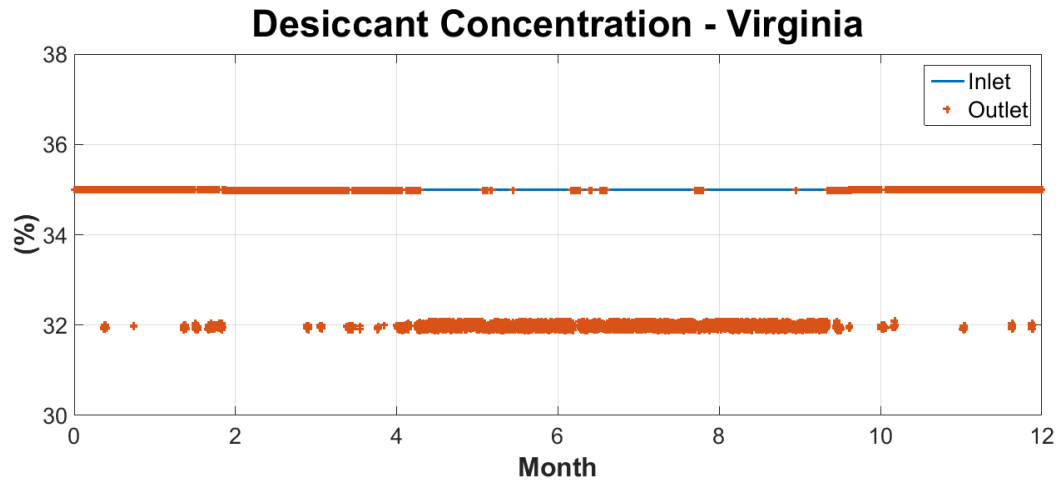

Texas Regenerator:

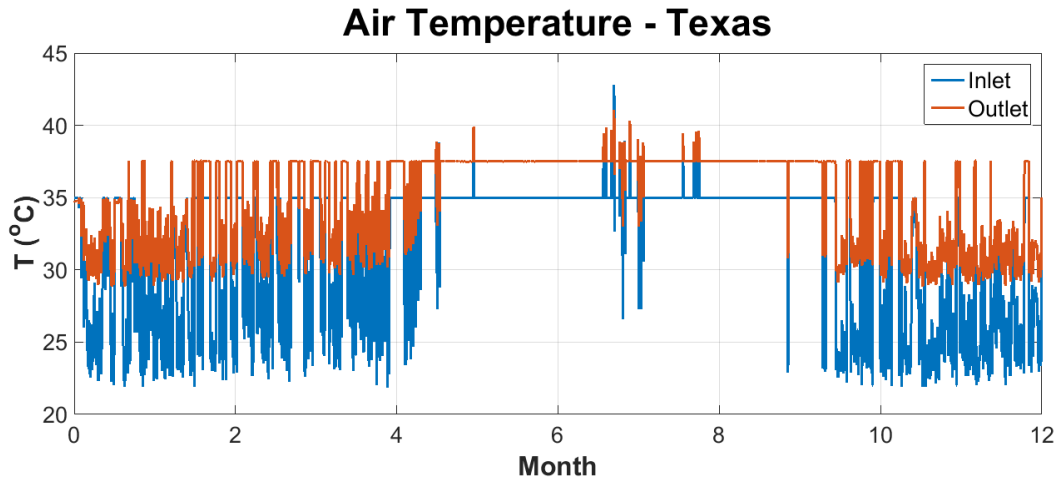

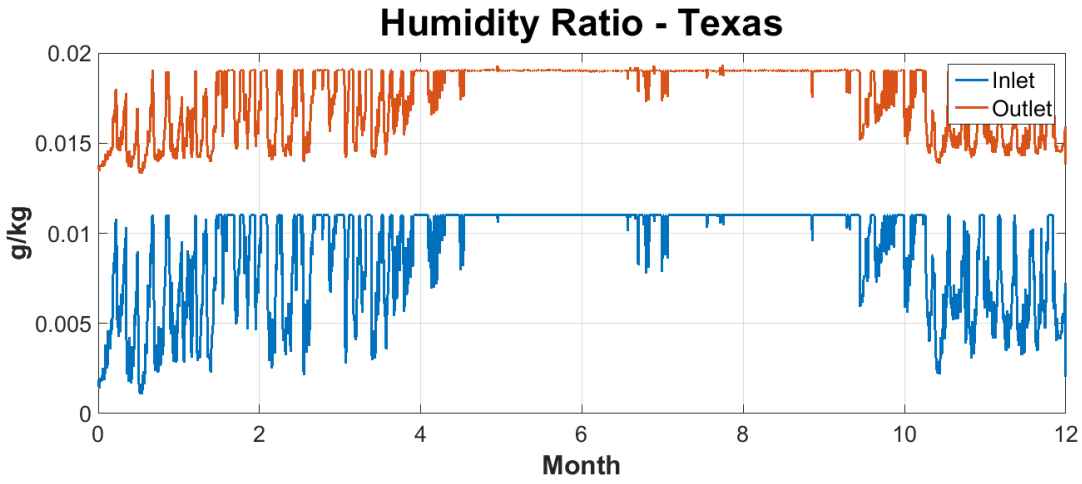
Humidity Ratio - Texas
g/kg
0.02
0.015
0.01
0.005
0
0
2
4
6
8
10
12
Month
Inlet
Outlet

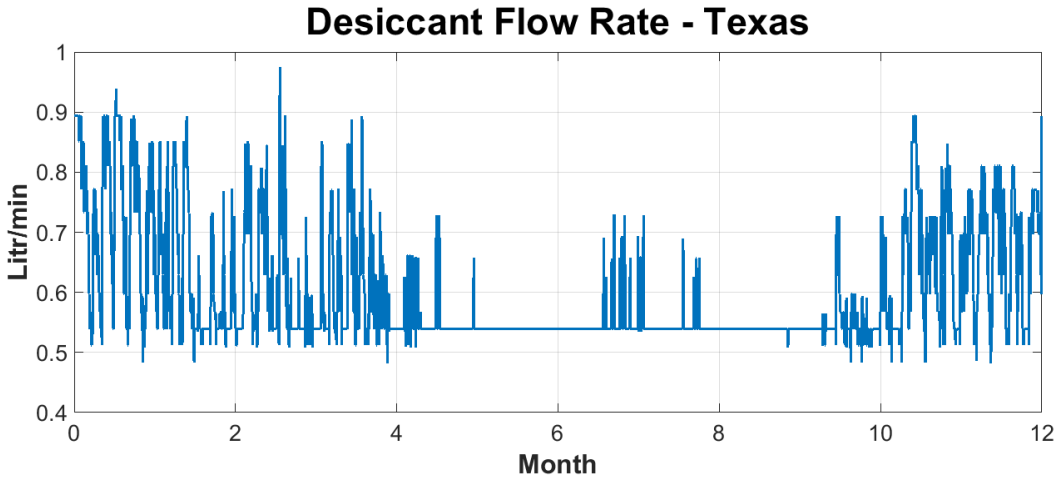
Desiccant Flow Rate - Texas
Litr/min
1
0.9
0.8
0.7
0.6
0.5
0.4
0
2
4
6
8
10
12
Month

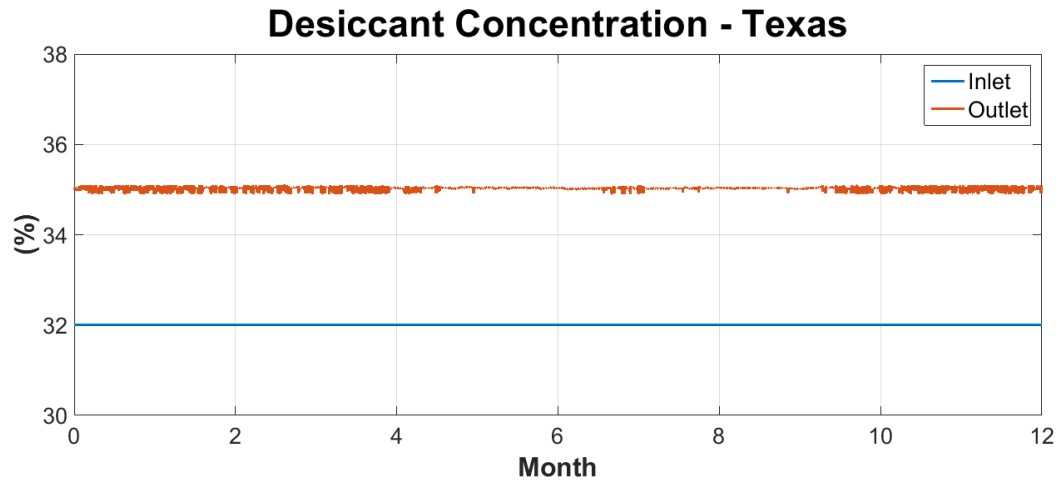
Desiccant Concentration - Texas
(%)
38
36
34
32
30
0
2
4
6
8
10
12
Month
Inlet
Outlet

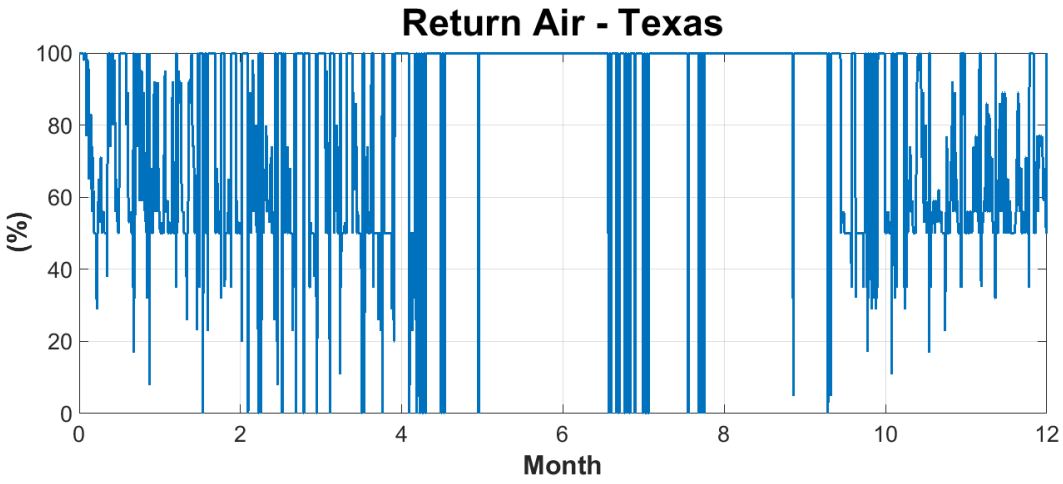

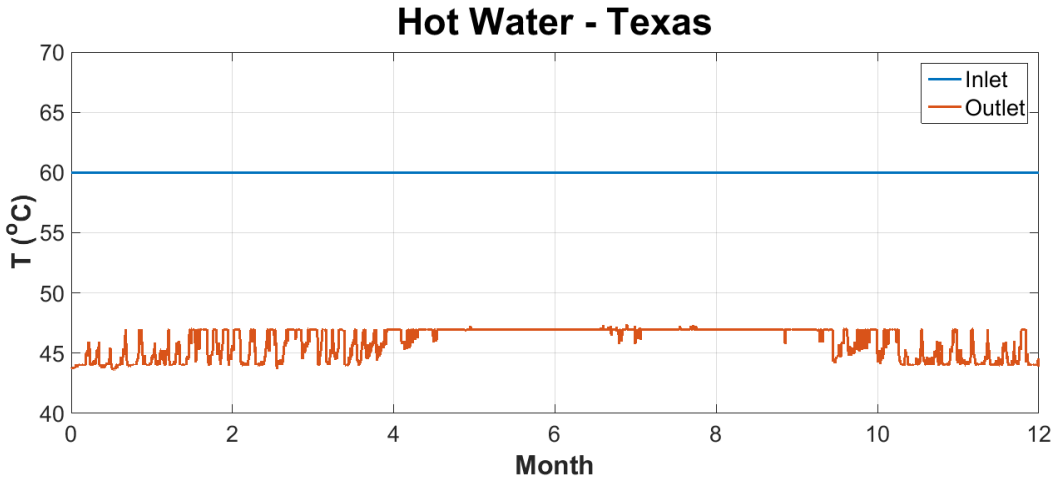

Texas Dehumidifier:

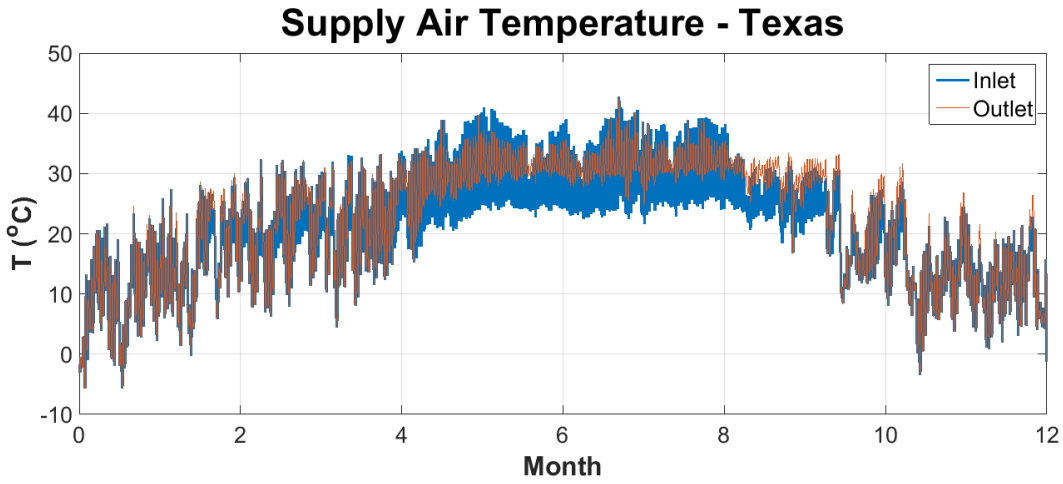

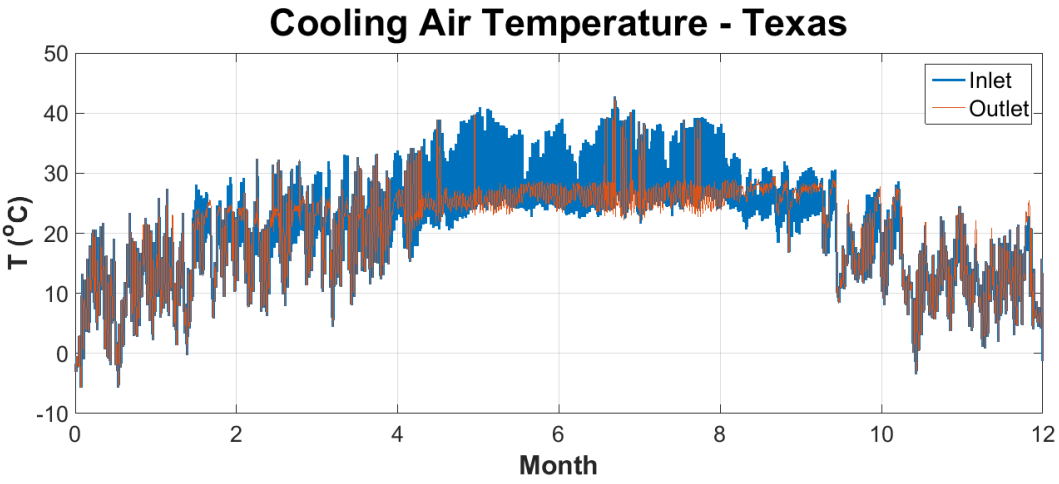
Cooling Air Temperature - Texas
Inlet
Outlet
T (°C)
Month

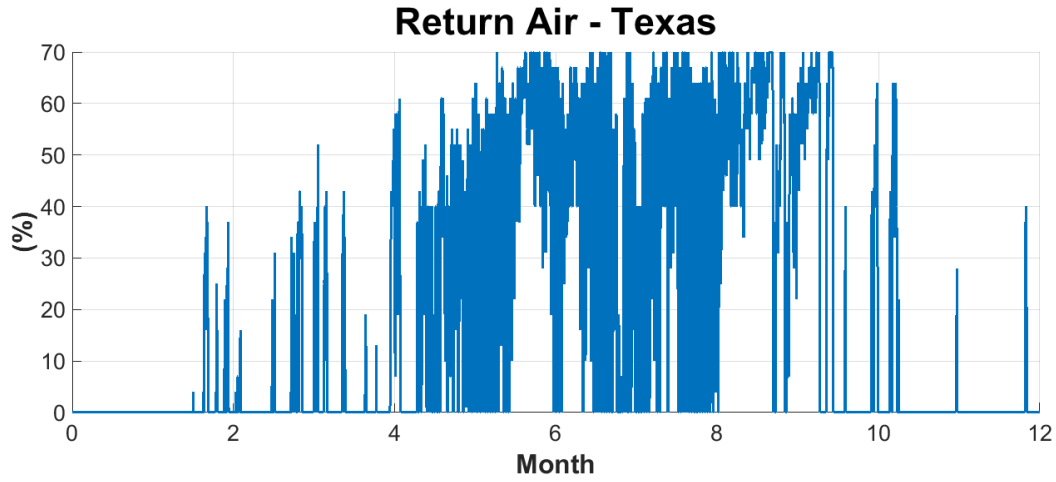
Return Air - Texas
(%)
Month

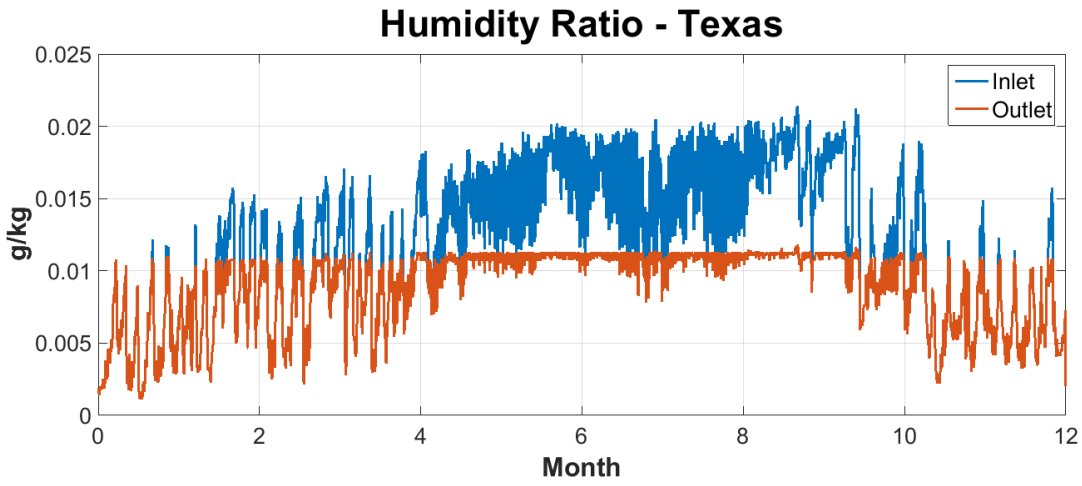
Humidity Ratio - Texas
Inlet
Outlet
g/kg
Month

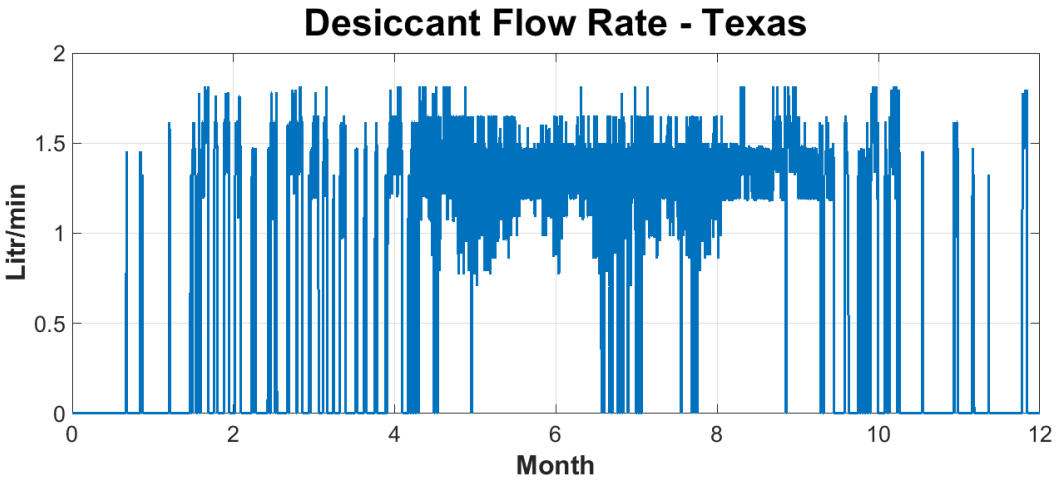

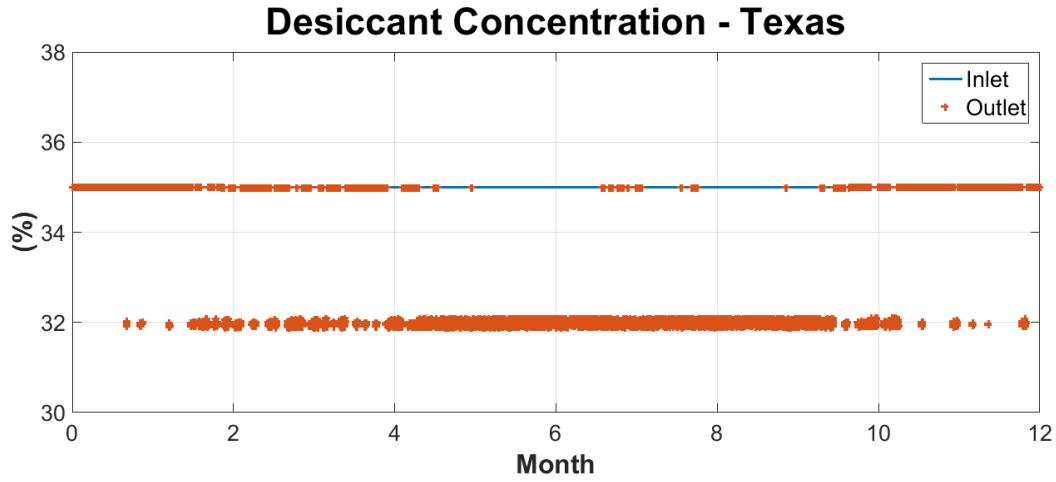

Iowa Regenerator:

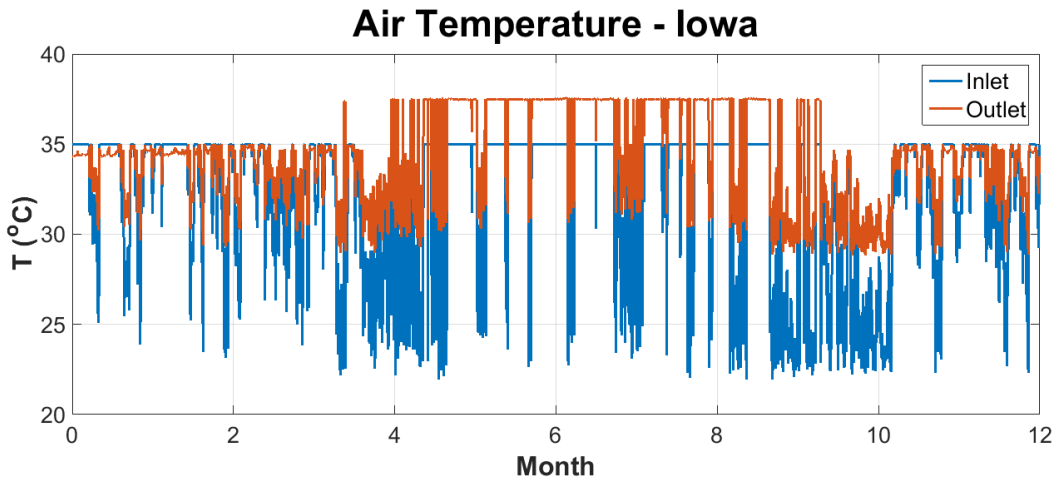

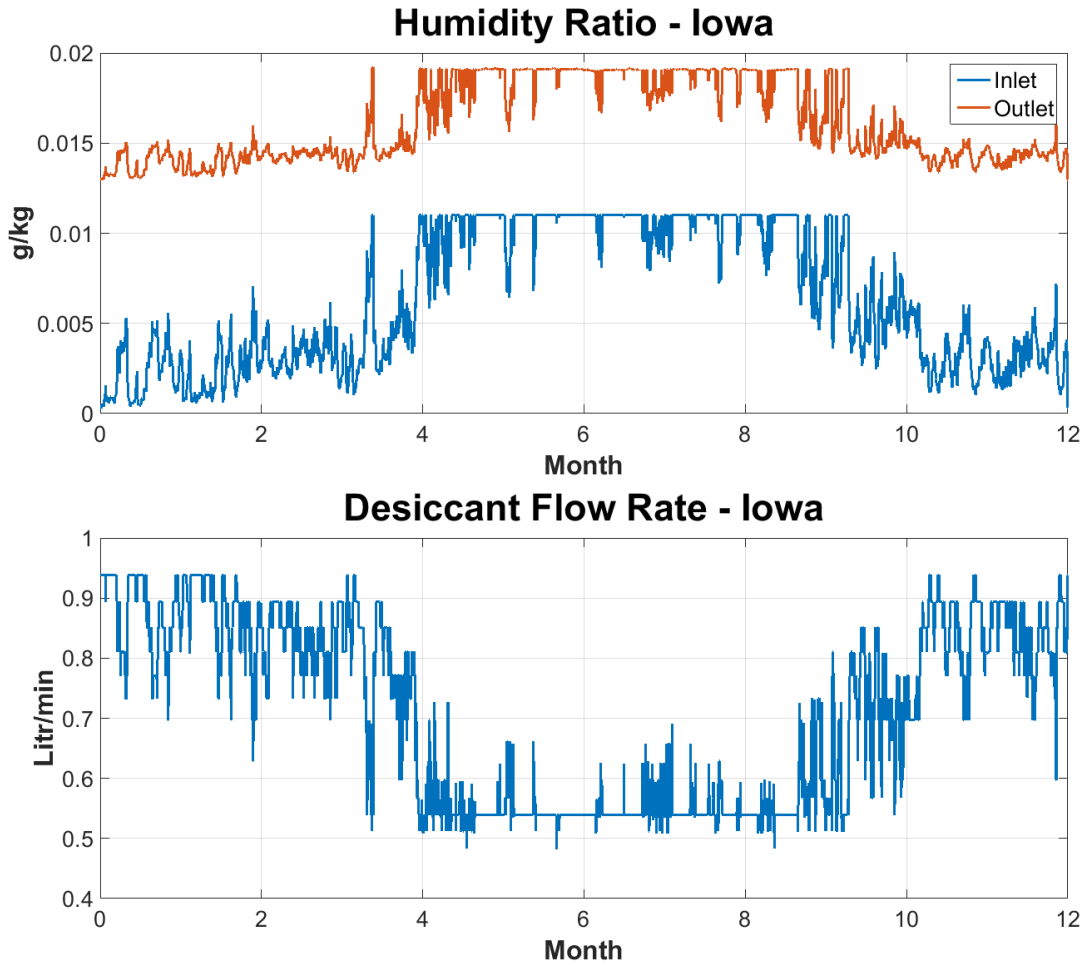
Humidity Ratio - Iowa
Inlet
Outlet
g/kg
0.02
0.015
0.01
0.005
0
0
2
4
6
8
10
12
Month
Desiccant Flow Rate - Iowa
Litr/min
1
0.9
0.8
0.7
0.6
0.5
0.4
0
2
4
6
8
10
12
Month

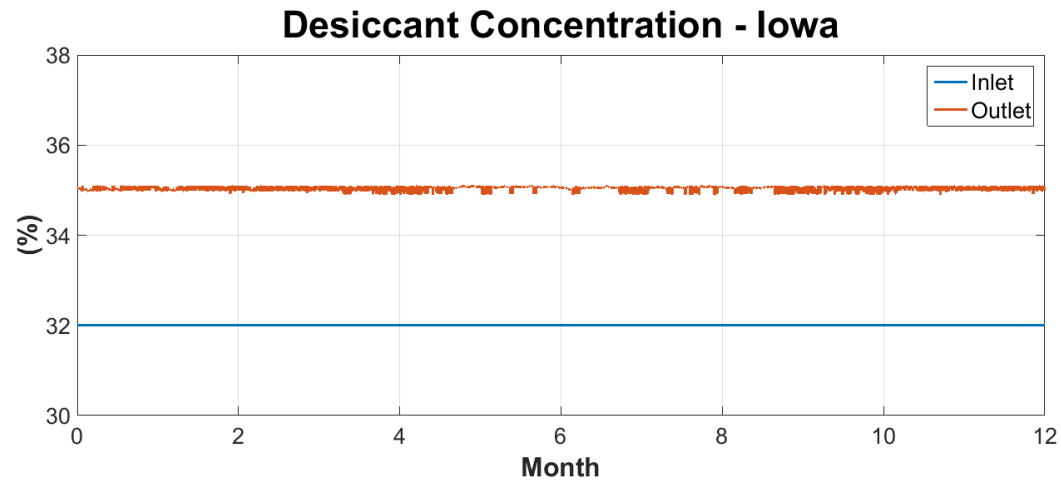

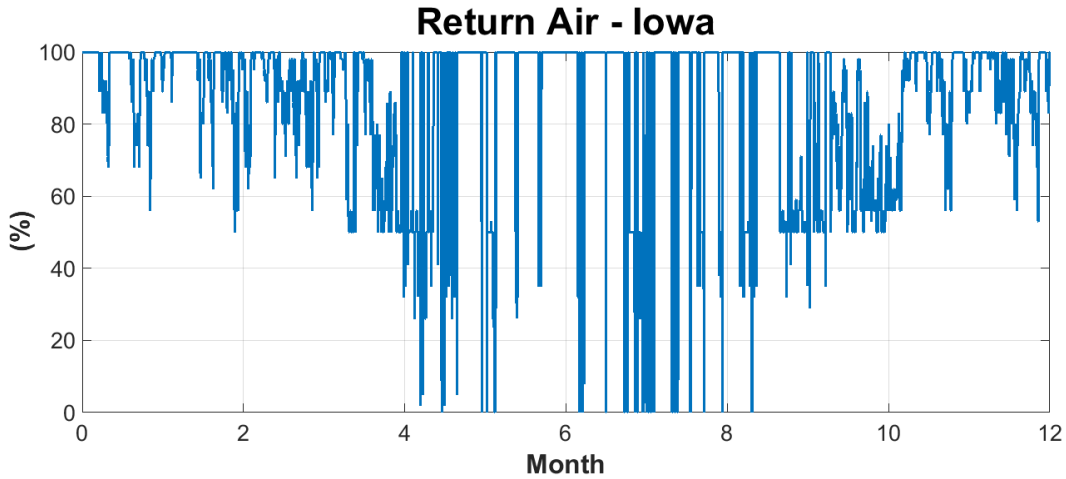

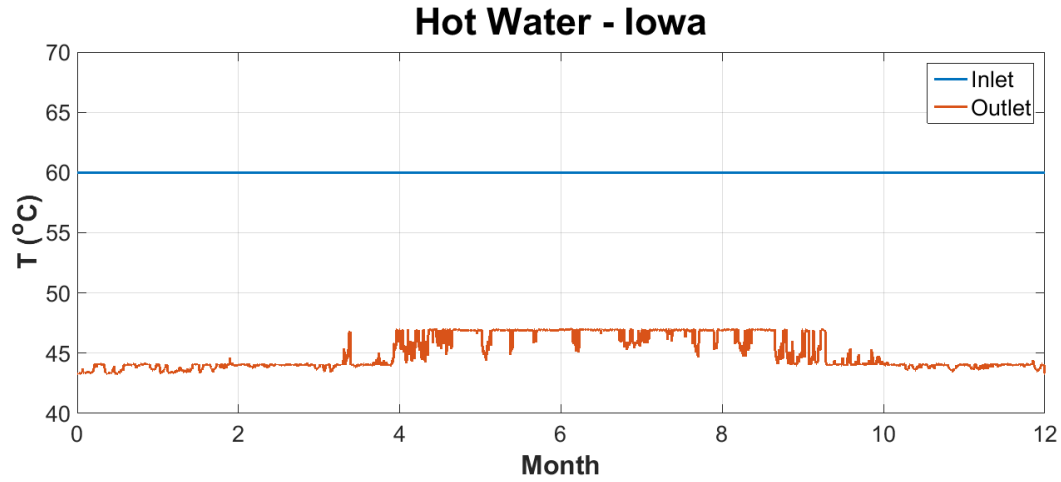

Iowa Dehumidifier:

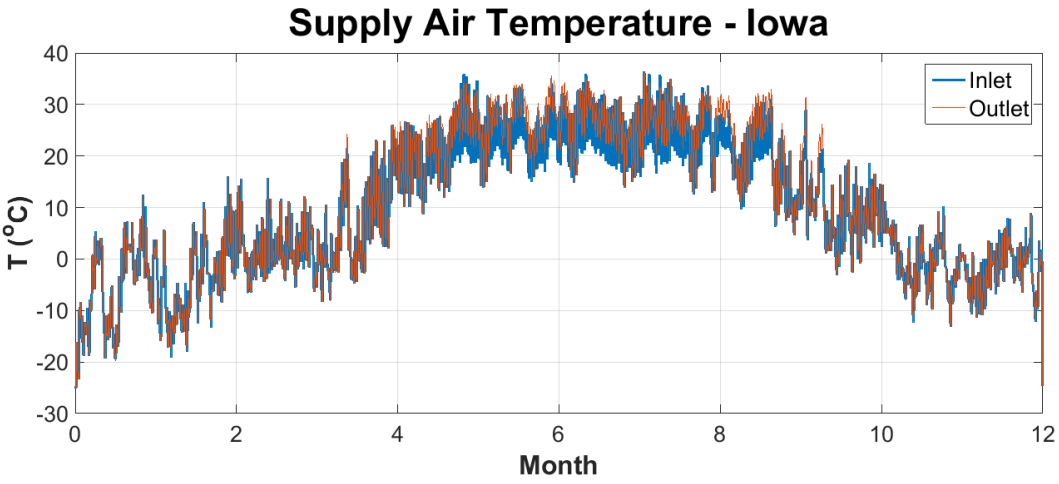
Supply Air Temperature - Iowa
Inlet
Outlet
T (°C)
Month

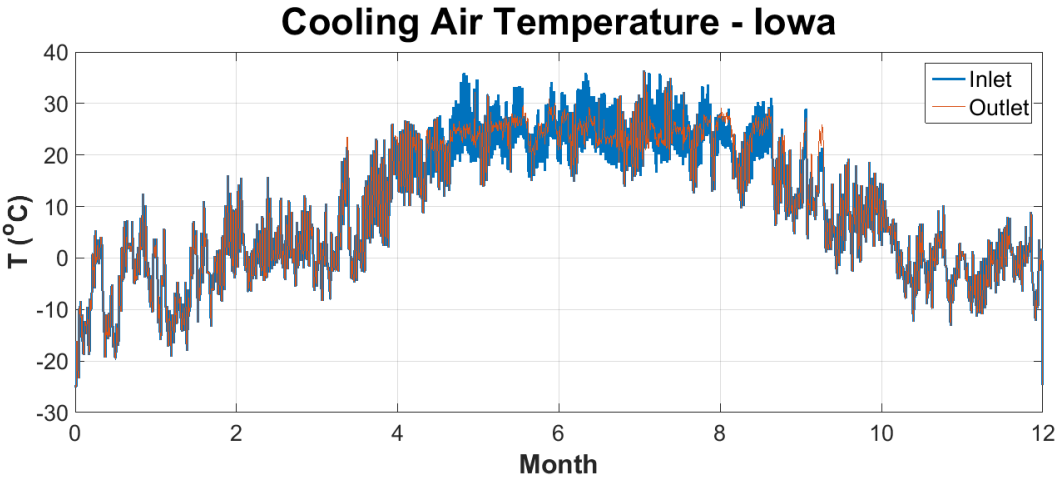
Cooling Air Temperature - Iowa
Inlet
Outlet
T (°C)
Month

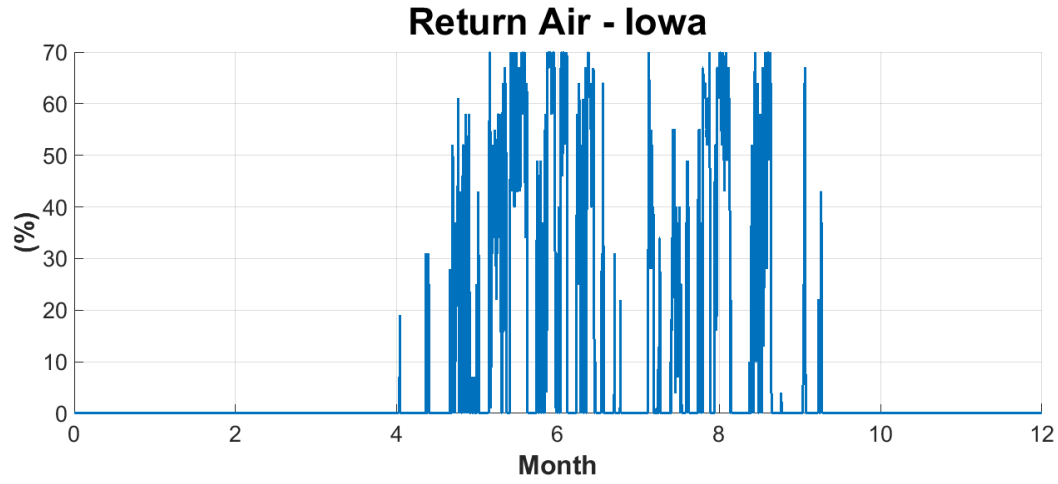
Return Air - Iowa
(%)
Month

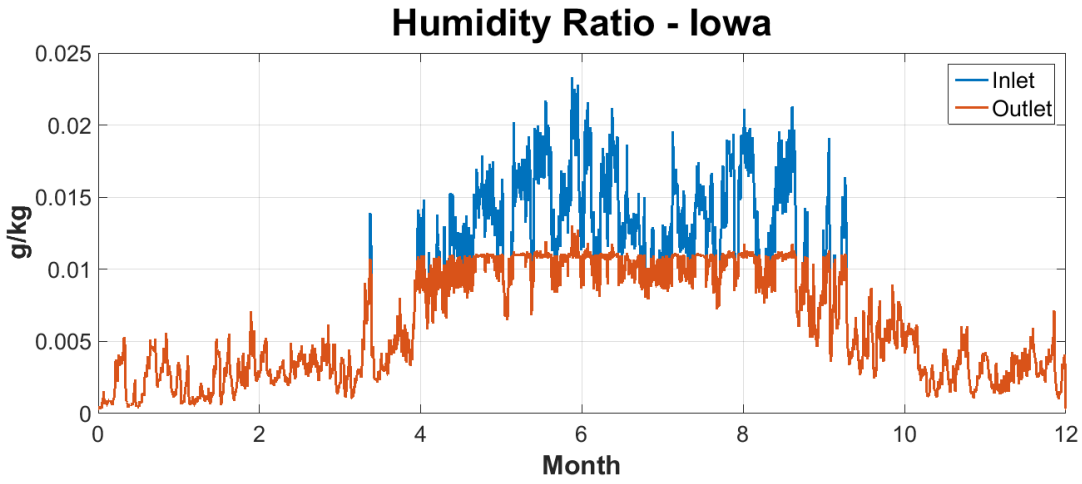

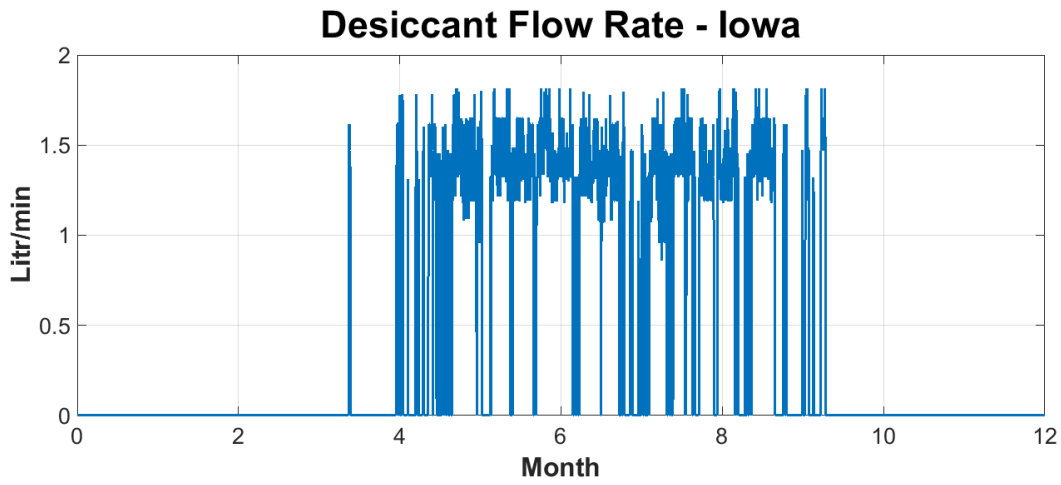

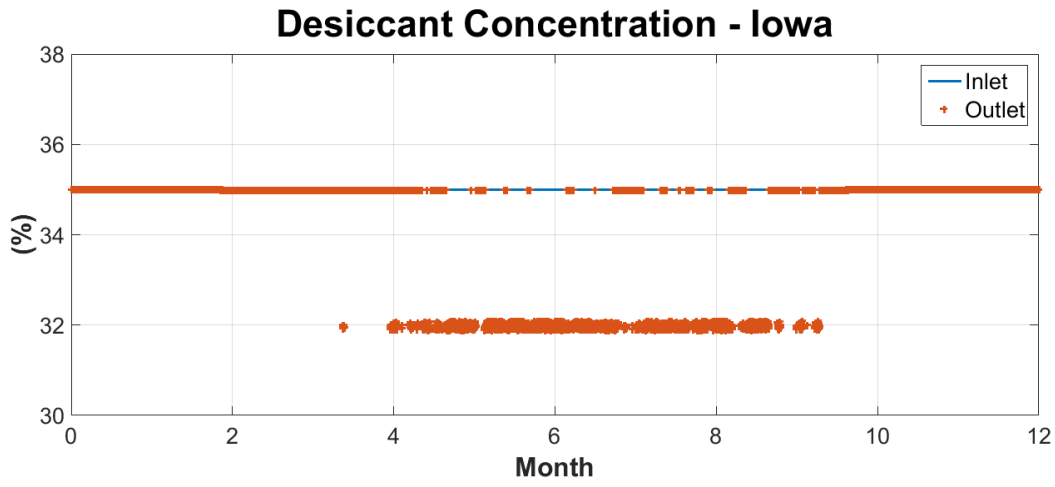

B.2. Row level results

Virginia Regenerator:

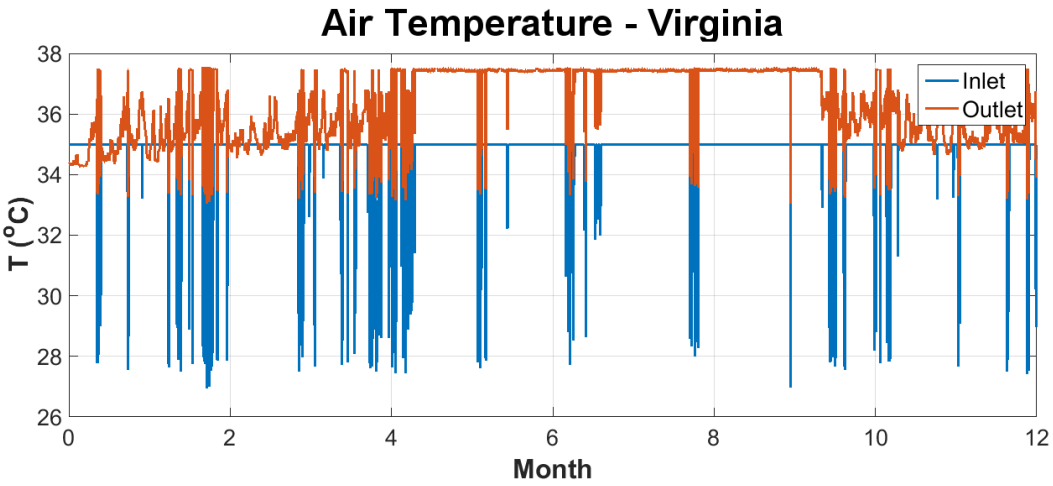
Air Temperature - Virginia
Inlet
Outlet
T (°C)
Month

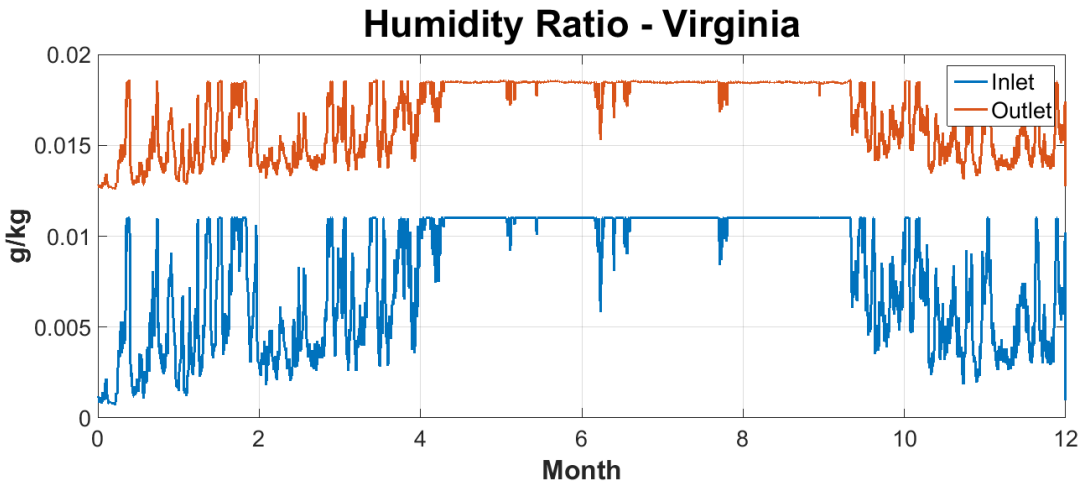
Humidity Ratio - Virginia
Inlet
Outlet
g/kg
Month

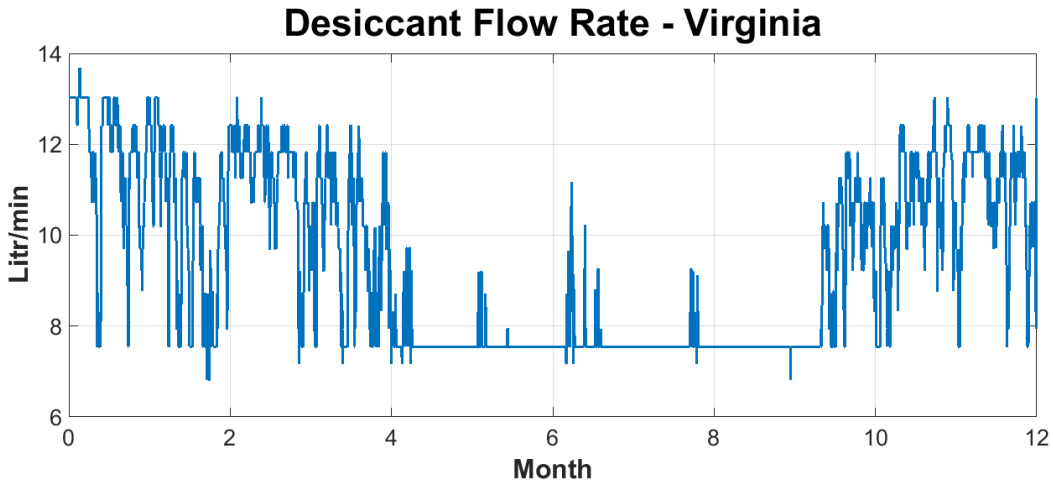
Desiccant Flow Rate - Virginia
Litr/min
Month

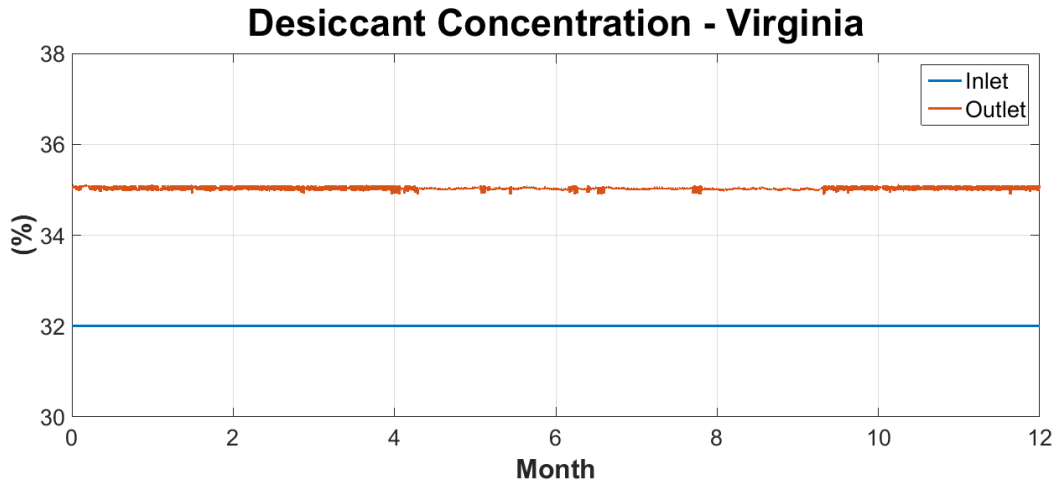

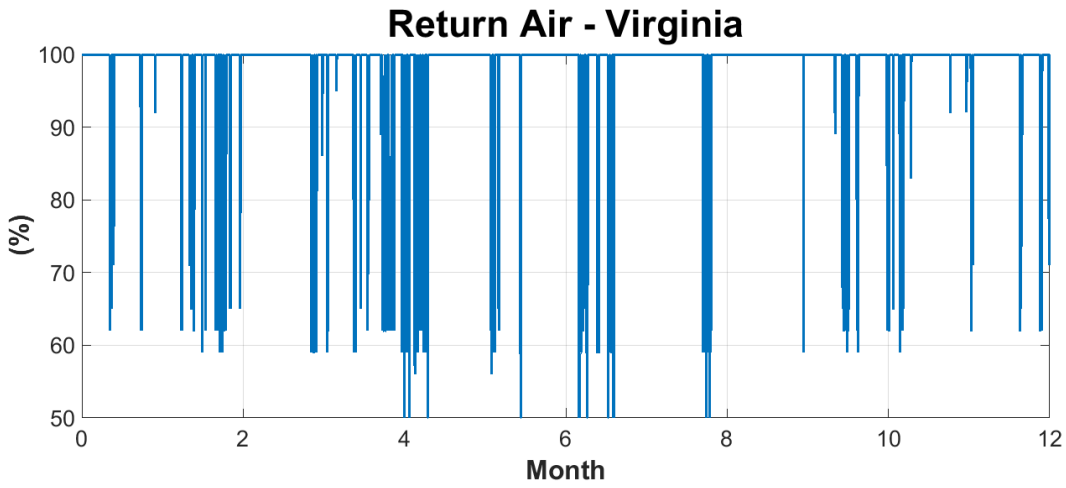

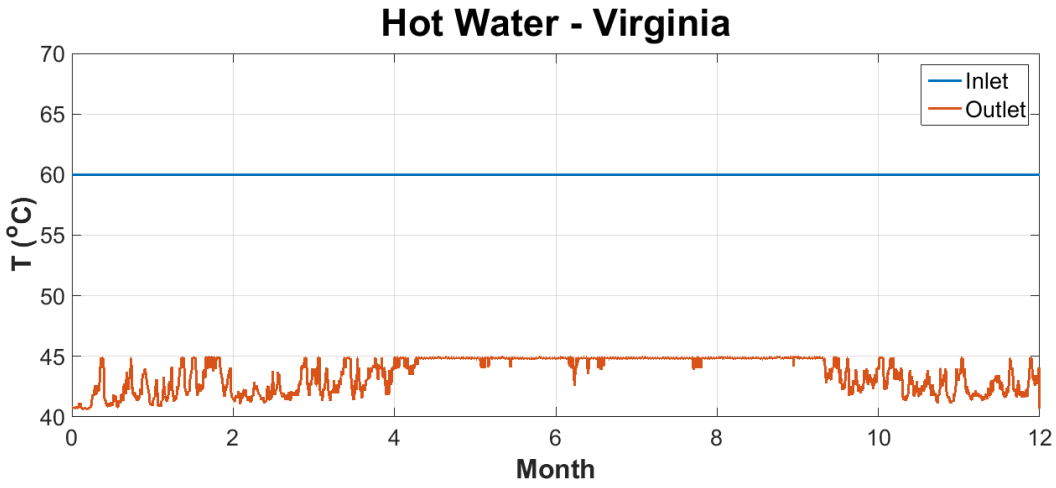

Virginia Dehumidifier:

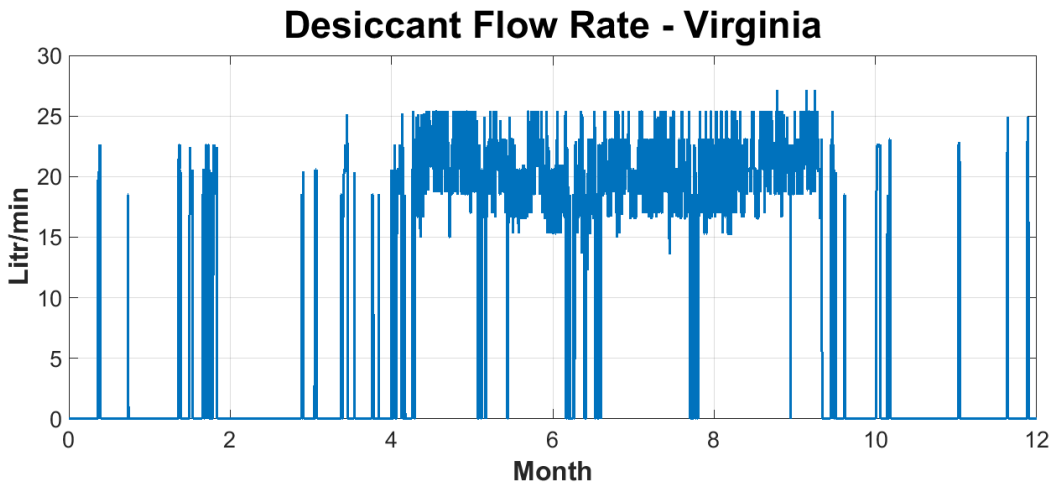

Texas Regenerator:

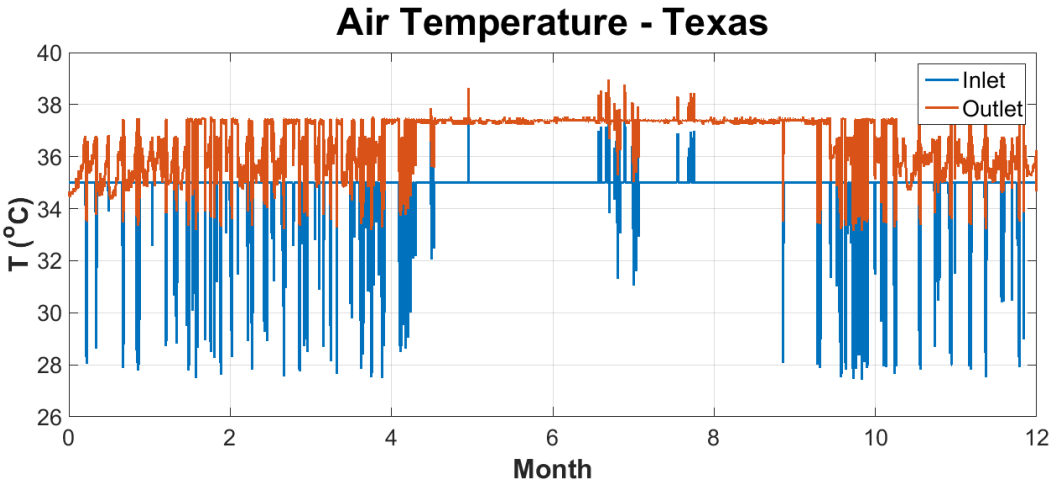

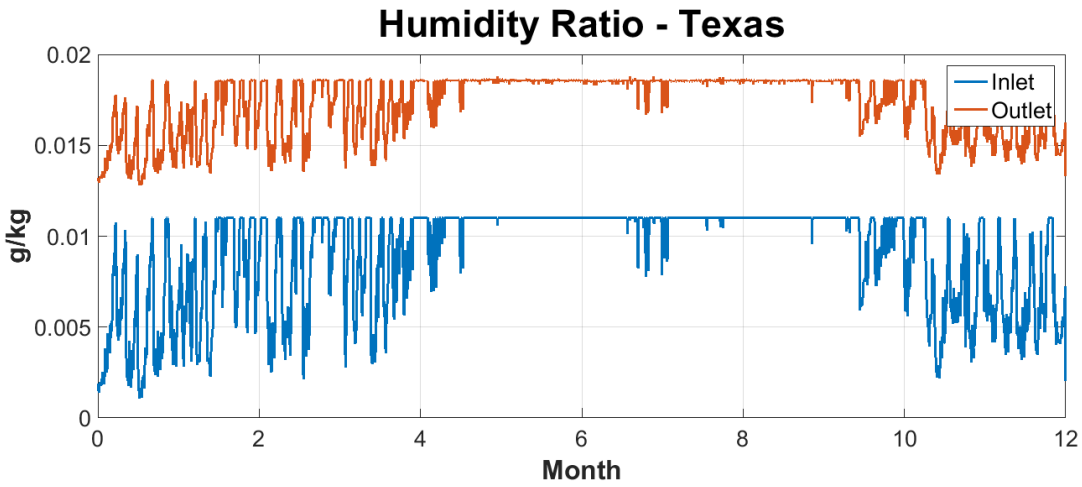

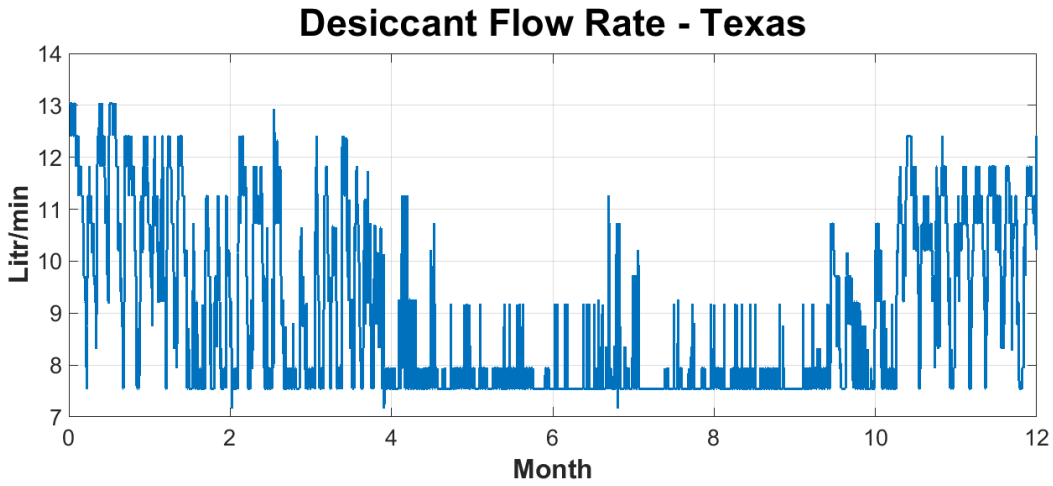
Desiccant Flow Rate - Texas
Litr/min
Month
14
13
12
11
10
9
8
7
0
2
4
6
8
10
12

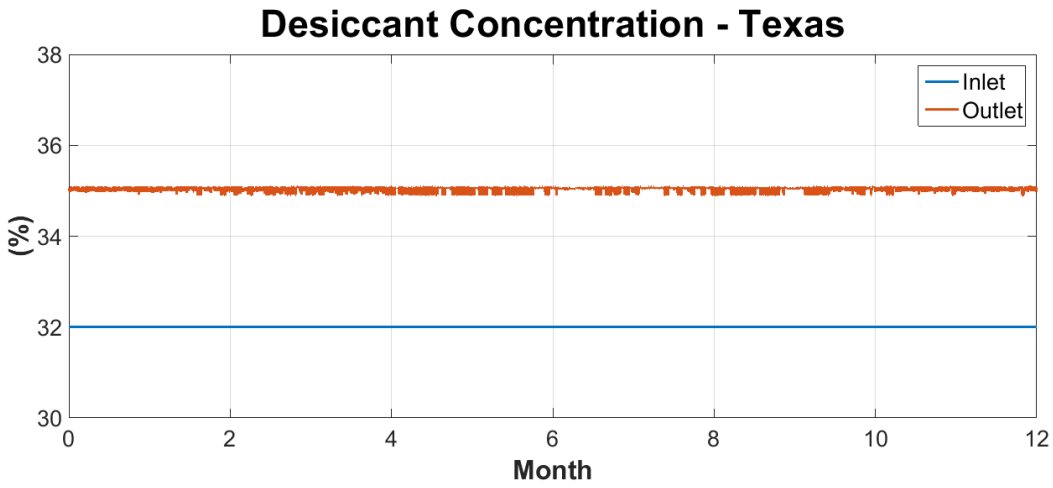
Desiccant Concentration - Texas
(%)
Month
Inlet
Outlet
38
36
34
32
30
0
2
4
6
8
10
12

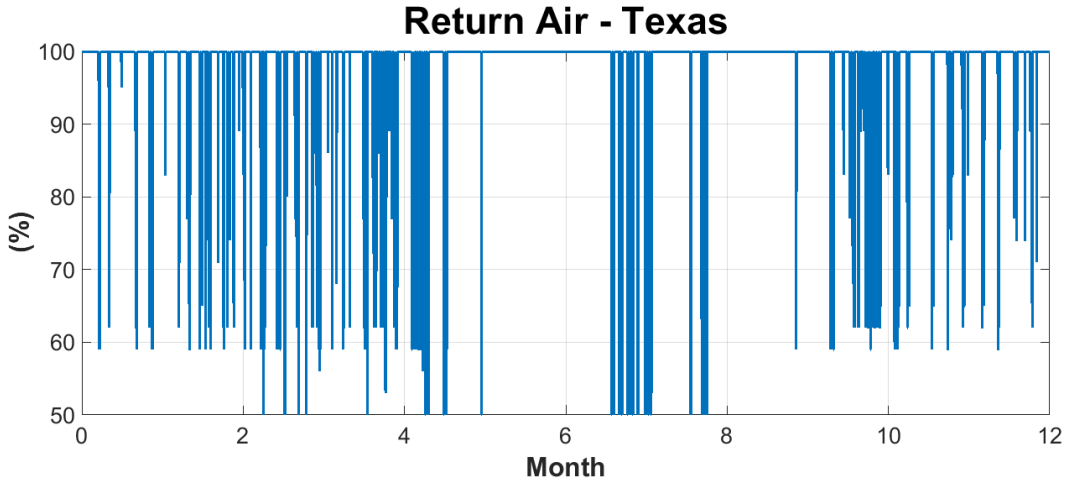
Return Air - Texas
(%)
Month
100
90
80
70
60
50
0
2
4
6
8
10
12

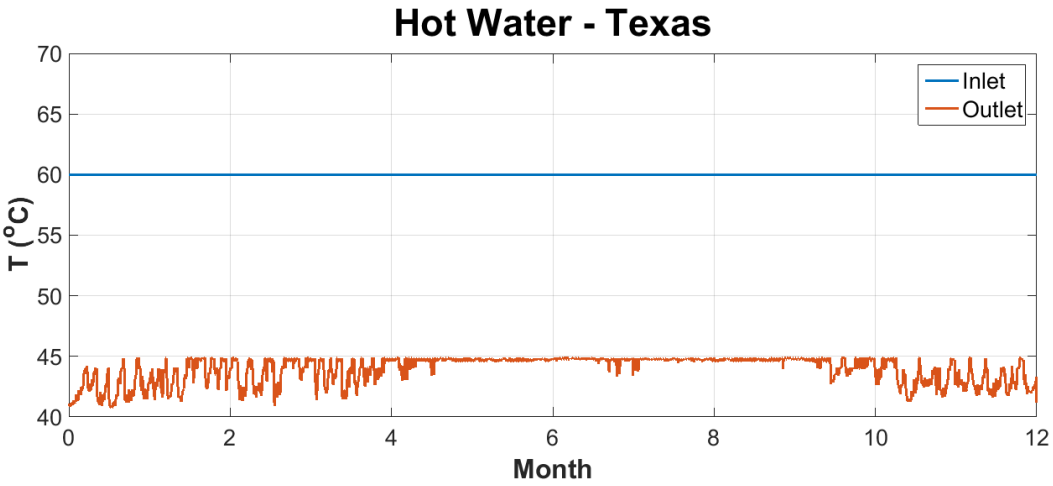

Texas Dehumidifier:

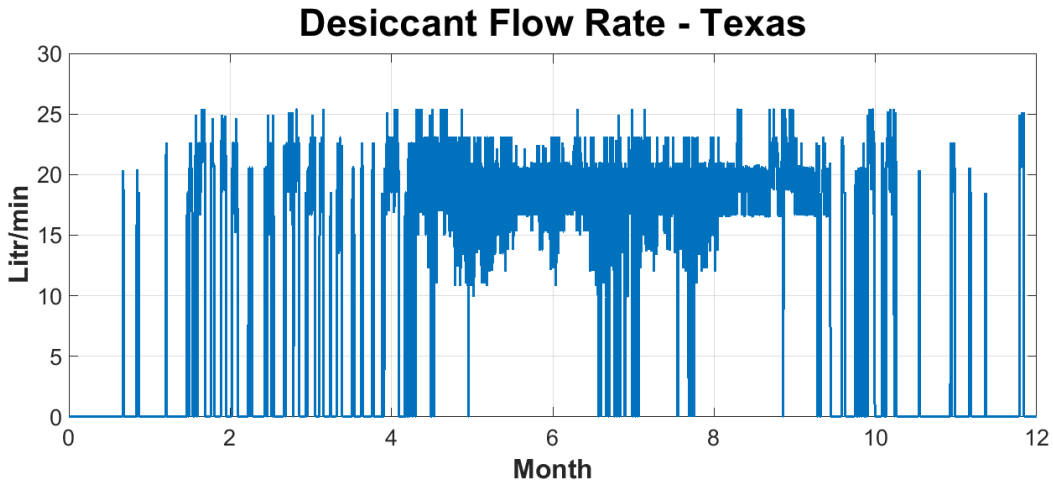

Iowa Regenerator:

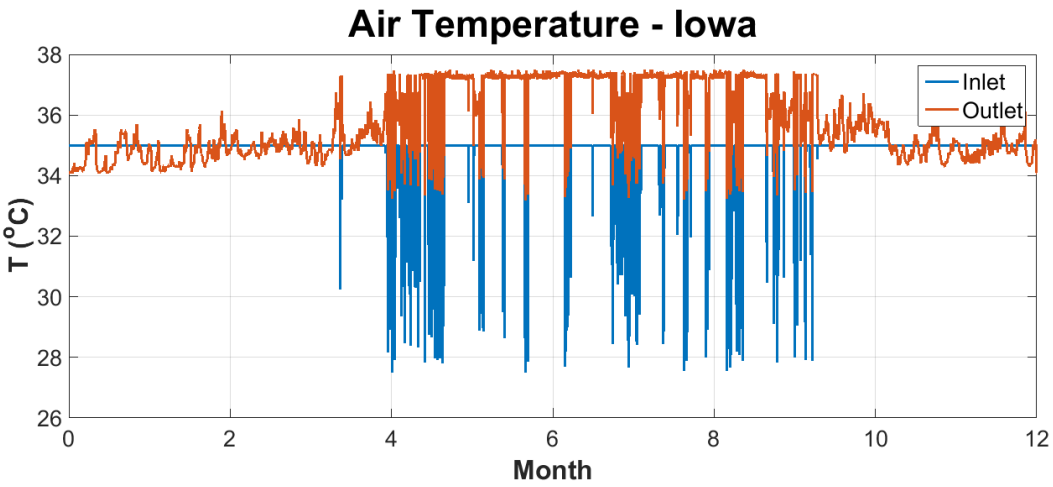

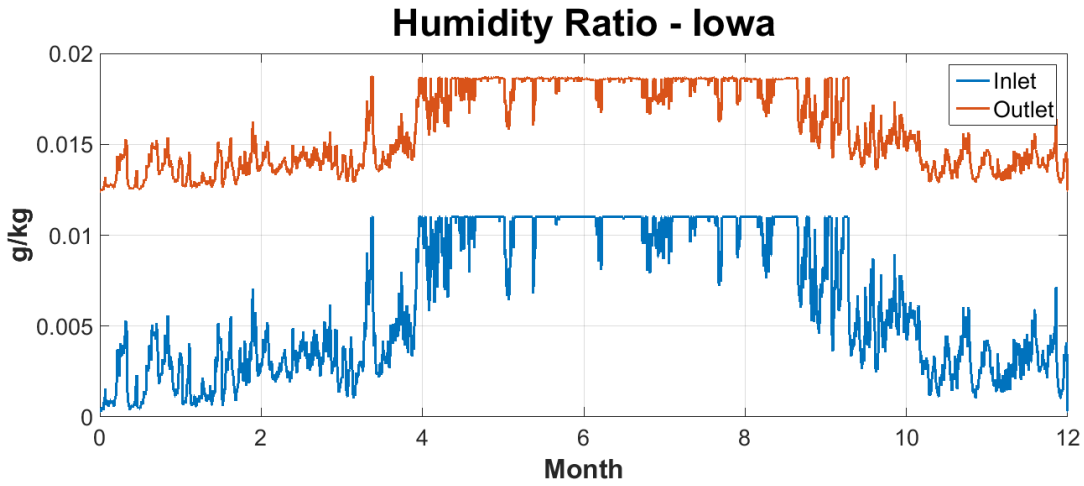
Humidity Ratio - Iowa
Inlet
Outlet
g/kg
0.02
0.015
0.01
0.005
0
0
2
4
6
8
10
12
Month

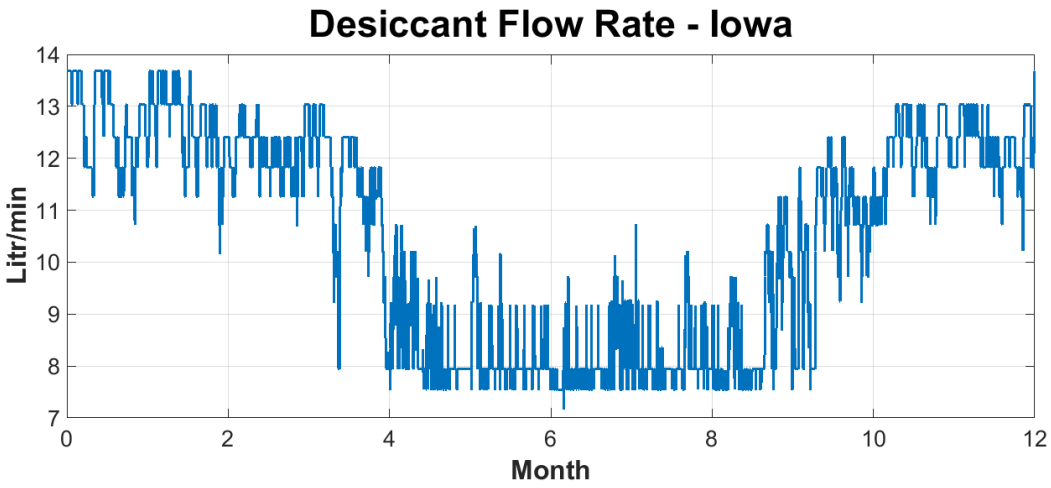
Desiccant Flow Rate - Iowa
Litr/min
14
13
12
11
10
9
8
7
0
2
4
6
8
10
12
Month

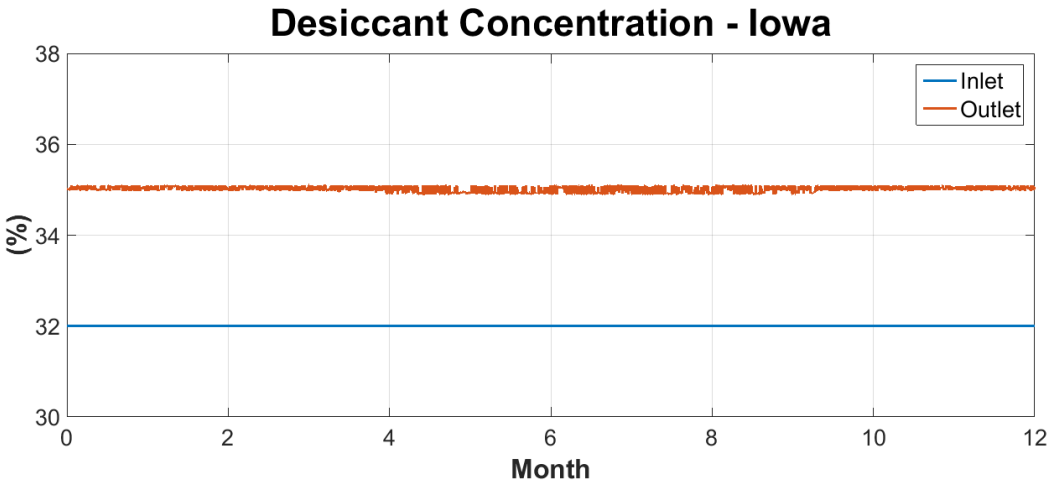
Desiccant Concentration - Iowa
Inlet
Outlet
(%)
38
36
34
32
30
0
2
4
6
8
10
12
Month

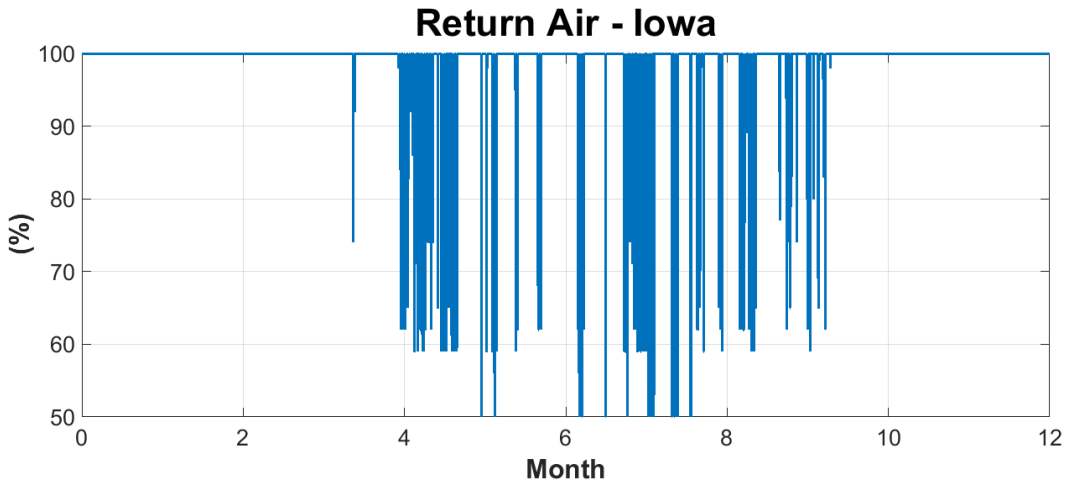

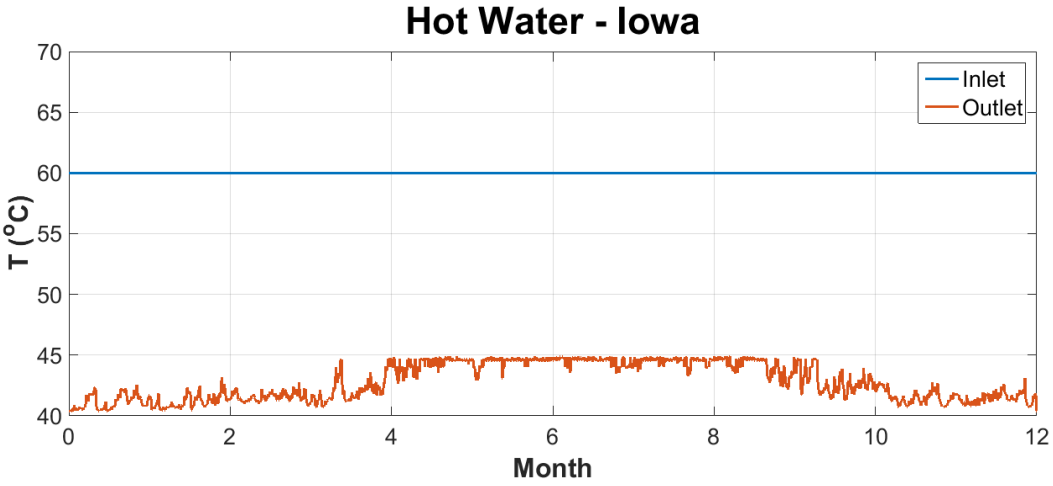

Iowa Dehumidifier: